EMMANUEL JESÚS VÁZQUEZ PEÑA

SIMULATION OF A SERIES HYBRID ELECTRIC VEHICLE POWERED BY BRAZILIAN HYDRATED ETHANOL ENGINE

Dissertação apresentada ao Departamento de Pós-Graduação em Engenharia Mecânica da Universidade Federal de Minas Gerais, como requisito parcial para a obtenção do título de Mestre em Engenharia Mecânica

Orientador: Prof. Dr. José Guilherme Coelho Baeta

BELO HORIZONTE

2019

V335s

Vázquez Peña, Emmanuel Jesús.
Simulation of a series hybrid electric vehicle powered by Brazilian hydrated ethanol engine [recurso eletrônico] / Emmanuel Jesús Vázquez Peña. - 2019.
1 recurso online (xx, 225 f. : il., color.) : pdf.

Orientador: José Guilherme Coelho Baêta.

Dissertação (mestrado) - Universidade Federal de Minas Gerais, Escola de Engenharia.

Anexos e apêndices: f. 175-224.

Bibliografia: f. 167-174.

Exigências do sistema: Adobe Acrobat Reader.

1. Engenharia mecânica - Teses. 2. Automóveis - Consumo de combustíveis - Teses 3. Combustíveis para motores - Teses. I. Baêta, José Guilherme Coelho. II. Universidade Federal de Minas Gerais. Escola de Engenharia. III. Título.

CDU: 621 (043)

Ficha catalográfica: Biblioteca Profº Mário Werneck, Escola de Engenharia da UFMG

UNIVERSIDADE FEDERAL DE MINAS GERAIS
PROGRAMA DE PÓS-GRADUAÇÃO EM ENGENHARIA MECÂNICA
Av. Antônio Carlos, 6627 - Campus Universitário
31270-901 – Belo Horizonte – MG
Tel.:+55 31 3409.5145
E-mail: cpgmec@demec.ufmg.br

"SIMULATION OF A SERIES HYBRID ELECTRIC VEHICLE POWERED BY BRAZILIAN HYDRATED ETHANOL ENGINE"

EMMANUEL JESUS VAZQUEZ PEÑA

Dissertação submetida à Banca Examinadora designada pelo Colegiado do Programa de Pós-Graduação em Engenharia Mecânica da Universidade Federal de Minas Gerais, como parte dos requisitos necessários à obtenção do título de **"Mestre em Engenharia Mecânica"**, na área de concentração de **"ENERGIA E SUSTENTABILIDADE"**.

Dissertação aprovada no dia 24 de maio de 2019.

Por:

Prof. Jose Guilherme Coelho Baeta
Orientador - Departamento de Engenharia Mecânica/ UFMG

Prof. Fabricio Jose Pacheco Pujatti
Departamento de Engenharia Mecânica/ UFMG

Prof. Ramon Molina Valle
Departamento de Engenharia Mecânica/ UFMG

Prof. Fernando Antonio Rodrigues Filho
Centro Federal de Educação Tecnológica de Minas Gerais

Prof. Luís Carlos Monteiro Sales
Pontifícia Universidade Católica de Minas Gerais/PUC-MINAS

DEDICATION

Este trabalho foi somente possivel devido ao suporte de meus pais, meu irmão, minha esposa e sua família.

Também quero agradecer a meus professores, companheiros e servidores da pos-graduação pela sua ajuda e suporte. Gostaria de agradecer especialmente a meu orientador José Guilherme Baeta e a meus companheiros Vinicius Roso e Thiago Silva pela assistência e colaboração que permitiu a realização e conclusão desta pesquisa.

ACKNOWLEDGEMENT

This work was possible due to the Conselho Nacional de Desenvolvimento Científico e Tecnológico (CNPq), which provided a scholarship and financial support to the author.

RESUMO

A busca de segurança energética e de redução em emissões de efeito estufa impulsou a comercialização de veículos híbridos elétricos (HEVs) e de combustíveis alternativos como duas possíveis soluções, de forma separada e não em conjunto. É bem sabido que os HEVs apresentam um menor consumo de combustível que os veículos convencionais, enquanto os veículos à etanol apresentam maior consumo que os veículos à gasolina. A presente dissertação analisa o uso de etanol hidratado (E100) em HEVs e seu efeito no consumo de combustível. Para isso, desenvolveu-se um modelo de HEV em série no software GT-Suite, o qual utilizou dados experimentais de dois motores de combustão interna, ambos operando com E100. Um deles foi o motor Ford Sigma 1.6L flex-fuel, o outro foi um motor protótipo sobrealimentado de 1.0L desenhado para operar exclusivamente com E100, o qual pode, ou não, operar com injeção de água. As simulações abrangeram 5 ciclos de condução standard e 2 ciclos em condições de condução reais. Os resultados mostraram que, nos ciclos urbanos, o modelo HEV em série apresentou menores consumos de combustível que em um modelo de veículo convencional utilizando o mesmo motor Ford Sigma flex-fuel. Também, obteve menores consumos que veículos convencionais à gasolina e à diesel; em alguns casos, teve menores consumos que HEVs com motor à gasolina e, inclusive, com motor HCCI. Da mesma forma, o emprego de injeção de água no motor apresentou menores consumos, que sem usar ela. Em conclusão, o uso de E100 em HEVs em serie se mostra como uma opção viável para diminuir o consumo de combustível nos veículos de aplicação urbana. Porém, o maior desafio para aplicar está tecnologia em outros países é o funcionamento em frio, o qual é agravado nos HEVs devido ao funcionamento intermitente do motor.

Palavras Chave: Veículos Híbridos Elétricos; Etanol hidratado; Consumo de Combustível; HEV, e; E100.

ABSTRACT

The search for energy security and lower greenhouse gas emissions promoted the commercialization of Hybrid Electric Vehicles (HEVs) and alternative fuels as two separated solutions, instead of together. It is well known that HEVs present better fuel consumption than conventional vehicles, contrarily; vehicles running on ethanol presents lower fuel consumption than vehicles running on gasoline. This thesis analyzes the use of Brazilian hydrated ethanol (E100) in HEVs and its effects on fuel consumption. Therefore, a series HEV model was developed in the GT-Suite software, which used experimental data of two internal combustion engines, both running on E100. The first engine was a Ford Sigma 1.6L flex-fuel while the other engine was a supercharged 1.0L prototype designed to operate exclusively with E100, which can operate with water injection. The simulations covered 5 standard driving cycles and 2 real-world driving cycles. The results showed that, in urban driving cycles, the series HEV model presented lower fuel consumptions than a conventional flex-fuel vehicle model with the same Ford Sigma flex-fuel engine. Furthermore, it also obtained lower consumptions than conventional gasoline and diesel vehicles; in some cases, it also had lower consumptions than HEVs with gasoline engines and, even, with HCCI engines. Similarly, the use of water injection presented better consumptions than without using it. In conclusion, employing E100 in HEVs looks like a viable option to diminish fuel consumption for urban vehicles. Nonetheless, the biggest challenge to apply this technology in other countries could be its cold start operation, which is exacerbated due to the start/stop operation of the HEV’s engine.

Keywords: Hybrid Electric Vehicles; Brazilian hydrated ethanol; Fuel consumption; HEV, and; E100.

ABBREVIATIONS

AC – Alternating Current

BDC – Bottom Dead Center

BLDC – Permanent Magnet Brushless DC

BMEP – Brake Mean Effective Power

BOT – Beginning of Test

CO2e – equivalent Carbon dioxide

CTM – Centro de Tecnologia da Mobilidade

DC – Direct Current

E10 – Fuel mixture of 10% ethanol and 90% gasoline

E100 – Brazilian hydrated ethanol

E5 – Fuel mixture of 5% ethanol and 95% gasoline

EC – Electric-equivalent Circuit

EREV – Extended Range Electric Vehicle

EV – Electric Vehicle

EVC – Exhaust Valve Close

EVO – Exhaust Valve Opening

FCEV – Fuel Cell Electric Vehicle

FMEP – Frictional Mean Effective Power

FTP-75 – Federal Test Procedure City Driving Cycle

GHG – Green House Gas

HCCI – Homogeneous Charge Compression Ignition

HEV – Hybrid Electric Vehicle

HF – Hibridization Factor

HSD – Hybrid Synergy Drive

HWFET – Highway Fuel Economy Driving Schedule

ICE – Internal Combustion Engine

IM – Induction Machine

IMEP – Indicated Mean Effective Power

INL – Idaho National Laboratory

IPM – Interior Permanent Magnet

IVC – Intake Valve Close

IVO – Intake Valve Opening

JC08 – Japan Chassis 08

LCA – Life Cycle Assessment

Li-ion – Lithium-ion battery

LTC – Low Temperature Combustion

MBT – Maximum Brake Torque

MEP – Mean Effective Power

MG1 – Motor Generator 1

MG2 – Motor Generator 2

MON – Motor Octane Number

MPC – Model Predictive Control

Na-NiAlCl2 – Sodium-Nickel Chloride battery

NEDC – New European Driving Cycle

Ni-MH – Nickel Metal Hydride battery

OCV – Open Circuit Voltage

PHEV – Plug-in Hybrid Electric Vehicle

PM – Permanent Magnet

PMEP – Pumping Mean Effective Power

PMP – Pontryagin's Minimum Principle

PWM – Pulse Width Modulation

RC – Resistor-Capacitor network

RCCI – Reactivity Controlled Compression Ignition

RCL – Rotor Copper Losses

RMS – Root Mean Square

RON – Research Octane Number

RTS – Regional Travel Survey

SCAG – Southern California Association of Governments

SCL – Stator Copper Losses

SFC – Specific Fuel Consumption

SI – Spark Ignition

SOC – State of Charge

SOH – State of Health

SPM – Surface Permanent Magnet

SRM – Switched Reluctance Machinw

SUV – Sport Utility Vehicle

TDC – Top Dead Center

UDDS – Urban Dynamometer Driving Schedule

UFMG – Universidade Federal de Minas Gerais

US06 – Suplemental Federal Test Procedure Aggresive Driving Cycle

USA – United States of America

USD – United States Dollars

VIN – Vehicle Identification Number

VSP – Vehicle Specific Power methodology

VVT – Variable Valve Timing

WI – Water Injection

WLTC – Wolrdwide Harmonized Light Duty Driving Test Cycle

LIST OF FIGURES

LIST OF TABLES

TABLE OF CONTENTS

1 INTRODUCTION

The transport sector is fundamental for every country's development, however, the increase of vehicles that burn fossil fuels generates two problems: increase of greenhouse gas (GHG) emissions and depletion of non-renewable fuels. The increase in GHG emissions is not only crucial for the mitigation of climate change but also for human health, since a big concentration of these gases are toxic to human health. In the year 2016, 9 out of 10 people worldwide breathed polluted air and approximately 4.2 million deaths were caused by exposure to ambient air pollution (WORLD HEALTH ORGANIZATION, 2018).

Just in Brazil, the total fleet growth from 64.8 million vehicles in 2010 to an estimated of 93.8 million in 2016. From which approximately 54.6% of the total fleet where cars, while motorcycles represent 22.3% (IBGE, 2016). An important characteristic of the Brazilian fleet is its high percentage of flex-fuel vehicles, those that work with gasoline, ethanol or any blend between both fuels. In the year 2017, the percentage of new flex-fuel light commercial vehicles and passenger cars were 88.6%. In contrast, 8.1% were diesel, 3.2% were gasoline, and 0.2% were hybrid or electric vehicles (ASSOCIAÇÃO NACIONAL DOS FABRICANTES DE VEÍCULOS AUTOMOTORES, 2018).

As the fleet continues to grow, different approaches have been researched to solve both problems. One approach focuses on the development of vehicles based on different energy sources, like renewable fuels or electricity. The other approach focuses on developing techniques that improve engine combustion and fuel consumption, making engines less polluters and more efficient. Among the main technologies for reducing fuel consumption in engines are stratified combustion, variable valve process, variable compression ratio, reduction of engine size (downsizing), and hybridization of thermal engines with electric motors.

The renewable fuels used in gasoline engines are usually alcohols, while in diesel engines are usually esters. Bioethanol is the most common renewable fuel used in Brazil, which is obtained from sugarcane fermentation. Renewable fuels can produce lower emissions, as reported in some studies from Brazilian bioethanol. A previous study showed that a flex-fuel vehicle using Brazilian bioethanol produces 5.1 times less equivalent carbon dioxide (CO_2e) than using pure gasoline, considering well to wheel emissions. This represents an 80% reduction of GHG emissions. In addition, Brazilian gasoline is added with 23% ethanol meaning that Brazilian gasoline releases 18% less GHG than pure gasoline (SOARES et al., 2009).

On the other hand, the idea of downsizing is to operate the engine in regions of better efficiency; this is done by reducing the engine displacement and operating it at higher loads. This is because the pumping losses generated by the throttle are bigger when the engine runs under low load conditions, therefore, obtaining lower efficiency than at higher loads. At the same time, operating at higher loads means higher risks of auto-ignition of the fuel mixture, also known as knocking. The main challenge of downsizing is improving the engine efficiency and, at the same time keeping the same torque and power output without increasing the occurrence of engine knocking (LEDUC et al., 2003).

One approach for downsizing is the use of ethanol as fuel, either pure or blended with gasoline. Since ethanol has a higher octane number, its use reduces the knock tendency, which in turn, allows for higher compression ratios and higher boosts in turbocharged engines (BORETTI, 2012). In addition, its faster laminar flame speed improves the combustion process and reduces knock tendency; furthermore, its oxygen content improves the combustion in the engine, decreasing hydrocarbon emissions (WANG et al., 2017).

Another trend is to increment the participation of electric motors into the vehicle's powertrain; this trend is usually known as vehicle electrification. An electric vehicle (EV) is a vehicle that is entirely propelled by an electric motor, instead of an internal combustion engine (ICE). Full EVs have zero tailpipe emissions, which contributes to the reduction of air pollution in the cities. Instead, the CO_2 emission are produced by the electric power plants.

Nonetheless, the emissions generated by EVs are transferred to the energy industry; thus, the emissions of an EVs depend on how the electricity is produced. In the case of Brazil, its electric matrix emitted 160.4 kg of CO_2 for every MWh of electricity produced, for the year 2014. This is 3 times less than the United States and 2.2 times less than the European Union (see figure 1). Furthermore, the Brazilian emissions due to electricity generation were even less in the year 2016 than in 2014, with 101.3 kg of CO_2 per MWh of electricity generated (EMPRESA DE PESQUISA ENERGÉTICA, 2017).

FIGURE 1 – KILOGRAMS OF CO_2 EMITTED FOR EVERY MWH OF ELECTRIC ENERGY GENERATED, FOR DIFFERENT COUNTRIES

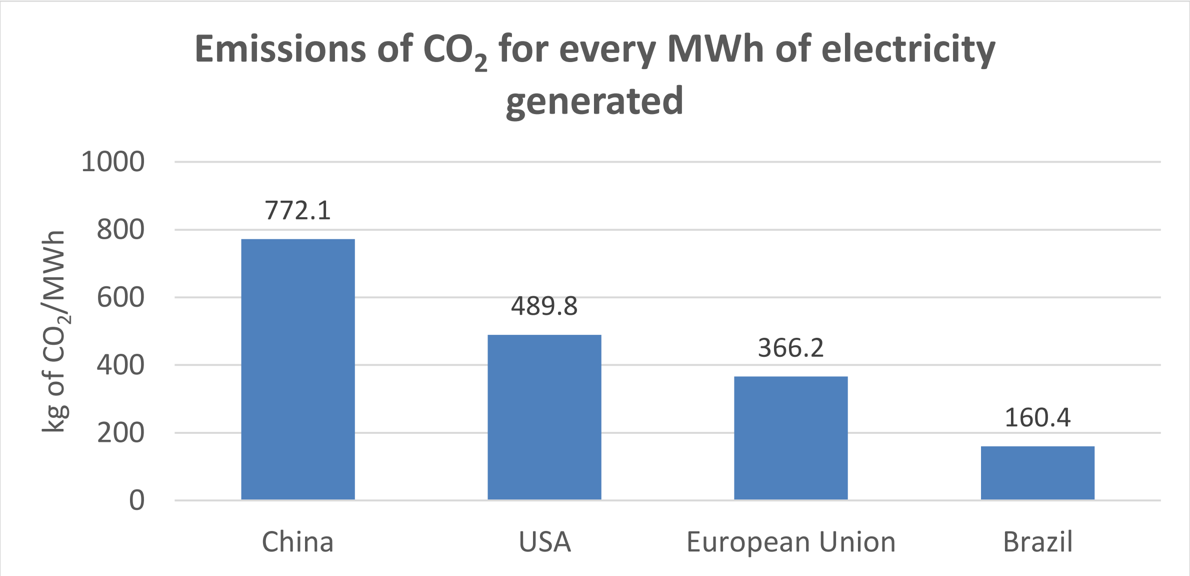

Source: Adapted from EPE (2017)

The biggest disadvantages from full EVs are their long recharge times and limited range per battery charge; additionally, they are also more expensive and heavier than vehicles with ICE. These limitations are inherent from the actual battery technology, however, they can be surpassed by hybrid vehicles.

A hybrid electric vehicle (HEV) use both ICE and electric motors. An HEV can avoid the problems of limited range and long recharge time by using the engine to recharge the battery while traveling. Depending on the HEV architecture, the ICE is still used to move the vehicle. In addition, HEVs consume less fuel, are less polluters, and are more efficient than conventional vehicles, but they are more expensive because of the need of two prime movers, bigger batteries, and more complex control of the powertrain. Although, the price of HEVs varies depending on market conditions, government incentives, electricity generation and way of use (HUTCHINSON; BURGESS; HERRMANN, 2014).

Little research was found about HEVs using ethanol fuels, almost all research focus on gasoline and diesel fuels. Since ethanol engines and HEV technologies seem complementary for downsizing, the combination of both technologies could generate further improves in fuel consumption and emissions. This could represent a sustainable and low investment solution, as ethanol engines and HEVs are commercially available and can be considered mature technologies. In addition, there is no need for increasing charging infrastructure, as HEVs can recharge their batteries with the engine generator. Moreover, the lower well to wheel emissions from ethanol engines and the adoption of plug-in hybrid electric vehicles (PHEV) could let to further reduction of emissions, due to the low emissions of the Brazilian electric matrix.

1.1 MAIN OBJECTIVE

This work explores the implementation of engines running with Brazilian hydrated ethanol (E100) into hybrid electric vehicles. Since the principal goal of HEVs is to increase the efficiency of vehicles, this work focuses only on the fuel consumption. Therefore, a simulation is carried out using data of two different engines, a Ford Sigma 1.6L flex-fuel engine and a prototype 1.0L turbocharged engine, both running with E100 fuel. In addition, both engines are analyzed for several driving cycles and for two different vehicle characteristics. Thus, the specific objectives are as follow:

- Develop a computational model of a hybrid electric powertrain, with the maps of an engine utilizing E100;
- Simulate the HEV model for the FTP-75, HWFET, US06, NEDC, WLTC Class 3 standard driving cycles, and two real-world driving cycles.
- Simulate the HEV model for two different vehicle characteristics;
- Analyze fuel consumption and performance of the HEV;
- Compare the results with previous studies of gasoline and diesel HEVs.

2 LITERATURE REVIEW

The literature review is divided into five sections. First, section 2.1 presents the definition of an HEV and the classification of different HEVs, their powertrain architectures, and their main control strategies; in addition, it summarizes the main characteristics and differences among the different HEVs architectures.

Section 2.2 presents the different models used for batteries and supercapacitors, ending with a brief review of the main battery technologies and its characteristics.

Next, section 2.3 focus on electric machines. The electric machines covered are: the DC machine, synchronous machines, induction machines, and switched reluctance machines. The operation of each machine is explained, as well as their characteristic torque curves and the equations that govern them. This section ends by presenting some comparisons among different electric motors used for automotive applications.

Then, section 2.4 presents the fundamentals of ICEs, together with their main operation characteristics, and their influence on the fuel consumption and performance of the engine. Additionally, it introduces the main techniques used for improving the performance of ICEs, together with the characteristics and properties of gasoline and ethanol fuels.

Finally, section 2.5 summarizes all the studies found on HEVs, it highlights the little research about HEVs using ethanol. Furthermore, table 14 recapitulate the main studies found on the topic and their gains in fuel consumption.

2.1 HYBRID ELECTRIC VEHICLES

In this work, a conventional vehicle is defined as one where the propulsion energy comes only from the chemical energy of a fuel and is transformed in mechanical energy by the use of a heat engine. Observe that this definition includes any type of fuel, such as gasoline, diesel, or ethanol.

On the other hand, an HEV is defined as “a vehicle in which propulsion energy is available from two or more kinds or types of energy sources or converters, and at least one of them can deliver electrical energy” (SHEN; SHAN; GAO, 2011, p. 2). Other propulsion sources could come from hydraulic energy, solar energy, a flywheel, and fuel cells. Nevertheless, this work focuses on vehicles where the propulsion comes from chemical or electrical energy.

Compared to a conventional vehicle, HEVs can save fuel for three main reasons:

1. It allows to recover some part of the vehicle’s kinetic energy and store it in the battery for later use, while braking or in a downslope.
2. It allows the use of ICE with smaller displacements without compromising vehicle performance.
3. It allows the ICE to operate in its most efficient point.

The main issue of HEVs is to define the optimization of the power-flow that obtain the best results (SHEN; SHAN; GAO, 2011). Hybrid electric vehicles can be classified in two ways: by their hybridization factor or by their powertrain architecture.

Section 2.1.1 shows the different type of HEVs according to its hybridization factor. While section 2.1.2 contains a review of the different powertrain architectures of HEVs. Then, section 2.1.3 presents a brief evaluation of different HEVs architectures. Finally, section 2.1.4 reviews different control strategies for HEVs.

2.1.1 Classification by Hybridization Factor

The hybridization factor could be seen as a way to measure the participation, and capabilities, of the electric motor on the vehicle’s propulsion. The Hybridization Factor (HF) is given by equation 1:

$$HF = \frac{P_{electric}}{P_{electric} + P_{ICE}} \tag{1}$$

Where:

- HF is the hybridization factor;

- $P_{electric}$ is the power of the electric motor, and;
- P_{ICE} is the power of the internal combustion engine.

According to equation 1, a vehicle can be classified as follows:

Conventional vehicles (HF=0): their propulsion energy comes only from the chemical energy of a fuel, and is transformed by the use of an ICE. Do not have an electric motor, besides the starter motor.

Micro Hybrids (0<HF<0.1): their electric motor is a combination of alternator and starter motor, enabling the ICE to be constantly switched on or off. This is also known as the start-stop system. This system allows the engine to be turned off when the vehicle is not in motion, resulting in lower fuel consumption when frequent stops, as in urban operation.

Mild HEV (0.1<HF<0.25): in addition to the start-stop system, also can use the electric motor for ICE assistance during accelerations and for regenerative braking. Nevertheless, the electric motor does not have the ability to move the vehicle by itself.

Full HEVs (0.25<HF<0.5): can operate exclusively on electricity for limited distances, without producing tailpipe emissions. Different from EVs, the battery life and maximum speed are not such important parameters because the ICE also guarantees the vehicle propulsion.

Plug-in Hybrids (HF>0.5): their main difference with a full HEV is that a Plug-in Hybrid can be recharged from the grid. According to Poullikkas (2015), a PHEV must fulfill the next requirements: the battery must have a storage capacity of 4 kWh or greater, it must have a range of at least 16 km in full electric mode, and must be able to recharge by an external source. To accomplish this last requirement, the car is usually integrated with a converter from alternating current (AC) to direct current (DC).

The optimal battery size for a PHEV depends on whether the goal is to reduce fuel consumption, battery maintenance or vehicle emissions. Additionally, Plug-in Hybrids must be able to withstand deeper battery discharges than full HEVs and, thus, they need more durable and larger batteries while offering as many cycles as possible. Figure 2 shows the comparison between the battery life cycles and their depths of discharge regions for typical PHEVs and full HEVs.

Pure Electric Vehicles (HF=1): their propulsion comes entirely from an electric motor and, hence, do not have an ICE; their energy source comes entirely from the batteries, instead of fuel. Therefore, the batteries are the most important factor of an EV since the propulsion completely depends on them (HANNAN; AZIDIN; MOHAMED, 2014; MOREDA; MUÑOZ-GARCÍA; BARREIRO, 2016; POULLIKKAS, 2015).

FIGURE 2 – COMPARISON BETWEEN LIFE CYCLES OF PHEV'S AND FULL HEV'S BATTERIES, ACCORDING TO THE DEPTH OF DISCHARGE.

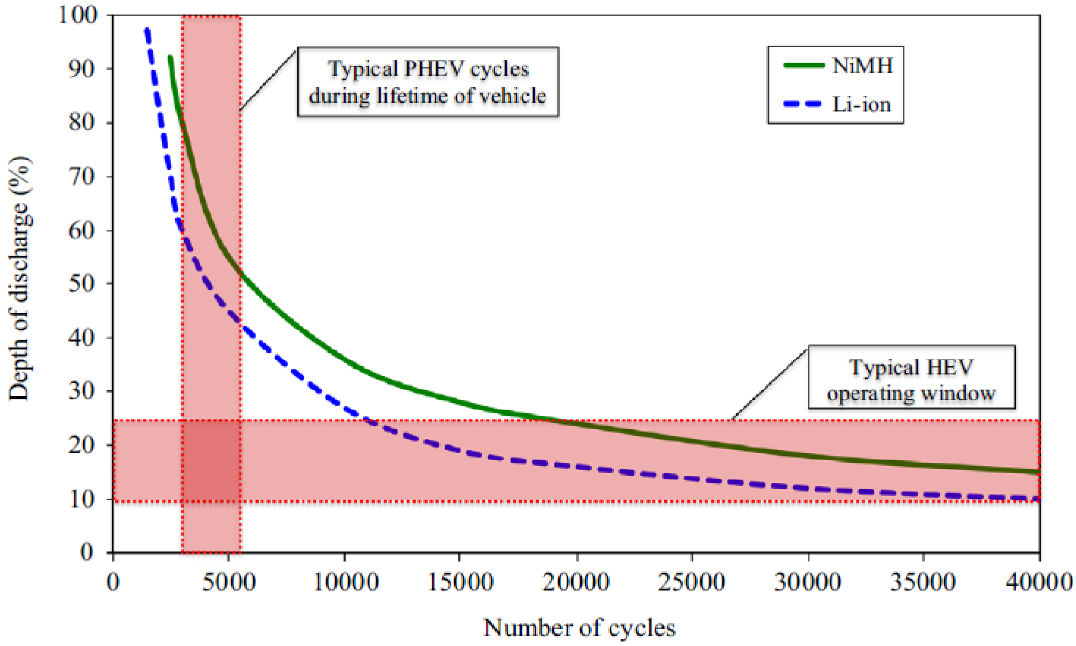

Source: Poullikkas (2015).

2.1.2 Classification by Powertrain Architectures

Traditionally HEVs have been classified by their mechanical connections into three types: series HEV, parallel HEV, or series-parallel HEV. These three configurations are shown in figure 3. Nevertheless, a complex HEV category can be added to include all the powertrain architectures that do not fit into any of the other three categories (CHAN, 2007; CHAU; WONG, 2002).

Besides the main three architectures, this work also focuses on the Hybrid Synergy Drive (HSD) adopted by Toyota; the series-parallel dual mode, and; the parallel all-wheel-drive architectures.

FIGURE 3 – MAIN TYPES OF POWERTRAIN ARCHITECTURES USED IN HEVS.

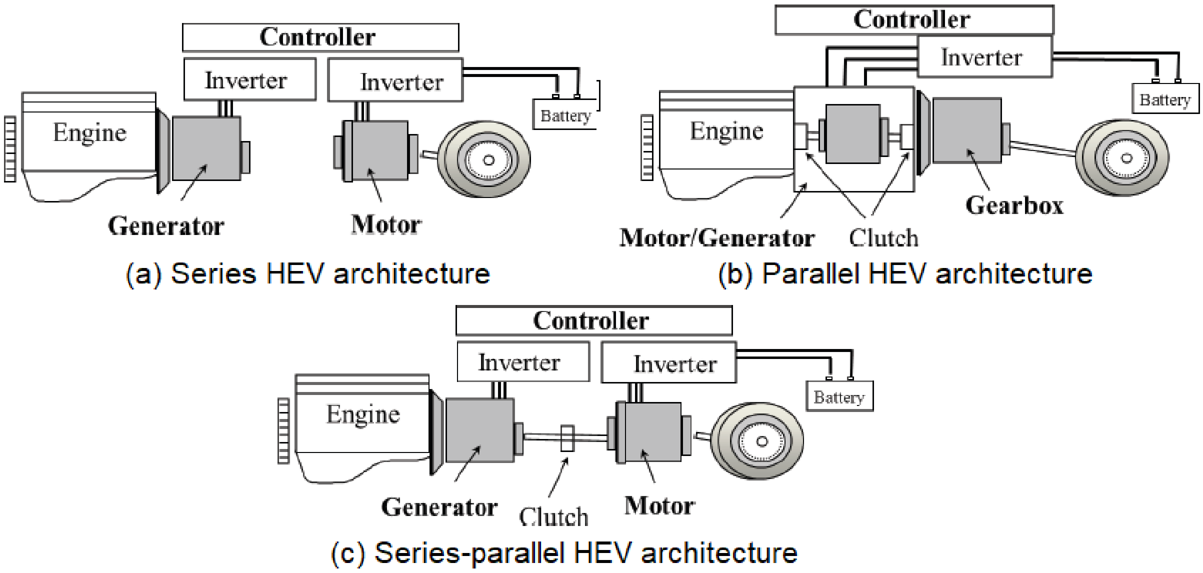

Source: Arata et al. (2014).

Series Architecture

Figure 3a shows the schematic of a series HEV powertrain. Notice that this architecture does not have mechanical connections between the ICE and the wheels; hence, the vehicle is driven exclusively by the electric motor. Because of this, the electric motor must satisfy all the power demanded by the wheels. On the other hand, the ICE functions as a generator allowing it to work at the point of maximum efficiency. This type of powertrain is widely used in heavy vehicles, buses and train locomotives (BAYINDIR; GÖZÜKÜÇÜK; TEKE, 2010; SHEN; SHAN; GAO, 2011).

Nevertheless, this architecture has low efficiency due to the various transformations of energy. This became evident in the next example, which analyzes the energy flow of a diesel-electric locomotive. First, the diesel engine receives the power from a fuel and transforms it into mechanical power with an efficiency “η_1”. Next, a generator coupled to the engine transforms the mechanical power into electrical power with an efficiency “η_2”. Later, the traction motors transform the electrical power into rotational mechanical power with an efficiency “η_3”. Finally, the gearing and wheels transform the rotational mechanical power into translational mechanical power with an efficiency “η_4”.

The main difference between a diesel-electric locomotive and a series HEV passenger car is that, normally, the locomotive does not use batteries. This means that the generator ensemble limits the total power of the traction motors (JEAN-MARC ALLENBACH, 2005).

Parallel Architecture

Figure 3b shows the schematic of a parallel HEV powertrain. Notice that this architecture does have a mechanical connection between the ICE and the wheels, contrary to the series architecture. Additionally, it only has one electric machine that acts as both motor and generator. The parallel architecture allows the electric motor and the ICE to provide power to the wheels at the same time or separately. Nevertheless, when the electric motor is powering the wheels, it cannot charge the batteries. Moreover, the speed of operation of the ICE depends on the power demanded by the wheels.

A common control method used in parallel HEVs is to maintain the ICE working at the maximum efficiency all the time. If the wheels require more power, then the electric motor is activated to supply it. On the contrary, if the ICE gives more power than needed by the wheels, the electric machine absorbs it and stores it in the batteries (BAYINDIR; GÖZÜKÜÇÜK; TEKE, 2010).

Nevertheless, parallel architectures can be a great limitation for hybridization of agricultural tractors. In agricultural tractors, a dedicated generator is of relevant importance since they do not only need to propel themselves but also need to transfer power to different gadgets (MOREDA; MUÑOZ-GARCÍA; BARREIRO, 2016).

Series-Parallel Architecture

Figure 3c shows the schematic of a series-parallel HEV powertrain. This architecture incorporates the features of the series and parallel architectures. As shown in figure 3, this architecture also has two electric machines, as in series architecture, but it has a mechanical connection between both electric machines. By using a clutch, it can disengage this mechanical connection to operate as a series HEV, or it can engage the clutch to operate as a parallel HEV.

The series-parallel architecture allows for more flexible control systems, but it is also more costly and complex to manufacture. In recent years, this architecture has become the standard for hybrid passenger vehicles (BAYINDIR; GÖZÜKÜÇÜK; TEKE, 2010; SHEN; SHAN; GAO, 2011).

Hybrid Synergy Drive Architecture

The most famous example of a series-parallel HEV is the Hybrid Synergy Drive (HSD), which is used in the Toyota Prius. The main difference between the series-parallel architecture motioned before and the HSD is the use of a planetary gear that couples together the ICE and the two electric machines without the need of a clutch.

In the HSD configuration, the transmission's planet carrier is connected to the engine, while the ring gear and sun gear are connected to the Motor Generator 1 (MG1) and Motor Generator 2 (MG2) respectively. Here, the MG1 is used predominantly as a generator, while MG2 is used as the traction motor and in regenerative braking. Figure 4 shows a planetary gear set and its ensemble, while figure 5 shows the complete powertrain architecture of a third generation Toyota Prius.

FIGURE 4 – SCHEMATIC OF THE HSD PLANETARY GEAR SET.

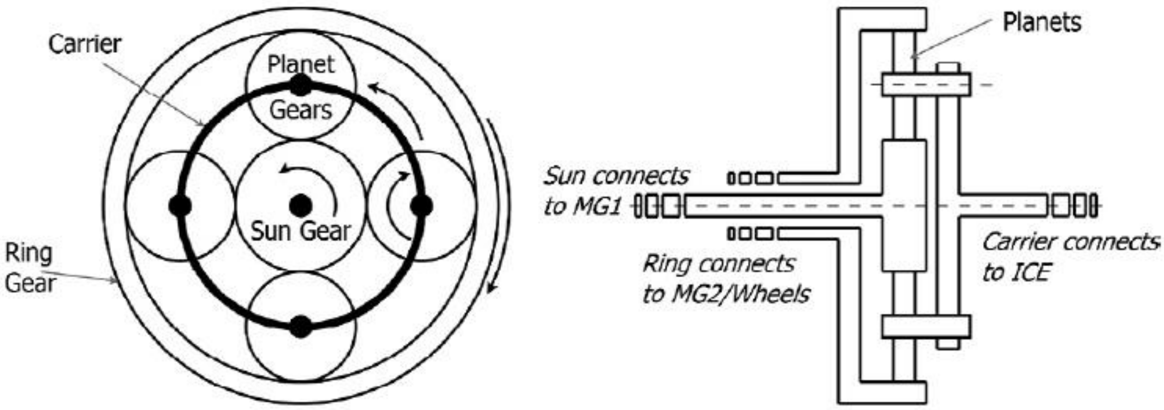

Source: Hutchinson, Burgess, and Herrmann (2014).

The use of a planetary gear allows to divide the engine force in two: one that transmits the force into the wheels and the other that drives the generator for battery recharge. Additionally, by controlling the speed of the MG1, the system can vary the gear ratio between the engine and the MG2, thus, eliminating the need for stepped gear shifting. Because of this, it is also known as an electronically-controlled continuously variable transmission.

An advantage of the HSD is its simple design since requires neither a clutch nor stepped gear shifting. But arguably its biggest advantage is that the engine load can be controlled by varying the outputs of MG1 and MG2. This means that the ICE can operate on the highest efficiency point for all operating speeds when supplying power to the wheels and, at the same time, the generator can absorb the extra torque to recharge the batteries (HUTCHINSON; BURGESS; HERRMANN, 2014)

Series-Parallel Dual Mode Architecture

The dual mode system has a similar operation to the HSD at low speeds and low loads, but it also has a second mode of operation designed for high speeds and high loads. Figure 6 shows that the system consists of an ICE, two electric motors, two planetary gear sets, and three clutches. The result is a system for vehicles with high power and torque that increases their efficiency during low loads. Due to its greater complexity, higher weight and higher cost this architecture is usually used in Sport Utility Vehicles (SUVs) and pickups (HUTCHINSON; BURGESS; HERRMANN, 2014).

FIGURE 5 – EXAMPLE OF THE HSD POWERTRAIN ARCHITECTURE FOUND IN THE 2013 TOYOTA PRIUS.

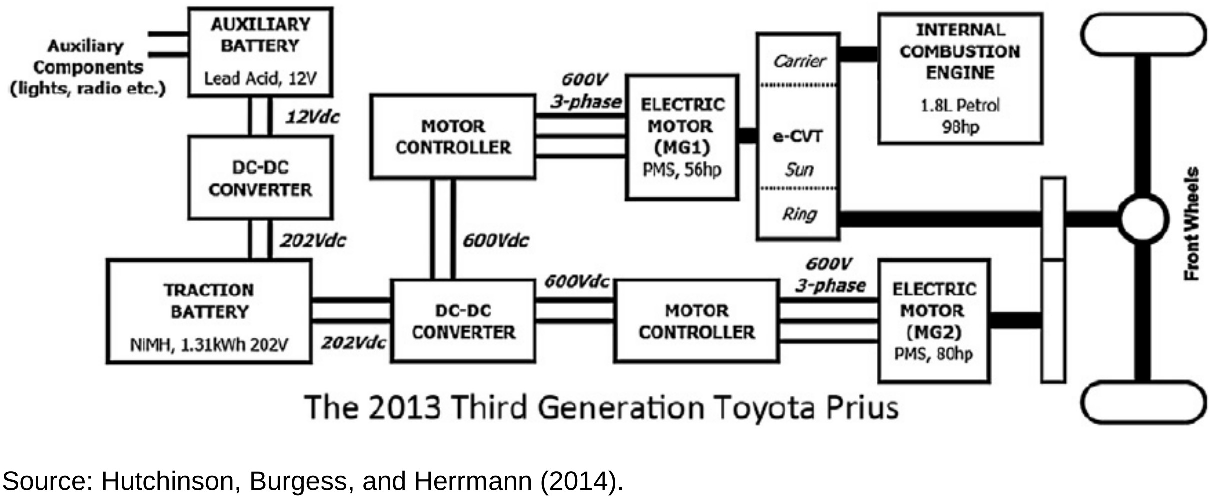

Source: Hutchinson, Burgess, and Herrmann (2014).

FIGURE 6 – EXAMPLE OF THE DUAL MODE IN SERIES-PARALLEL POWERTRAIN FOUND IN THE 2013 CHEVROLET TAHOE HYBRID.

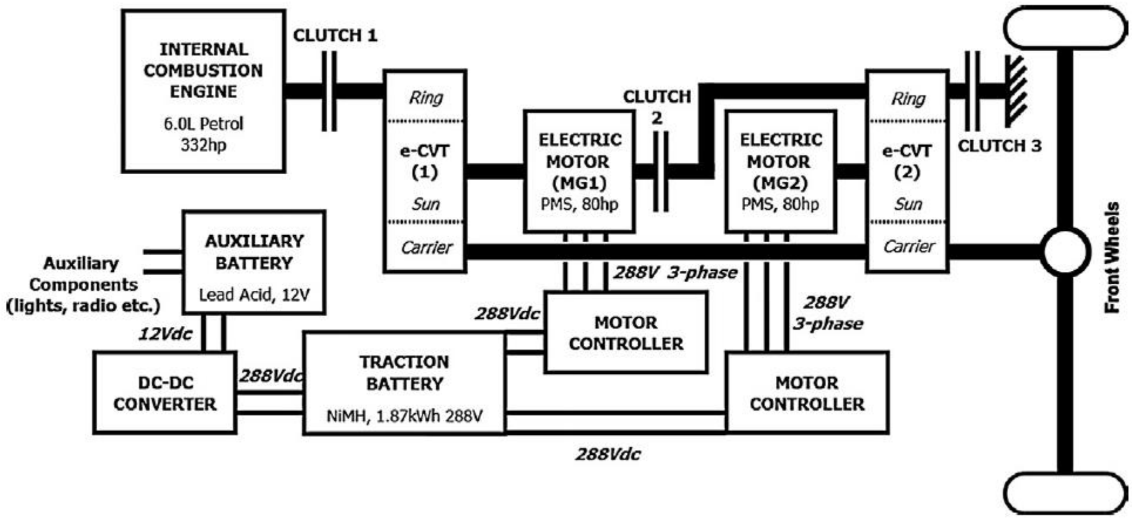

Source: Hutchinson, Burgess, and Herrmann (2014).

All-Wheel-Drive Parallel Architecture

This powertrain architecture can be found on the PSA Hybrid4 vehicles, from the Peugeot and Citroën manufacturers, and is presented in figure 7. It consists of connecting the electric motor to one axle, and connecting the ICE-generator ensemble to the other axle; resembling a parallel architecture. In this case, the generator is coupled to the ICE by a fixed gear ratio, which in turn is coupled to a clutch that allows it to disconnect from the front axle differential. On the other hand, the electric motor can be used for vehicle propulsion and for regenerative braking.

Nevertheless, this architecture allows for traction in the four wheels and, consequently, it has better regenerative braking capabilities. Wang, Guo, and Yang (2015) assessed the energy performance of an all-wheel-drive parallel architecture and found that fuel consumption decreased by 47.45% compared to a conventional powertrain. It also affirmed an increase in the regenerative braking performance, even working in conditions of low adherence.

FIGURE 7 – EXAMPLE OF THE ALL-WHEEL-DRIVE PARALLEL ARCHITECTURE FOUND IN THE 2012 PEUGEOT 3008 HYBRID4.

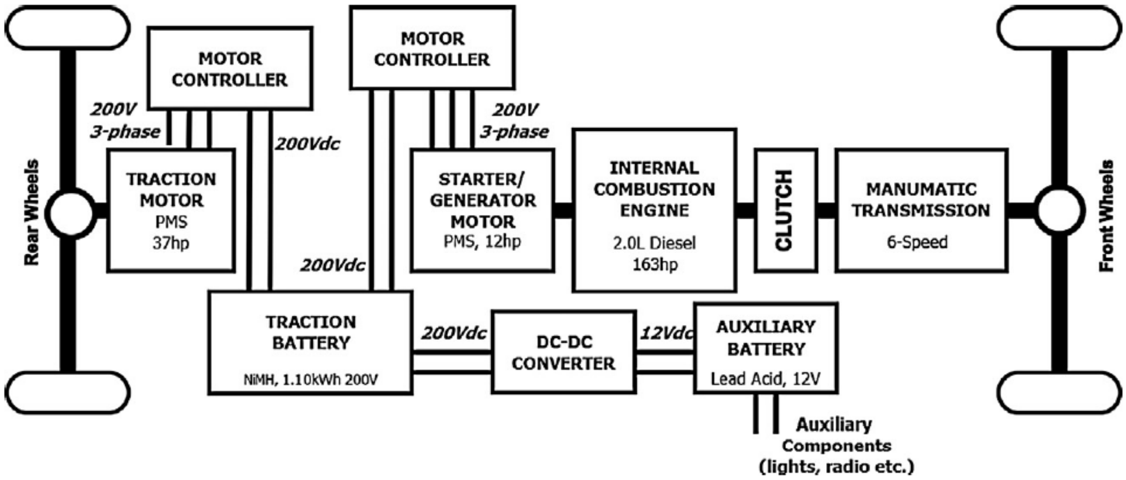

Source: Hutchinson, Burgess, and Herrmann (2014).

2.1.3 Evaluation of Different HEV Architectures

In comparison to conventional vehicles, HEVs can take advantage of the kinetic energy of the vehicle through regenerative braking, which otherwise is lost as heat. In addition, hybrid vehicles can operate the ICE in the maximum efficiency zone, thus, they can be designed with engines of smaller displacement without compromising the vehicle performance, which in turn allows the use of downsizing technologies.

On the other hand, the biggest challenge of HEVs is the control of power supplied to the wheels, this is due to the multiple energy sources found in HEVs (SHEN; SHAN; GAO, 2011). Moreover, including supercapacitors in the battery pack adds an extra system to control the power storage, which could be reflected in a higher initial cost of the vehicle.

Hutchinson, Burgess, and Herrmann (2014) conducted a Life Cycle Assessment (LCA) of emissions and total life cost for the markets of United States of America (USA) and the United Kingdom. They collected data from 44 different HEVs, covering the 6 different HEVs architectures that are available in the USA. The results showed that the Mild HEV had the lowest life cost for the highway cycle, while the series HEV and HSD Plug-in had the lowest life cost for the urban cycle. It is concluded that economic saves are highly dependent on the way the vehicle is used, as well as market conditions. They also noted that it is more important to match the battery life with the car life, rather than lowering the cost of the battery.

For the case of all-wheel-drive parallel architecture, Wang, Guo, and Yang (2015) evaluate the powertrain's energy of a transit bus with this architecture. The powertrain consisted of a natural gas engine, a Permanent Magnet (PM) synchronous motor, a PM synchronous generator, and a clutch. The authors found that fuel consumption decreased by 47.45% compared to a conventional powertrain and that the regenerative braking capabilities increased, even in low adherence conditions.

Finally, Asfoor, Sharaf, and Beyerlein (2014) simulated a conventional vehicle powertrain and three different HEV powertrains: series, parallel, and series-parallel architectures. All four powertrain models used the same 2.0L gasoline engine and covered the FTP-75, HWFET, US06, and NEDC driving cycles.

The results showed that the series-parallel HEV architecture had the best gas mileage in every cycle, with an average of 54.46% improvement compared to the conventional vehicle. On the other hand, the parallel architecture had better gas mileage than the conventional vehicle in all the driving cycle, however, it also had lower mileage than the series architecture in the NEDC. Finally, the series HEV architecture presented better gas mileage than the conventional vehicle in both the FTP-75 and NEDC driving cycles. Figure 8 presents the average gas mileage for the four powertrains and for each driving cycle.

FIGURE 8 – MILEAGE OBTAINED FOR FOUR DIFFERENT POWERTRAINS IN FOUR DIFFERENT DRIVING CYCLES

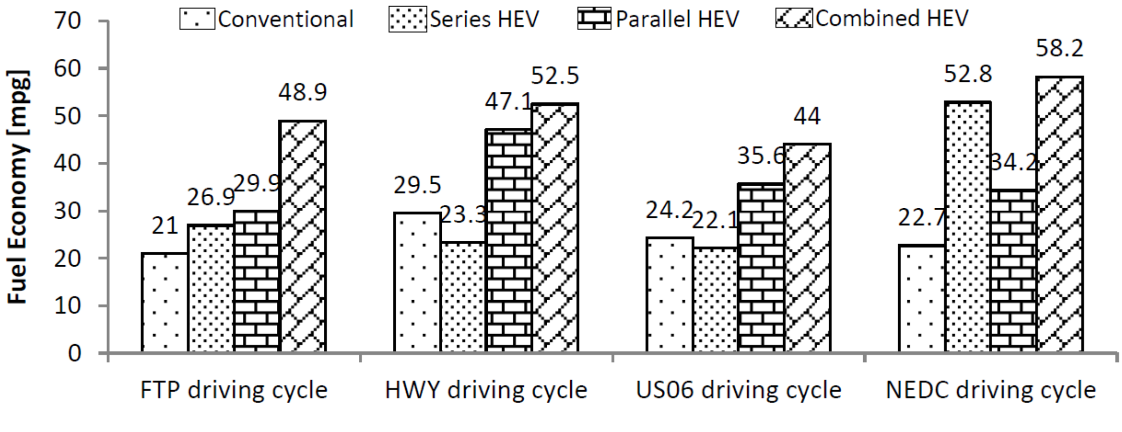

Source: Asfoor Sharaf and Beyerlein (2014).

2.1.4 Control Strategies of HEVs

The control strategies of hybrid vehicles are usually carried out aiming at one of the following objectives:

- Minimizing fuel consumption;
- Minimizing emissions of pollutants, or;
- Optimization of the driving performance.

This section explains the difference between rule based and global optimization control strategies, as well as, the difference between the charge depleting and charge sustaining modes. Figure 9 shows the different power management strategies that are possible for HEVs.

FIGURE 9 – DIFFERENT CONTROL STRATEGIES FOR HEVS.

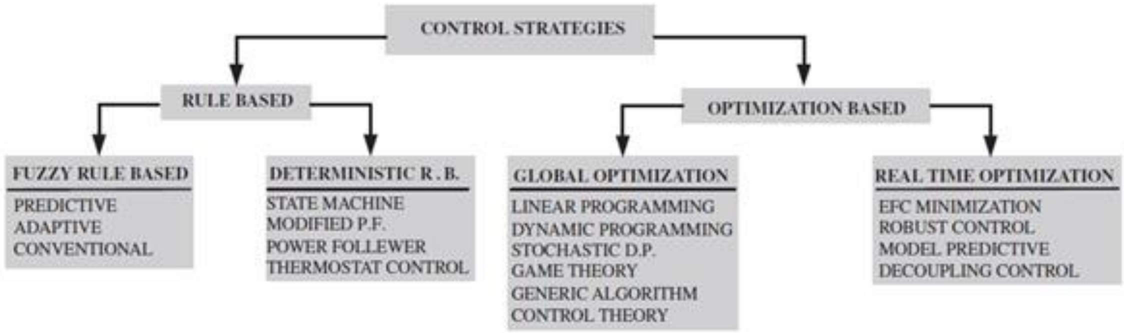

Source: Bayindir, Gözüküçük and Teke (2010).

Charge Depleting Mode

In charge depleting mode, the power of the battery is used to move the vehicle until a certain state of charge (SOC) is reached or until is completely discharged. Due to this, the autonomy and operation of the vehicle only depend on the energy of the battery. An example of charge depleting mode is a pure EV, in which the battery cannot be recharged during its operation since they do not have an ICE.

Charge Sustaining Mode

In charge sustaining mode the ICE generates just the electric power needed to power the vehicle. This charging mode is used on diesel-electric locomotives. Figure 10a shows the case where the power generated is equal to the power demanded by the wheels; however, this way of charging needs that the ICE operates at different speeds and loads.

Another approach for sustaining charge can be seen in figure 10b, where the engine operates only at two speeds and loads: "P_{ECO}" and "P_{MAX}". If the ICE supplies more power than needed by the vehicle, then the excess power is used to recharge the batteries. This last method allows the ICE to operate at a fixed speed, preferably at the highest efficiency or the lowest fuel consumption (RIBAU et al., 2012).

Global Optimization Methods

Global optimization methods maximize powertrain efficiency while reducing losses. Optimum torque ranges and gear ratios are calculated by minimizing a cost equation, which generally represents fuel consumption or emissions. If this optimization is performed on a driving cycle, it obtains an optimal global solution for that specific driving cycle.

However, these methods require a substantial amount of computational time and, hence, cannot be used in real-time. Nevertheless, they help to evaluate the quality and operation among different control strategies. To develop a cost function that could work in real-time, the variation of the battery SOC must be taken into account.

FIGURE 10 – EXAMPLE OF TWO DIFFERENT CHARGE SUSTAINING MODES.

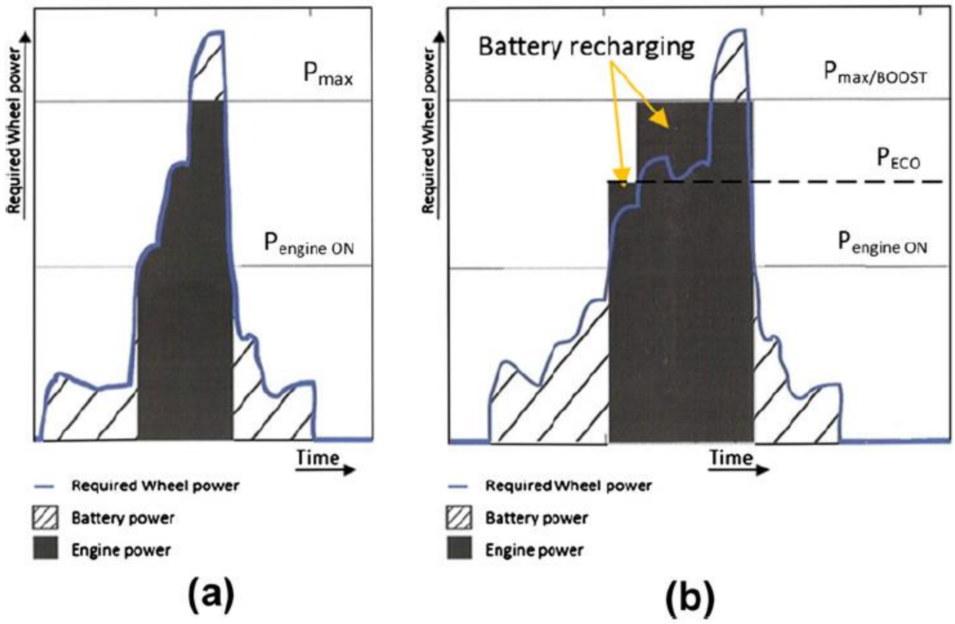

Source: Ribau et al. (2012).

Rule Based Methods

As shown in figure 9, rule based methods can be divided into deterministic and fuzzy methods. Deterministic rule-based methods are based on the efficiency, emissions, or fuel consumption engine maps. With those maps, operating rules are designed to control the flow of energy in the HEV; this is usually implemented through reference tables. This method allows the reduction of computational time because it only optimizes the instantaneous time, although, its biggest advantage is the possibility to be applied in real-time.

There are several approximations to solve deterministic problems, however, this work only focuses on the Pontryagin's Minimum Principle (PMP) optimization. The PMP is a general case of the Euler-Lagrange equation in the calculation of variations, which considers the optimization of a single trajectory. The PMP control can be considered as inferior to the dynamic programming; on the other hand, the PMP requires less computational time because it is based on instant Hamiltonian minimization.

Kim, Cha, and Peng (2010) demonstrated that PMP algorithm could be used to optimize the control of hybrid vehicles, for real-time control. While Shen, Bensch, and Müller (2015) actually applied the PMP to optimize the fuel consumption of an extended range electric vehicle (EREV). Similarly, Solouk et al. (2017) investigated the ideal fuel consumption of a low-temperature combustion (LTC) when using the PMP algorithm in an EREV.

In addition, fuzzy control methods can also be used to perform real-time control of HEVs. Fuzzy control methods have two greatest advantages. The first is its robustness since they are tolerant to imprecise measurements and variation in components. The second is its adaptability since the rules used can easily be adjusted if necessary (BAYINDIR; GÖZÜKÜÇÜK; TEKE, 2010; SHEN; SHAN; GAO, 2011).

Yu et al. (2016) propose a conventional diffuse control method with the objective of increasing the battery life cycle and minimizing the total cost of energy. In addition, it uses the genetic algorithm to optimize the functions of the diffuse control method, achieving a performance almost identical to a dynamic programming control method. Their proposed approach avoids the need for manual tuning of the parameters, which can become into an arduous and time-consuming task when tunning a large number of parameters.

2.2 BATTERY

In the case of EV and HEV modeling, the estimation of the battery SOC is more important than the current-voltage curve of the battery. Indeed, the SOC is essential to calculate the range of an EV, this is because the SOC directly affects the behavior of the battery. Young et al. (2013) defines the battery SOC as the remaining percentage of the battery, which can be found by equation 2:

$$SOC = \frac{Remaining\ Capacity}{Maximum\ Capacity} = \frac{Capacity\ Discharge - Maximum\ Capacity}{Maximum\ Capacity} \tag{2}$$

However, the SOC cannot be measured directly. One way to estimate the SOC is with the Coulomb Counting method, which integrates the load current to find the remaining capacity. In practice, the Coulomb Counting method cannot be applied due to miscalculations caused by wrong initial SOC, noise, or measurement error. Even though, it can be used as an ideal reference for other methods.

Another way to calculate the SOC is to use look-up tables or polynomial functions that relate the SOC to the Open Circuit Voltage (OCV). However, batteries that have large flat regions in the SOC-OCV curve could miscalculate the SOC, thus, they cannot be considered for this method. Additionally, this method cannot handle conditions not considered during the design process; therefore, lots of data is needed to cover all the variables.

Nevertheless, the most used method to estimate the SOC is by using recursive adaptive filters, such as the Kalman filter. These methods estimate the error between the battery output and the prediction of the battery model, hence, the battery model needs good accuracy. This method usually has a large error at the beginning, but as the prediction iterations progress the error decreases.

Besides the SOC, other important factors that modify the battery behavior are the operating temperature, the battery aging, and the current rate. The variation in operating temperature affects the battery capacity and if exceeding the operation range, it may even damage the battery. In addition, battery aging can lead to a loss of capacity and growth of internal resistance. The battery aging is measured in a parameter called battery State of Health (SOH).

Another important factor is the current rate since it changes the energy obtained from the battery, thus, models for low discharge rates may not work well at high discharge rates. Therefore, high discharge rates need to be contemplated when modeling EVs. Furthermore, low computational effort is also needed for real-time computations (FOTOUHI et al., 2016).

On the other hand, batteries can be modeled by three different approaches: mathematical models, electrochemical models, and electrical-equivalent circuit (EC) network models. A review of the mathematical and electrochemical models is made in section 2.2.1 and 2.2.2, respectively. While EC network models are reviewed in section 2.2.3. Finally, a summary of the characteristics of different battery types and supercapacitors is made in section 2.2.4.

2.2.1 MATHEMATICAL MODELS

Mathematical models are further divided into analytical or stochastic models. In analytical models, the properties of the battery are expressed as mathematical functions. On the other hand, stochastic models have random variables and estimate the probability distributions of the model.

An example of an analytical model is the Kinetic Battery Model (KiBaM), shown in figure 11. In KiBaM, the battery is considered like two tanks full of liquid. One tank represents the available charge "I" and the other represents the bound charge "j". The available charge is connected directly to the load "I", while the bound charge tank is connected to the available charge tank through a valve of coefficient "k". This way the KiBaM model can be described by the two differential shown in equation 3:

$$\begin{cases} \dfrac{di}{dt} = -I + k(h_2 - h_1) \qquad where\ i = h_1 * c \\ \dfrac{dj}{dt} = -k(h_2 - h_1) \qquad where\ j = h_2(1-c) \end{cases} \tag{3}$$

FIGURE 11 – ANALYTICAL KINETIC BATTERY MODEL (KIBAM).

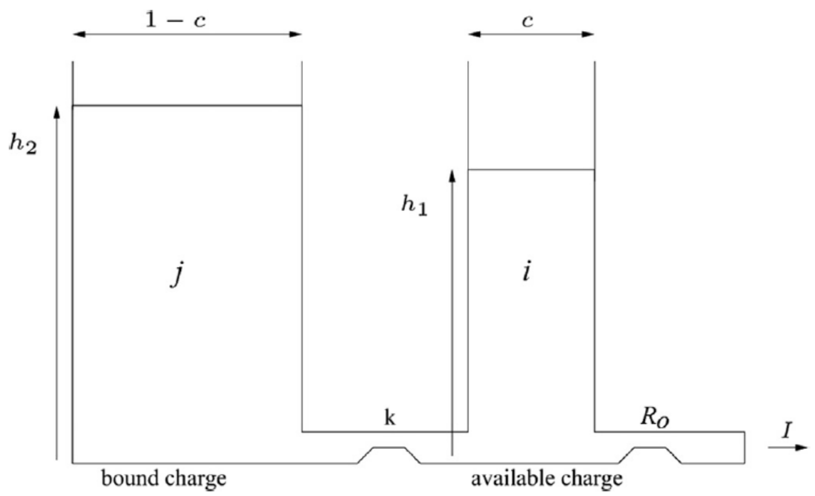

Source: Fotouhi et al. (2016).

Similarly, figure 12 shows a stochastic version of the KiBaM. This model is represented by three parameters "i", "j", and "t". Where "i" represents the available charge, "j" represents the bound charge, and "t" represents the time. In addition, every transition of a stage is associated with a different probability. This way, the stochastic KiBaM can be described by equation 4:

$$(i,j,t) \rightarrow \begin{cases} (i+Q, j-Q, t+1) & with\ probability\ of\ p_r(i,j,t) = q_0 p(t) \\ (i,j,t+1) & with\ probability\ of\ p_{nr}(i,j,t) = q_0(1-p(t)) \\ (i-I+J, j-J, 0) & with\ probability\ of\ q_I \end{cases} \quad (4)$$

FIGURE 12 – STATE TRANSITION DIAGRAM OF THE STOCHASTIC KINETIC BATTERY MODEL (KIBAM).

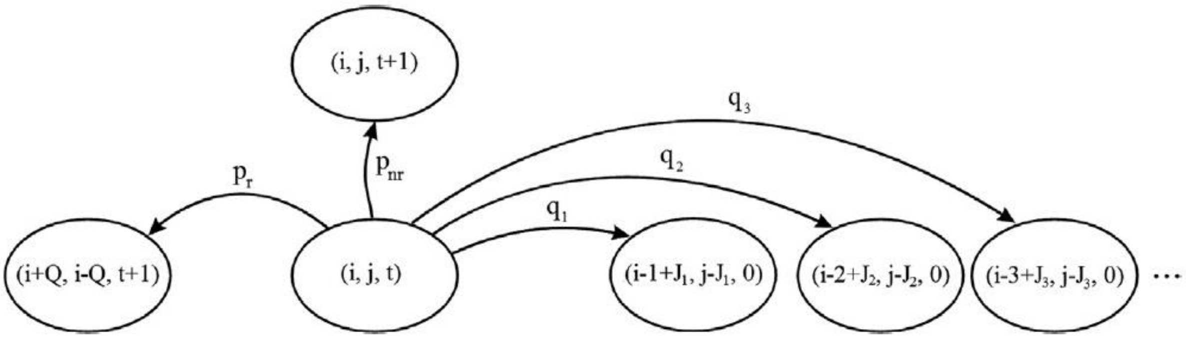

Source: Fotouhi et al. (2016).

2.2.2 ELECTROCHEMICAL MODELS

Electrochemical models are the most accurate of the three types. They consist of a set of coupled partial differential equations that provides information about the chemical reactions of the battery. Due to this, the internal states of the battery are fully observable, allowing for virtual measurements of values that cannot be measured in practice. In addition, thermal equations can be coupled to the electrochemical equations for more detailed models, resulting in very high order models.

Nevertheless, electrochemical models are too complex and, consequently, need high computational effort. This can be solved by using Reduced-Order Models, where discretization techniques are used without losing important model dynamics. Thus, special care should be taken with simplification assumptions since different application problems can give different results. Table 1 lists different discretization techniques.

TABLE 1 – BATTERY MODEL DISCRETIZATION METHODS.

Discretization method	Description
The Analytical Method	Finding an exact solution using analytical approaches such as the eigenfunction series expansion or the Laplace transform.
Integral Approximation Method	Assuming a distribution across the cell for the distributed variable of interest and integrating the governing equations to convert the PDE to a single ODE.
Padé Approximation Method	Approximating the transfer function that is obtained using the analytical method to desired order exponentials. In other words, Padé approximation is utilised to expand the infinitely differentiable hyperbolic functions in a power series at the origin.
Finite Element Method	Approximating the response over subdomains and then developing transfer functions or state-space equations for the nodal dynamics.
Finite Difference Method	Similar to the Finite Element Method with more simplicity but no convergence guarantee.
Ritz Method	Approximating the response by continuous functions over the whole domain such as Fourier series with the sinusoidal functions.

Source: Fotouhi et al. (2016).

2.2.3 ELECTRICAL EQUIVALENT CIRCUIT NETWORK MODELS

Electric-equivalent circuit network models are constructed by putting resistors, capacitors, and voltage sources in a circuit. Figure 13a shows the simplest battery model: the internal resistance model (FOTOUHI et al., 2016; YAN; WANG; HUANG, 2012).

By adding a Resistor-Capacitor (RC) network the polarization characteristics of the battery can be considered, and the battery can be modeled as a resistive Thevenin EC model (YAN; WANG; HUANG, 2012). Figure 13b shows the Thevenin EC model. Adding more RC networks improves the accuracy of the model, but also increases the complexity and the computational effort.

Once the structure of the EC is chosen, experimental tests are performed to determine the parameters of the model. Therefore, the lowest difference between the model results and the experimental results must be ensured. This process is known as system identification technique.

A common identification technique is the Electrochemical Impedance Spectroscopy, from which the Randles model is commonly employed. This is because in the Randles model relates every component of the electrical model to an electrochemical process in the cell. Figure 13c shows the Randles EC model.

In practice, EC models are developed from test data or offline data. Thus, all the data must contemplate the expected variables and operation conditions, since it does not consider other conditions than those designed for. Moreover, EC models are only available after the battery is manufactured.

Adaptive models are used to solve this problem, which can change by obtaining the battery parameters online. Nevertheless, EC models cannot predict the internal variables of the cell and, hence, cannot quantify the battery SOH (FOTOUHI et al., 2016).

FIGURE 13 – A) INTERNAL RESISTANCE BATTERY MODEL. B) THEVENIN MODEL OR ONE RC MODEL. C) RANDLES MODEL.

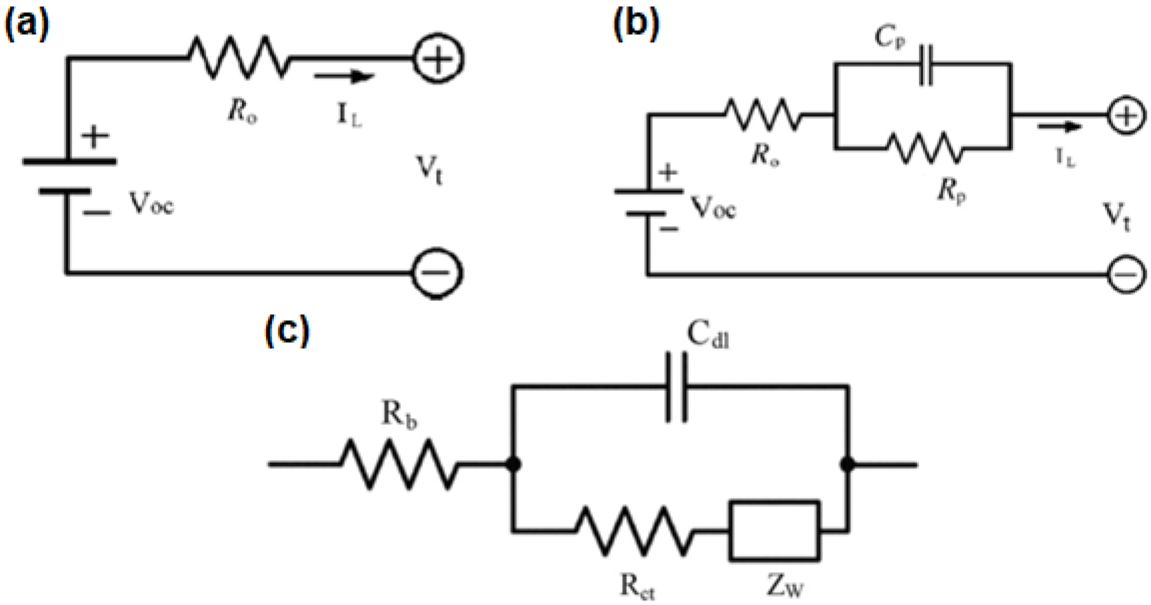

Source: adapted from Fotouhi et al. (2016).

2.2.4 DIFFERENT BATTERY TYPES

There are many types of batteries; however, the batteries that are more common in automotive applications are Lead-Acid, Nickel Metal Hydride (Ni-MH), Lithium-ion (Li-ion), and Sodium-Nickel Chloride ($Na\text{-}NiAlCl_2$). Table 2 lists different EVs in production with their respective battery type. This section summarizes the main characteristics of the batteries listed before. In addition, a review of supercapacitors is made.

TABLE 2 – DIFFERENT LI-ION BATTERY PACKS ACCORDING TO THE MANUFACTURERS AND EVS THAT USE THEM.

Cathode material types	EVs battery packs manufacturers	EVs developers and EV models	Battery packs usable capacity (kW h)
Lithium Cobalt Oxide (LCO)	Panasonic,	Tesla–Roadster	56
	Tesla	Daimler Benz–Smart EV	16.5
Lithium Manganese Oxide (LMO)	AESC, EnerDel,	Think–Think EV	23
	GS Yuasa, Hitachi, LG Chem, Toshiba	Nissan–Leaf EV	24
Lithium Iron Phosphate (LFP)	A123, BYD, GS	BYD–E6	57
	Yuasa, Lishem, Valence	Mitsubishi–iMiEV	16
Lithium Nickle–Manganese–Cobalt Oxide (NMC)	Hitachi, LG Chem, Samsung	BMW–Mini E	35

Source: Fotouhi et al. (2016).

The two main parameters used to compare different batteries are the specific energy and the specific power. Figure 14 compares these two parameters for different types of batteries. In addition, table 3 compares the technical characteristics of the main battery technologies.

FIGURE 14 – SPECIFIC ENERGY AND POWER OF MAIN BATTERY TECHNOLOGIES AND SUPERCAPACITORS

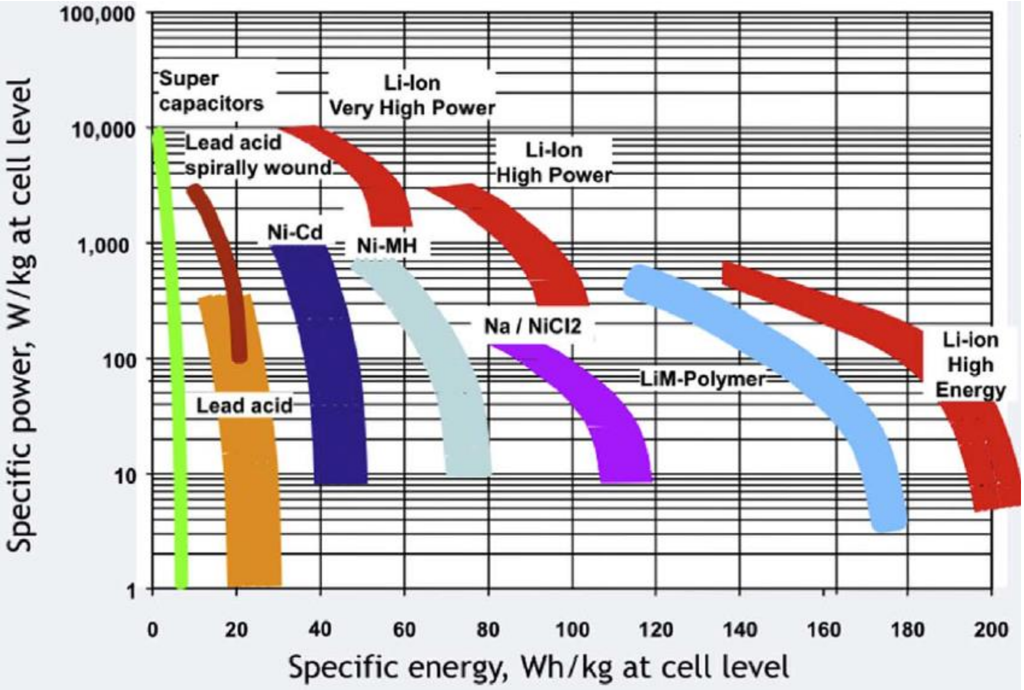

Source: Andwari et al. (2017).

TABLE 3 – TECHNICAL CHARACTERISTICS OF MAIN BATTERY TECHNOLOGIES

Battery technology (type)	Specific energy (Wh/kg)	Energy/ Volume coefficient (Wh/L)	Power/ Weight coefficient (W/kg)	Self-discharge coefficient (% per 24 h)	Number of recharging cycles
Pb-acid	40	70	180	1	500
NiMH	70	250	1000	2	1350
Li-ion	125	270	1800	1	1000
Li-ion polymer	200	300	3500	1	1000
Na–NiCl	125	300	1500	0	1000

Source: Manzetti and Mariasiu (2015).

Lead-Acid Battery

Lead-acid batteries are a mature and well-known technology. They have the lowest cost (about 100 USD/kWh), however, also have low specific energy (20-30 Wh/kg). Additionally, they have low life cycles, low calendar life, and are hazardous for human health due to the acid and lead. They are considered appropriate for vehicles with low performance and short-range requirements.

Nickel Metal Hydride Battery (Ni-MH)

Nickel Metal Hydride batteries have a high cost, between 700 to 800 USD/kWh, but still lower than Li-ion batteries. In addition, they have high self-discharge coefficient and intermediate specific energy, between 60 to 80 Wh/kg. The hybrid Toyota Prius uses this type of batteries.

Lithium-ion batteries (Li-ion)

Lithium-ion batteries are considered the most promising battery technology. They have the highest specific energy, as well as high efficiency and long lifespan. Nevertheless, they can set on fire if overcharged and are the most expensive battery type, costing more than 700 USD/kWh (ANDWARI et al., 2017).

Lithium-ion batteries can have different types of chemistries, thus, they can be further divided into Lithium Cobalt Oxide, Nickel Cobalt and Aluminium, Lithium Nickel-Manganese-Cobalt Oxide, Lithium Iron Phosphate, and Lithium Polymer. Table 4 compares the advantages and disadvantages of each Li-ion battery chemistry.

TABLE 4 – COMPARISON OF DIFFERENT LI-ION BATTERY TECHNOLOGIES

Technology	Advantages	Disadvantages
Lithium Cobalt Oxide ($LiCoO_2$)	Power and energy density	Safety, cost
Nickel Cobalt and Aluminium (NCA)	Power and energy density, calendar and cycle life	Safety
Nickel Manganese Cobalt (NMC)	Power and energy density, Cycle and calendar life	Safety
Lithium Polymer ($LiMnO_4$)	Power density	Calendar life
Lithium iron phosphate ($LiFePO_4$)	Safety	Energy density, calendar life

Source: Andwari et al. (2017).

Sodium Nickel Chloride (Na-$NiAlCl_2$)

Also known as Zebra batteries, they use a molten salt electrolyte and operate at temperatures of 270 to 350 °C. They also have long life cycles and can bear high deep of discharges without degrading its life expectancy. In addition, they are considered low cost (240 USD/kWh) and have a specific energy comparable to Li-ion batteries. Despite all that, its main disadvantage is their low specific power (150 W/kg), which could be solved by operating them together with supercapacitors (ANDWARI et al., 2017; MANZETTI; MARIASIU, 2015).

Supercapacitors

Supercapacitors, also known as ultracapacitors, are characterized by having higher power density and longer life cycles than batteries; however, they also have lower specific energy. This means that the supercapacitors' role in electric vehicles is not to deliver energy, instead they aid the battery when high power demand is needed.

They also smooth the current fluctuation of the batteries, which in turn reduce the battery's temperature, increasing its lifespan (ANDWARI et al., 2017).

A supercapacitor can be modeled by a capacitance and a series of resistances, this EC is shown in figure 15a. On the other hand, figure 15b shows a supercapacitor EC that includes its dynamic characteristics during charging and discharging.

As mentioned before, the main role of a supercapacitor in electric vehicles is to aid the batteries. Therefore, according to Bayindir, Gözüküçük, and Teke (2010), supercapacitors complement the batteries by providing the next features:

- Assisting the batteries during hard transient states.
- Increasing the batteries' lifespan and decreasing their size.
- Offering good performance independent of the battery state.
- Increasing the available power and, consequently, the hybrid vehicle autonomy.
- Improving the energetic efficiency of the regenerative braking.

FIGURE 15 – A) SIMPLE EC SUPERCAPACITOR MODEL. B) SUPERCAPACITOR MODEL WITH DYNAMIC CHARACTERISTICS

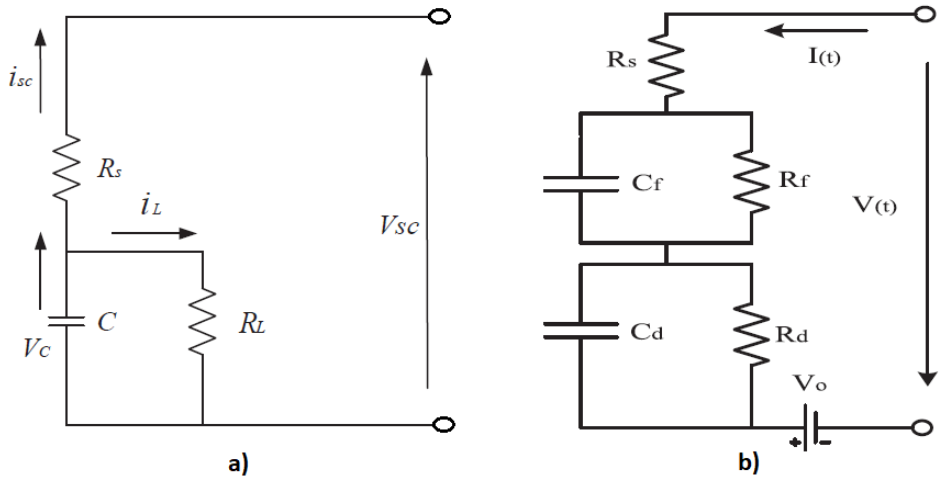

Source: adapted from Hannan, Azidin and Mohamed (2014) and Santucci, Sorniotti and Lekakou (2014).

2.3 ELECTRIC MACHINES

An electric machine is defined as: “A device that can convert either mechanical energy to electric energy or electric energy to mechanical energy.” (CHAPMAN, 1991, p.1). Figure 16 presents a classification of different types of electric machines.

FIGURE 16 – CLASSIFICATION OF DIFFERENT EV DRIVES

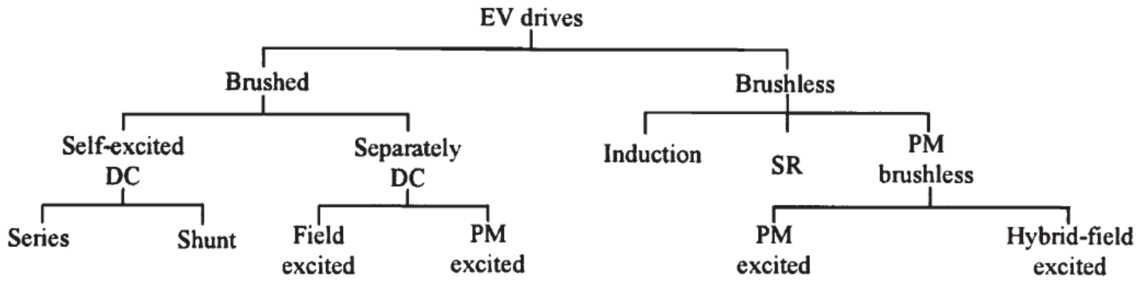

Source: Chau, Chan, and Liu (2008).

An electric machine consists of two main parts: the *rotor* and the *stator*. The *rotor* is the part of the machine that rotates and is connected to the output shaft, while the *stator* remains static and is fixed to the ground. In addition, the distance between the stator and the rotor is called *air gap*. Also, every electrical machine have two windings: the *armature winding*, which induce a voltage, and the *field winding*, which produce a magnetic flux

The maximum power that a machine can deliver is limited by the maximum temperature that a winding can bear without degrading its insulation (CHAPMAN, 1991). The size of an electric motor is given by the torque, and not by the power, since the heat produced is mainly dependent on the current and torque (HOPFERWIESER, 1956).

Thus, the torque that an electric machine can deliver in a continuous manner without overheating is called the *rated torque.* Although every electric machine can deliver higher torques, prolonged operation over the rated torque can reduce the motor’s life.

Since it is desired to maintain a constant voltage, the current drawn by the machine is determined by the variation in load; however, the variation in current and load is not necessarily proportional to each other. Therefore, the *rated current* of the machine is obtained only when running at rated voltage and rated torque.

Every electric drive can operate as motor or as generator. Contrary to what can be thought, the mode of operation is not defined by the direction of rotation but by the operating speed and its interaction with the external forces. If an external force is applied against the direction of rotation, the machine operates as a motor. On the other hand, if an external force is applied in favor of the direction of rotation, the machine operates as a generator.

When the supply of the machine comes from a battery, like in EVs, the machine works as motor if the battery voltage is greater than the induced voltage, and as generator if the induced voltage is greater than the battery voltage.

Sections 2.3.1 to 2.3.4 introduce the fundamentals of four electric machines, as well as the main equations that govern them. These are the Direct Current machines, the Synchronous machines, the Induction machines, and the Switched Reluctance Machines, which are presented in the same order. Finally, section 2.3.5 presents some comparisons among different electric motors used in automotive applications.

2.3.1 DIRECT CURRENT MACHINES

All DC machines have their armature windings located in the rotor, and its field windings located on the stator, although, its torque-speed characteristic is affected by the way in which the field flux of a DC motor is originated. Therefore, DC motors can be classified according to the arrange of their field flux as separately excited, shunt, series, compounded, and permanent magnet. This thesis focuses on shunt DC motors only.

Figure 17 shows the EC of separately excited and shunt DC motors. Notice that the field current of a separately excited DC motor is supplied from a separate power supply, while a shunt DC motor obtains its power directly from the armature terminals of the motor. Other than that, both motors are the same.

FIGURE 17 – EC FOR SEPARATELY EXCITED AND SHUNT DC MOTORS

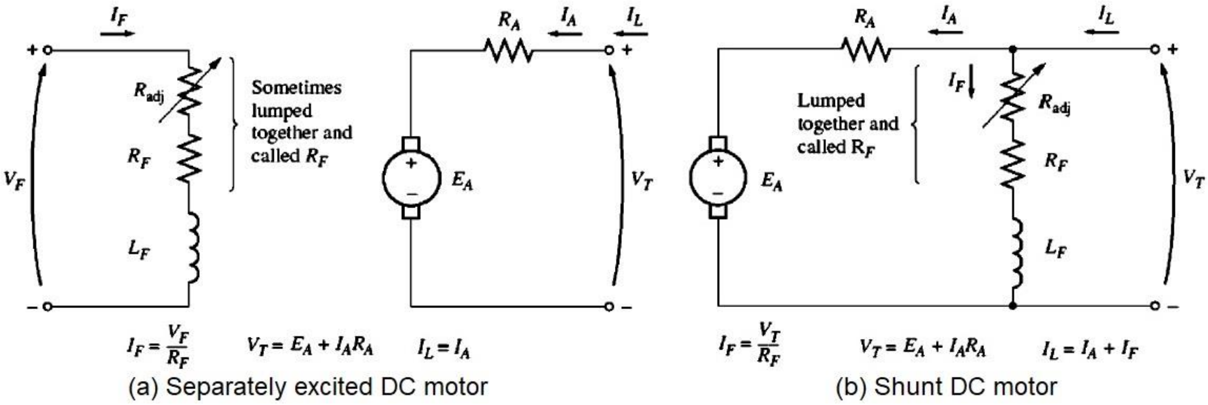

Source: adapted from Chapman (1991).

In order to maintain a constant DC output voltage, a DC machine uses a commutator. The commutation process is defined as: “the process of switching the loop connections on the rotor of a DC machine just as the voltage in the loop switches polarity” (Chapman 1991, p. 225).

Moreover, the commutation process is the most critical part of a DC machine and is accomplished by adding two semicircular conducting segments at the end of the loop wire, named *commutator segments*. Then, two fixed contacts, named *brushes*, are set up in such way that when the voltage in the loop is zero the brushes short-circuit the commutator segments.

In this way, every time that the induced voltage in the wire switch direction the commutator segment also switch connections, obtaining a voltage output that is always positive. Figure 18 shows the commutation process.

Induced voltage in DC machines

According to Chapman (1991), the induced voltage of a real DC machine is given by equations 5 and 6:

$$E_A = \frac{ZP}{2\pi a}\omega\phi = K\omega\phi \tag{5}$$

$$E_A = \frac{ZP}{60a}n\phi = K'n\phi \tag{6}$$

Where:

- E_A is the induced voltage in the armature;
- ω is the rotational speed of the motor, in rad/s;
- n is the rotational speed of the motor, in rev/s;
- Φ is the flux in the machine;
- P is the number of poles of the machine;
- a is the number of current paths, and;
- Z is the total number of conductors, given by equation 7:

$$Z = 2CN_C \tag{7}$$

From which:

- C is the number of coils on the rotor, and;
- N_C is the number of turns per coil.

Thus, the voltage in any real DC machine depends on three factors:

1. The flux in the machine;
2. The speed of rotation, and;
3. A constant "K" representing the construction of the machine.

FIGURE 18 – PROCESS OF COMMUTATION

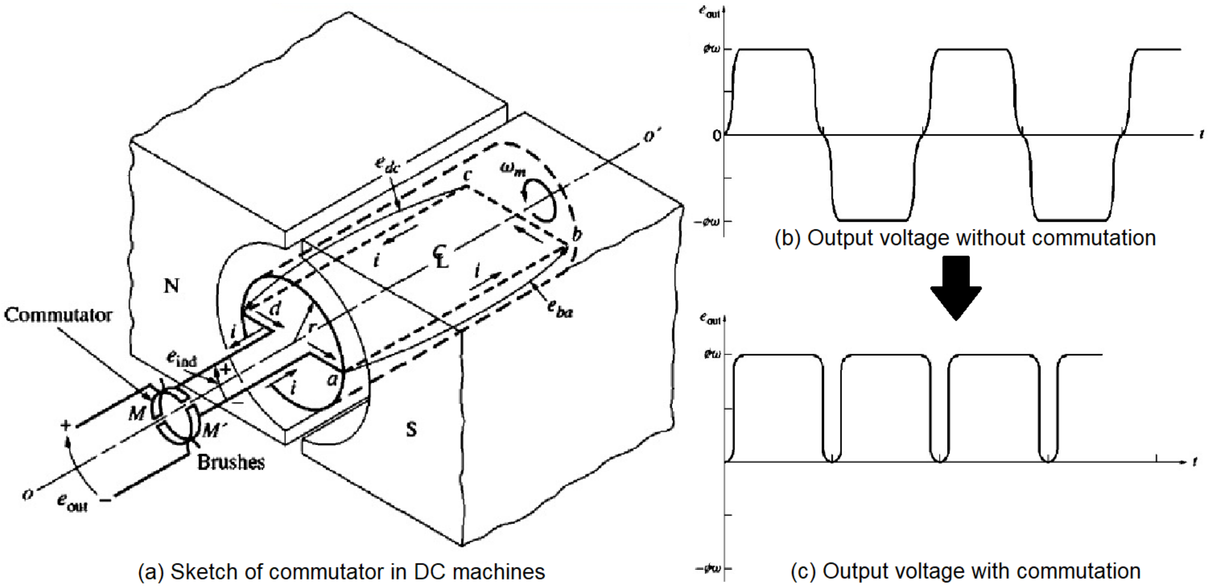

(a) Sketch of commutator in DC machines

(c) Output voltage with commutation

Source: adapted from Chapman (1991).

Induced torque in DC machines

On the other hand, equation 8 gives the induced torque of real DC machines:

$$\boldsymbol{\tau_{ind} = \frac{ZP}{2\pi a} I_A \Phi = K\Phi I_A} \qquad (8)$$

Where:

- τ_{ind} is the total induced torque;
- I_A is the current in the rotor armature;
- Φ is the flux in the machine;
- Z is the total number of conductors (see equation 6);
- P are the number of poles in the machine, and;
- a is the number of current paths.

Thus, the induced torque of any real DC machine depends on the next three factors:

1. The flux in the machine;
2. The current in the machine, and;
3. A constant "K" representing the construction of the machine.

In addition, the torque-speed characteristic curve of a shunt DC motor is described by equation 9:

$$\omega = \frac{V_T}{K\phi} - \frac{R_A}{(K\phi)^2}\tau_{ind} \qquad (9)$$

Figure 19 shows the torque-speed characteristic curve of a shunt DC motor, based on equation 9. Notice that the curve gives a straight line with a negative slope. This means that an increase in the shaft's load induces a torque of the same magnitude, but at a lower speed.

FIGURE 19 – TORQUE-SPEED CHARACTERISTIC OF THE MOTOR WITH ARMATURE REACTION “AR” PRESENT

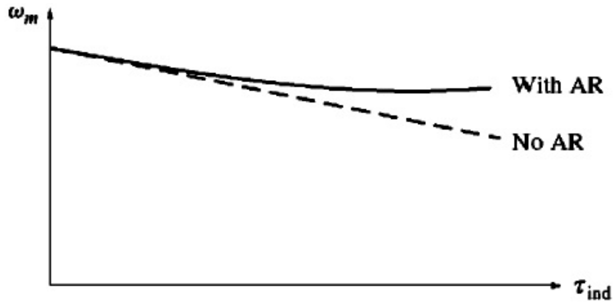

Source: Chapman (1991).

Speed control of DC Shunt Motors

There are three methods to control a shunt DC motor, which are:

1. Varying the field flux;
2. Varying the terminal voltage applied to the armature, and;
3. Inserting a resistor in series with the armature circuit

The easiest way of varying the field flux is by increasing the field resistance “R_F”. Figure 20a shows how no-load speed rises when field resistance is increased. Observe that, at very slow speeds, the increase in the field resistance actually decreases the speed. Thus, this control method is only used for speeds above the base speed, since trying to achieve lower speeds than the base speed results in really high field currents, which could burn the field windings.

In addition, if the armature reaction is too severe, an increase in load can weaken its flux too much, overspeeding the motor and losing its control. This condition is known as *runaway* condition. Special care should be taken to protect the field circuit, which can be achieved by including a *field loss relay* to disconnect the motor in case of runaway condition.

FIGURE 20 – DIFFERENT CONTROL METHODS FOR DC MOTORS

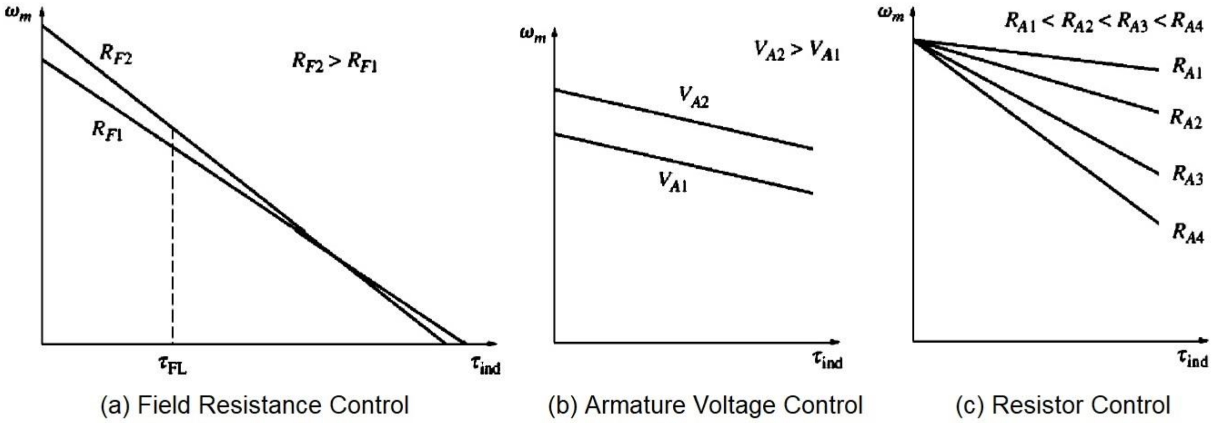

Source: adapted from Chapman (1991).

The effect of changing the armature voltage is shown in figure 20b. In armature voltage control, an increase in the voltage increases the speed of the motor. However, the maximum speed is reached at the rated armature voltage. Trying to achieve a speed faster than the base speed requires excessive armature voltage, which could damage the armature circuit. Hence, this type of control is only used for speeds below the base speed of the motor.

As it can be deduced, these two control techniques are complementary. Field resistance control is used for speeds above the motor's base speed, while armature voltage control is used for speeds below the base speed. By combining the two control methods, a motor with a wide range of speed variation is obtained. However, the limiting factor for both control methods is the heating of the motor.

The third control option is achieved by varying a resistor that is in series with the armature. The effect of this resistor is shown in figure 20c; nonetheless, this kind of motor control is very inefficient.

Power-flow and losses of DC machines

Figure 21 shows the power-flow of a DC machine. Notice that there are five types of losses that occur in any DC machine, which are classified as next:

1. Electrical or copper losses (I^2R losses);
2. Brush losses;

3. Core losses;
4. Mechanical losses, and;
5. Stray load losses.

The copper losses refer to the losses that occur in both the armature and field windings. These losses can be calculated by equations 10 and 11:

$$P_A = {I_A}^2 * R_A \tag{10}$$

$$P_F = {I_F}^2 * R_F \tag{11}$$

Where:

- P_A is the armature power lost;
- I_A is the armature current;
- R_A is the armature resistance at normal operating temperature;
- P_F is the field power lost;
- I_F is the field current, and;
- R_F is the field resistance at normal operating temperature.

The brushes losses refer to the power lost across the contact between the brushes and the commutator segments, and is given by equation 12:

$$P_{BD} = V_{BD} I_A \tag{12}$$

Where:

- P_{BD} is the brush drop loss;
- I_A is the armature current, and;
- V_{BD} is the brush voltage drop, usually assumed to be 2 V.

The core losses are due to hysteresis losses and eddy current losses. These losses vary with the square of the flux density “B^2” for the field winding, and with the 1.5 of the speed of rotation “$n^{1.5}$” for the armature winding.

The mechanical losses are caused by the friction between the moving parts and the air inside the motor, and by the friction of the bearings. Finally, the stray load losses are the losses that cannot be classified in any of the other types, they are usually considered to be 1% of the full load (CHAPMAN, 1991).

FIGURE 21 – POWER-FLOW DIAGRAM OF A DC MOTOR

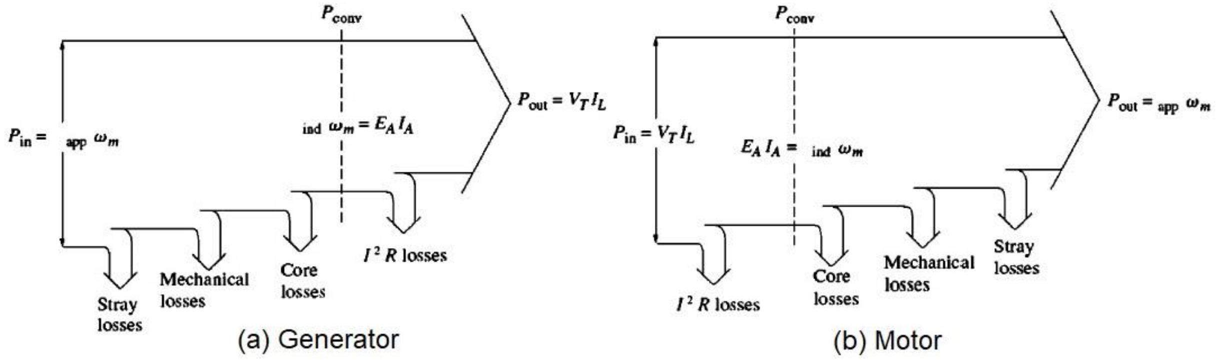

Source: adapted from Chapman (1991).

2.3.2 Synchronous Machines

The AC machines that have their electrical frequency synchronized to the mechanical speed are called *Synchronous Machines*. Thus, their electrical frequency is defined by equation 13:

$$f_e = \frac{P * n_{sync}}{120} \tag{13}$$

Where:

- f_e is the electrical frequency, in Hz;
- P is the number of poles of the machine, and;
- n_{sync} is the synchronous speed in rev/min, which is equal to the mechanical speed of the rotor.

Synchronous machines require DC current to be supplied to their rotor field windings. This can be made by two different approaches: with the help of a *brushless exciter* or with the help of *slip rings* and brushes.

A brushless exciter is a small AC generator mounted in the synchronous motor shaft, as shown in figure 22. The use of brushless exciters reduce the motor's maintenance since there is no mechanical contact between the shaft and the power source. On the contrary, the use of slip rings increase the amount of maintenance needed in the machine; in addition, slip rings might have lower efficiency due to drop voltages in the brushes.

FIGURE 22 – BRUSHLESS EXCITER CIRCUIT

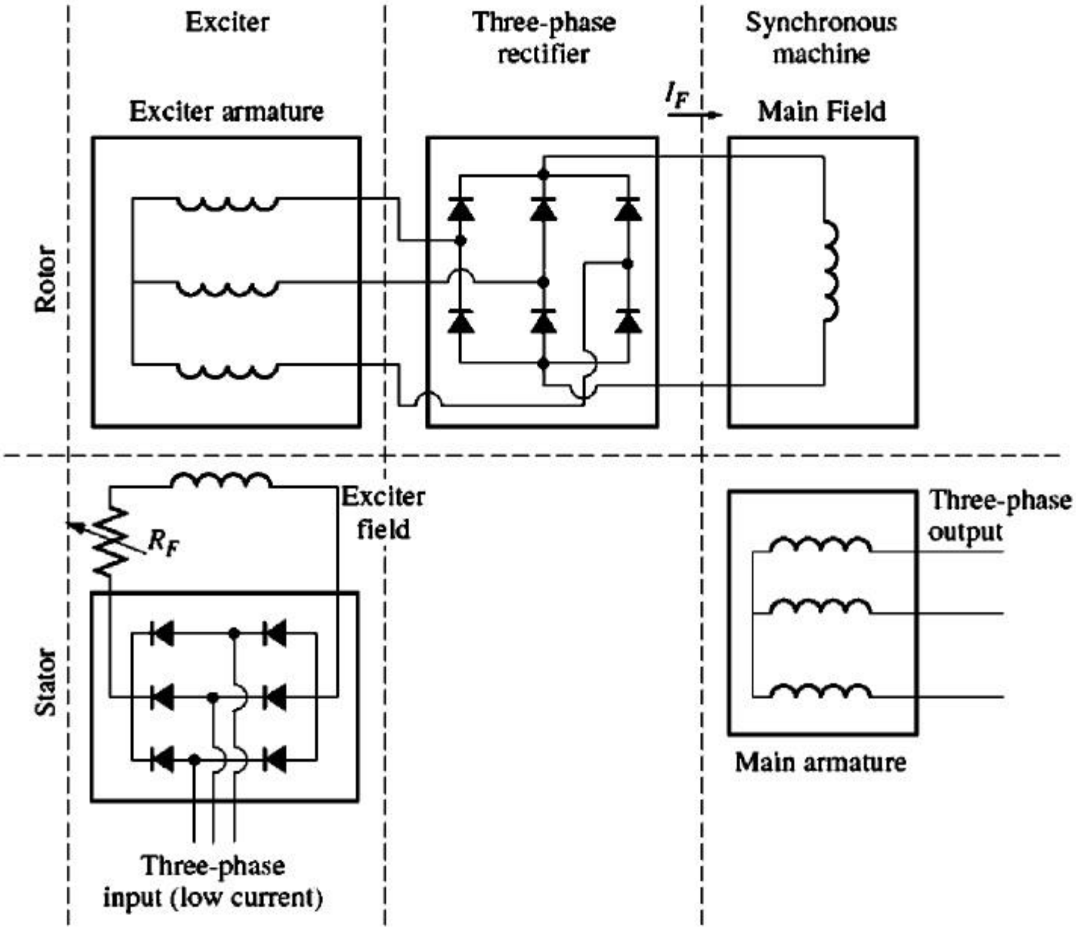

Source: Chapman (1991).

Induced voltage in Synchronous machines

At no-load condition, the output voltage of a synchronous machine can be described by equations 5 or 6. Nevertheless, at load condition the output voltage is determined by four main factors, which are:

1. The effect of armature reaction;
2. The self-inductance generated in the armature coils;
3. The resistance of the armature coils, and;
4. The effect of salient-poles rotor.

The armature reaction can be modeled as an inductor in series with the voltage that it generates, as shown in the right side of the EC of figure 23a. Additionally, the self-inductance in the armature coils have its own reactance and resistance. Thus, a better description of the induced voltage is obtained by equation 14:

$$V_\phi = E_A - jXI_A - jX_AI_A - R_AI_A \tag{14}$$

Where:

- V_ϕ is the total voltage on a phase;
- E_A is the armature voltage;
- jXI_A is the voltage generated by the armature reaction;
- jX_AI_A is the voltage generated by the self-inductance on the stator coils;
- R_A is the stator resistance, and;
- I_A is the armature current.

By combining both reactances, it results in resultant *synchronous reactance* "X_S" as given in equation 15. Therefore, the voltage phase of a synchronous generator, when loaded, can be obtained by equation 16.

$$X_S = X + X_A \tag{15}$$

$$V_\phi = E_A - jX_SI_A - R_AI_A \tag{16}$$

Figure 23 shows the per-phase equivalent circuit of a synchronous generator and a synchronous motor. Notice that the only difference between both circuits is the direction of I_A; thus, the phase voltage of a synchronous motor is defined by equation 16, but with the opposite sign:

$$V_\phi = E_A + jX_SI_A + R_AI_A \tag{17}$$

Notice that equation 16 and 17 do not consider the effect of salient-poles, which is not discussed in this work. However, the armature reaction has the largest influence of the four factors, thus, equation 16 and 17 gives a good approximation.

FIGURE 23 – PER-PHASE EQUIVALENT CIRCUIT OF SYNCHRONOUS MACHINE

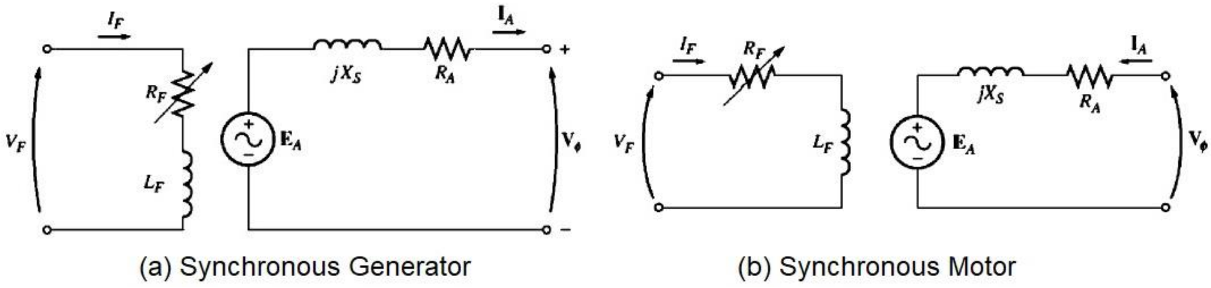

Source: adapted from Chapman (1991).

On the other hand, the terminal voltage is related to the phase voltage by equation 18 when Y-connected, and by equation 19 when Δ-connected. However, the three phases have the same voltages and currents only if the loads attached to them are balanced.

$$V_T = \sqrt{3}V_\phi \tag{18}$$

$$V_T = V_\phi \tag{19}$$

Induced torque in Synchronous machines

In AC machines, the interaction of the stator magnetic field and the rotor magnetic field is responsible for the induced torque. Nevertheless, a synchronous generator must maintain a constant speed regardless of the power demand. If not, the output frequency supplied by the generator will be unstable.

The power of a synchronous machine is given by equation 20. Notice that the maximum value of the power is at an angle δ=90° (or sin δ=1); thus, the maximum power of a synchronous machine is given by equation 21:

$$P = \frac{3V_\phi E_A \sin\delta}{X_S} \tag{20}$$

$$P_{max} = \frac{3V_\phi E_A}{X_S} \tag{21}$$

If the converted power is equal to the product of induced torque and mechanical speed, then equations 22 and 23 can be rewritten as:

$$\tau_{ind} = \frac{3V_{\phi}E_A \sin\delta}{\omega_m X_S} \quad (22)$$

$$\tau_{max} = \frac{3V_{\phi}E_A}{\omega_m X_S} \quad (23)$$

Where:

- τ_{ind} is the induced torque;
- τ_{max} is the peak torque;
- V_{ϕ} is the total voltage on a phase;
- E_A is the armature voltage;
- ω_m is the mechanical speed, in rad/sec, and;
- X_S is the synchronous reactance.

Figure 24 shows the torque curve of a synchronous machine. Notice that the mechanical speed motor is always locked with the applied electric frequency, so the speed of the motor is constant regardless of the load. Nevertheless, the torque angle "δ" increases with the increase in load. Since usually the voltage and frequency remain constant, then the current also increases with load.

FIGURE 24 – TORQUE-SPEED CURVE OF SYNCHRONOUS MACHINE

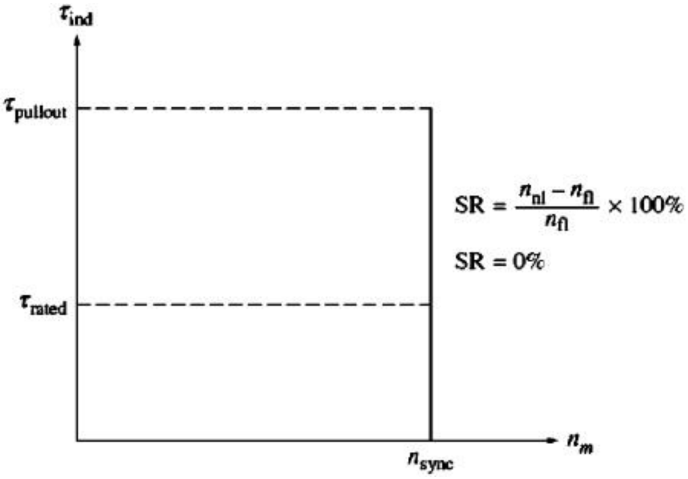

Source: Chapman (1991).

Power-flow and losses of Synchronous machines

The losses of an AC machine can be categorized in the same way that for DC machines, however, the brush losses can be ignored since AC machines do not have brushes. Figure 25 shows the power-flow diagram of a three-phase synchronous generator and a three-phase synchronous motor.

The rotor copper losses (RCL) of synchronous machines are the same that for DC machines and are given by equation 11. On the other hand, the stator copper losses (SCL) of a three-phase synchronous machine are three times the losses established for DC machines, and are given by equation 24:

$$P_{SCL} = 3{I_A}^2 R_A \tag{24}$$

Where:

- P_{SCL} is the stator copper power lost;
- I_A is the current flowing in each armature phase;
- R_A is the resistance of each armature phase;

FIGURE 25 – POWER-FLOW DIAGRAM OF A THREE-PHASE AC MACHINE

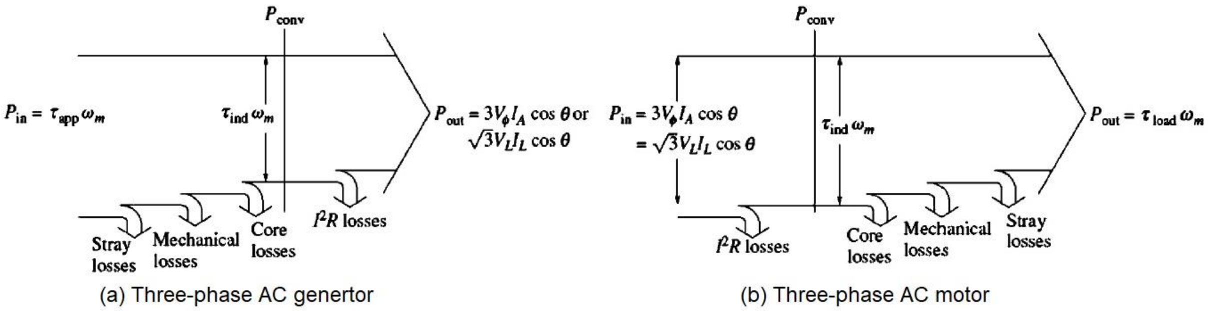

Source: Chapman (1991).

2.3.3 INDUCTION MACHINES

Induction machines (IM) have the same stators than synchronous machines, thus, the difference resides in their rotor construction. In IMs, the field current is induced in the rotor by the use of amortisseur winding, which are special bars laid into notches carved in the face of the rotor and, then, shorted out on each end by a large *shorting ring*. Another difference with synchronous machines is that IMs can start at full load and do not need to supply current to their rotors.

The rotors of IMs can be of two types: squirrel-cage rotor or wound rotor. A *squirrel-cage rotor* consists of a series of conducting bars located in the surface of the rotor and shorted at both ends by shorting rings (see figure 26). On the other hand, *wound rotors* have three-phase windings that mirror the stator windings, and the end of the rotor windings are fixed to slip rings on the rotor's shaft. Nevertheless, wound motors are more expensive, need more maintenance, and require more complex control circuit than squirrel-cage motors.

In induction machines, the induced voltage is produced by the relative motion between the stator magnetic field and the speed of the rotor. The greater the relative motion, the greater the resulting voltage. Thus, the induced voltage is zero when the rotor is turning at synchronous speed, while the induced voltage is at its highest when the rotor is stationary. As a result, an IM never reaches synchronous speed.

FIGURE 26 – SQUIRREL CAGE ROTOR OF INDUCTION MACHINES

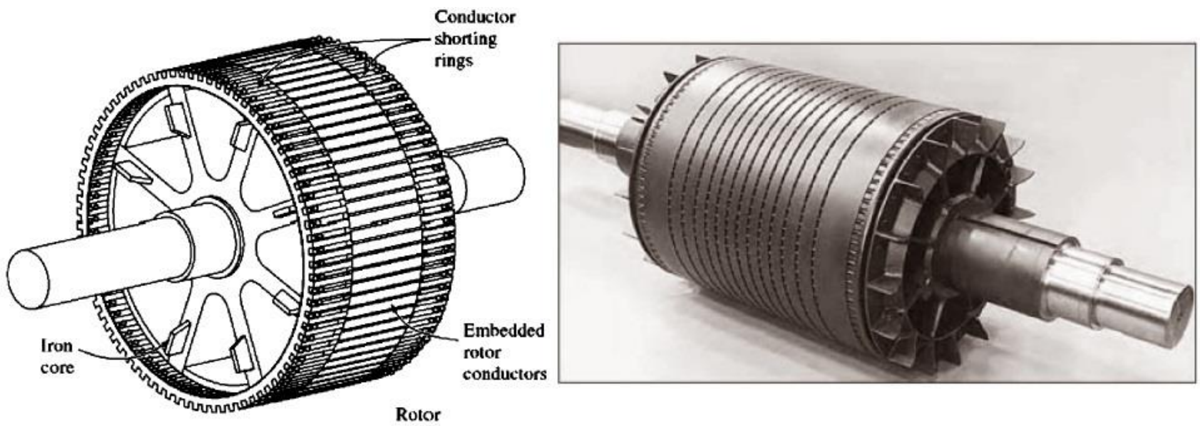

Source: adapted from Chapman (1991).

The difference between synchronous speed and the rotor speed is known as the *slip speed*. On the other hand, the relation between synchronous speed and the slip speed is known as *slip*, and is given by in equation 25:

$$s = \frac{n_{slip}}{n_{sync}} = \frac{n_{sync} - n_m}{n_{sync}} \tag{25}$$

Where:

- s is the *slip*;
- n_{slip} is the *slip speed*;
- n_{sync} is the speed of the magnetic fields, and;
- n_m is the mechanical shaft speed of the rotor.

Notice that when s=0 the motor is running at synchronous speed, and when s=1 the rotor is stationary. Therefore, the mechanical speed of the rotor shaft can be rewritten in terms of slip and synchronous speed, as in equation 26 and 27:

$$n_m = (1 - s)n_{sync} \tag{26}$$

$$\omega_m = (1 - s)\omega_{sync} \tag{27}$$

Induced current in Induction machines

Figure 27a shows the circuit model of a transformer, from which the rotor circuit of the IM is deduced. Figure 27b shows the rotor circuit of an IM, notice that the rotor's induced voltage can be express in function of the slip ($E_R = sE_{R0}$). In addition, the rotor's induced voltage also have a constant resistance "R_R", and a reactance that varies with the slip of the motor ($X_R = sX_{R0}$). Finally, it is also possible to treat all the rotor effects as being caused by a varying impedance "Z_R". Therefore, the current induced in the rotor is given by equation 28:

$$\boldsymbol{I_R = \frac{E_R}{R_R + jX_R} = \frac{sE_{R0}}{R_R + jsX_{R0}} = \frac{E_{R0}}{R_R/s + jX_{R0}} = \frac{E_{R0}}{Z_R}} \tag{28}$$

Where:

- I_R is the induced current in the rotor;
- E_R is the induced voltage when the rotor is stationary;
- E_{R0} is the induced voltage at synchronous speed;
- R_R is the resistance of the rotor;
- jX_R and jX_{R0} are the rotor reactances, and;
- s is the slip of the motor, and;
- Z_R is the rotor impedance that can be used to represent all rotor effects.

FIGURE 27 – DEDUCTION OF THE CIRCUIT MODEL OF THE ROTOR OF AN INDUCTION MACHINE

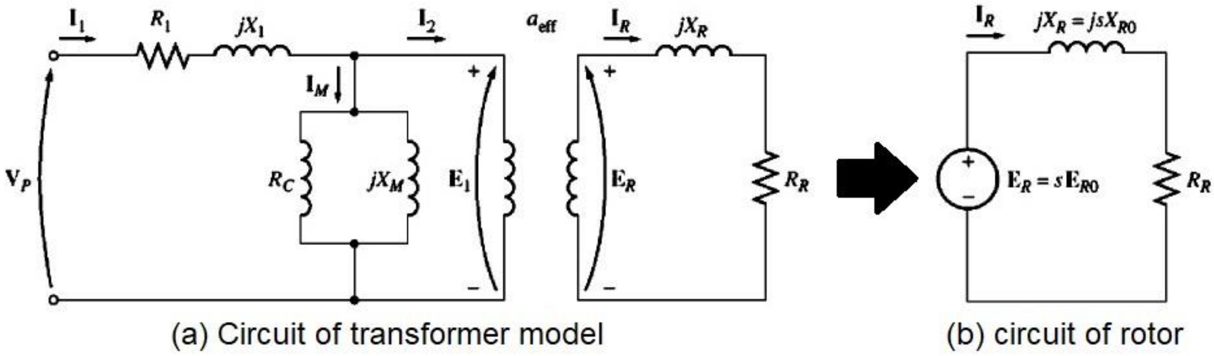

Source: adapted from Chapman (1991).

Power-flow and losses of Induction machines

Figure 28 shows the power-flow diagram of an induction motor. The RCL and SCL of an IM are described by equations 4 and 26, respectively.

On the other hand, figure 29 shows the per-phase equivalent circuit of an induction motor. Observe that it marked the developed mechanical power "P_{conv}", the RCL, the SCL, and the core losses, which can be obtained by equation 29:

$$P_{core} = \frac{3{E_1}^2}{R_C} \tag{29}$$

FIGURE 28 – POWER-FLOW DIAGRAM OF AN INDUCTION MOTOR

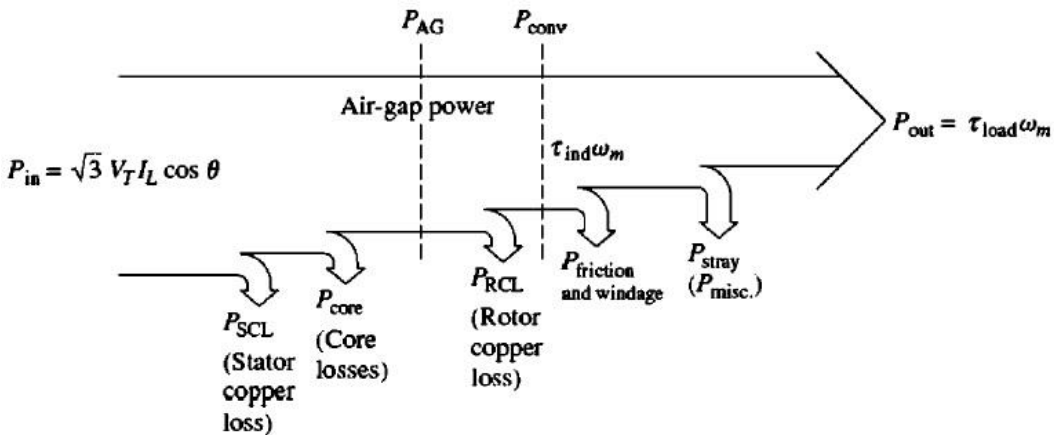

Source: Chapman (1991).

FIGURE 29 – PER-PHASE EQUIVALENT CIRCUIT OF INDUCTION MACHINES

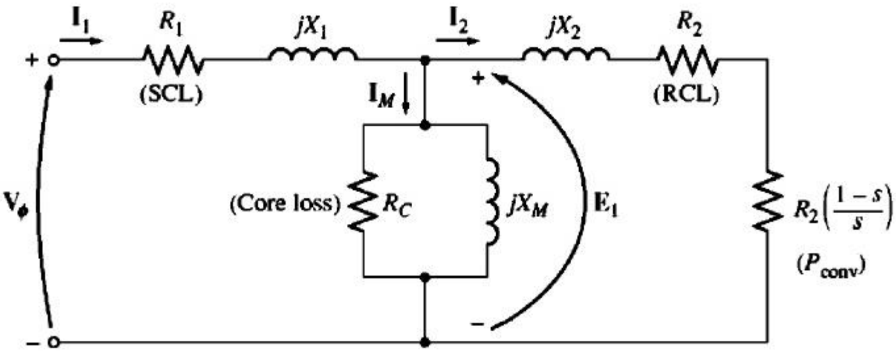

Source: Chapman (1991).

Induced torque in Induction machines

As shown in figure 28, the developed mechanical power is obtained after the subtraction of air gap power losses and rotor copper losses. Thus, the converted power is given by equation 30, while the induced torque is given by equation 31:

$$P_{conv} = 3{I_2}^2 R_2 \left(\frac{1-s}{s}\right) = P_{AG} - P_{RCL} = (1-s)P_{AG} \tag{30}$$

$$\boldsymbol{\tau_{ind}} = \frac{\mathbf{(1-s)}\boldsymbol{P_{AG}}}{\mathbf{(1-s)}\boldsymbol{\omega_{sync}}} = \frac{\boldsymbol{P_{AG}}}{\boldsymbol{\omega_{sync}}} \tag{31}$$

Where:

- P_{conv} is the power converted by the induction machine;
- τ_{ind} is the induced torque in the machine;
- ω_{sync} is the synchronous speed, in rad/s;
- s is the slip of the machine, and;
- P_{AG} is the air gap power losses, given by equation 32:

$$P_{AG} = 3{I_2}^2 \frac{R_2}{s} = \frac{P_{RCL}}{s} \tag{32}$$

At no loads, the slip of the motor is very small and, consequently, the rotor's voltage and current is small too and almost in phase with each other. However, a rise in motor's load increases the slip, which in turn increases the voltage and current of the rotor. This is shown in figure 30, which plots the induced rotor current in function of the percentage of synchronous speed.

On the other hand, figure 31 shows the complete torque-speed curve of an IM, including the motoring region, generating region, and braking region. From this figure, various observations can be made:

1. The induced torque of the motor is zero at synchronous speed;
2. The torque-speed curve is nearly linear between the no-load and full load region. In this range the rotor current and the induced torque increase linearly with slip;
3. The pullout torque is two to three times higher than the rated full-load torque;
4. The starting torque on the motor is slightly larger than the full-load torque;
5. The torque for a given slip varies as the square of the applied voltage.
6. The machine works as a generator when the rotor speed is faster than synchronous speed.
7. By inverting two stator phases, the induced torque will stop the machine very rapidly and try to rotate in the opposite direction.

FIGURE 30 – ROTOR CURRENT IN FUNCTION OF ROTOR SPEED

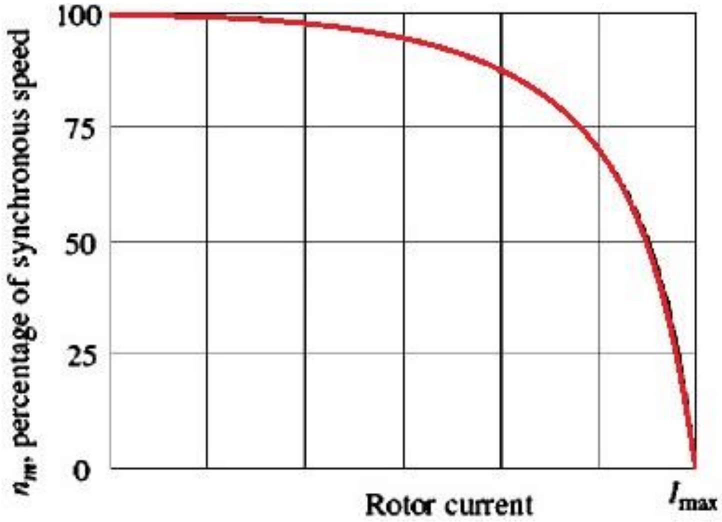

Source: adapted from Chapman (1991).

FIGURE 31 – INDUCTION MACHINE TORQUE-SPEED CHARACTERISTIC CURVE

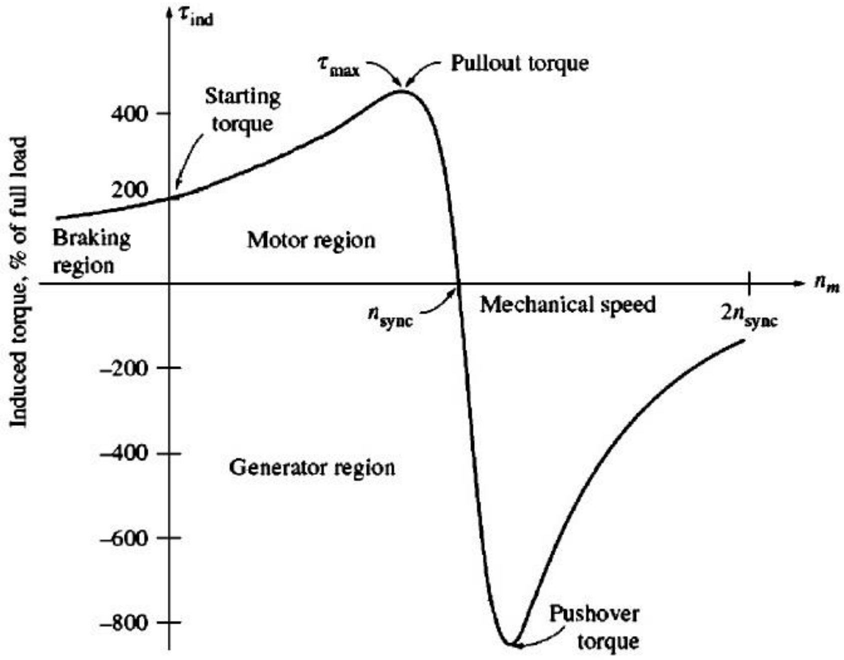

Source: adapted from Chapman (1991).

In the case of an induction generators, the greater the torque applied to the shaft the greater its resulting power would be; however, exceeding the pushover torque results in over speeding. Additionally, an induction generator consumes reactive power; thus, it must have an external source to maintain its stator magnetic field.

The biggest advantage of induction generators is their simplicity since require very simple control methods and little maintenance. As long as the speed still greater than "n_{sync}", it functions as a generator. Nevertheless, its biggest problem is the high variation in voltages with the change in load. To avoid this, the power supply must control the voltage at terminals (CHAPMAN, 1991).

On the other hand, figure 32 shows how the torque curve changes for different rotor resistance. Notice that an IM with high rotor resistance have a high starting torque but low efficiency, and vice versa. Induction motors with wound-rotors can insert extra resistances into the rotor to solve this dilemma. Nonetheless, this is not possible in squirrel cage-rotors.

FIGURE 32 – SPEED CONTROL BY VARYING THE ROTOR RESISTANCE

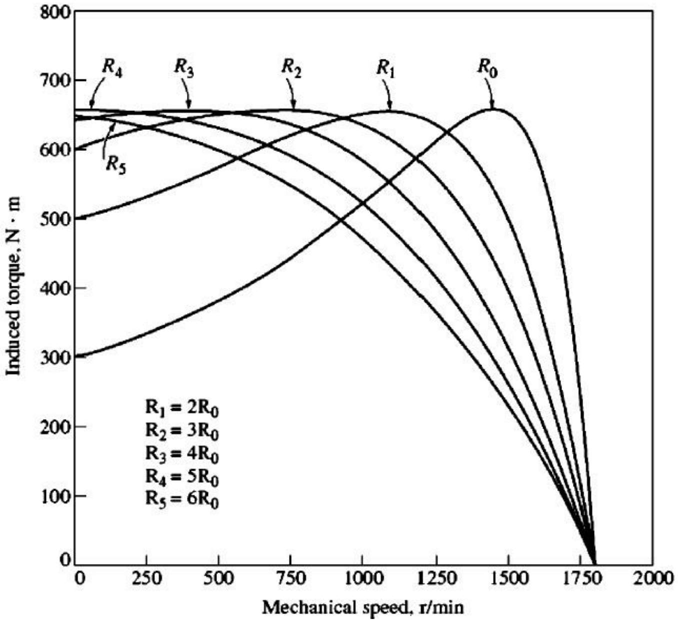

Source: Chapman (1991).

Even though, squirrel-cage machines can vary the rotor resistance by changing the shape of the rotor bars. In general, the deeper the bar is into the rotor the greater its leakage and, hence, the larger its reactance. On the contrary, bars placed near the rotor's surface have a small leakage, resulting in a lower reactance. Figure 33 shows different lamination designs of squirrel-cage rotor bars, and their respective torque-speed curves.

FIGURE 33 – TORQUE-SPEED CURVES FOR DIFFERENT IM ROTOR DESIGNS

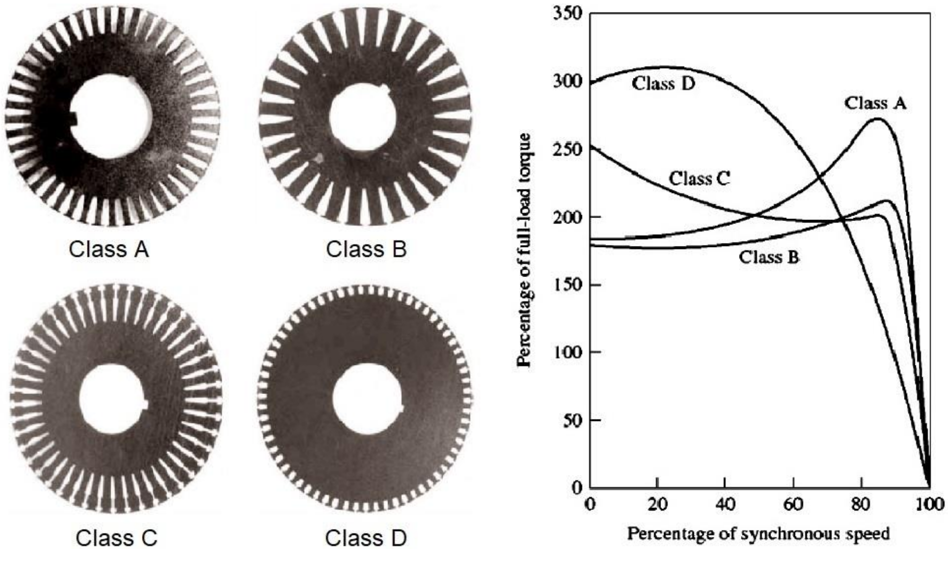

Source: adapted from Chapman (1991).

Nowadays, the most common control method for induction drives is achieved by Pulse Width Modulation (PWM) techniques. Moreover, this method can be used with both types of IMs. Figure 34b illustrates the manner in which the PWM can control output frequency while maintaining a constant Root Mean Square (RMS) voltage level. On the other hand, figure 34c illustrates the control of RMS voltage while maintaining a constant frequency (CHAPMAN, 1991).

FIGURE 34 – FREQUENCY AND VOLTAGE CONTROL WITH A PWM WAVEFORM

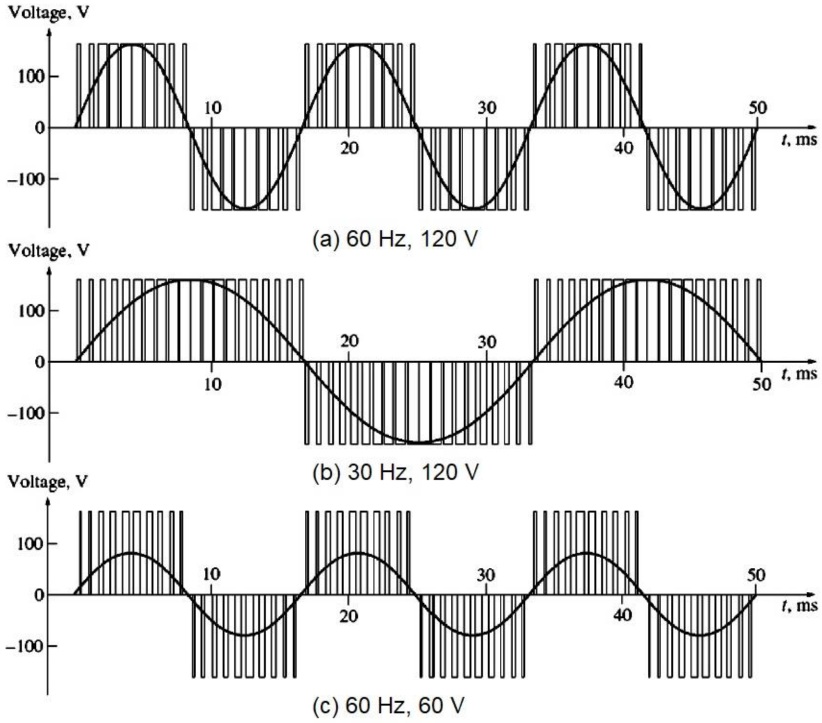

Source: adapted from Chapman (1991).

2.3.4 SWITCHED RELUCTANCE MOTORS

According to Miller (1993 p.1): “A reluctance motor is an electric motor in which torque is produced by the tendency of its moveable part to move to a position where the inductance of the excited winding is maximized”. In addition, a reluctance motor has the next characteristics:

1. The stator and the rotor have salient poles;
2. Each of the stator windings is wound on one pole;

3. The excitation of the phases is obtained by current pulses;
4. The flux waveform of the coils is triangular or sawtooth and do not vary with the current;
5. The commutation of the phase currents is synchronized with the rotor position. Therefore, a shaft-position sensor is usually used.

Aligned and unaligned rotor positions

The *aligned position* is given when the rotor poles are aligned with the stator poles, as shown in figure 35a; thus, the air gap distance between the rotor and stator poles is at its minimum, having the lowest reluctance and the maximum inductance. Due to this, the aligned position is susceptible to saturation.

On the other hand, the *unaligned position* is given when the interpolar axis of the rotor is aligned with the stator poles, as shown in figure 35b; thus, the air gap distance between the rotor and stator poles is at its maximum, having the lowest inductance and the highest reluctance. This position is of unstable equilibrium since any displacement to either side will attract the rotor to the nearest aligned position, generating a torque (MILLER, 1993).

FIGURE 35 – ROTOR POSITIONS OF A 6/4 REGULAR SRM

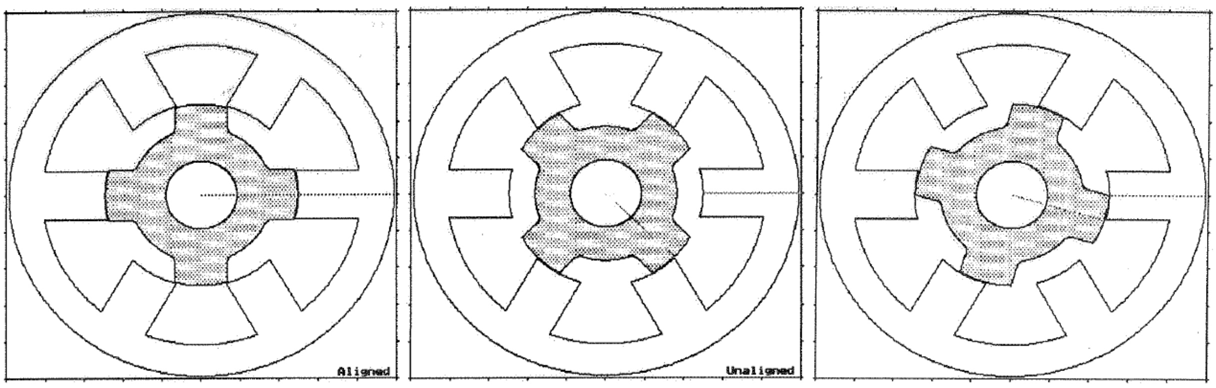

(a) aligned position (b) unaligned position (c) intermediate postion

Source: adapted from Miller (1993).

Figure 36 presents the magnetization curves of one phase of a SRM. Notice that the highest value is for the aligned position, while the lowest value represents the unaligned position. All other the other positions are between those two values and are called *intermediate positions*, see rotor position shown in figure 35c.

In practice there might be some interaction between phases, however, this is undesirable since any overlap of two phases could cause the saturation of the poles. The interaction between phases can be minimized by reducing geometrical asymmetries and eccentricities.

FIGURE 36 – MAGNETIZATION CURVES FOR ONE PHASE OF A SRM (X-AXIS: CURRENT, AND Y-AXIS: FLUX LINKAGE)

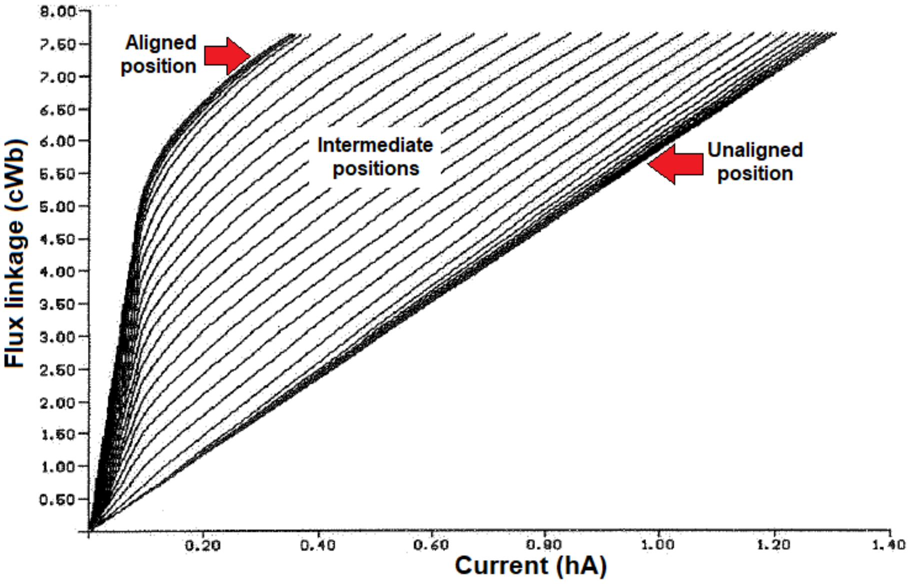

Source: Miller (1993).

Number of phases and poles

A Switched Reluctance Machine (SRM) with stator and rotor poles symmetrical about their centerlines and with equally spaced poles around their rotor and stator is known as a *regular SRM*. In regular SRMs, there is always the option to have two less or two more stator poles. The advantage of having more stator poles is the lower torque-dips; however, it would have higher core losses because of higher switching frequencies.

The configuration of SRM poles is usually denoted by the N_s/N_r nomenclature. Where "N_s" is the number of stator poles and "N_r" is the number of rotor poles. The simplest and cheapest SRM would be a machine with one-phase, however, it would need an assisting mechanism to overcome its starting problem caused by big zones where the torque is zero, also known as *dead zones*.

Similarly, in two-phase SRMs the aligned position for one phase is the unaligned position for the other phase that result in two dead zones, represented by the grey boxes in figure 37a. Nevertheless, this problem can be overcome by using *stepped gaps*, observe the grey box reduction in figure 37b. The idea of the stepped gap is to have positive phase inductance at any rotor position, and it is accomplished by changing the rotor pole geometry, as shown in figure 37c. Finally, table 5 categorize all possible SRMs according to the number of poles they have.

FIGURE 37 – STEPPED GAP ROTOR AND ITS EFFECTS

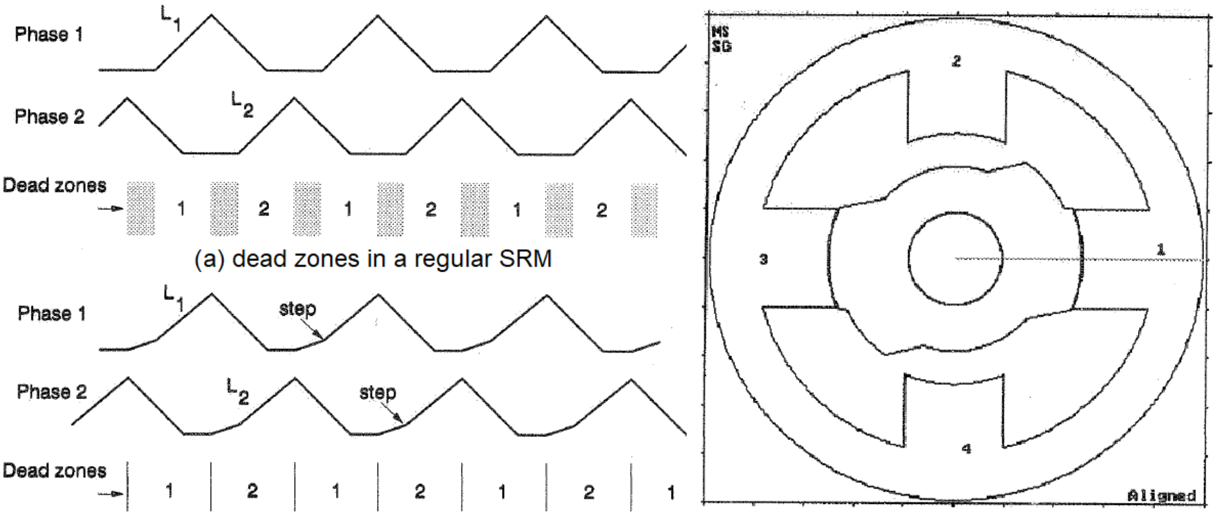

Source: adapted from Miller (1993).

Induced torque and peak volt-ampere rating

When a phase is excited, the rotor moves to the position of maximum inductance, hence, the direction of torque is always towards the nearest aligned position. In addition, the inductance of a phase varies in function of the rotor position and the phase current. Figure 38 shows the inductance variation according to the rotor position, as well as the effect of saturation as current increases.

TABLE 5 – CLASSIFICATION OF POSSIBLE SWITCHED RELUCTANCE MOTORS

m	N_s	N_r	μ	ε °	Strokes/rev	F	Examples/comment/[Ref]
1	2	2	1	180	2	*	Horst [22]; Compter [21]
2	4	2	1	90	4	NS	Byrne [9,19]
3	6	2	1	69	6	SG	$\rho_E < 1$
3	6	4	1	30	12	OK	Uneven torque
3	6	8	1	15	24	OK	HP Draftmaster/Warner [13]
3	12	8	2	15	24	OK	Allenwest MotionMaster
3	18	12	3	10	36	OK	Low λ
3	24	16	4	7.5	48	OK	Low λ
4	8	6	1	15	24	OK	OULTON
4	16	12	2	7.5	48	OK	Low λ
5	10	4	1	20	18	OK	
5	10	6	1	12	30	OK	
5	10	8	1	9	40	OK	
5	10	8	2	18	20	OK	Magna Physics [26]
6	12	10	1	6	10	?	
6	24	20	2	3	120	?	
6	12	14	1	4.29	84	?	
7	14	10	1	5.14	70	?	
7	14	12	1	4.29	84		See Pollock [30]

m = No. of phases; N_r = rotor poles; N_s = stator poles; ε = stroke; F = Feasibility; NS = Non-symmetric rotor; SG = stepped-gap rotor. μ = No. of working pole-pairs/phase (or "multiplicity"); ε = stroke angle. * Needs "assist" for starting.

Source: Miller (1993).

FIGURE 38 – VARIANCE IN PHASE INDUCTANCE AND CURRENTS ACCORDING TO ROTOR POSITION

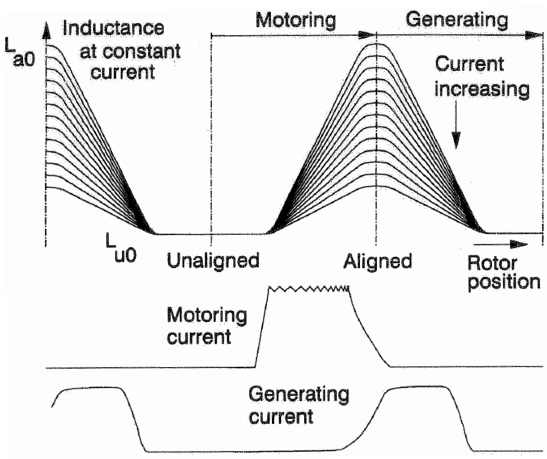

Source: Miller (1993).

From figure 38 notice that, for motoring operation, the phase is energized before the aligned position when the inductance is increasing. While for generator operation, the phase is energized after the aligned position when the inductance is decreasing. Observe that in both cases the excitation current is always positive.

In a SRM, not all the energy supplied to the phase is transformed into mechanical work, instead, some of this energy is stored in the magnetic field. Therefore, the energy conversion cycle can be divided into two phases: when the energy is supplied to the rotor through the transistors and when the energy flows back to the supply through the diodes. The current rate of both phases is represented in figure 39 by line O-C. Notice that the aligned and unaligned lines follow the magnetization curve presented in figure 36.

At first, near the unaligned position, the current rises linearly while the inductance is low. But, when the poles start to overlap an increase in inductance generates a counter-electromotive force that reduces the rate in current. When point C is reached the commutation is made, and the supply voltage is reversed. Then, the energy left in the magnetic field that was not converted to mechanical energy returns to the supply through the diodes. As shown in figure 39b, the area "W_{md}" represents the energy stored that is further utilized during the diode conduction period (MILLER, 1993).

FIGURE 39 – ENERGY-CONVERSION CYCLE OF A SRM

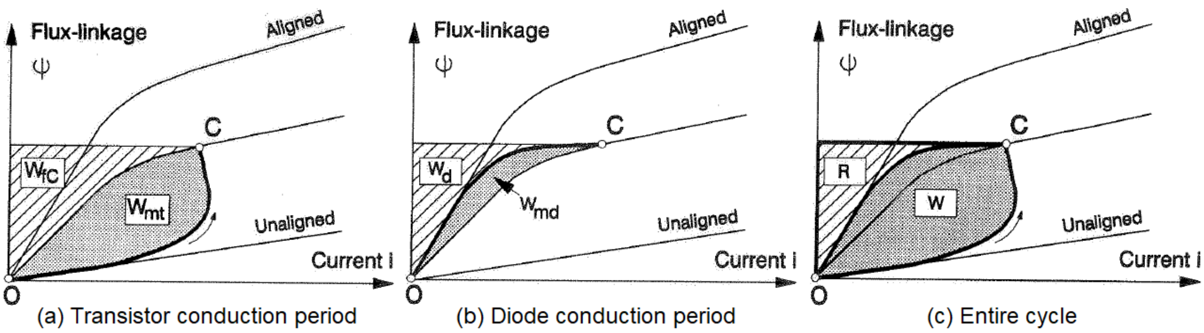

Source: adapted from Miller (1993).

The mechanical work done during the transistor conduction period and the diode conduction period are expressed by equations 33 and 34, respectively:

$$W_{mt} = U - W_{fC} \tag{33}$$

$$W_{md} = W_{fC} - W_d \tag{34}$$

Where:

- W_{mt} is the mechanical work done during the transistor conduction period;
- W_{md} is the mechanical work done during the diode conduction period;
- W_d is the energy returned to the supply, also denoted as R;
- W_{fC} is the energy stored in the magnetic field during the transistor conduction period, and;
- U is the total energy supplied to the phase.

The entire energy conversion cycle, or stroke cycle, combines the transistor and diode conduction periods (see figure 39c). Thus, the total energy supplied by the controller is given by equation 35, while the total mechanical work done in the stroke is given by equation 36. On the other hand, equation 37 presents the *energy ratio* available to mechanical conversion:

$$U = W + R \tag{35}$$

$$W = W_{mt} + W_{md} \tag{36}$$

$$E = \frac{W}{U} = \frac{W}{W + R} \tag{37}$$

Finally, the average torque is given by the number of conversion cycles done in each revolution. Assuming that all the phases have the same energy conversion cycle, then, the average torque is given by equation 38:

$$\boldsymbol{T = \frac{mN_r}{2\pi} * W} \tag{38}$$

Where:

- T is the average torque in one revolution;
- N_r is the number of rotor poles;
- m is the number of phases, and;
- W is the total mechanical work given by equation 36.

On the other hand, the peak volt-ampere rating of a SRM can be described by equation 39:

$$Q_m = \frac{2\pi T\omega}{N_r E k \delta} = \frac{4P_{gap}}{Ek} \tag{39}$$

Where:

- Q_m is the peak volt-ampere rating;
- T is the motor torque, obtained by equation 39;
- ω is the motor speed in rad/s;
- N_r is the number of poles;
- E is the energy ratio, obtained by equation 38;
- k is the utilization ratio, and;
- P_{gap} is the air gap power;

Since “E” and “k” depend from the magnetization curves, then the unaligned and aligned magnetization curves influence “Q_m”, which also depends from “N_r”.

In addition, real SRMs have torque-dips that occur near commutation from one phase to the next. Figure 40 shows the current of a SRM, and the torque it generates. Observe that the current drops after commutation, causing a torque drop during the diode conduction period.

FIGURE 40 – THREE PHASE CURRENTS AND THE TORQUE THAT GENERATES

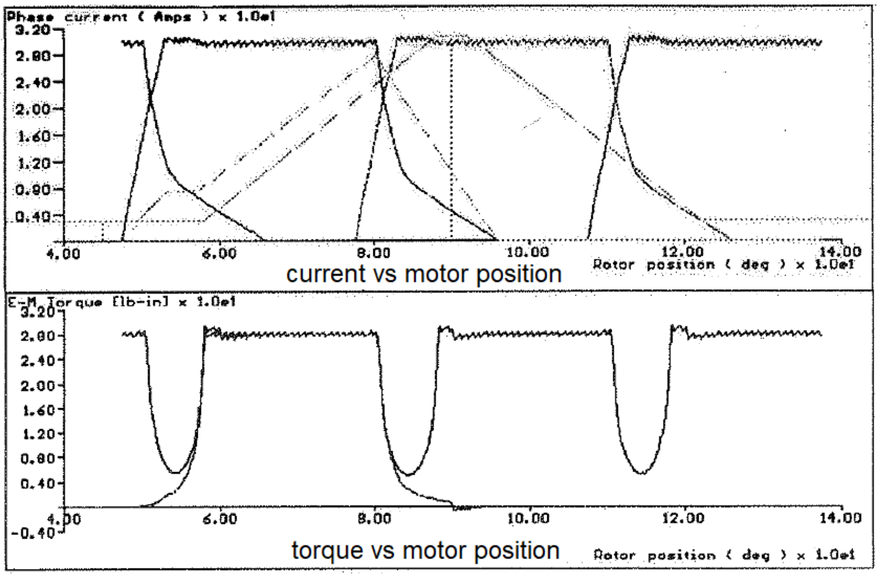

Source: adapted from Miller (1993).

This problem can be reduced by boosting the current in the regions of torque-dip, by increasing the number of phases, or by widening the stator and rotor poles. Nevertheless, the latter option increases copper losses, thus, four phase motors are preferable when a smooth torque is wanted.

To better illustrate how the number of phases reduces torque-dips, figure 41 presents the torque waveforms of 3, 4 and 5-phase motors. Notice that 4-phase SRMs do not have torque-dips, however, they have high inductance ratios. On the other hand, 5-phase SRMs alleviate the torque-dips without the loss of inductance ratio; although, they also can produce torque-peaks. In addition, 4 and 5-phase machines allow to operate various phases at the same time, leading to more stable operation when running without shaft position feedback.

Figure 42a shows the flux-paths of a 10/8 SRM with two phases operating at the same time, notice that both phases are producing positive torque. While figure 42b shows the flux paths of a 12/8 SRM, which is essentially a 6/4 SRM with twice the poles. Observe that the 12/8 SRM would have shorter flux paths than the 6/4 SRM shown in figure 35; thus, minimizing the copper losses and decreasing the unaligned inductance (MILLER, 1993).

FIGURE 41 – TORQUE WAVEFORMS OF 3, 4, AND 5-PHASE MOTORS

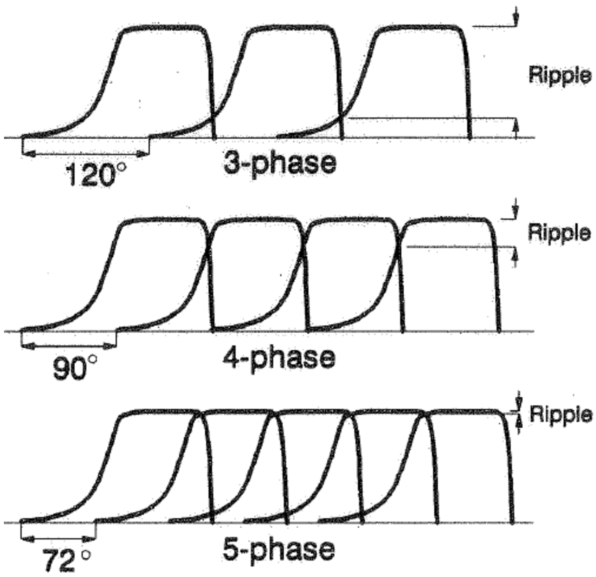

Source: Miller (1993).

FIGURE 42 – REPRESENTATION FLUX-PATHS OF TWO DIFFERENT SRM

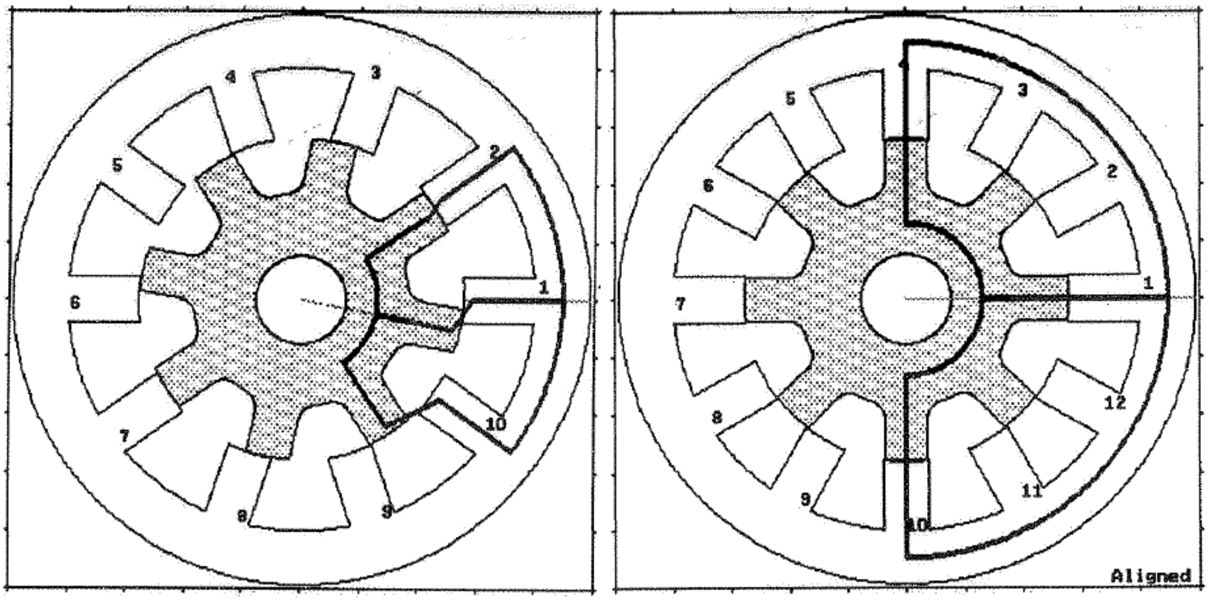

(a) 5-phase 10/8 SRM (b) 3-phase 12/8 SRM

Source: adapted from Miller (1993).

Working as generator

The switched reluctance machine is capable of operating continuously as a generator by retarding the firing angles, allowing for the majority of the winding conduction period to happen after the aligned position.

In such cases, the generated power returns to the source during the diode conduction period, however, excitation power also must be provided during the transistor conduction period. Thus, the energy returned during the diode period must exceed the energy supplied during the transistor period. In addition, excitation energy must be delivered every stroke; in EVs and HEVs, the battery gives this energy (MILLER, 1993).

Advantages and disadvantages of SRM

Finally, the advantages and disadvantages of the switched reluctance motor and its controller are given in table 6 and 7, respectively:

TABLE 6 – ADVANTAGE AND DISADVANTAGE OF SWITCHED RELUCTANCE MOTORS.

Motor – positive impressions		Motor –negative impressions	
P1	Low manufacturing cost	**N1**	High scrap in punching
P2	Low material cost	**N2**	Small shaft diameter
P3	Minimal temperature effects	**N3**	Small air gap
P4	High-speed operation possible	**N4**	Large coil cross-section may lead to hot-spots
P5	Low inertia	**N5**	Shaft position sensor needed
P6	Ease of repair	**N6**	Doubly-salient structure will cause noise, torque ripple
P7	Short end-turns, with no crossovers	**N7**	Apparently high windage loss at high speed
P8	Low rotor losses	**N8**	Long, two-pole flux-path
P9	Fault tolerant	**N9**	Cannot start direct on-line

Source: adapted from Miller (1993).

TABLE 7 – ADVANTAGE AND DISADVANTAGES OF THE SRM CONTROLLER.

Controller – positive impressions		Controller –negative impressions	
P10	The number of transistors is the same as, or less than, the number required for an AC drive with the same number of phases	**N10**	The circuit cannot use phaselog modules developed for AC inverters
P11	The use of one half-bridge per phase winding provides protection against shoot-through failures	**N11**	Both ends of every phase winding appear to need a connection
P12	There is a high degree of independence between phases	**N12**	The non-uniform torque may lead to a high filter-capacitor requirement
P13	There is a wide variety of circuit topologies for different applications	**N13**	The non-uniform torque/ampere may limit the servo bandwidth
P14	The control is well suited for digital implementation with linear current regulation	**N14**	High di/dt is a possibility, mandating the use of short, low-inductance cables
P15	Reluctance motors have a wide speed range at constant power	**N15**	Reluctance motors have a high kVA requirement
P16	No open-circuit voltage	**N16**	Commutation frequency is higher than in AC motor with the same rotor pole number
P17	No suited short-circuit current	**N17**	Lack of short-circuit current may limit applications as a generator; no dynamic braking

Source: adapted from Miller (1993).

2.3.5 COMPARISON BETWEEN DIFFERENT ELECTRIC MOTORS

This section presents four studies that evaluate various electric machines for automotive application. First, Xue, Cheng, and Cheung (2008) compared the efficiency, weight, and cost of a DC motor, an IM, a Permanent Magnet Brushless DC (BLDC) motor and a Switched Reluctance Motor (SRM). Table 8 shows the notes they gave for each motor, in which 5 represents the highest efficiency, lowest weight, and lowest cost.

TABLE 8 – COMPARISON AMONG FOUR TYPES OF ELECTRIC MOTORS

Index	DC motor drives	IM drives	PM BLDC motor drives	SRM drives
Efficiency	2	4	5	4.5
Weight	2	4	4.5	5
Cost	5	4	3	4
Total	9	12	12.5	13.5

Source: Xue, Cheng, and Cheung (2008).

Additionally, they said that the torque-speed curve of SRM matched very well with the load requirements of an EV; because of its low rotor inertia, it had rapid acceleration and a high speed operation range, making them especially suitable for gearless operation. The SRM is also insensitive to high temperatures and very easy to cool down. Nonetheless, it suffers from torque ripple and higher acoustic noise.

On the other hand, the BLDC motor is known for its high efficiency and high power density; however, the rare-earth PM makes them the most expensive of the four motors. Moreover, the PM have limited field weakening capability due to a fix magnetic flux, which in turn restricts its maximum speed. The authors concluded that DC motors will continue to be used in the future since they have the lowest cost. On the other hand, if these three factors were the main decision parameters, then the SRM would be the best choice.

Yang et al. (2015) compared the performance, efficiency, and vibration of an IM, a SRM, and two interior permanent magnet (IPM) synchronous motors. From which one had distributed windings and the other had concentrated windings. The specifications for each motor are given in table 9, in which the 48/8 IPM is the one with distributed windings and is based on the motor of the second generation Toyota Prius.

The Noise Vibration and Harshness (NVH) analysis revealed that the 48/8 IPM have the lowest harmonic order and, therefore, should have the quietest operation. Additionally, it also had the lowest stator core deformation under a 50 Nm load at 1000 rpm, whereas the 12/8 IPM and SRM motors had the highest deformation. The SRM had the highest deformation under a 50 Nm load at 5000 rpm, while the other three motors have a lower deformation than those under 50 Nm load at 1000 rpm due to field weakening control at high speed.

TABLE 9 – SPECIFICATION OF MOTORS COMPARED BY YANG ET AL. (2015)

Parameter		48/8 IPM	12/8 IPM	48/36 IM	12/8 SRM
Maximum dc-link voltage (V)		500			
Peak power (kW)		50			
Maximum rotational speed (rpm)		6000			
Peak torque (Nm)		300			
Designed rated operating point	Torque (Nm)	100*	120	90	100
	Speed (rpm)	3000*	2500	3300	3000
Pole pairs		4	4	2	–
Stator outer diameter (mm)		269			
Stator inner diameter (mm)		161.9	166	177.9	172
Rotor inner diameter (mm)		110	100	94	90
Stack length (mm)		83.82	83.82	108	105
Air gap length (mm)		0.73	0.7	0.45	0.5
Rotor inertial moment (kg m^2)		0.042	0.047	0.081	0.069
Armature core weight (kg)		17.3	13.75	17.25	17.83
Armature copper weight (kg)		5.9	8.13	13.05	15.39
Rotor core steel weight (kg)		5.37	6.7	10.06	9.24
Magnet weight (kg)		1.23	1.3	–	–
Rotor bar and ring (kg)		–	–	8.43	–
Total weight (kg)		29.8	30	48.8	42.5
Magnet type		N36Z_20			
Magnet size (mm)		18.9*6.5	19.1*6.8	NA	
Characteristic current (A)		105	98		
Steel lamination		M19-29G			

*Estimated value.

Source: Yang et al. (2015).

Regarding the efficiency of the motors, they found that both IPMs can offer efficiency as high as 97%; however, the 12/8 IPM have higher efficiency at low speed, and over 5000 rpm the eddy current losses of the PMs increase by 50 times. On the other hand, the IM can have an efficiency of up to 96% at high speed, but it has the widest low-efficiency region at low speed due to copper losses. In addition, IM and SRM have lower peak power densities than both IPM. Therefore, the 12/8 SRM may need more current to deliver the same torque than the other motors. While the 12/8 IPM may need more PM material for the same torque.

Similarly, Pellegrino et al. (2012) compared an IM, a surface-mounted permanent-magnet (SPM) and an IPM synchronous motor. The specifications of the three motors are given in table 10. These motors were compared in terms of energy consumption for the New European Driving Cycle (NEDC), as shown in figure 43.

FIGURE 43 – ENERGY LOSSES OVER THE NEDC FOR THREE DIFFERENT TYPES OF MOTORS.

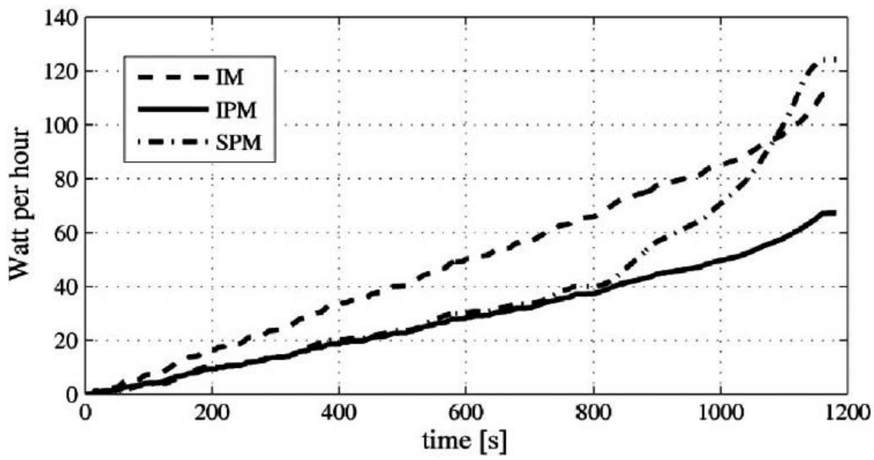

Source: Pellegrino et al. (2012).

The results show that IPM and SPM motors are very similar during urban operation, but when higher speeds are needed the SPM had very high losses. As for the IM, it had higher losses than the IPM, however, both have a constant rate of energy consumption during all the cycle.

It was concluded that the SPM had severe limitations at high speed due to PM losses. On the other hand, the IPM had the best efficiency of the three at any load and any speed, due to a proper design; additionally, it also had the best power overload curve. Finally, the IM had similar power overload curves than the IPM, although the IM was penalized by the cage losses both at low and high speeds.

Finally, Jack, Mecrow, and Weiner (1999) compared the electromagnetic limits of PM motors and SRMs. This was made by comparing the flux-linkage/current diagrams since they represent the energy converted to torque in one electrical cycle. They argue that this methodology can be used to compare motors of any size.

TABLE 10 – SPECIFICATIONS OF MOTORS COMPARED BY, PELLEGRINO ET AL. (2012)

		IM	IPM	SPM
Pole pairs		2		
Stator slots		48	6	
Stator outer diameter	mm	216		
Stator bore diameter	mm	142	131	
Stack length	mm	170		
Airgap	mm	0.7		
Number of turns		20	23	
Copper fill factor		0.4		
End connections (per side)	mm	150	77	
Max speed	rpm	12000		
Continuous torque *	Nm	110	160	130
Speed at continuous torque *	rpm	4000	3800	3800
Maximum speed **	rpm	11300	12000	10300

		IM	IPM	SPM
Current at continuous torque	A pk	200	255	294
Overload torque	Nm	210	210	150
Overload current	A pk	360	360	360
Characteristic current (150°C)	A pk		205	193
Phase rated voltage	V pk	173	173	173
Phase back-emf (12000 rpm, 20°C)	V pk		170	540
Stator resistance (130°C)	Ω	0.027	0.027	0.021
Rotor resistance (180°C)	Ω	0.018		
Steel grade		M250–35A		
PM grade			BMN-42SH	
PM mass	kg		1.95	1.35
Rotor temperature		180° C	150° C	150° C

Source: adapted from Pellegrino et al. (2012).

Additionally, they made a cost analysis, which is shown in table 11. They concluded that both motor types can be used for vehicle applications, in which the fully pitched SRM is the better option when based only on a cost basis.

TABLE 11 – COMPARISON OF SRM AND PM MOTOR COSTS PER UNIT TORQUE (£/NM)

Motor	Stator core	Rotor core	Magnet	Copper	Total
SRM short pitched	0.31	0.12	-	0.28	0.71
SRM fully pitched	0.18	0.07	-	0.15	0.4
PM motor	0.15	0.03	1.36	0.17	1.71

Source: adapted from Jack, Mecrow, and Weiner (1999).

2.4 INTERNAL COMBUSTION ENGINES

An internal combustion engine is a machine that transforms the chemical energy of a fuel into mechanical energy. There are several types of internal combustion engines, but this work only focuses on four-stroke spark-ignition engines. For this, the engine operates a piston that moves back and forth inside a cylinder. This piston is connected to a rod and crank mechanism as shown in figure 44.

Notice the Top Dead Center (TDC) position corresponds to the position with the minimum cylinder volume, also called *clearance volume* "V_c". On the other hand, the Bottom Dead Center (BDC) position corresponds to the maximum volume of the cylinder or *total volume* "V_t", which is the sum of the *displaced volume* "V_d" and the clearance volume. The ratio between these two volumes is known as the *compression ratio,* and is given by equation 40:

$$r_c = \frac{maximum\ cylinder\ volume}{minimum\ cylinder\ volume} = \frac{V_d + V_c}{V_c} \tag{40}$$

FIGURE 44 – BASIC GEOMETRY OF AN INTERNAL COMBUSTION ENGINE

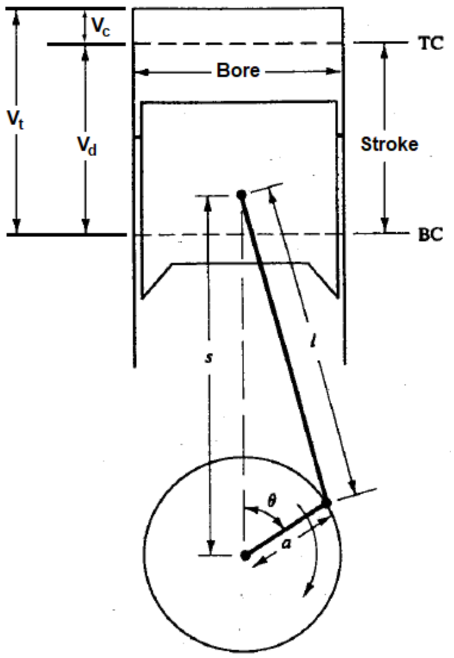

Source: adapted from Heywood (1988).

2.4.1 FUNDAMENTALS OF OTTO CYCLE ENGINES

Four-Stroke Cycle

The Otto cycle is based on the four-stroke cycle which can be observed in figure 45. This cycle requires that each cylinder had two crankshaft revolutions per each power stroke, and is resumed next:

1. The *intake stroke* starts with the piston at TDC and ends at BDC. During this stroke the inlet valve is maintained open, drawing fresh mixture into the cylinder during the piston displacement.
2. The *compression stroke* occurs when the piston moves from BDC to TDC. Since both valves are closed the mixture inside the cylinder is compressed. Toward the end of the stroke, the combustion of the mixture is initiated and the cylinder pressure rises more rapidly.

FIGURE 45 – FOUR-STROKE OPERATING CYCLE

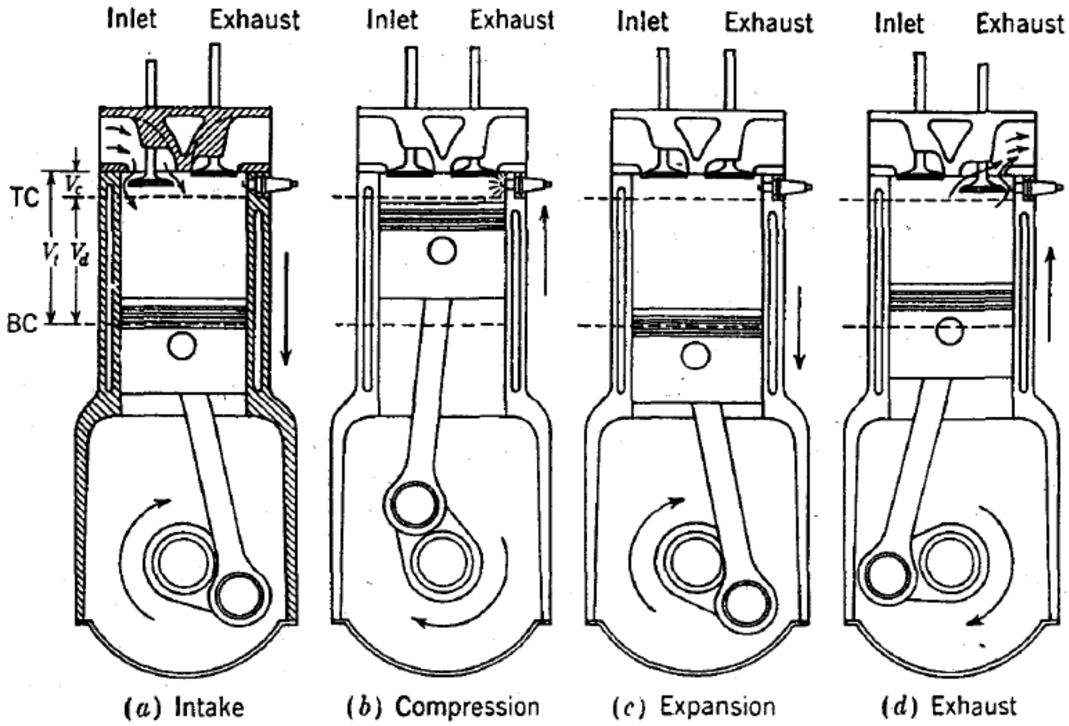

Source: Heywood (1988)

3. The *expansion stroke*, or power stroke, starts with the piston at TDC and ends at BDC. The high-temperature and high-pressure gases resulting from the combustion pushes the piston down and force the crank to rotate, generating work.
4. The *exhaust stroke* occurs with the exhaust valve open, letting the burned gases to exit the cylinder. At first, the burned gases leave the cylinder due to the difference in pressures, but later on, they are swept out by the piston as it moves back to TDC.

Ideal air standard cycle

The ideal air cycle assumes that the compression and expansion processes are reversible and adiabatic (no heat transfer), hence isentropic. Figure 46 shows the processes of the ideal air standard Otto cycle, which are:

1–2 Isentropic compression of air to a volume ratio (compression ratio);

2–3 Addition of heat at constant volume;

3–4 Isentropic expansion of air to the original volume;

4–1 Rejection of heat at constant volume.

FIGURE 46 – P-V DIAGRAM OF THE IDEAL AIR STANDARD OTTO CYCLE

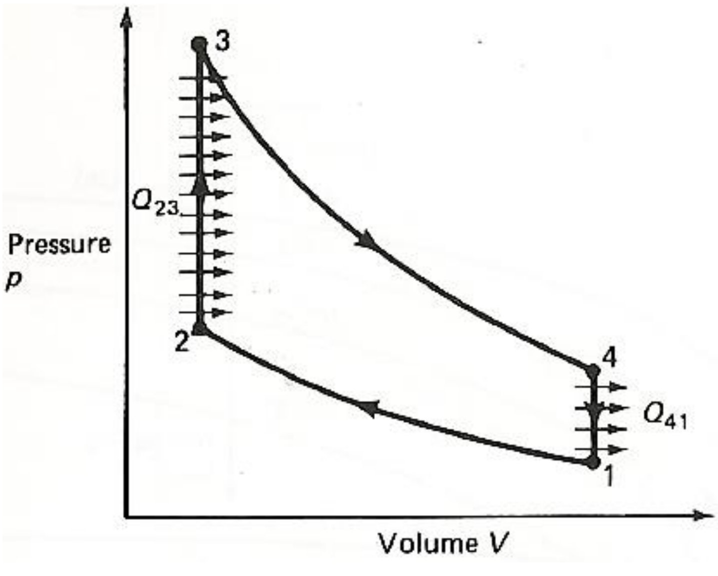

Source: adapted from Stone (1992).

Additionally, it is assumed that the fluid is comprised of air and that it behaves as a perfect gas. Therefore, the fluid's specific heats are assumed constant and equal to the air; hence, the mass of air that is transferred by the heat are:

$$Q_{23} = m * c_v(T_3 - T_2) \tag{41}$$

$$Q_{41} = m * c_v(T_4 - T_1) \tag{42}$$

Thus, the efficiency of the Otto cycle is given by equation 44:

$$\eta_{Otto} = \frac{W}{Q_{23}} = \frac{Q_{23} - Q_{41}}{Q_{23}} = 1 - \frac{Q_{41}}{Q_{23}} = 1 - \frac{T_4 - T_1}{T_3 - T_2} \tag{43}$$

In addition, the isentropic processes 1-2 and 3-4 are expressed by equations 44 and 45:

$$\frac{T_2}{T_1} = \left(\frac{v_1}{v_2}\right)^{k-1} = r_c{}^{k-1} \tag{44}$$

$$\frac{T_3}{T_4} = \left(\frac{v_4}{v_3}\right)^{k-1} = r_c{}^{k-1} \tag{45}$$

From which $k = c_p/c_v$. Since $v_1 = v_4$ and $v_2 = v_3$, then the efficiency of the Otto cycle can be rewritten as equation 46:

$$\boldsymbol{\eta_{Otto} = 1 - \left(\frac{v_2}{v_1}\right)^{k-1} = 1 - \frac{1}{r_c{}^{k-1}}} \tag{46}$$

Fuel-air cycle

The ideal air standard cycle overestimates the engine thermal efficiency. In the fuel-air cycle model, the molar constant-volume heat capacity varies; therefore, the ratio of heat capacities "k" also varies. Additionally, this cycle considers the presence of fuel and combustion products. All this result in the fuel-air cycle having a better approximation than the ideal air standard cycle.

The fuel-air cycle is the same than the ideal air standard Otto cycle, hence, also assumes no heat transfer, instantaneous complete combustion, and reversible compression and expansion processes. Nevertheless, the fuel-air cycle represents the real thermodynamic behavior of the gases (GIACOSA, 1979; STONE, 1992).

Differences between the ideal and real Otto cycles

According to Giacosa (1979), there are four main differences between the ideal and the real Otto cycle, which are shown as the shaded areas of figure 47, and are explained next:

A. *Heat losses*. The ideal cycle did not considered heat losses; in reality, some heat of the fluid is transmitted to the cylinder walls. Therefore, the expansion and compression processes are rather polytrophic, not adiabatic, with an exponent “n” instead of “k”.
B. *Finite combustion time*. The ideal cycle assumes that the heat addition is done at constant volume, hence, it is instantaneous. In reality, the combustion takes a certain time, thus it is necessary to anticipate the ignition so the combustion can take place when the piston is near TDC.

FIGURE 47 – COMPARISON BETWEEN THE THEORIC AND INDICATED OTTO CYCLES

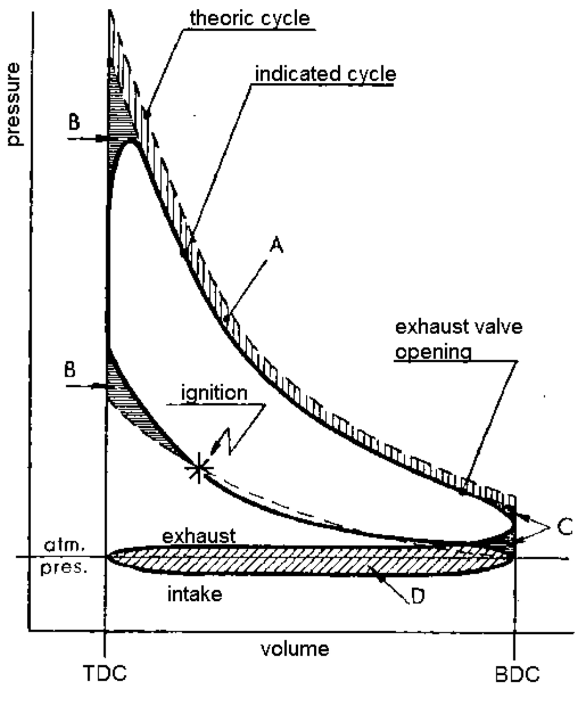

Source: adapted from Giacosa (1979).

C. *Valve losses*. In addition, the ideal cycle considered that the heat subtraction is done instantaneously at BDC. But in real engines, the exhaust valve must be open before BDC to let the cylinder pressure drops near the manifold pressure before the exhaust stroke begins, aiming to reduce the pumping work.
D. *Pumping work*. Is the engine work needed to carry out the intake and exhaust process. This because in the intake stroke the cylinder pressure is lower than atmospheric pressure, while in the exhaust stroke the cylinder pressure is higher than the atmospheric pressure.

The optimum spark timing is an empirical compromise, since starting the combustion too late causes most of the combustion to develop after TDC (see figure 48a). On the other hand, starting the combustion too early causes most of the combustion to develop before TDC resultin in higher pressures than normal; thus, increasing the compression work and, hence, decreasing the net work (see figure 48b).

FIGURE 48 – INFLUENCE OF IGNITION TIMING IN THE INDICATED OTTOCYCLE

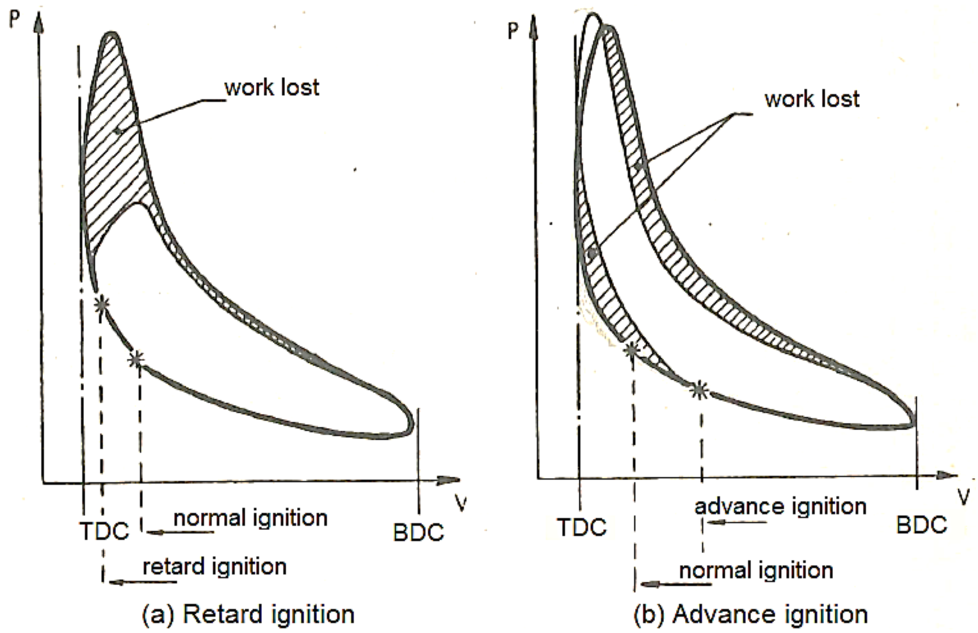

Source: adapted from Giacosa (1979).

Regarding the valve losses, the Intake Valve Opening (IVO) is made before TDC mainly because of the limits in the valve's acceleration and velocity, hence, faster engines need a higher advance in IVO. The delay in the Intake Valve Close (IVC) allows for the use of the fluid inertia during the intake process. The higher the engine speed the higher the inertia of the fluid, hence, higher delay values of IVC should be used. Advance in the Exhaust Valve Opening (EVO) is mainly due to reducing the pressure of the gases before the exhaust stroke, matching its pressure to that of the exhaust manifold. Finally, the delay in the Exhaust Valve Close (EVC) considers the inertia of the gases, as well as the gradual and progressive way in which the valve closes (GIACOSA, 1979).

Additionally, figure 49 shows the cylinder pressure, the cylinder volume, and the mass fraction burned against crank angle. The crank angle is used because the engine processes occupy almost constant crank angle intervals over a wide range of engine speeds.

The top half of figure 49 shows the rise on pressure when the fuel-air mixture is burned (solid line), which is higher than the generated by the compression alone (dashed line). Nevertheless, the shape of the pressure curve is different among each cylinder, and among each cycle. This is because the development of each combustion process varies as a result of different flow patterns and mixture compositions among each cycle and each cylinder (HEYWOOD, 1988).

FIGURE 49 – SEQUENCE OF EVENTS IN AN SI ENGINE OPERATING CYCLE

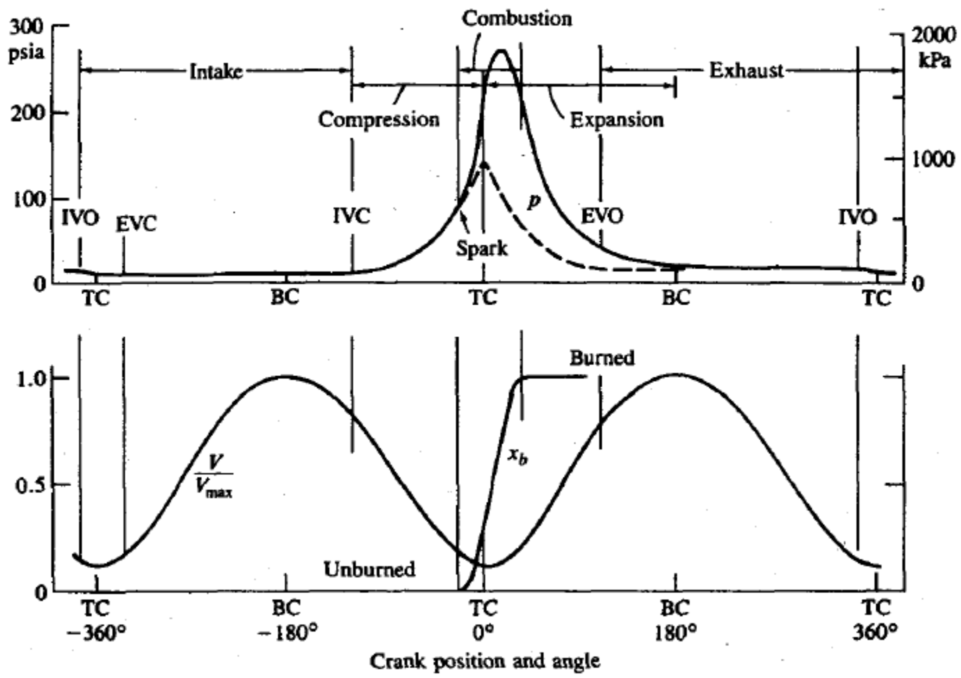

Source: Heywood (1988).

Indicated Work per Cycle

The indicated work of a given cycle on a given cylinder can be obtained by integrating the pressure around the curve of a p-V diagram, as in equation 47:

$$W_{c,i} = \oint p\, dV \tag{47}$$

Although, the indicated work can be defined as gross or net. *Gross indicated work* considers only the work done during the compression and expansion strokes, while the *net indicated work* considers the work delivered by the piston during the entire four-stroke cycle.

The shaded areas of figure 50 show the difference between gross and net indicated work. The areas B and C marked in figure 50b indicate the work done during the intake and exhaust strokes. The sum of these two areas gives the pumping work.

FIGURE 50 – P-V DIAGRAMS FOR GROSS AND NET INDICATED WORKS

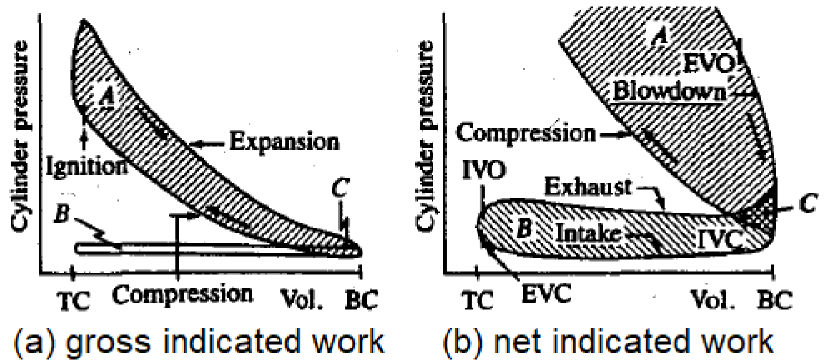

Source: Heywood (1988).

Indicated quantities are mainly used to identify the performance impact of the intake, combustion, and exhaust processes. The indicated power per cylinder, for a four-stroke cycle, can be obtained by equation 48. Also differs from the brake power since indicated quantities do not count for the power needed to overcome engine friction, driving engine accessories, and the pumping work (if gross indicated power is used). Therefore, an alternative way of estimating the gross indicated power "P_{gi}" is by summing the brake power "P_f" and the friction power "P_f", as shown in equation 49:

$$P_i = \frac{W_{c,i} N}{2} \tag{48}$$

$$P_{gi} = P_b + P_f \tag{49}$$

Where:

- P_i is the indicated power per cylinder;
- $W_{c,i}$ is the indicated work per cylinder, and;
- N is the crankshaft rotational speed in rev/s.
- P_{gi} is the gross indicated power;
- P_b is the brake power, and;
- P_f is the power used to overcome friction.

Finally, the power and torque also can be obtained by equations 50 and 51, respectively:

$$P = \frac{\eta_f \eta_v N V_d Q_{HV} \rho_{a,i} (F/A)}{2} \tag{50}$$

$$\tau = \frac{\eta_f \eta_v V_d Q_{HV} \rho_{a,i} (F/A)}{4\pi} \tag{51}$$

Where:

- P is the engine power;
- τ is the engine torque;
- η_f is the fuel conversion efficiency, given by equation 63;
- η_v is the volumetric efficiency, given by equation 54;
- N is the engine speed in revolutions per minute;
- V_d is displaced volume;
- Q_{HV} is the heating value of the fuel;
- $\rho_{a,i}$ is the air density at intake;
- (F/A) is the air-fuel ratio, defined by equation 65.

Mechanical Efficiency

Heywood (1988) defines the mechanical efficiency "η_m" as "The ratio of brake (or useful) power delivered by the engine to the indicated power", which is defined by equation 52:

$$\eta_m = \frac{P_b}{P_{gi}} = 1 - \frac{P_f}{P_{gi}} \tag{52}$$

Additionally, the mechanical efficiency can be defined using the mean effective pressure (see section 2.4.2), as in equation 53:

$$\eta_m = \frac{BMEP}{IMEP} = 1 - \frac{FMEP}{IMEP} \tag{53}$$

Volumetric Efficiency

Heywood (1988) defines the volumetric efficiency as the rate of air into the intake system divided by the rate at which the volume is displaced by the piston. Thus, the volumetric efficiency can be obtained by equation 54:

$$\eta_v = \frac{2\dot{m}_a}{\rho_{a,i} V_d N} = \frac{m_a}{\rho_{a,i} V_d} \tag{54}$$

Where:

- η_v is the volumetric efficiency;
- $\dot{m}_a$ is the air mass flow rate;
- m_a is the mass of air introduced into the cylinder;
- $\rho_{a,I}$ is the inlet air density;
- V_d is the displaced volume by the cylinder, and;
- N is the crankshaft speed in rev/s.

The volumetric efficiency is used as an overall measure of the effectiveness of the induction and exhaust processes of the engine and has a direct influence in power output. Since the mass of air in the cylinder determines the amount of fuel that can be burnt. Thus, it also depends on the density of the gases at the induction process, which in turn depends on the temperature and pressure of the charge.

Therefore, if the air density in the intake manifold is considered, then the volumetric efficiency only measures the pumping performance of the intake port and valve. On the other hand, if the atmospheric air density is considered, it measures the pumping performance of the entire intake system. For supercharged engines, the compressor or intercooler delivery conditions should be considered, instead of the ambient conditions.

Since the air flow constrains the maximum engine power during wide-open throttle engine, then, higher volumetric efficiencies allow for higher power at full load. Finally, the factors that affect the volumetric efficiency are listed next:

- Fuel characteristics, latent heat of vaporization, fuel/air ratio, and fraction of fuel vaporized in the intake system;
- Mixture temperature as influenced by the heat transfer;
- Ratio of exhaust to inlet manifold pressures;
- Compression ratio;
- Engine speed;
- Intake and exhaust manifold and port design;
- Intake and exhaust valve geometry, size, lift, and timings.

Instantaneous and mean piston speed

The gas-flow velocities in the intake and the cylinder scale with the mean piston speed, which is given by equation 55:

$$\bar{S}_p = 2LN \tag{55}$$

While the instantaneous piston velocity is given by equation 56:

$$S_p = \frac{ds}{dt} \tag{56}$$

Where:

- $\bar{S}_p$ is the mean piston speed;
- S_p is the instantaneous piston velocity;
- N the crankshaft speed in rev/s;
- L the stroke length (see figure 44), and;
- s the distance between the piston and the crankshaft (see figure 44).

2.4.2 Operation Characteristics of Otto Cycle Engines

This section explores how different characteristics affect the performance of an engine. The characteristics covered in this section are the compression ratio, mean effective pressure, specific fuel consumption, equivalence ratio, spark timing, and exhaust gas recirculation.

Compression ratio

The compression ratio is defined as the ratio between the total volume of the cylinder and the clearance volume by the cylinder, and it can be obtained with equation 40. Figure 51 shows that higher compression ratios give higher fuel conversion efficiencies.

Besides the fuel conversion efficiency, the compression ratio also influences the heat transfer, friction, combustion rate and combustion stability of the engine. These variables, together with the octane quality of the fuel, limit the maximum possible compression ratio. Moreover, the actual compression and expansion processes in engines depend on valve timing, and not just in the geometrical compression ratio.

Figure 52 shows the effect of the compression ration on the Indicated Mean Effective Pressure (IMEP) and on the fuel conversion efficiency "$\eta_{f,ig}$". Observe that for compression ratios higher than 17, the IMEP and $\eta_{f,ig}$ decrease slightly. This is due to the increasing surface/volume ratio and slower combustion.

FIGURE 51 – VARIATION OF FUEL CONVERSION EFFICIENCY WITH THE COMPRESSION RATIO

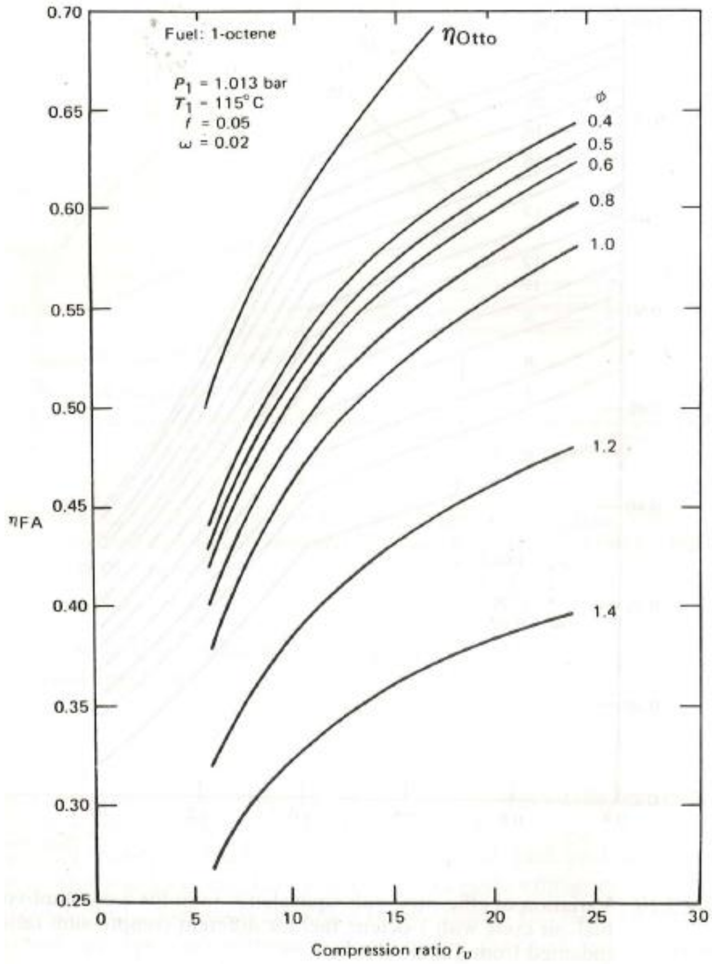

Source: Stone (1992).

Heywood (1988) reports that fuel conversion efficiency and engine power raises approximately 3 percent per each unit of compression ratio increased. In addition, both the maximum fuel conversion efficiency and the compression ratio needed for maximum efficiency depends on cylinder size. Moreover, the exhaust temperature and heat losses decrease as compression ratio and fuel conversion efficiency increase.

FIGURE 52 – EFFECT OF COMPRESSION RATIO ON IMEP AND FUEL CONVERSION EFFICIENCY

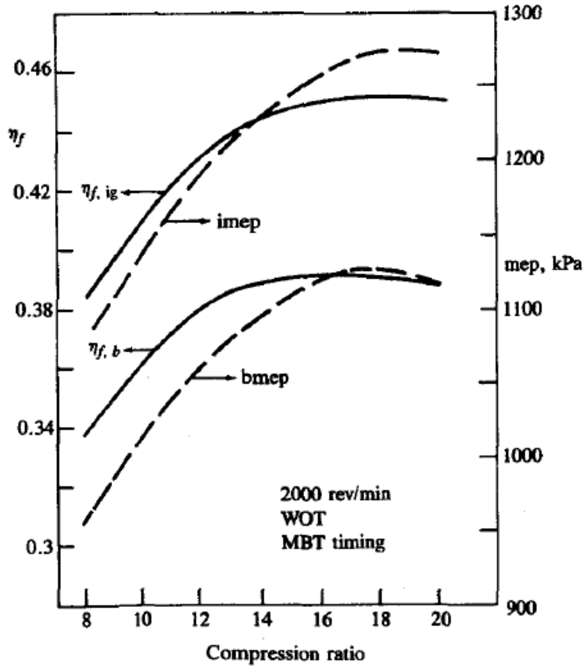

Source: Heywood (1988).

Mean Effective Pressure

The Mean Effective Pressure (MEP) is obtained by dividing the work per cycle by the volume displaced per cycle. The work per cycle can be obtained by solving equation 48 for the work "W", thus the MEP is given by equation 57. In addition, it can be expressed in terms of torque by equation 58:

$$MEP = \frac{2P}{NV_d} \tag{57}$$

$$MEP = \frac{12.56 * T}{V_d} \tag{58}$$

The MEP also can be related to other engine parameters by equation 59:

$$MEP = \eta_f \eta_v Q_{HV} \rho_{a,i} (F/A) \tag{59}$$

Where:

- MEP is the mean effective pressure in kPa;

- P is the power per cylinder in kW;
- N is the crankshaft speed in rev/s;
- V_d is the volume swept in dm^3;
- T is the torque in Nm;
- η_f is the fuel conversion efficiency, see equation 63;
- η_v is the volumetric efficiency, given by equation 54;
- Q_{HV} is the heating value of the fuel;
- $\rho_{a,i}$ is the air density at intake, and;
- F/A is the fuel air/ratio.

In addition, the MEP can be measured in indicated or brake values. The Indicated Mean Effective Pressure (IMEP) considers only the work done by the gas in the piston and measures the indicated work output per unit of swept volume. The IMEP from naturally aspirated engines is lower than for similar turbocharged engines. Moreover, the IMEP is independent of the engine size, the number of cylinders, and the engine speed.

The IMEP can be further divided into gross IMEP and net IMEP. Net IMEP does not considers the pumping losses, or Pumping Mean Effective Pressure (PMEP). Therefore, the gross IMEP is defined by equation 60:

$$gross\ IMEP = net\ IMEP + PMEP \tag{60}$$

On the other hand, the Brake Mean Effective Pressure (BMEP) measures the work output of an engine, as measured by a dynamometer. Is important to say that the BMEP is the measure of output work, and not of pressures. Since the BMEP is independent of the engine size, it can be used to evaluate how effective different engines use their displaced volume.

Finally, the Frictional Mean Effective Pressure (FMEP) accounts for the friction losses of the engine, and is defined in equation 61:

$$FMEP = IMEP - BMEP \tag{61}$$

Figure 53 shows the curve for the gross indicated, brake, and friction power (P_i, P_b, and P_f), the IMEP, the BMEP, and the FMEP for a full-throttle spark-ignition engine. Notice that the P_i curve follows the IMEP curve, this is because at full-throttle the IMEP and power variates along with the volumetric efficiency. On the other hand, FMEP increases almost linearly with the increase in speed, while P_f increases more rapidly. Thus, mechanical efficiency decreases with increasing speed, causing BMEP to reach its peak at a lower speed than IMEP (HEYWOOD, 1988; STONE, 1992).

FIGURE 53 – CHANGE IN GROSS INDICATED, BRAKE, AND FRICTION POWER, IMEP, BMEP, AND FMEP WITH VARYING SPEED AT FULL-THROTTLE

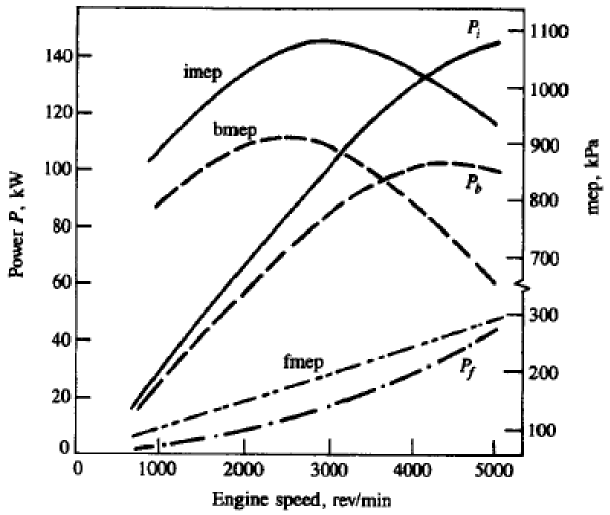

Source: adapted from Heywood (1988).

Specific Fuel Consumption

The Specific Fuel Consumption (SFC) measures how efficiently the engine's fuel is used to produce work, and is given by equation 62. In addition, the SFC is related to the fuel conversion efficiency "η_f" by equation 63:

$$SFC = \frac{\dot{m}_f}{P} \quad (62)$$

$$\eta_f = \frac{W_c}{m_f * Q_{HV}} = \frac{P}{\dot{m}_f * Q_{HV}} = \frac{1}{SFC * Q_{HV}} \quad (63)$$

Where:

- SFC is the specific fuel consumption in mg/J;
- m_f is the mass flow of fuel in g/s;
- P is the power in kW;

- η_f is the fuel conversion efficiency, and;
- Q_{HV} is the heating value of the fuel in MJ/kg.

Notice that not all the energy provided by the fuel is going to be released as thermal energy in the combustion process; this is because the actual combustion process is incomplete. If enough oxygen is present during the combustion, more than about 96% of the energy's fuel can be converted to working fluid (HEYWOOD, 1988).

Lower values of SFC means better fuel economy, while higher values of fuel conversion efficiency are desired. In addition, the Brake Specific Fuel Consumption (BSFC) can be plotted in a contour graph of the engine speed versus the BMEP, like in figure 54. Notice that the upper line of figure 54 corresponds to the open-throttle performance, with the maximum BMEP occurring in the mid-speed range. On the other hand, the points the open-throttle line correspond to the part-load performance, with the minimum BSFC island located at a slightly lower speed and part-load.

In ICE the heat loss through the walls prevails at low speeds, while at high speeds the friction losses are more relevant. Therefore, with increasing speeds the rate consumption grows faster than the effective power and, in consequence, the specific consumption also grows.

FIGURE 54 – EXAMPLE OF A TYPICAL FUEL CONSUMPTION MAP

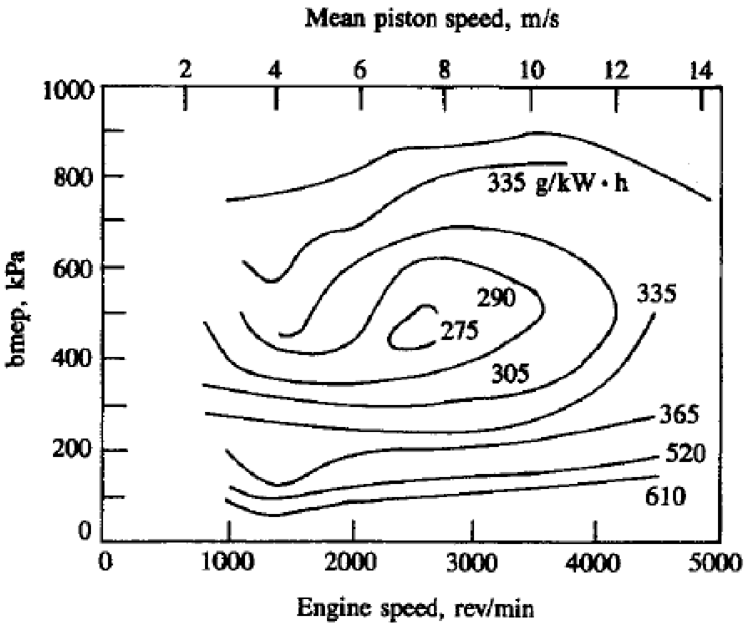

Source: Heywood (1988).

Figure 55 shows how fuel consumption changes with load, at fixed engine speed. Notice that fuel consumption grows with the closing of the throttle, due to the growth in pumping work. Additionally, figure 56 shows the change in SFC with varying speed and load. Observe that the SFC varies more with load than with engine speed.

FIGURE 55 – TYPICAL CURVE OF FUEL CONSUMPTION WITH LOAD VARIATION

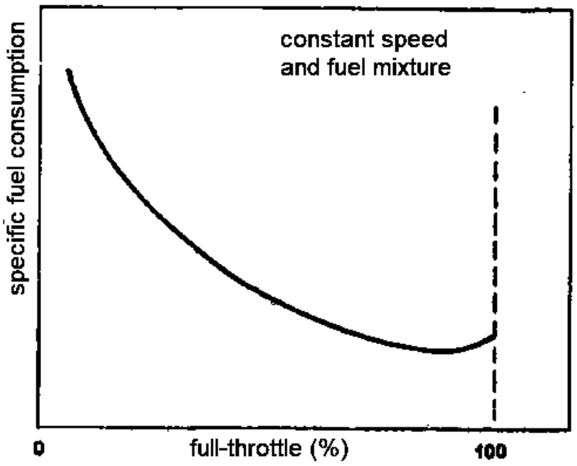

Source: adapted from Giacosa (1979).

FIGURE 56 – VARIATION OF FUEL CONSUMPTION WITH MEP AND SPEED

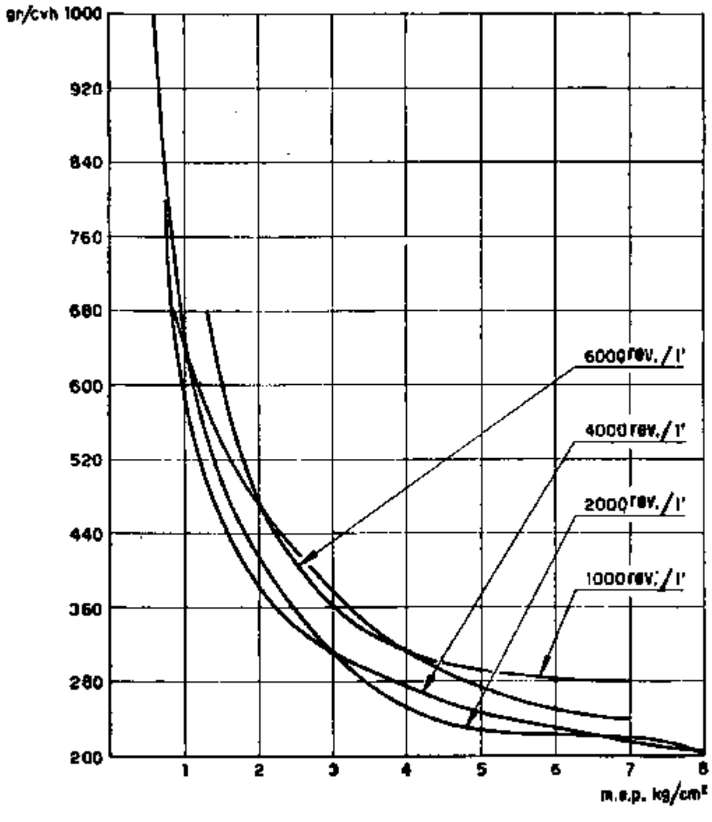

Source: adapted from Giacosa (1979).

Fuel/Air, Air/Fuel, and Equivalence Ratios

The fuel/air and the air/fuel ratios are the relationship between the air mass flow rate "$\dot{m}_a$" and the fuel mass flow rate "$\dot{m}_f$", and are given by equations 64 and 65:

$$Air/fuel\ ratio\ (A/F) = \frac{\dot{m}_a}{\dot{m}_f} \tag{64}$$

$$Fuel/air\ ratio\ (F/A) = \frac{\dot{m}_f}{\dot{m}_a} \tag{65}$$

A conventional gasoline engine operates between air/fuel ratios of 12 to 18. Equation 66 can be used to convert the air/fuel ratio to equivalence ratio when using gasoline:

$$\phi \approx \frac{14.6}{A/F} \tag{66}$$

The exhaust gas temperature varies with the equivalence ratio, obtaining the maximum temperature at the stoichiometric point and decreasing as the mixture is richened or leaned. Nevertheless, the ideal equivalence ratio is the one that gives the minimum BSFC at the required load.

For satisfactory spark ignition and flame propagation, the air/fuel mixture must be close to stoichiometric. Even though, the maximum power is obtained at rich mixtures were the oxygen is consumed as much as possible; this also means higher unburnt fuel and reduced fuel conversion efficiency. On the other hand, the maximum economy is obtained at lean mixtures, were the fuel is burnt as much as possible.

Thus, figure 57 presents the variance in IMEP and fuel conversion efficiency "η_f" for different equivalence ratio. Figure 57a establishes that the IMEP peaks between Φ=1 and Φ=1.1, at slightly rich mixtures. On the other hand, figure 57b presents that the fuel conversion efficiency decrease for mixtures above stoichiometric (Φ>1). Moreover, it shows that the leaner the mixture the greater the fuel conversion efficiency.

FIGURE 57 – VARIATION OF FUEL CONVERSION EFFICIENCY WITH EQUIVALENCE RATIO

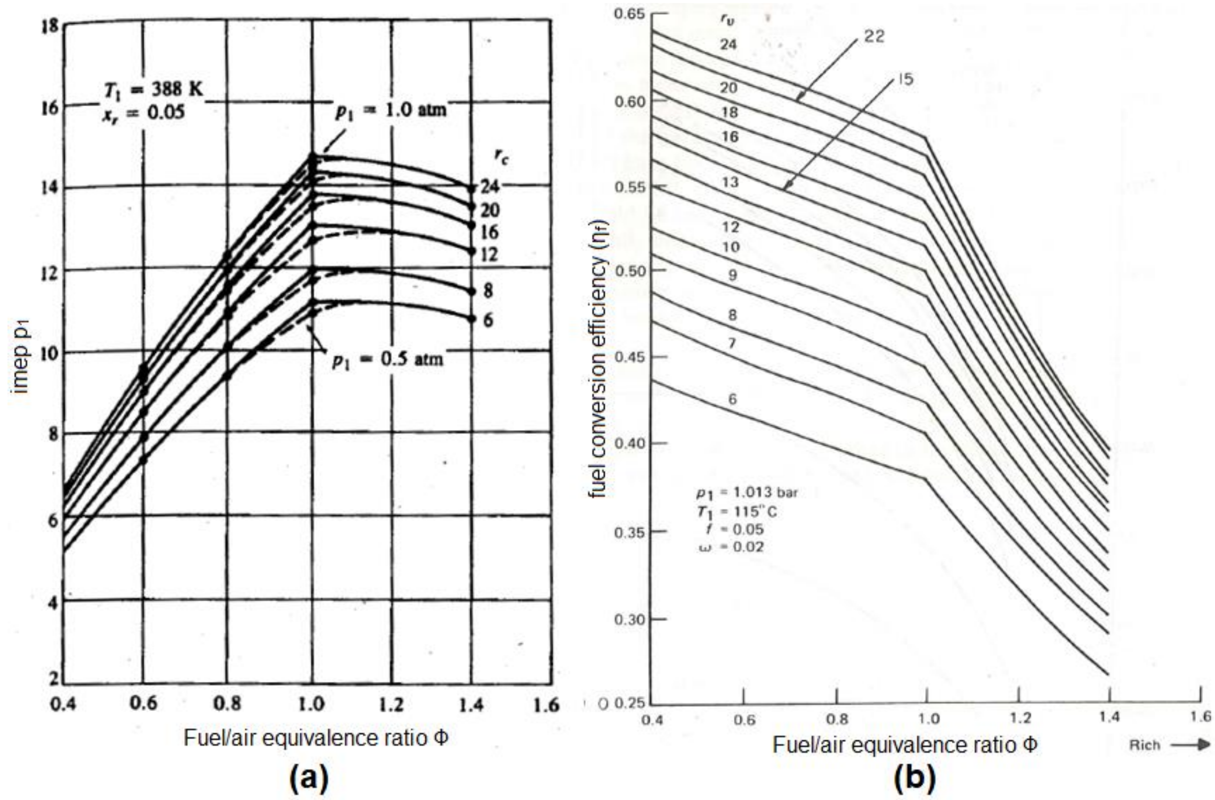

Source: adapted from Stone (1992) and Heywood (1988).

In real engines, as the mixture becomes leaner the combustion becomes incomplete and the fuel conversion efficiency falls again. This is because of the leaner the mixture, the slower the burning process and the greater the cycle-to-cycle pressure fluctuations. Additionally, the fuel consumption of engines operating with lean mixtures depend on the combustion chamber design, including the compression ratio and the quality of the mixture preparation (HEYWOOD, 1988; STONE, 1992).

Spark timing

The variations in spark timing relative to the crank angle position affect the pressure curve. If the ignition is too late, the work done to the piston during the expansion stroke is reduced, since the pressure is also reduced. Furthermore, there is a risk of the combustion being incomplete before the exhaust valve opens, which could overheat the exhaust valves.

If the ignition is too early, too much pressure will rise before the end of the compression stroke reducing the power obtained. Thus, the work done during the compression stroke will be greater than the work done during the expansion stroke. In addition, the pressure and temperature could be high enough to cause knocking. Figure 58a shows the effects on the cylinder pressure with varying spark timing.

The spark timing that gives the maximum engine torque at a fixed flow rate, speed, and mixture composition is called the Maximum Brake Torque (MBT) timing. Figure 58b shows the variation in torque with varying spark timing. The MBT timing depends on engine speed; as speed increases the spark must be advanced to maintain optimum timing, due to an increase in the duration of the combustion process.

Furthermore, the spark timing also depends on the engine load. With the decrease in load and intake pressure, the spark timing must be advanced to maintain optimum engine performance.

Besides the effect in peak cylinder pressures, the spark timing also influences the exhaust temperature. Retarding the timing from MBT increases the temperatures in exhaust gases, hence, reducing the thermal efficiency and the heat lost through the walls. Moreover, changes in spark timing could be used for NO and HC emission control, and to avoid knocking (HEYWOOD, 1988).

FIGURE 58 – EFFECTS OF SPARK TIMING IN TORQUE AND CYLINDER PRESSURE

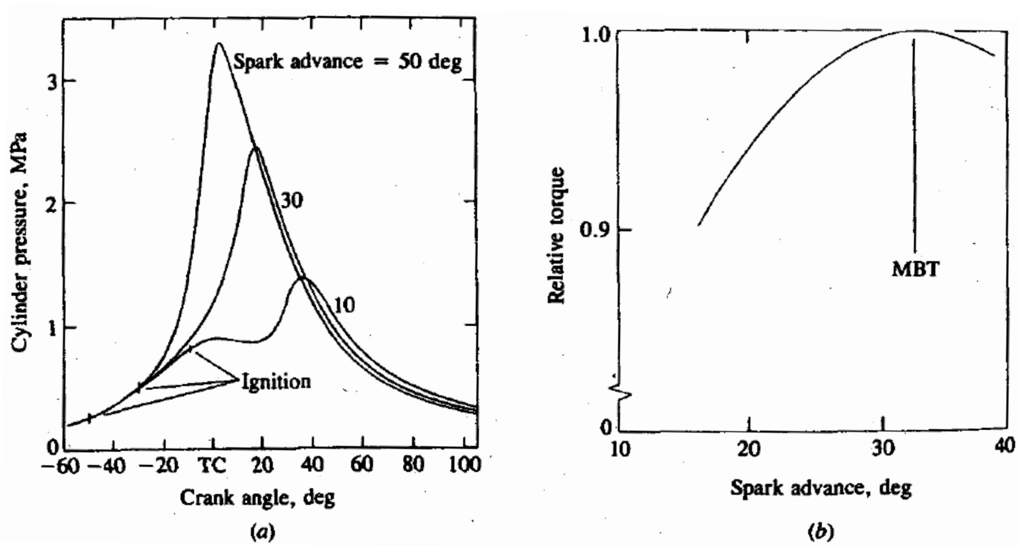

Source: Heywood (1988).

2.4.3 TECHNIQUES FOR IMPROVING PERFORMANCE

Different technologies have been developed for improving the efficiency and performance of ICEs. Between the most used technologies can be listed the Atkinson cycle, turbocharging, Variable Valve Timing (VVT), direct injection, Exhaust Gas Recirculation (EGR), and lean-burn engines. This section covers all these technologies with the exception of the lean-burn engines.

Exhaust gas recirculation

The Exhaust Gas Recirculation (EGR) is when a fraction of the exhaust gases is recycled from the exhaust to the intake system of the engine. The EGR acts as an additional diluent of the unburned gas mixture, reducing the burned gas temperature and, thereby, the NO_x emissions. Thus, the total burned gas fraction is comprised of residual gas fractions from both the previous cycle and the exhaust gas recycled to the intake, as shown in equation 67:

$$x_b = \left(\frac{EGR}{100}\right)(1 - x_r) + x_r = \frac{m_{EGR} + m_r}{m_c} \tag{67}$$

Where:

- x_b is the burned gas fraction;
- x_r is the residual gas fraction;
- EGR is the percentage of exhaust gas recycled;
- m_{EGR} is the mass of exhaust gas recycled;
- m_r is the residual mass, and;
- m_c is the mass of charge trapped in the cylinder.

Figure 59 shows a considerable reduction of NO emissions between 10 to 20% of EGR; however, the hydrocarbon emissions increase for these EGR ratios. Moreover, the higher the EGR the longer the flame development and propagation process, thus, resulting in a decrease in combustion stability.

FIGURE 59 – VARIATION OF NO EMISSIONS WITH THE PERCENTAGE OF EGR

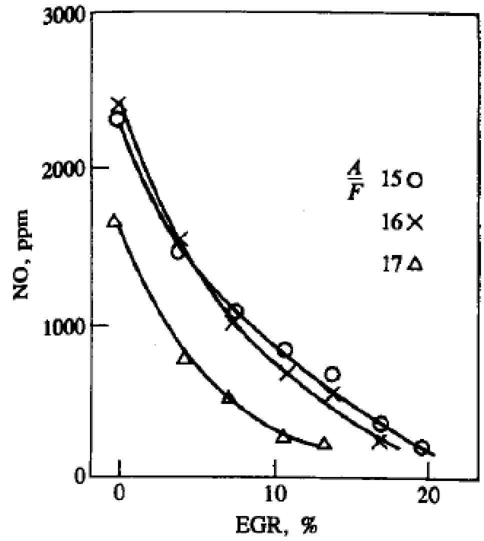

Source: Heywood (1988).

The amount of EGR that an engine tolerates depends on its combustion characteristics, engine speed, engine load, and equivalence ratio. Therefore, faster-burning engines tolerate higher EGR.

FIGURE 60 – EFFECTS IN BSFC AND MBT WITH EGR RATE

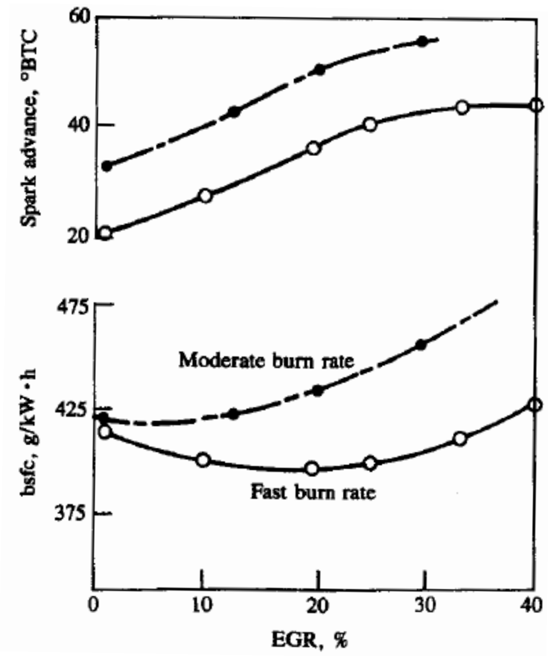

Source: Heywood (1988).

Figure 60 shows that, at constant burn duration, the BSFC and exhaust temperature decreases with increasing EGR. According to Heywood (1988), this improvement in fuel consumption is due to three factors: 1) reduced pumping work, 2) reduced heat loss to the walls, and 3) a reduction in the degree of dissociation.

Atkinson cycle

According to Stone (1992), the Atkinson cycle “is commonly used to refer to any cycle in which the expansion stroke is greater than the compression stroke”. Figure 61 shows an ideal air standard Atkinson cycle represented by line 1-2-3-4, while the standard Otto cycle is represented in line 1-2-3-A. Therefore, the shaded area 1-A-4 correspond to the increased work of the Atkinson cycle, over the Otto cycle.

FIGURE 61 – IDEAL AIR STANDARD ATKINSON CYCLE

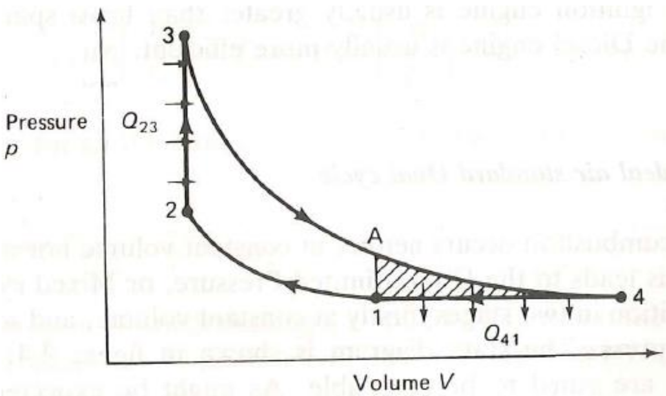

Source: Stone (1992).

Forced induction

Since power, torque, and MEP are proportional to the mass of air introduced per cycle, which is influenced primarily on the inlet air density; then, the performance of an engine can be increased by compressing the inlet air prior to entry to the cylinder. Nevertheless, the propensity to knock increases due to the rise in the end-gas temperature and pressure.

This work only focuses on turbocharging, however, there are three types of forced induction:

1. *Mechanical supercharging*, where the compressor or pump is driven by the power of the engine;
2. *Turbocharging*, where a turbine connected to a compressor is driven by the energy available in the exhaust system of the engine;
3. *Pressure wave supercharging*, where wave action in the intake and exhaust system is used to compress the intake mixture.

If a naturally SI engine is compared to a turbocharged engine of smaller swept volume, but with the same maximum power, then the turbocharged engine have a lower specific weight and volume. In addition, smaller turbocharged engines should have better fuel economy at part load, due to their higher mechanical efficiency.

To control the knock occurrence in turbocharged engines, the next variables must be adjusted: compression ratio, spark retard from MBT, charge air temperature, and fuel/air equivalence ratio.

As mentioned before, the compression of the inlet air results in higher temperatures and pressures of the end-gases. Therefore, lowering the air temperature before entering the cylinder allows for higher compression ratios at a given boost level.

In addition, retarding the spark time allows higher boost pressures; however, as the retard is increased the gains in BMEP obtained from higher boosts decreases. Precise control of ignition timing is critical; therefore, retarded spark timing should only be used to avoid fuel consumption penalty at high boost pressures.

Moreover, to avoid knock, boost must be limited at medium and high engine speeds, by keeping the boost pressure approximately constant. This is achieved by bypassing a fraction of the exhaust around the turbine through a flow control valve, thus, reducing the exhaust flow as speed increases.

Figure 62, shows the temperature-entropy diagram for a turbocharger. Thus, equation 68 and 69 respectively give the work done by the turbine “W_t” and by the compressor “W_c”, for adiabatic processes and semi-perfect gases:

$$W_t = h_3 - h_4 = c_p(T_3 - T_4) \tag{68}$$

$$W_c = h_2 - h_1 = c_p(T_2 - T_1) \tag{69}$$

While equations 70 and 71 presents the isentropic efficiency of the turbine "η_t" and compressor "η_c", respectively:

$$\eta_t = \frac{h_3 - h_4}{h_3 - h_{4s}} = \frac{T_3 - T_4}{T_3 - T_{4s}} \tag{70}$$

$$\eta_c = \frac{h_{2s} - h_1}{h_2 - h_1} = \frac{T_{2s} - T_1}{T_2 - T_1} \tag{71}$$

FIGURE 62 – TEMPERATURE-ENTROPY DIAGRAM FOR A TURBOCHARGER

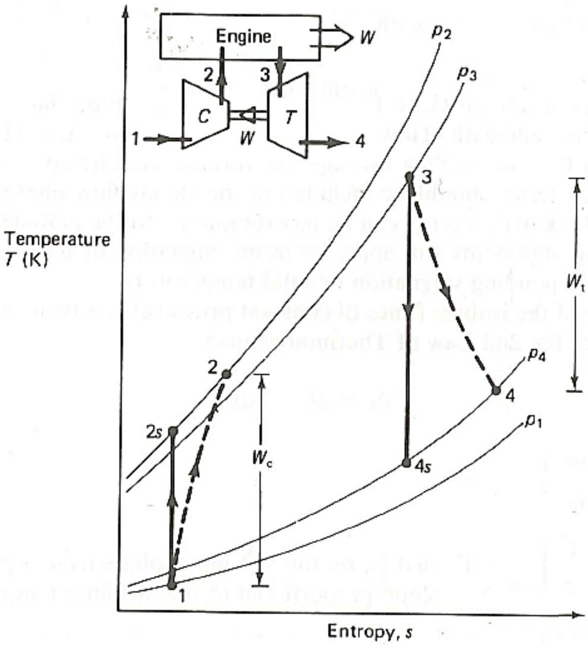

Source: adapted from Stone (1992).

In addition, the mechanical efficiency "η_m" of the turbocharger can be obtained by equation 72:

$$\eta_m = \frac{W_c}{W_t} = \frac{m_{12} c_{p12} (T_2 - T_1)}{m_{34} c_{p34} (T_3 - T_4)} \tag{72}$$

Also, the isentropic temperature ratio can be found from the pressure ratio, as shown in equation 73:

$$\frac{T_{2s}}{T_1} = \left(\frac{p_2}{p_1}\right)^{(\gamma-1)/\gamma} \ and \ \frac{T_3}{T_{4s}} = \left(\frac{p_3}{p_4}\right)^{(\gamma-1)/\gamma} \tag{73}$$

To produce good scavenging in constant-pressure turbochargers, it is preferable that the intake pressure be greater than the exhaust pressure ($p_2/p_3 > 1$).

If equation 73 is solved for T_{2s} and if substituted in equation 71, then the air temperature that enters to the cylinder is given by equation 74:

$$T_2 = T_1\left[1+\frac{(p_2/p_1)^{(\gamma-1)/\gamma}-1}{\eta_c}\right] \tag{74}$$

Equation 74 is obtained by assuming an ideal gas, thus, by applying the Gas Law the density ratio can be found, as shown in equation 75:

$$\frac{\rho_2}{\rho_1} = \frac{p_2}{p_1}\left[1+\frac{(p_2/p_1)^{(\gamma-1)/\gamma}-1}{\eta_c}\right]^{-1} \tag{75}$$

The effect of compressor efficiency on the intake air density is shown in figure 63a. Is important to mention that the temperature rise in the compressor also reduces the density ratio. Additionally, higher intake temperatures increase the thermal load of the engine. Therefore, if the compressor operates in an efficient part of the regime, the temperature rises and the work input needed is minimized.

FIGURE 63 – EFFECT OF COMPRESSOR EFFICIENCY "η_c" AND CHARGE COOLING ON INTAKE AIR DENSITY

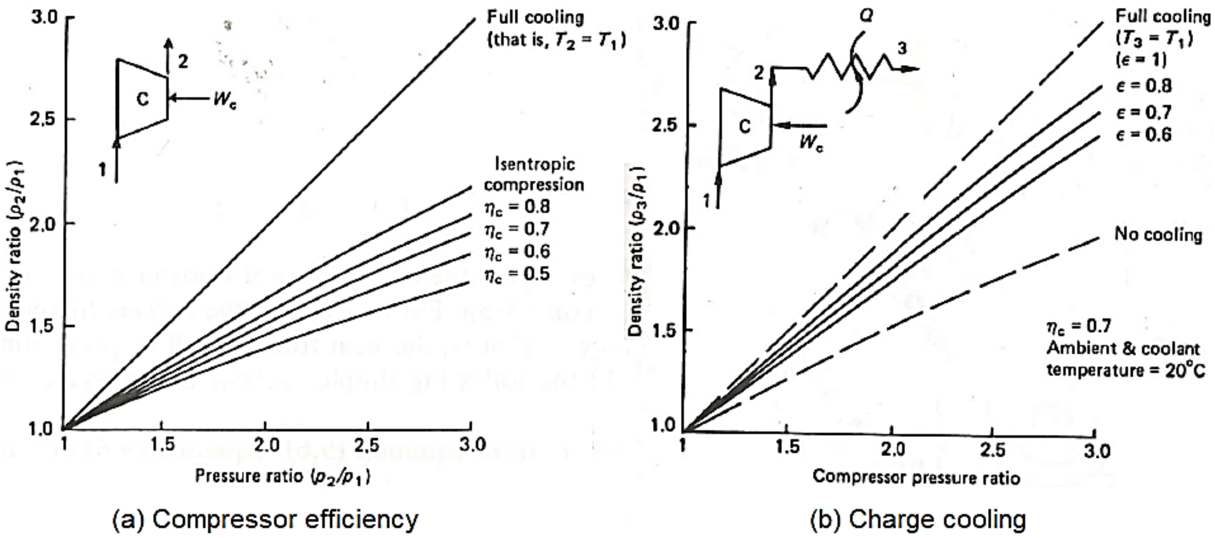

Source: adapted from Stone (1992).

Moreover, the use of inter-cooler allow for better charge cooling, thus, figure 63b shows the effect of charge cooling, by using an intercooler. The effectiveness of the inter-cooler is given by equations 76 and 77:

$$\varepsilon = \frac{actual\ heat\ transfer}{maximum\ possible\ heat\ transfer} = \frac{T_2 - T_3}{T_2 - T_1} \tag{76}$$

$$T_3 = T_2(1 - \varepsilon) + \varepsilon T_1 \tag{77}$$

Thus, by substituting equation 74 into equation 77, the charge temperature out of the inter-cooler is obtained by equation 78, which corresponds to the air temperature at cylinder intake. Furthermore, the new density ratio is given by equation 79:

$$T_3 = T_1 \left[1 + (1 - \varepsilon)\frac{(p_2/p_1)^{(\gamma-1)/\gamma} - 1}{\eta_c}\right] \tag{78}$$

$$\frac{\rho_3}{\rho_1} = \frac{p_2}{p_1}\left[1 + (1 - \varepsilon)\frac{(p_2/p_1)^{(\gamma-1)/\gamma} - 1}{\eta_c}\right]^{-1} \tag{79}$$

On the other hand, figure 64 compares the BSFC map of a turbocharged and a naturally aspirated engine; both were scaled to represent engines of different swept volumes but with the same engine torque. Notice that the turbocharged engine, with smaller displacement and lower compression ratio, shows a reduction in BSFC at low speed and at part load due to better mechanical efficiency.

The benefits of using a turbocharged engine of smaller size but with equal power are estimated in function of engine load. Thus, “At full load the average efficiencies should be comparable; at half load, the turbocharged engine should show a benefit of about 10 percent, the benefit increasing as load is decreased.” (HIERETH AND WITHALM, 1979 apud HEYWOOD, 1988, p. 874)

Finally, the main considerations for matching the engine with the turbocharger, are:

- Ensure that turbocharger operates at an efficient regime;
- Ensure that the compressor operates away from the surge line;
- Ensure good transient response.

FIGURE 64 – COMPARISON OF BSFC BETWEEN A NATURALLY ASPIRATED AND A TURBOCHARGED ENGINE

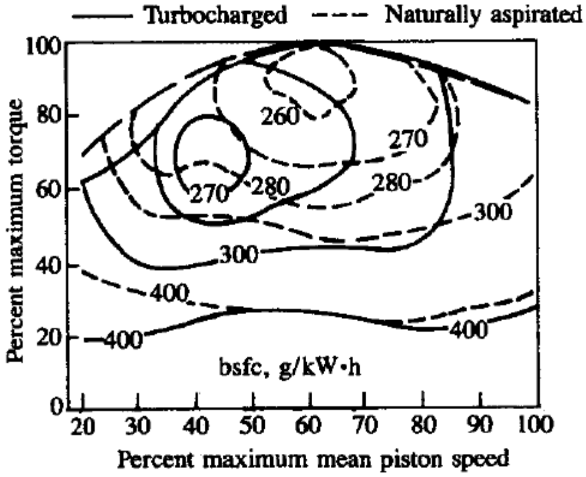

Source: Heywood (1988).

Direct fuel injection

In direct injection engines, the fuel injector is located inside the cylinder near the spark plug. The fuel must be injected at high pressures to reduce the size of fuel droplets and, hence, achieving a more efficient mixing. Additionally, if the fuel is injected adjacent to the spark plug, the fuel mixture is richer near the spark plug allowing for better ignition. Moreover, the direct injection of fuel cools the intake air, reducing knock and, in consequence, allowing the engine to operate at higher compression ratios.

Nevertheless, direct fuel injection has reduced time for preparation of a homogeneous mixture and need high-pressure injectors. In addition, the injectors would have to withstand the high temperatures and pressures during combustion and be resistant to the build-up of combustion deposits. Finally, gasoline direct injection also results in higher NO_x emissions (EHSANI; GAO; EMADI, 2013).

Variable valve timing

As mentioned before, the optimum valve timing must be optimized for each engine, but also for specific operating conditions since the volumetric efficiency fluctuates with the variance in speed. The variance in volumetric efficiency is due to the resistance found by the fluid, which depends on the speed of the fluid and on the dimension and the shape of the pipes. Therefore, using variable valve timing (VVT) allows for better control of the amount of mixture introduced, reducing fuel consumption and emissions (EHSANI; GAO; EMADI, 2013).

The greater the quantity of air introduced, the greater the fuel that can be burned; thus, higher energy and higher indicated power is obtained. In general, longer opening valve times results in higher volumetric efficiency at high speeds, obtaining a higher maximum engine speed and a higher power at high speeds. These gains are similar to those of using bigger valves and pipes. Nevertheless, at low engine speeds the power is reduced due to the lower inertia of the introduced gases.

FIGURE 65 – ENGINE PARAMETERS FOR TWO DIFFERENT VALVE TIMES

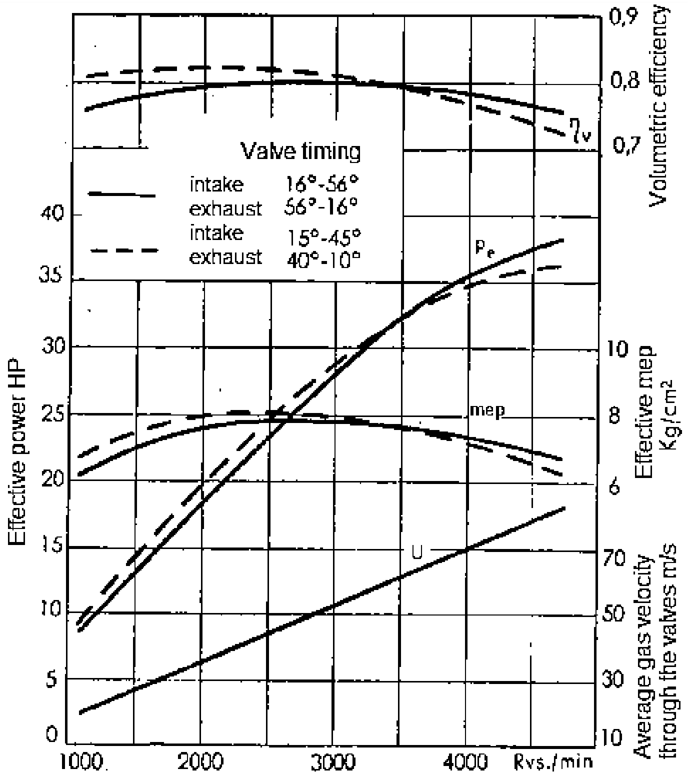

Source: adapted from Giacosa (1979).

On the other hand, shorter opening valve times reduces the maximum engine power and speed; instead, the engine have higher power at lower engine speeds. Figure 65 shows the variation in volumetric efficiency, effective power, pme, and average speed of the gases for long opening valve times (dashed line) and for short opening valve times (solid line).

In summary, long opening times are adopted when maximum power outputs are desired, like in sports vehicles. While short opening times are adopted when long life is desired, as in stationary engines.

2.4.4 Gasoline & Ethanol Fuels

This section presents the main characteristics of gasoline and ethanol fuels, together and their effect in SI engines. First, the characteristics of gasoline are presented, followed by the characteristics of ethanol.

Characteristics of Gasoline

The two most important characteristics of gasoline is their volatility and octane number. If the fuel is not sufficient starting the engine could be difficult, especially at low ambient temperatures. The volatility also influences the fuel consumption at cold start, increasing the volatility at low temperatures improves the fuel economy during and after starting.

On the other hand, the engine's octane requirement varies with compression ratio, with operation conditions, and with geometrical and mechanical considerations. Therefore, the higher the octane number of the fuel, the higher the compression ratio that the engine could use and, in consequence, better fuel economy.

There are two octane scales, the Research Octane Number (RON) and the Motor Octane Number (MON). The test conditions for each scale are presented in table 12. There is not necessarily any correlation between MON and RON since the fuel components of different volatility varies, and the more volatile components are the ones that determine the knocking occurrence (STONE, 1992).

TABLE 12 – SUMMARY OF RON AND MON TEST CONDITIONS

Test conditions	Research octane number	Motor octane number
Engine speed [rpm]	600 ± 6	900 ± 9
Crankcase oil temperature	135 ± 15°F (57 ± 8.5°C)	135 ± 15°F (57 ± 8.5°C)
Coolant temperature range	212 ± 3°F (100 ± 1.5°C)	212 ± 3°F (100 ± 1.5°C)
Coolant temperature constant within	± 1°F (0.5°C)	± 1°F (0.5°C)
Intake air humidity [grains of water per lb. of dry air]	25-50	25-50
Intake air temperature	See ASTM Standard Part 47	100 ± 5°F (38 ± 2.8°C)
Mixture temperature	-	300 ± 2°F (149 ± 1.1°C)
Spark advance [deg. btdc]	13	14-26 Accord to compr. ratio
Fuel/air ratio	Adjusted for max. knock	-

Source: adapted from Stone (1992).

Characteristics of Ethanol

As mentioned before, if the compression ratio is raised and the combustion time is minimized, then the fuel conversion efficiency and power output of the engine increases. Therefore, ethanol can reduce the combustion time due to its faster laminar speed, and tolerate higher compression ratios due to its higher octane number; thus, allowing for better fuel conversion efficiency.

Additionally, ethanol has a greater evaporative cooling effect due to a small amount of fuel that evaporates during the mixture preparation. Stone (1992, p. 38-39) confirms that: “Evaporation can cool the charge by as much as 25 K, and alcohol fuels have much greater cooling effects; this improves the volumetric efficiency.”

Alcohols also can operate with leaner mixtures than gasoline, leading to lower emissions. This lower air/fuel ratio means that ethanol’s chemical energy per kg released during combustion is greater than petrol, at stoichiometric air/fuel mixture.

Finally, ethanol is entirely miscible with gasoline making it a good additive. Goodger (1975 apud Stone, 1992) reports that gasoline mixtures with up to 25% ethanol yields a linear increase in RON. Furthermore, Palmer (1986 apud Stone, 1992) noted that “all oxygenate blends gave better anti-knock performance during low speed acceleration than hydrocarbons fuels of the same octane rating.”

Regarding the fuel consumption of ethanol-gasoline blends, Palmer (1986 apud Stone, 1992) reports that: “Fuel consumption on a volumetric basis is almost constant as the percentage of oxygenate fuel in the blend increases.”

Nevertheless, the ethanol-gasoline miscibility is reduced with the presence of water and low temperatures. In addition, ethanol can absorb moisture that can lead to corrosion and fuel separation problems, however, its main disadvantage is the lower volatility. Beckwith et al. (1986 apud Stone, 1992) report that for cold starting below 10º C, priming agents need to be added to improve the low temperature vapor pressure and the flammability.

2.5 STATE OF THE ART REVIEW

This section summarizes the research found referent to HEVs. It was found that Toyota is planning to launch the first HEV utilizing a flex-fuel engine, reporting that the main challenge of this technology is the cold start of the flex-fuel engine (ENOSHITA, 2018; RIBEIRO, 2018). Additionally, in Oliveira Jr. (2017) it is briefly discussed that the use of ethanol in HEVs could reduce the GHG emissions from well to wheel, as shown in figure 66. Unfortunately, it was not possible to find the source of this figure and no information was obtained about how the CO_2 values were calculated for the ethanol hybrid. Besides that, no scientific research was found regarding HEVs running with ethanol.

Moreover, the only research found that studied the effect of ethanol emissions in HEVs was the one of Suarez-Bertoa and Astorga (2016), however, the effects of fuel consumption were not studied. In this research an HEV and PHEV euro 5 vehicles were tested over the WLTC driving cycle, evaluating the effects of temperatures (23°C and -7°C) and two different commercial fuels (European E5 and E10) in various regulated emissions (CO, CO_2, NO_x, THC, CH_4, and NMHC) and unregulated emissions (NH_3, CH_3CHO, and ethanol). The study suggests that low ambient temperatures lead to higher regulated and unregulated emissions, while no significant difference in emissions was observed between E5 and E10. However, the unregulated emissions of both vehicles were comparable to the emissions of conventional Euro 5 gasoline vehicles.

FIGURE 66 – TOTAL GHG EMISSIONS, FROM WELL TO WHEELS, FOR DIFFERENT VEHICLE PROPULSION SYSTEMS

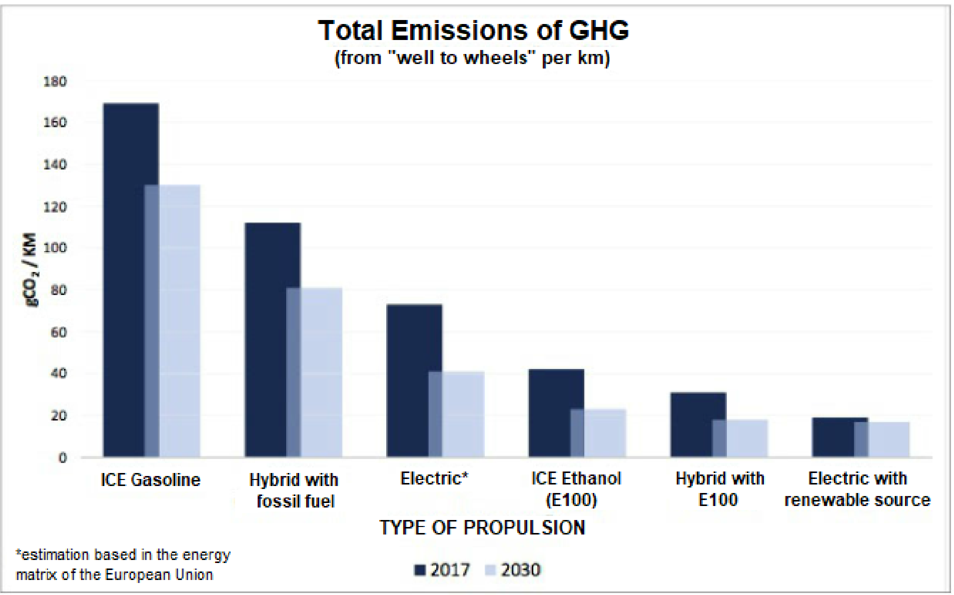

Source: translated from Oliveira Jr. (2017)

On the other hand, there were found many studies about HEV using gasoline or diesel engines. Asfoor, Sharaf and Beyerlein (2014) used the software GT-Suite to simulate a conventional powertrain and three different HEV powertrains (series, parallel, and series-parallel architectures). Then, the fuel economy of all powertrains was compared among four driving cycles (FTP-75, HWFET, US06, and NEDC). The models of all four powertrains used the same 2.0-liter gasoline engine.

The results showed an average fuel consumption, of 73.9 g/km for the conventional vehicle, while the series HEV, parallel HEV, and series-parallel HEV get an average of 64.17 g/km, 49.77 g/km, and 33.65 g/km, respectively. The average gas mileage obtained for each vehicle was shown in figure 8. However, it is important to mention that the series HEV model had a higher fuel consumption for the HWFET and US06 driving cycles than the conventional vehicle.

Similarly, Ogilvie (2011) used the software GT-Suite to simulate a Ford Escape Hybrid SUV. The hybrid Ford Escape was equipped with a 2,261cc gasoline engine, running with Atkinson cycle. The developed model was compared to previous dynamometer results, concluding that the GT-Suite model was valid due to the similarity of both results. No quantitative results were given.

Likewise, Al-Samari (2017) simulated a parallel HEV in the next driving cycles: UDDS, FTP-75, HWFET, and a real-world driving cycle representing the vehicle conditions of Baqubah city, Iraq. The results showed up to 68% fuel economy improvement and about 40% CO_2 emissions decrease for the parallel HEV on the real-world driving cycle. However, the fuel economy and emission reduction in the highway driving cycle were limited to 10% and 11%, respectively.

Tate, Harpster, and Savagian (2008) analyzed the Regional Travel Survey (RTS) data from the Southern California Association of Governments (SCAG). The data was reduced to 621 traces of speed and of ignition key state versus time, with each trace corresponding to one vehicle instrumented. The analysis studied the fuel economy of a conventional vehicle, an HEV, an EREVE, and two different PHEVs powertrains. Compared to the conventional vehicle, the HEV fuel economy improved in 25%, while both PHEVs improved 55% in average, and the EREV improved 85%. Additionally, it compares the RTS data with the UDDS, HWFET, and US06 driving cycles concluding that the RTS data is not represented by those driving cycles. Finally, the EREV produced 70% fewer emissions, consumed 50% less fuel, and was ten times more likely to finish the day in EV mode, when compared to a PHEV.

On the other hand, Duarte et al. (2014) studied the effect of battery SOC on the fuel consumption and emissions of a full hybrid. The authors drove a Toyota Prius for 3 days, conducting test measurements under urban, extra-urban, and highway conditions around Lisbon metropolitan area. The Vehicle Specific Power (VSP) methodology was used to analyze the data from real driving conditions, and implement it into the NEDC driving cycle. The results showed a fuel consumption reduction of 3.2%, while the CO_2 and NO_x emissions were 18.1% and 26.2% higher than the NEDC certification. Additionally, lower SOC levels resulted in higher fuel consumptions and higher CO_2 emissions.

Wang, Guo, and Yang (2015) simulated an all-wheel-drive parallel powertrain architecture for heavy-duty applications in Matlab/Simulink and Advisor. The system consists of a natural gas engine, two PM synchronous machines, and a clutch. The author utilized the Standard Transit Bus City Driving Cycle to evaluate the powertrain, which showed a 47.45% fuel consumption reduction and better regenerative braking even in low adherence conditions.

Similarly, Qin et al. (2015) propose a series-parallel dual mode architecture for application in transit buses, with a diesel engine. Additionally, a prototype with a battery of approximately 37.1 kWh was build to validate the powertrain model. The validation tests followed the Chinese national standard tests for heavy-duty commercial vehicles (GB2784) and for energy consumption of heavy-duty HEV (GB19754). The results showed that the prototype fulfills the performance requirements while showing a 39% more fuel economy than a conventional powertrain system.

Yan, Wang, and Huang (2012) presented a torque-split control strategy, which aims for the lowest fuel consumption of a parallel HEV. To evaluate the proposed Model Predictive Control (MPC) algorithm, the author compared three different methods in a city driving cycle. The first method was the “MPC-TR” that utilized the proposed MPC strategy with an experimentally validated transient diesel-engine model. The second method was the “MPC-SS” that utilized the same MPC design but with a steady-state model of the diesel engine. The third method was the “SOC-PID” that utilized a proportional-integral-derivative (PID) controller to maintain the battery SOC at a desired value.

As seen in figure 67, the SOC-PID method consumed near to 1,060 g of fuel, while the MPC-SS consumed near to 390 g, and the MPC-TR near to 290 g. These results showed that both MPC methods improved the HEV fuel economy; moreover, the incorporation of a transient model can further benefit the fuel economy.

Likewise, Kitayama et al. (2015) developed a torque control strategy to reduce fuel consumption, CO_2 and NO_x emissions for a parallel HEV. To reduce the simulation time, a Sequential Approximate Optimization with a Radial Basis Function network was adopted to find the values of the seven design variables.

FIGURE 67 – FUEL COSTS AND BATTERY SOC IN THE THREE TORQUE-SPLIT CONTROL METHODS

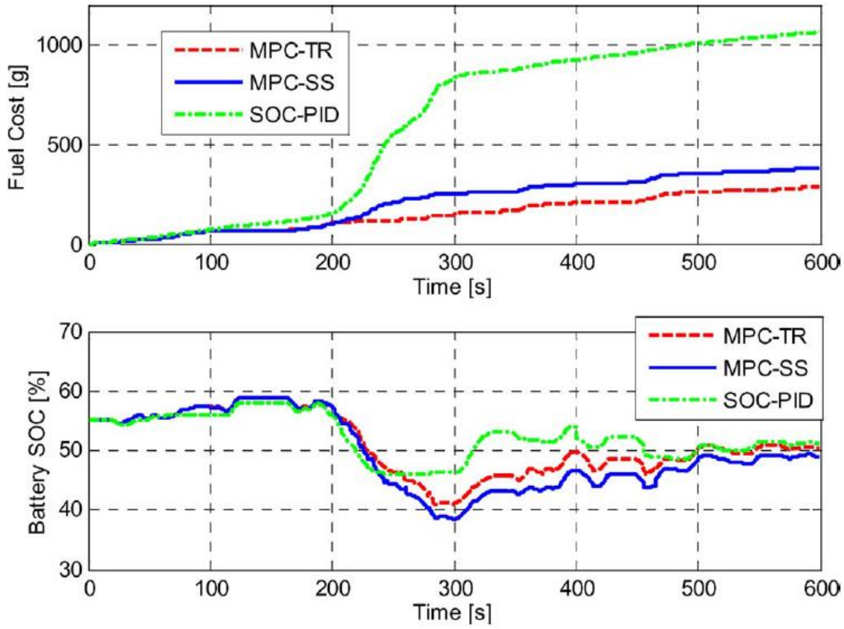

Source: Yan, Wang, and Huang (2012).

This control strategy was validated in the NEDC, Japan Chassis 08 (JC08), and Worldwide Harmonized Light Duty Driving Test Cycle (WLTC). The results showed that the control strategy reduced CO_2 and NO_x emissions in 28.14% and 59.07%, respectively, for the NEDC; in 30.76% and 60.07% for the JC08; and between 18.57% to 19.68% and 32.96% to 34.62% for the WLTC.

Williamson, Lukic, and Emadi (2006) analyzed the drive train efficiency and fuel economy of two conventional vehicles and two parallel HEVs, while in the UDDS and HWFET driving cycles. The HWFET resulted in a 46.7% decrease in fuel consumption for the gasoline HEV and 30.3% for the diesel HEV, when compared to conventional vehicles with the same engine. On the other hand, the UDDS resulted in a 67% decrease in fuel consumption for the gasoline HEV and 60.5% for the diesel HEV, when compared to their respective conventional vehicles. In addition, all vehicles showed higher drivetrain efficiencies in the HWFET, which was attributed to the ICE operating in regions of lower fuel consumption at high speeds. Finally, the authors concluded that the higher the hybridization factor of an HEV, the larger the drive train efficiency.

On the other hand, Howey et al. (2011) analyzed the energy consumption and CO_2 wheel-to-tank emissions of 51 vehicles, which included 20 HEVs, 16 EVs, 1 hydrogen fuel-cell electric vehicle, 13 conventional vehicles with diesel engines and 1 with a gasoline engine. The vehicle size varied from small and regular passenger vehicles, to sports vehicles and light commercial vehicles. In addition, the tests were done in a 57 mile driving route of urban and extra-urban.

Table 13 shows the results of the energy consumption and CO_2 emissions for each vehicle type. The authors concluded that, on average, the EVs used the least amount of energy, followed by the HEVs in second and the conventional vehicles in third. This demonstrated that EVs and HEVs have a greater tank-to-wheel efficiency than conventional vehicles. Additionally, 16 of the 51 vehicles analyzed exceeded the CO_2 tailpipe emissions limit for the NEDC; however, the emissions results are subjected to the CO_2 emissions conversion factor assumed in the work.

TABLE 13 – SUMMARY OF WHEEL-TO-TANK ENERGY CONSUMPTION AND CO_2 EMISSIONS OF 51 VEHICLES ANALYZED BY HOWEY ET AL. (2011).

Vehicle type	Energy consumption (MJ/km)	Fuel consumption (L/100 km)*	CO2 emissions (g/km)
EV	0.5-1 (0.615)	1.6-3.2 (2.0)	76-151 (93)
HEV	0.7-2.1 (1.14)	2.3-6.8 (3.7)	52-157 (85)
ICE	0.9-2.4 (1.68)	2.9-7.8 (5.54)	67-168 (118)
HFEV	1.2	3.9	110

Values in parentheses correspond to the average

*Factor conversion of MJ/km to L/100 km petrol equivalent is 3.25

Source: Howey et al. (2011).

Additionally, Also, Solouk et al. (2017) studied an Extended Range EV equipped with an engine able to work as Homogeneous Charge Compression Ignition (HCCI), Reactivity Controlled Compression Ignition (RCCI), Spark Ignition (SI), and in multi-mode, which can switch among the other three modes. The UDDS cycle showed that the single-modes HCCI and RCCI have respectively 11% and 5.4% fuel consumption improvement, in comparison with the SI single-mode. These improvements increase to 12.1% and 9.1% in the HWFET driving cycle. On the other hand, the multi-mode offer up to 1.4% more fuel consumption improvement, when compared to the best fuel consumptions of the single-modes.

Gao (2005) studied two hybrid power systems for a fuel cell electric vehicle (FCEV), one power system utilized ultracapacitors and the other utilizing lead-acid batteries. It concluded that including ultracapacitors can improve both fuel economy and vehicle acceleration performance; however, a FCEV having ultracapacitors as the only energy storage could have a poor operation during the vehicle start-up.

Finally, Shukla (2005) developed a dynamic mathematical model of the overall powertrain components of an HEV equipped with a turbocharged diesel engine. The work includes models for the tyres, suspension, aerodynamic behavior, a continuous variable transmission, a dynamic Li-ion battery model, a frictional torque function to predict all mechanical and electrical losses, and a d-q frame model for the PM motor, the PM generator, and the DC/AC and AC/DC converters.

Table 14 summarizes the main research mentioned in the state of the art, which shows the fuel economy improvements obtained achieved by employing HEV technology. Additionally, details the vehicle type, engine type, and driving cycle used in each research.

TABLE 14 – STATE OF THE ART SUMMARY

Paper reference	**Vehicle**	**Driving cycle**	**Engine type**	**Fuel economy improvement**
Duarte et al. (2014)	Prius 3rd. Gen	NEDC	Gasoline engine	3.20%
Al-Samari (2017)	Parallel HEV	FTP-75, UDDS, HWFET, and real-world cycle	SI engine	Real world: 68% Highway: 10%
Wang, Guo, and Yang (2015)	Series-parallel 4WD Heavy-Duty	Chines Transit Bus City Driving Cycle	Natural gas engine	47.45%
Qin et al. (2015)	Transit bus with 2 planetary gear sets	Chines Transit Bus City Driving Cycle	Diesel engine	39%
Solouk et al. (2017)	Range extended	UDDS, HWFET, and US06	HCCI, RCCI, SI engines	*HCCI: 11% *RCCI: 5.4%
Yan, Wang, and Huang (2012)	Parallel HEV	First 600 sec. of FTP-75	Diesel engine	MPC-TR: 72% MPC-SS: 63%
Williamson, Lukic, and	Paralel HEV	UDDS, and HWFET	Gasoline and Diesel engines	Gasoline: 46.7-67% Diesel: 30.3-60.5%
Tate, Harpster, and Savagian (2008)	Mid-size HEV, PHEV, and EREV	Regional Travel Survey data	Gasoline engine	HEV: 25% PHEV: 55% EREV: 85%

*Comapared to the SI range extended electric vehicle

Source: elaborated by the author.

3 METHODOLOGY

This work studied the fuel consumption obtained by a series HEV model, developed in the GT-Suite software. Therefore, various simulations were conducted with characteristics of the vehicles Ford Fiesta and Volvo XC60. Additionally, the effect of two different engines was evaluated, a Ford Sigma 1.6L flex-fuel engine and a 1.0L turbocharged prototype engine, both utilizing E100 as fuel. Also, each simulation was conducted for five standard driving cycles (FTP75, HWFET, US06, NEDC, WLTC Class 3) and two real-world driving cycles (Intense Traffic and Low Traffic). The battery conditions were maintained constant through all the simulations.

In addition, the series HEV model was simulated with the characteristics of the vehicles shown in the papers of Al-Samari (2017), Asfoor, Sharaf, and Beyerlein (2014), Solouk et al. (2017), and Williamson, Lukic, and Emadi (2006). For each of these four cases the Sigma and prototype engines were simulated. Finally, a conventional vehicle model was simulated to compare the results obtained. The conventional vehicle used the Sigma engine and the characteristics of the Ford Fiesta.

The simulation model was developed in the GT-Suite software, from Gamma Technologies Incorporated. GT-Suite is a multi-physics platform, which allows the simulation of complex systems by using different pre-made models contained in the software libraries. These pre-made models can interact with each other through an easy to understand visual interface (GAMMA TECHNOLOGIES, [s.d.]).

The series architecture was chosen because of three main reasons. The first reason was that, in a series HEV, all the factors that influence the ICE-Generator ensemble can be summarized into only one: the electrical power demanded by the motor. The second reason was due to its easier control since the ON/OFF control of the engine only depends on the battery SOC. Finally, it is expected a better evaluation of the engine’s downsizing capabilities, since the ICE-Generator ensemble limits the total power of the traction motor (JEAN-MARC ALLENBACH, 2005).

As mentioned before, the model was simulated for the characteristics of two different vehicles. The main reason to choose the characteristics of the Ford Fiesta sedan was that the engine Sigma 1.6L was originally commercialized in this vehicle. On the other hand, the Volvo XC60 Hybrid was mainly chosen to observe the effects of heavier vehicles. Table 15 shows the characteristics of both vehicles.

A proper electric motor was chosen for each vehicle, for this, the power demand was analyzed for both vehicles and for each of the five standard driving cycles. This analyzis is shown in appendixes C and D. The motor selection was made among seven electric machines from two different companies: EMRAX d.o.o. and Yasa Limited. Both companies advertise their products as suitable for automotive applications and provide the motor maps freely on their websites.

In order to evaluate the potential of E100 in HEVs, two different engines were simulated. The Sigma engine is flex-fuel, due to its lower compression ratio, needed for run with gasoline, it cannot exploit to the maximum the properties of the E100 fuel. On the other hand, the prototype engine was designed to run only with E100, and to exploit all the properties of this fuel. Moreover, the prototype engine also was tested with water injection strategy, further improving the performance of the engine. The engine maps of both engines were obtained experimentally by the Mobility Technologies Center (*Centro de Tecnologias da Mobilidade-CTM*) of the Federal University of Minas Gerais (*Universidade Federal de Minas Gerais-UFMG*).

In the case of the Sigma engine, each vehicle was simulated for eight different power modes. On the other hand, the prototype engine was simulated for two different Power Modes, one for each fuel injection strategy. The electric machines used as generators also varied depending on the vehicle and on the engine. In all Power Modes, it was looked to obtain the best efficiency of the ICE-Generator ensemble. Tables 23, 25, and 26 show a summary of each Power Mode used, while appendixes E, F, and G show the variables of all the gear ratios studied.

In order to evaluate vehicle mileage, every simulation was conducted for five standard driving cycles and two real-world driving cycles. The two real driving cycles followed the same path and were obtained by accumulative measures at three different days. Both real-world cycles should represent Brazilian driving style at low and intense traffic conditions. More detailed information about both real driving cycles is given in section 3.6, or it can be consulted directly from Roso (2016).

The battery variables of the model were kept constant for every simulation and corresponded to a data average of four different 2016 Chevrolet Volt batteries. This data was obtained experimentally by the Advance Vehicle team of the Idaho National Laboratory (INL). The battery of the Chevrolet Volt was selected for being manufactured by LG Chem, the same company that manufactures Volvo's batteries (LG CHEM, [s.d.]); moreover, it represents recent battery technology since it was tested in 2017.

Finally, the results of the simulations were compared with the results of gasoline and diesel HEVs obtained from four different papers previously discussed in the state of the art. For this, the vehicle characteristics were changed to better match the ones of the papers. To compare the mileage improvements fo the Ford Fiesta, a conventional vehicle model was simulated with the same maps of the Sigma engine and the characteristics of the Foer Fiesta.

3.1 MODEL DESCRIPTION

GT-Suite is a software developed by Gamma Technologies. This software was used for all the simulations done in this research. GT-Suite have a graphical representation for all objects, resulting in an easy to understand interface. The interaction among the objects is represented by arrows of different colors, with each color representing a different type of connections.

Two documents were studied to understand the software interface and how to employ the model objects. The first one was the GT-Suite "Vehicle Driveline and HEV" tutorial (GAMMA TECHNOLOGIES, 2016). The other one was the research of Ogilvie (2011), in which a model of series-parallel HEV was developed in GT-Suite. This latter document help to understand which objects were better to use in the model.

The model was developed from several objects of four main libraries: the Mechanical, Control, Electromagnetic, and General libraries. The appendix A lists all the objects used in the model, with their respective attribute values. The attributes not listed in appendix A were kept as zero, default "def", or ignore "ign".

The series HEV model is detailed through the next sections. First, the “Main” assembly is presented in section 3.1.1, this assembly contains all the objects of the model, however, it was divided into five subassemblies to ease the organization of this work. These five subassemblies are presented and explained through section 3.1.2 to 3.1.6.

For better understanding, the names of the object templates, as they are in the library, are written between single quotation marks (‘ ’). While the names assigned by the author to the different parts are written between quotation marks (“ ”). Finally, the names of the input or output signals are written in *italics*.

3.1.1 MAIN ASSEMBLY

The “Main” assembly of the Series HEV powertrain is shown in figure 68. This assembly is primarily compound by a ‘Battery’, a ‘BatteryPowerLim’, an ‘EngineState’, two ‘MotorGeneratorMap’, and two ‘GearConn’ objects. Additionally, it also contains five subassemblies, which are: the “Vehicle”, the “Generator_Control”, the “Motor_Control”, the “Brake_Control” and the “ECU” subassemblies.

FIGURE 68 – MAIN ASSEMBLY OF THE SERIES HEV MODEL

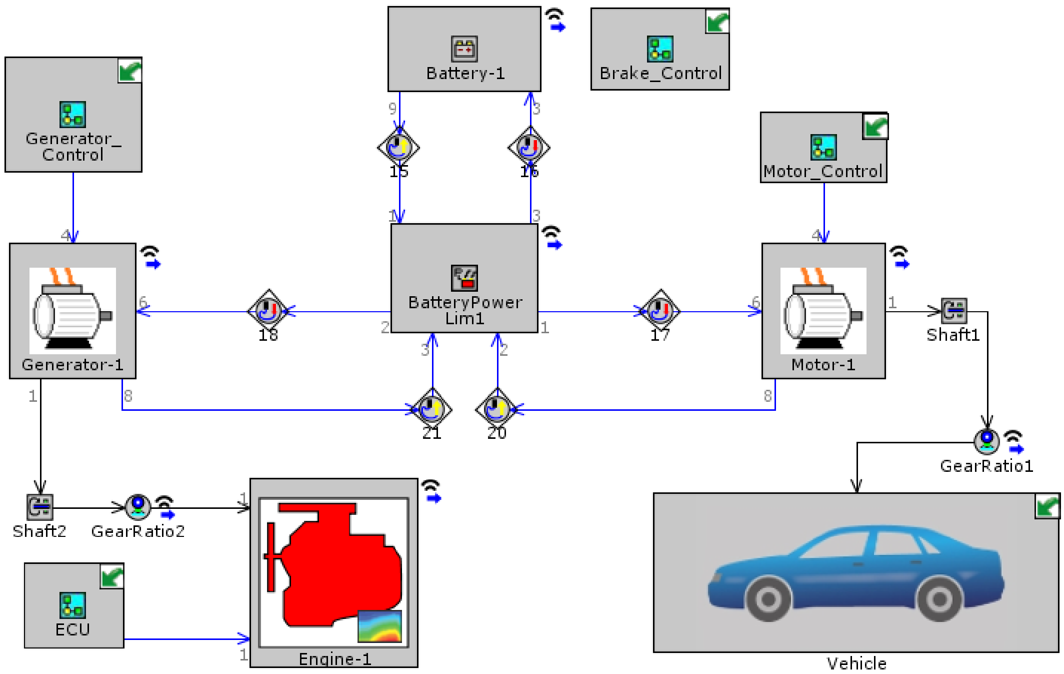

Source: Elaborated by the author

The icon of the subassemblies is denoted by a green arrow in the upper-right edge of the object's icons (see figure 68). Each subassembly will be explained in its own section, thus, this section focuses on the structure of the main assembly and the objects it contains.

To understand the series HEV model first must be noticed that there are no connections between the "Engine-1" part and the "Vehicle" subassembly (see Figure 68). This confirms that the model corresponds to a series architecture. Also notice that the right side contains the "Motor-1" part and the "Vehicle" subassembly, representing the power-flow from the motor to the wheels. While the left side of the figure contains the "Generator-1" and "Engine-1" parts corresponding to the ICE-Generator ensemble. For better understanding, the model explanation starts with the 'Battery' and 'BatteryPowerLim', followed by the right side of figure 68, and finishing with the left side of the same figure.

Initially, the "Battery-1" part communicates the *Maximum Available Power* to the "BatteryPowerLim1", which in turn communicates the *Power Consumed* back to the "Battery-1".

Then, the "BatteryPowerLim1" sends the *Electrical Request Discharge Limit* signal to the "Motor-1", which receives it as the *Maximum Electrical Power (Discharge)* signal. At the same time, the "Motor-1" sends back the *Requested (Unlimited) Electrical Power* signal that enters in the "BatteryPowerLim1" as the *Electrical Power Request*.

The previous signals are connected in the same way for the "Generator-1" part. Therefore, special care must be taken when linking the signals to the 'BatteryPowerLim' object, so that the signals of the electrical machine 1 do not mix with the electrical machine 2.

Additionally, the "Motor-1" part receives the *Requested Brake Power* signal from the "Motor_Control" subassembly. Then, the "Motor-1" shaft link is connected to a 'Shaft' object, which is connected to a 'GearConn' object. The 'GearConn' object, named as "GearRatio1", is connected to the 'Differential' object contained in the "Vehicle" subassembly, see figure 69 in section 3.1.2.

Since the ‘Differential’ object also has a gear ratio, the final drive ratio is given by the multiplication of the “GearRatio1” and “Differential-1” gear ratios. In this work, the value of the “Differential-1” gear ratio had a constant value of 3.2 for all simulations; thus, only “GearRatio1” was varied (see table 15). Section 3.4 explains the selection of the gear ratios.

Now, the left side of figure 68 is explained that consists of the ICE-Generator ensemble. As mentioned before, the connections between the “BatteryPowerLim1” and “Generator-1” are made in the same way as with “Motor-1”. In addition, the *Requested Brake Power* signal of the “Generator-1” is received from the “Generator_Control” subassembly, while the “Generator-1” shaft is linked to a ‘Shaft’ object that connects to a ‘GearConn’ object named as “GearRatio2”.

The “Engine-1” part is an ‘EngineState’ object and receives the *Accelerator Position (Dynamic)* signal from the “ECU” subassembly. Moreover, the “Engine-1” flywheel connects to the “Generator-1” shaft, through the “GearRatio2” part. This gear ratio allows the generator and engine to operate at their points of maximum efficiency.

Special care must be taken when connecting both ‘GearConn’ objects. If the arrows are connected in the opposite direction, then the gear ratio values will represent the inverse values of the ones used in this work.

Finally, observe that the “Brake_Control” subassembly does not have any direct connection (see figure 68). This is because the *Brake Pedal Position* signal is wirelessly sent to the brakes in the “Vehicle” subassembly. This is mainly done to facilitate the reading of the diagram. The parts that send wireless signals are designated with an antenna over a blue arrow symbol, located at the right side of the object’s icon.

The equations that govern the ‘Battery’, ‘MotorGeneratorMap’, and ‘EngineState’ objects are presented in annexes A, B, and C, respectively. In addition, details of the OCV and resistance maps used for the “Battery-1” part is given in section 3.2, together with the calculations for the attributes of the “BatteryPowerLim1” part. On the other hand, the maps of the “Engine-1”, “Motor-1”, and “Generator-1” parts change according to the simulation. Section 3.3 to 3.5 gives more information about this, together with the gear ratios used.

3.1.2 VEHICLE SUBASSEMBLY

The “Vehicle” subassembly models the power flow through the powertrain, from the electric motor to the tires. It also models the interaction between tires and road, and between the vehicle body and the environment. Figure 69 shows the components of this subassembly, which are a ‘VehicleBody’, ‘VehicleAmbient’, ‘Road’, ‘Differential’, and ‘Shaft’ objects. In addition, it has four ‘Axle’ objects, four ‘TireConnRigid’ objects, and four ‘Brake’ objects.

FIGURE 69 – VEHICLE SUBASSEMBLY OF THE SERIES HEV MODEL

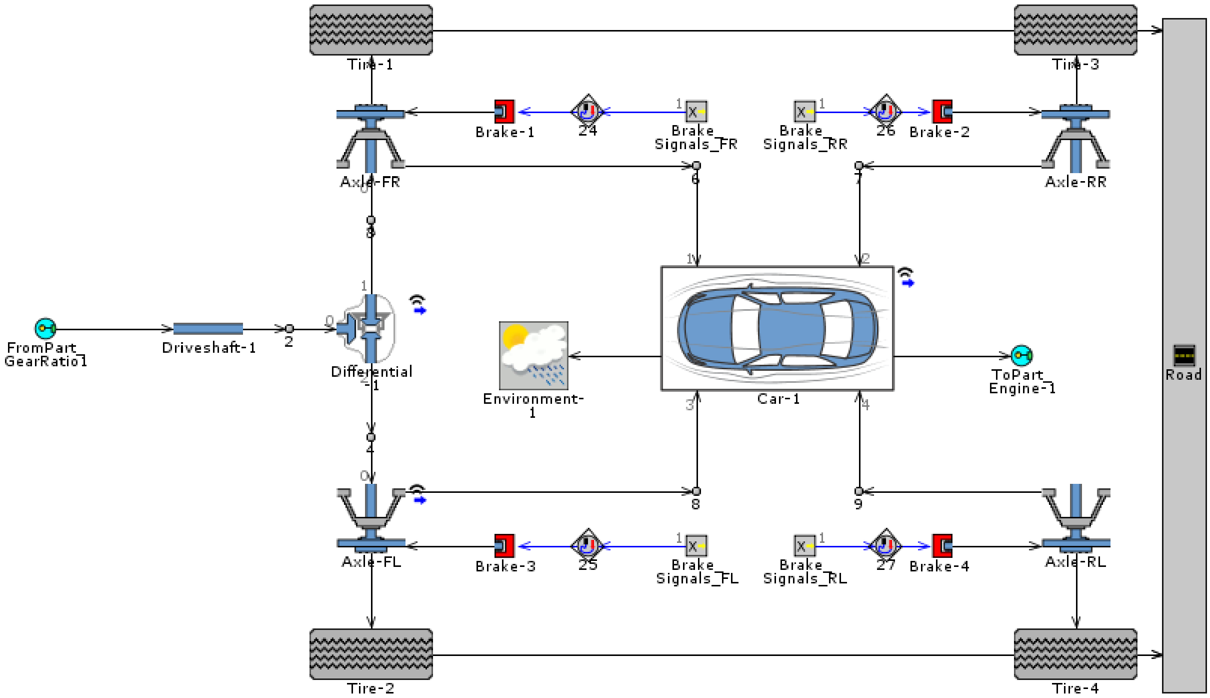

Source: Elaborated by the author.

The power-flow through the subassembly starts when the “Driveshaft-1” part receives the power from “Motor-1”. Then, the power is spread to both “Axle-FR” and “Axle-FL”, which in turn transmit it to “Tire-1” and “Tire-2” respectively. Therefore, the “Tire-1” and “Tire-2” parts represent the powering wheels, while the “Tire-3” and “Tire-4” parts represent the follower wheels.

The four ‘Axle’ objects have the same attributes among them, this is also true for the ‘Brake’ and ‘TireConnRigid’ objects (see appendix A). Additionally, all four ‘Brake’ objects receive the Brake Pedal Position signal from the “BrakeController1” part, located in the “Brake_Control” subassembly. Also, notice that the four ‘TireConnRigid’ objects are connected to the ‘Road’ object.

Finally, the ‘VehicleBody’ object, named as “Car-1”, contains the attributes needed to calculate the motion of the vehicle. As mentioned before, two different vehicles were simulated. The characteristics of the first vehicle are similar to a Ford Fiesta sedan, while the characteristics of the second are similar to a Volvo XC60 Hybrid. The attribute’s values of both vehicles are shown in table 15.

TABLE 15 – CHARACTERISTICS OF THE VEHICLES SIMULATED

Vehicle Characteristic	Ford Fiesta	Volvo XC60
Vehicle weight	1226 kg	2103 kg
Vehicle top speed	180 km/h	220 km/h
Drag coefficient	0.32	0.32
Frontal area	2.16 m^2	2.61 m^2
Wheelbase	2489 mm	2865.12 mm
Tire resist. coef.	0.01	0.01
Tire radii	300.5 mm	372 mm
Electric Motor	Yasa P400	Yasa P400
GRtotal	5.024	5.088
GR1	1.57	1.59
GRdiff	3.2	3.2

Source: adapted from Folha de Londrina [S.D.], and Volvo Group (2018a, 2018b).

3.1.3 ECU SUBASSEMBLY

Figure 70 shows the “ECU” subassembly, which is explained from left to right. The main function of the “ECU” subassembly is to control the engine’s operating point and when it should be turned on or off. The engine’s operating point is controlled by defining the generator’s load that is exerted in the engine.

First, the “IfThenElse” object named as “SOC_Control1”, defines the *Charging State* signal that corresponds to the on or off state fo the engine. To accomplish this, the *State of Charge* from “Battery-1” and the *Old Charging State* are needed. The old state is obtained by sending the *Charging State* signal to a ‘TimeDelay’, which is returned to the “SOC_Control1” as the *Old Charging State*.

The “SOC_Control1” output signal depends only in the *State of Charge* signal. The engine turns on if the SOC is lower than 0.7 and it runs off if the SOC is greater than 0.8. To better understand how this object was programmed see figure A1 in appendix A.

Then another ‘IfThenElse’ object named as “ICE_state1”, gives the *Desired Engine Speed*, *Engine Power Demand*, and *Engine ON/OFF* signals, according to the *Charging State* received from “SOC_Control1”. Thus, the *Desired Engine Speed* and *Engine Power Demand* values varies accordingly to tables 23, 25, and 26 found in section 3.5.

FIGURE 70 – ECU SUBASSEMBLY OF THE SERIES HEV MODEL

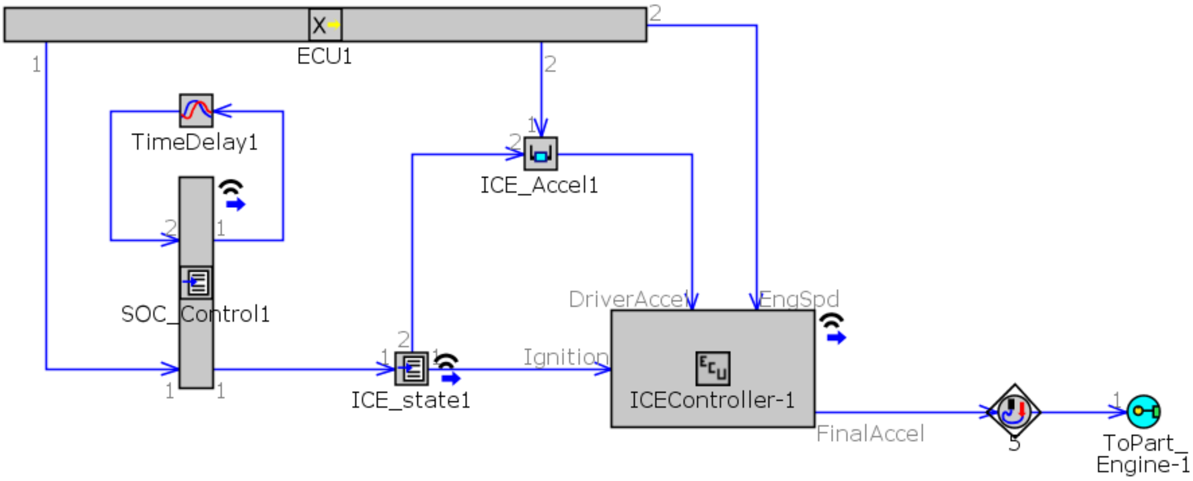

Source: Elaborated by the author.

Next, a ‘PIDController’ object, named as “ICE_Accel1”, is used to define the *Driver Accelerator Position* signal, which is then sent to the “ICEControlle-1”. The ‘PIDController’ object needs two inputs, the *Target for the Input Signal* and the *Input.* Thus, the *Desired Engine Speed* from “ICE_state1” and the instantaneous *Engine Speed* from “Engine-1” were introduced as *Target for the Input Signal* and *Input*, respectively.

Finally, the ‘ICEController’ requires three input signals: the *Engine Ignition State*, the *Driver Accelerator Position*, and the instantaneous *Engine Speed*, which are respectively received from the “ICE_state1”, “ICE_Accel1”, and “Engine-1” parts. Then, the ‘ICEController’ outputs two signals: the *Engine Accelerator Position* that is sent directly to “Engine-1” and the *Engine StarterState* that is sent wirelessly to the “Generator_Control” subassembly.

Besides the *Engine Starter State*, other three signals are sent wirelessly to the “Generator_Control” subassembly. These signals are the *Desired Engine Speed* and *Engine Power Demand* from the “ICE_state1” and the *Charging State* from the “SOC_Control1”.

3.1.4 GENERATOR_CONTROL SUBASSEMBLY

The “Generator_Control” subassembly allows to control the engine’s load, also it defines the torque needed to start the engine. Therefore, the only output of this subassembly corresponds to the *Requested Brake Power* of “Generator-1”. Figure 71 shows the components of this subassembly, which are: an ‘EventManager’, an ‘IfThenElse’, a ‘Lookup1D’, a ‘MathEquation’, and a ‘Gain’ objects.

This subassembly has seven inputs, which are the instantaneous *Engine Speed* and *Engine On/Off State* from the “Engine-1” part; the *Speed* signal from the “Generator-1” part, and the *Engine Starter State*, the *Desired Engine Speed*, the *Charging State*, and the *Engine Power Demand* from the “ECU” subassembly.

FIGURE 71 – GENERATOR_CONTROL SUBASSEMBLY OF THE SERIES HEV MODEL

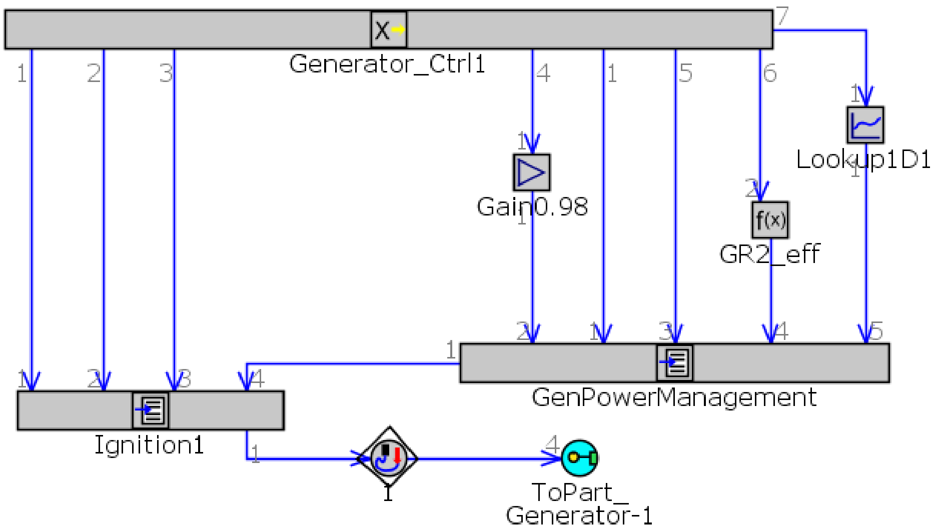

Source: Elaborated by the author.

For better understanding, figure 71 is explained from right to left, starting with the ‘Lookup1D1’ object. This object uses a lookup table in which the *Speed* of the “Generator-1” is introduced and the maximum *Continuous Power* of the generator is returned. Then, the *Continuous Power* signal is sent to the “GenPowerManagement”. The continuous power is different for each the electric machine and it varies with the operation speed. Annexes G to J show the continuous power of the electric machines.

Besides the *Continuous Power*, the “GenPowerManagement” needs the instantaneous *Engine Speed* from “Engine-1”, the *Charging State* from “SOC_Control1”, the *Desired Engine Speed* and *Engine Power Demand* from “ICE_state1”. Nevertheless, the *Engine Power Demand* signal is multiplied by the “GearRatio2” efficiency before entering into the “GenPowerManagement”. This is done the “GR2_eff” part in order to account for the mechanical losses through the gear ratio.

Similarly, the “Gain.098” multiplies the *Desired Engine Speed* by 0.98, before entering into the “GenPowerManagement”. This speed is compared to the instantaneous *Engine Speed*, if the *Engine Speed* is lower than 98% of the *Desired Engine Speed* then no load is applied to the engine. This is done to prevent the engine from receiving a high load before reaching the *Desired Engine Speed*, thus, preventing the engine from being locked in an undesirable speed. Additionally, no load is applied if the engine is off (*Charging State*=0).

Exceeding the continuous power for long periods of time might damage the generator, thus, this was used as the maximum power limit of the generator. To avoid crossing the power limit, the “GenPowerManagement” checks that the *Engine Power Demand* stays lower than the *Continuous Power*. If not, the output value corresponds to the *Continuous Power* given by the ‘Lookup1D’. For all other conditions, the output corresponds to the *Engine Power Demand*. Table 16 shows the *Engine Load* output signal according to each condition, while figure A5 of annex A presents the configuration of the “GenPowerManagement” part.

Finally, the “Ignition1” part controls when the engine must be turned on. Therefore, the *Requested Brake Power* from “Ignition1” is sent directly to the “Generator-1”. While the engine is off, the generator’s *Requested Brake Power* value is zero. As soon as the *Engine Starter State* gives the signal, the generator delivers 10 kW to start the engine. After the *Engine Speed* exceeds 1000 rpm, the generator torque request becomes the negative value of the *Engine Load* that came from the “GenPowerManagement”.

If in any moment the *Engine Speed* falls from 900 rpm and, at the same time, receives the signal to turn the engine off, then the generator’s *Requested Brake Power* value goes back to zero. The *Requested Brake Power* stays at zero until the signal to start the engine is given and the cycle repeats again. A detailed description of the “Ignition1” part is shown in figure A6 in appendix A.

TABLE 16 – CONDITIONS OF THE “GENPOWERMANAGEMENT” PART AND ITS RESPECTIVE OUTPUT

Action	**Condition**	***Engine Load* (Output 1)**
If	*Engine Speed* <(0.98**Desired Engine Speed)*	0
Elseif	*Charging State* =0	0
Elseif	*Charging State* ≠0 AND *Engine Power Demand*<*Continuous Power*	*Continuous Power*
Else	-	*Engine Power Demand*

Source: Elaborated by the author.

3.1.5 BRAKE_CONTROL SUBASSEMBLY

The main function of the “Brake_Control” subassembly is to define the *Mechanical Braking Power* and the *Regenerative Braking Power* signals, according to one of four braking operation modes. The main objects of the subassembly are two ‘IfThenElse’, a ‘BrakeController’, an AND ‘LogicOperator’, an OR ‘LogicOperator’, and several ‘Switch’ objects.

This subassembly needs nine signal inputs, which are: the *State of Charge* from “Battery-1”, the *Vehicle Acceleration* from “Car-1”, the *Electrical Request Charge Limit* from “BatteryPowLim1”, and *Speed* from any ‘Axle’ object; as well as the *Power Demand* and *Torque Demand*, both from the “ControllerHEVehicle1”, and the *Brake Power*, *Speed*, and *Requested (Unlimited) Electrical Power* from “Motor-1”. Figure 72 shows the “Brake_Control” subassembly which is explained from the top to the bottom.

FIGURE 72 – BRAKE_CONTROL SUBASSEMBLY OF THE SERIES HEV MODEL

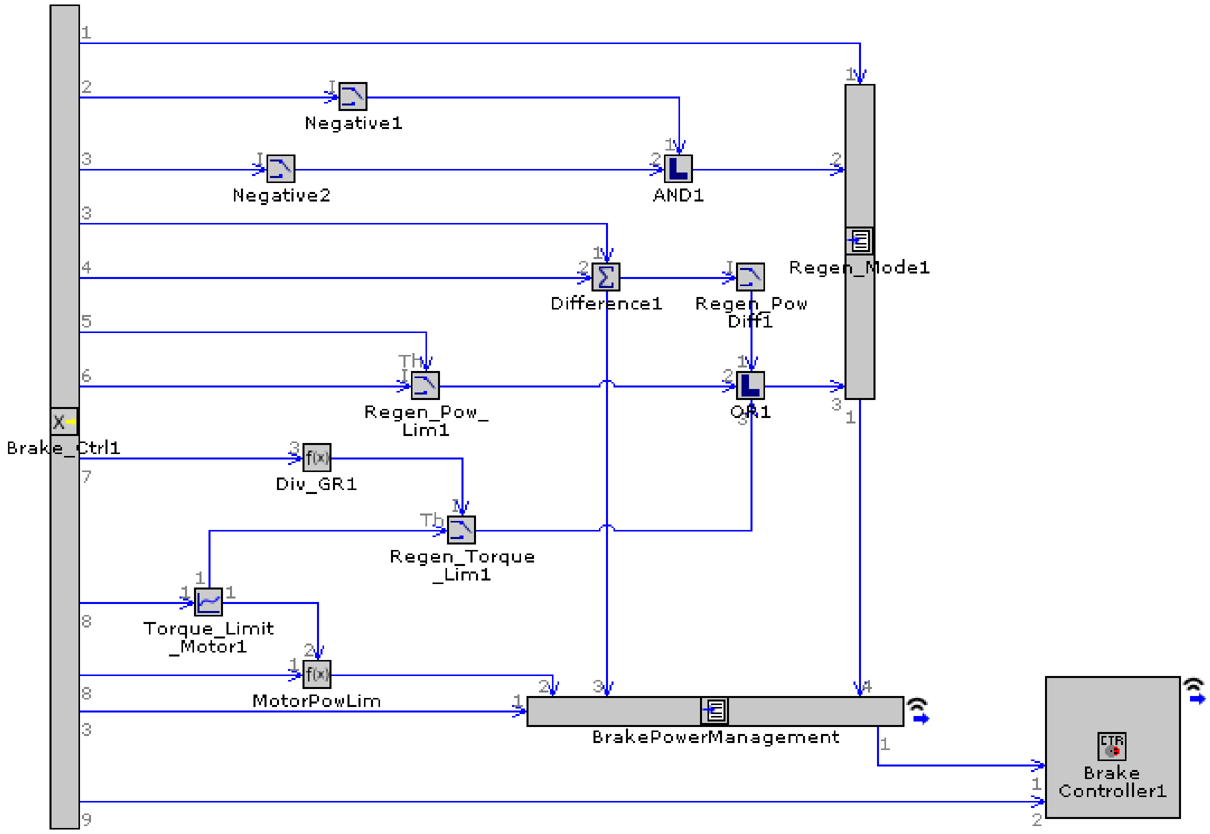

Source: Elaborated by the author

The first two 'Switch' objects, "Negative1" and "Negative2", analyze if the *Vehicle Acceleration* and the vehicle *Power Demand* are negative. Then, both switch outputs are sent to the "AND1" part, which in turn outputs a true value if both signals are negative and a false value if any of the two is positive.

The 'Sum' object, named as "Difference1", subtracts the vehicle *Power Demand* by the motor *Brake Power*. The difference is sent to the "BrakePowerManagement" and to the 'Regen_PowDiff1'. If the *Power Demand* is higher than the power regenerated by the motor, while braking, then the "Regen_PowDiff1" output is true.

Next, the "Regen_Pow_Lim1" compares the *Requested (Unlimited) Electrical Power* with the *Electrical Request Charge Limit*. If the *Electrical Request Charge Limit* is higher than the *Requested (Unlimited) Electrical Power* then the output signal is true, if not the output signal is false.

On the other hand, the switch “Regen_Torque_Lim1” compares the vehicle *Torque Demand* with the motor’s *Minimum Torque Limit*. However, the vehicle *Torque Demand* is previously divided by the final drive ratio of the vehicle; thus, the “Div_GR1” part follows equation 80:

$$Div\_GR1 = Torque\ Demand/(GR_1 * GR_{diff}) \tag{80}$$

Additionally, the ‘Lookup1D’ object, named as “Torque_Limit_Motor1”, gives the *Minimum Torque Limit* according to the instantaneous motor speed. This lookup table corresponds to the negative value of the peak torque map of the motor, which is defined in section 3.4.

Then, the outputs of “Regen_Pow_Diff1”, “Regen_PowLim1” and “Regen_TorqueLim1” are feed to “OR1”, which in turn sends a true value if any of the inputs are true and a false value if all the inputs are false.

The “Regen_Mode1” part, analyze the outputs of “AND1” and “OR1”, plus the battery *State of Charge*. With these three input signals, the “Regen_Mode1” selects one of four braking modes: No Braking Event, Regenerative+Mechanical Braking, Only Mechanical Braking, and Only Regenerative Braking.

If the output of “AND1” is false, then both the *Vehicle Acceleration* and the vehicle *Power Demand* are positive; thus, the No Braking Event mode is selected. For all the other three modes the output of “AND1” must be true. In addition, if the battery *State of Charge* is higher than the maximum usable SOC, the Only Mechanical Braking mode is selected. If the output of “OR1” is false, the Only Regenerative Braking mode is selected. In the other hand, if the output of “OR1” is true, the Mechanical+Regenerative Braking mode is selected.

Next is the “MotorPowLim”, which calculates the motor’s mechanical *Power Limit* by using the motor *Speed* signal and the “Torque_Limit_Motor1” lookup table previously mentioned. Thus, the equation to find the motor’s *Power Limit* is given by equation 81:

$$P_{lim} = \left(\frac{\omega * \tau_{lim} * \pi}{30}\right) \tag{81}$$

Where:

- P_{lim} is the mechanical power limit of the motor, in Watts;
- ω is the actual speed of the motor, in rpm; and,
- τ_{lim} is the torque limit of the motor, in Nm.

Then, the “BrakePowerManagement” defines the *Mechanical Braking Power* and the *Regenerative Braking Power*, for each braking mode. Table 17 shows the conditions and braking power distribution for each braking mode. In which “OR1” and “AND1” correspond to the outputs of the parts with the same names, where a false value corresponds to 0 and a true value corresponds to 1.

Finally, a ‘BrakeController’ object is used to calculate the *Brake Pedal Position*, needs the axle *Speed* and the *Mechanical Braking Power*. Afterward, the *Brake Pedal Position* is sent wirelessly to each ‘Brake’ object found in the “Vehicle” subassembly. While the *Regenerative Braking Power* is sent wirelessly, from the “BrakePowerManagement” to the “Motor_Control” subassembly.

TABLE 17 – CONDITIONS AND BRAKING POWER DISTRIBUTION FOR THE FOUR BRAKING MODES

Braking Mode	Conditions	Mechanical Braking Power	Regenerative Braking Power
No braking event	AND1 output=0	0	0
Only mechanical braking	AND1 output=1 SOC>=MAX	Power Demand	0
Only regenerative braking	AND1 output=1 SOC<MAX OR1 output=0	0	Power Demand
Mechanical + Regenerative braking	AND1 output=1 SOC<MAX OR1 output=1	Power Demand – Motor Brake Power	Power Limit

Source: Elaborated by the author

3.1.6 MOTOR_CONTROL SUBASSEMBLY

The “Motor_Control” subassembly calculates the vehicle *Requested Brake Power* of “Motor-1”. Figure 73, shows the objects that compose this subassembly, which are a ‘SignalGenerator’, a ‘ControllerHEVehicle’, and a ‘Switch’.

First, the ‘SignalGenerator’, named as “Driving_Cycle1”, gives the instant *Target Speed* of the driving cycle simulated. Therefore, the “constant_or_reference” attribute was selected for the ‘Signal Generator’, while the reference object attribute corresponds to the respective driving cycle. All five standard driving cycles were found in the ‘ProfileTransient’ object’s libraries, while both real-world driving cycles were introduced manually.

FIGURE 73 –MOTOR_CONTROL SUBASSEMBLY OF THE SERIES HEV MODEL

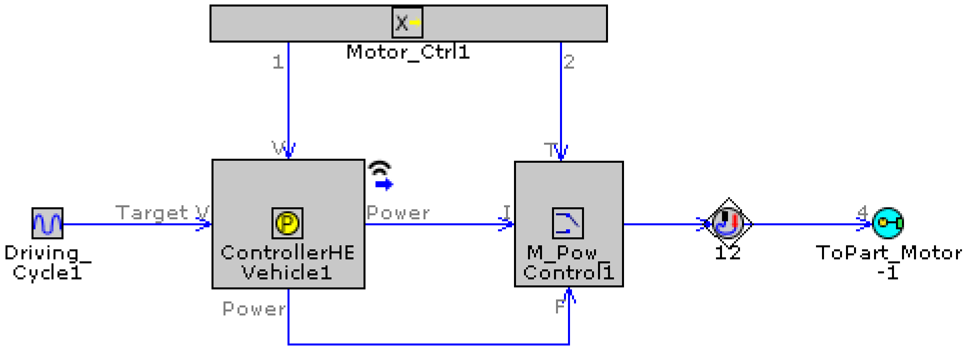

Source: Elaborated by the author

Next, the ‘ControllerHEVehicle’ calculates the necessary tractive power required for the *Target Speed*. Thus, the output of “Driving_Cycle1” is introduced as the *Target Vehicle Speed*, while the *Vehicle Speed* signal from “Car-1” is introduced as the *Actual Vehicle Speed*. The attributes of the “ControllerHEVehicles1” were defined according to table 15, while the model for the ‘ControllerHEVehicle’ object is detailed in annex D.

Finally, the “M_Pow_Control1” is a ‘Switch’ that evaluates if the vehicle *Power Demand* is positive. As long as it stays positive, the *Requested Brake Power* send to “Motor-1” is equal to the output of “ControllerHEVehicle1”. On the other hand, if the *Power Demand* is negative, the *Requested Brake Power* corresponds to the *Regenerative Braking Power* from the “Brake_Control” subassembly (see table 17).

3.2 BATTERY

As mentioned before, the GT-Suite model utilizes the ‘Battery’ object. This object does not need connections to an electric circuit model since it operates on the concept of SOC. This allows to model the power electronics just with control elements instead. Nevertheless, it requires the internal resistance and OCV maps of the battery.

The battery maps corresponded to an average of four 2016 Chevrolet Volt batteries, which were obtained experimentally by the Advance Vehicle team of the INL. These tests followed the "Battery Test Manual for Plug-In Hybrid Electric Vehicles" from the United States Advance Battery Consortium (IDAHO NATIONAL LABORATORY, [s.d.]).

The battery from the Chevrolet Volt was chosen for being manufactured by the same company that made Volvo's batteries (LG CHEM, [s.d.]); moreover, these batteries should represent recent battery technology since they were tested in 2017. Table 18 presents the specifications of the 2016 Chevrolet Volt battery. As an example, annex K shows the figures contained in one of the reports.

TABLE 18 – BATTERY SPECIFICATIONS OF THE 2016 CHEVROLET VOLT, SUPPLIED BY THE MANUFACTURER

Battery Specification of 2016 Chevrolet Volt			
Manufacturer:	LG Chem	**Type:**	Lithium-ion
Number of Cells:	96	**Thermal Management:**	Active-Liquid Cooled
Minimum Cell Voltage:	3.00 V	**Maximum Cell Voltage:**	4.15 V
Nominal Cell Voltage:	3.80 V	**Nominal System Voltage:**	360 V
Rated Pack Energy:	18.9 kWh	**Rated Pack Capacity:**	52 Ah
Pack Volume[1]:	140.5 L	**Pack Mass:**	182.8 kg

[1] Battery pack volume is approximate and is based on the overall rectangular envelope less any significat voids

Source: adapted from INL ([s.d.]) reports for VIN 1377, 4657, 4673, and 4913.

Both the OCV the resistance maps were obtained from the four reports previously mentioned, each report corresponds to a different 2016 Chevrolet Volt with its own Vehicle Identification Number (VIN). The "WebPlotDigitizer" tool was used to extract the data from the reports, this tool is of free access and was developed by Rohatgi (2018).

All the reports contained data of two tests, the Beginning of Test (BOT) and the ICD 1. From now on, all information refers only to the BOT values. Table 19 shows the VIN, the date of test, and the mileage for the four vehicles at the BOT.

TABLE 19 – BATTERY LABORATORY TEST RESULTS SUMMARY, BEGINNING OF TEST DATA

VIN	Date of Test	Vehicle Odometer (mi)	Measured Average Capacity (Ah)	Measured Average Capacity (kWh)
1377	30/03/2016	4008	48.5	17.3
4657	21/03/2016	4000	49.9	17.5
4673	30/03/2016	4000	49.8	17.4
4913	02/04/2016	4065	49.6	17.3

Source: adapted from INL ([s.d.]) reports for VIN 1377, 4657, 4673, and 4913.

The OCV values contained in the reports corresponded to the average of three test iterations. These OCV values were obtained by measuring “the charge and energy capacities of the battery between maximum and minimum pack voltages when discharged at a constant current calculated to approximate 10 kW discharge rate” (IDAHO NATIONAL LABORATORY, 2017, p. 2). For the case of the 2016 Chevrolet Volt, the discharge current was constant at 29.15 A.

Nevertheless, the data of the model corresponds to an average OCV of the four reports with the VINs shown in table19. Figure 74 shows the average OCV values introduced in the model, which correspond to both the charge and the discharge maps.

FIGURE 74 – OPEN CIRCUIT VOLTAGE MAP USED IN THE SERIES HEV MODEL

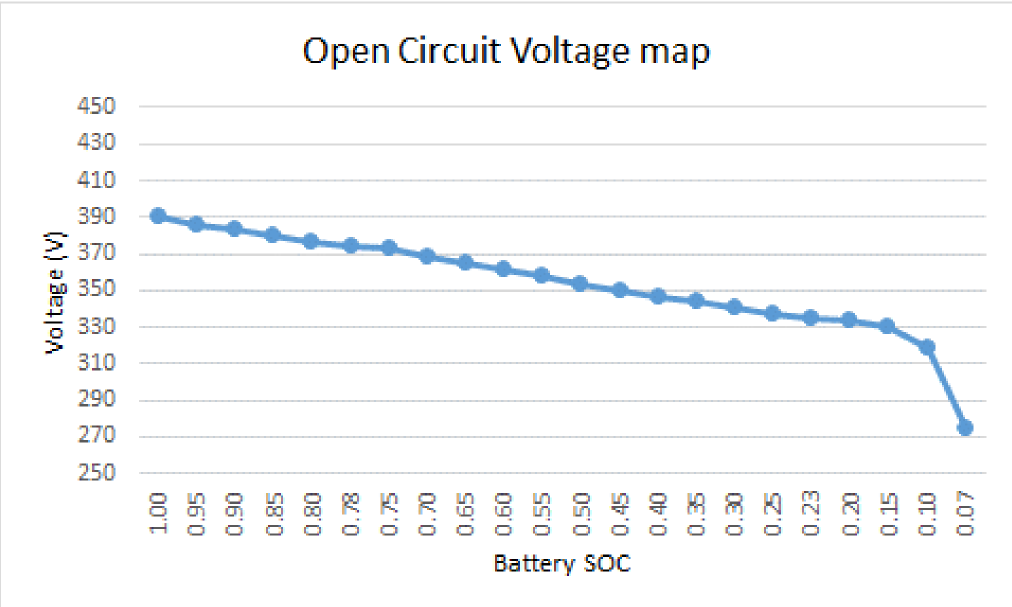

Source: adapted from INL ([s.d.]) reports for VIN 1377, 4657, 4673, and 4913.

Regarding the internal resistance maps, the INL obtained them by characterizing the pulse power capability of the battery at intervals of 10% depth-of-discharge. The same method was used for both charging and discharging. The resistance maps introduced to the model are shown in figure 75, for charging, and in figure 76, for discharging. Both figures are an average of the four vehicle reports with the VINs shown in table19.

FIGURE 75 – INTERNAL RESISTANCE MAP, AT CHARGE, USED IN THE SERIES HEV MODEL

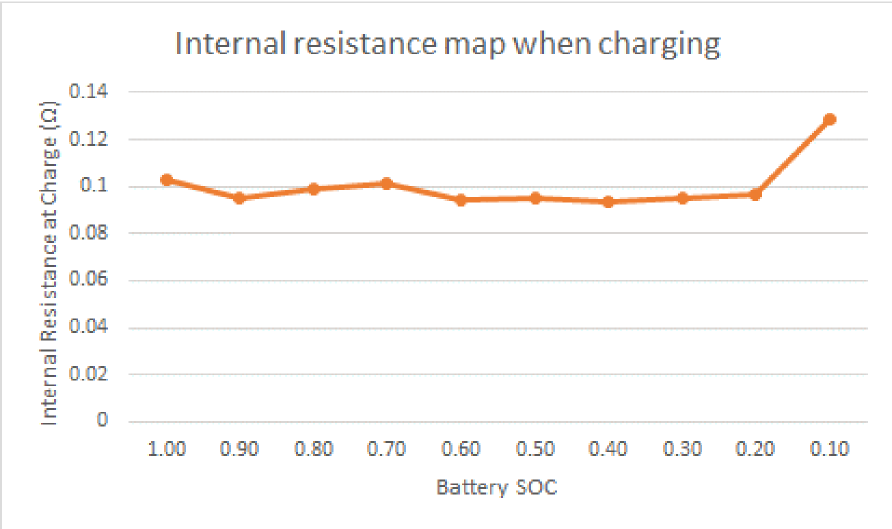

Source: adapted from INL ([s.d.]) reports for VIN 1377, 4657, 4673, and 4913.

FIGURE 76 – INTERNAL RESISTANCE MAP, AT DISCHARGE, USED IN THE SERIES HEV MODEL

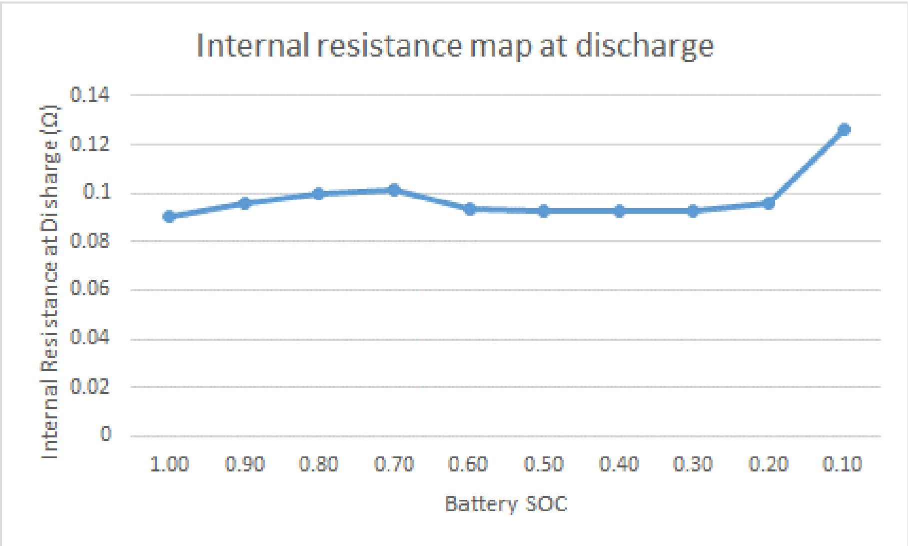

Source: adapted from INL ([s.d.]) reports for VIN 1377, 4657, 4673, and 4913.

Notice that the data from the reports is in function of the capacity discharged, in Ah (see annex K). Nevertheless, the software requires the maps to be in function of the battery SOC; therefore, the data was converted into SOC by using equation 2. For all calculations, a maximum capacity of 52 Ah was used, since this is the value specified by the manufacturer, as shown in table 18.

Next, the voltage and current limits of the battery were defined for the “BatteryPowerLim1”. This object is used together with the ‘Battery’ object to ensure that the power limits of the battery are not exceeded. Moreover, the use of the ‘BatteryPowerLim’ object allows to connect two electric machines, hence, limiting the power of the motor and generator at the same time.

The Maximum Charge Voltage Limit attribute was defined as the nominal voltage specified by the battery manufacturer, which is 360 V (see table 18). While the Minimum Discharge Voltage Limit attribute was kept at 0 V. Nevertheless, a different approach was used to define the maximum current limits, as shown next.

First, the discharge and charge power capabilities for the VIN 4673 were obtained from figure A59 in annex K. The maximum value found for the discharge pulse power was 389 kW, while the maximum value for the charge pulse power was 384.3 kW. Next, both values were divided by the Maximum Discharge Current Limit, as shown in equations 82 and 83:

$$Maximum\ Discharge\ Current = \frac{389\ kW * 1000}{360\ V} = 1080.72\ A \approx \mathbf{1050\ A} \qquad (82)$$

$$Maximim\ Charge\ Current = \frac{384.3\ kW * 1000}{360\ V} = 1067.7\ A \approx \mathbf{1060\ A} \qquad (83)$$

To have some tolerance, the final values introduced were 1050 A for the Maximum Discharge Current Limit and 1060 A for the Maximum Charge Current Limit. Just for comparison purpose, the vehicle Tesla Model S can deliver approximately 1000 amps of current (TESLA MOTORS INC, 2011).

The Initial SOC for the model was defined as 0.7. It is important to remember that the “SOC_Control1” part, found in the “ECU” subassembly, was programmed to start the engine when the battery SOC<0.7, and to turn it off when the SOC≥0.8. Since the Initial SOC was defined also as 0.7, the engine always turn on when the vehicle starts moving.

On the other hand, the Battery Capacity was based on the battery of the commercial Volvo XC60 (see table 15). The Battery Capacity must be entered in Ah, hence, it was divided by the Maximum Discharge Voltage Limit, as shown in equation 84:

$$Battery\ Capacity = \frac{10.4\ kWh * 1000}{360\ V} = 28.8\ Ah \tag{84}$$

Finally, it is emphasized that the battery data was kept constant through all the simulations. Nevertheless, some comparison simulations required to change the battery parameters, section 3.6.3 explains those simulations.

3.3 ETHANOL ENGINES

This work simulated two different engines, the engine Ford Sigma 1.6L flex-fuel and the engine prototype 1.0L turbocharged. The latter engine was designed to only run with E100; thus, it was designed to fully take advantage of all E100 properties. Additionally, this prototype engine was also tested with water injection fuel strategy.

To characterize both engines, the GT-Suite model used the 'EngineState' object, which mathematical model is presented in Annex C. In order to simulate a dynamic engine, this object needs the mechanical output and friction maps, which must be measured before any accessory load is connected to the engine. In addition, the fuel consumption map of both engines was introduced in order to evaluate the fuel economy. The maps of both engines were acquired while running with E100, and were obtained experimentally by the CTM laboratory, located inside the UFMG.

The Ford Sigma is an inline 4-cylinder engine with a displacement of 1596 cm^3 and was commercialized in the Brazilian Ford Fiesta from 2008 to 2014. The maps correspond to the engine version without VVT, and comes form Rückert et al (2019) research. Annex F presents the engine data of the Ford Sigma used in the model.

On the other hand, the prototype engine is a turbocharged inline 3-cylinder, with a displacement of 996 cm^3. In this engine the fuel is injected directly into the cylinder by an air guided system, and also has a VVT system in the intake valves. Additionally, it possesses a second injection strategy that injects water into the intake manifold, improving engine performance.

Different to the Ford Sigma flex-fuel engine, which can run with both ethanol and gasoline fuels, the engine prototype was designed to run only with ethanol. Therefore, the prototype engine can operate at higher compression ratios without knocking problems, due to the higher octane number of ethanol.

The tests of the prototype engine were performed at steady-state and stoichiometric conditions at 2500 rpm; thus, only data for this operation speed was obtained, which is presented in Annex L. Swirl type injectors introduce the fuel directly to the camera at 180 bar and 298 K. While the water is injected into the intake manifold at 7 bar and 298 K (BAETA et al., 2018).

Table 20 shows the characteristics of both engines simulated. Observe that the maximum power and torque given for the prototype engine correspond to a speed of 2500 rpm. Since the data was obtained by tests at this speed, the maximum power and torque through all the operation range are unknown.

TABLE 20 – CHARACTERISTICS OF BOTH ENGINES SIMULATED

	Ford Sigma engine	**Prototype engine**
Engine type	Natural Aspirated SI	Turbocharged SI
Fuel Injection system	PFI	DI (Air-Guided System)
Water injection system	N/A	PFI
Displacement (cm^3)	1596	993
Number of cylinders	4	3
Engine layout	L-4	L-3
Compression ratio	11	13.3
Bore (mm)	79	70
Stroke (mm)	81.4	86
Valves per cylinder	4	2
Max. power (kW @rpm) [fuel strategy used]	80,4 @6250 [gasoline] 85,8 @5500 [ethanol]	51,67 @2500 [E100]* 68,4 @2505 [E100+WI]*
Max. torque (Nm @rpm) [fuel strategy used]	151,2 @4250 [gasoline] 158,9 @4250 [ethanol]	197,35 @2500 [E100]* 260,74 @2505 [E100+WI]*

* Maximum output for that given speed, and not for all the operation speed range

Source: Baeta et al. (2018) and Rückert et al. (2019).

This also means that the prototype engine only was simulated for these two operation conditions. In reality, a slightly lower load was selected for both operation points, to avoid exceeding the maximum load. Therefore, the prototype engine running with E100 and water injection was operated at 66 kW and 2505 rpm; on the other hand, the prototype engine running only with E100 was operated at 50 kW and 2500 rpm.

Finally, table 21 shows the E100 fuel values used for both engines. It is highlighted the relevance of the fuel density since it is needed to convert the fuel consumption from massic values (g/km) to volumetric values (km/l).

TABLE 21 – MAIN PROPERTIES OF THE BRAZILIAN HYDRATED ETHANOL USED IN THE PROTOTYPE ENGINE TESTS

Brazilian hydrated ethanol - E100			
Density (kg/m3)	808.7	Carbon (%)	50.7
MON	91.8	Hydrogen (%)	13
RON	> 100	Oxygen (%)	36.3
Heat value (MJ/kg)	24.76	Fuel formulation	$CH_{30}O_{0.53}$

Source: adapted from Baeta et al. (2018).

3.4 ELECTRIC MOTOR SELECTION

The model utilized a ‘MotorGeneratorMap’ object to model both electric machines. This object needs the electromechanical efficiency and brake torque maps. In both electric machines, the Brake-Power attribute was chosen as the load control. The equations that govern the ‘MotorGeneratorMap’ object are presented in annex B.

To obtain the efficiency and torque maps an internet search was made, resulting in seven electric machines found from two different companies. The first company is Yasa Limited, which commercialize two motors the Yasa P400 RS and the Yasa 750R. The second company is EMRAX d.o.o., which commercialize five axial flux synchronous PM machines of different sizes. Both companies advertise their product as suitable for automotive applications. Table 22 shows the characteristics of the seven electric machines considered through the work.

In order to select a proper electric motor for the model, the motor power demand was analyzed for the Volvo XC60. This analysis was carried out for the five standard driving cycles, and its results are shown in appendix B.

TABLE 22 – CHARACTERISTICS OF THE SEVEN ELECTRIC MACHINES FOUND

Motor	Yasa P400 R	Yasa 750 R	EMRAX 188	EMRAX 208	EMRAX 228	EMRAX 268	EMRAX 348
Peak Power (kW@V)	160@700	200@700	60	75	100	220	400
Continuous Power (kW)	100	70	32	40	55	110	200
Peak Torque (Nm@A)	370@450	790@450	90	140	230	500	1000
Cont. Torque (Nm)	250	400	50	80	120	250	500
Max. Speed (rpm)	8000	3250	6500	6000	5500	4500	4000
Mass (kg)	24	37	7.3	9.4	12.4	20.5	40
Max. Voltage (Vdc)	700	800	400	470	670	700	800
Max. Current (Arms)	450	450	800	800	900	1000	1100
Cont. Current (Arms)	-	-	400	400	450	500	550
Max. Temperature (C.)	-	-	120	120	120	120	120

Source: adapted from EMRAX d.o.o (2018), YASA Limited (2018a), and YASA Limited (2018b).

It was concluded that a motor with a peak power higher than 100 kW was needed, in order to ensure good performance for the Volvo XC60. Thus, the Yasa P400 was selected as the traction motor. The power, torque and efficiency curves of the Yasa P400 are shown in annex G. It is important to mention that the model used the torque and power curves at 700 V.

The Yasa P400 was used as the motor of both the Ford Fiesta and the Volvo XC60 models, however, the gear ratio was different for each vehicle. The values of 'GearRatio1' were chosen by matching the vehicle's top speed (see table 15) with the motor's top speed of 8000 rpm.

First, the vehicle's top speed must be converted to revolutions per minute using equation 85. Since the differential gear ratio was previously defined as 3.2, then the 'GearRatio1' can be found by equation 87:

$$\omega_v = \frac{v}{\pi * r_d} * 8.33 \tag{85}$$

$$GR_{Total} = \frac{\omega_1}{\omega_2} \tag{86}$$

$$GR_1 = \frac{GR_{Total}}{GR_{diff}} = \frac{GR_{Total}}{3.2} = \frac{\omega_1}{\omega_2 * 3.2} \quad (87)$$

Where:

- ω_v is the top speed of the vehicle, in rev/min;
- v is the vehicle speed in km/h;
- r_d is the dynamic radio of the wheel in meters;
- GR_{Total} is the total gear ratio of the power train, and corresponds to the product between the motor and differential gear ratios;
- GR_1 is the gear ratio of the motor;
- GR_{diff} is the gear ratio of the differential, defined as 3.2;
- ω_1 corresponds to the maximum speed of the motor in rpm, and;
- ω_2 corresponds to the vehicle's top speed fo the wheel in rpm.

In summary, the motor used for both vehicles corresponds to the Yasa P400 electric machine. The torque and power curves at 700 V were chosen, and are presented in annex G. Finally, a one stage transmission with fix gear ratio was used for the Ford Fiesta and Volvo XC60, which were defined as 1.57 and 1.59 respectively.

3.5 GENERATOR SELECTION

In a series HEV, the ICE and generator are linked together and operate independently of the tires. This means that the ICE can operate at maximum efficiency independently of the vehicle power demand, however, the generator also must operate at its maximum efficiency. This is achieved with a transmission between the ICE and generator. By choosing a proper gear ratio for the transmission, both the ICE and the generator can operate at their maximum efficiency points.

The process to select the optimal operation point of both ICE and generator was as follows. First, it was selected the power at which the ICE will operate, now on referred to as *Power Mode*. Then, with the help of the BSFC map, the operation point of lowest fuel consumption was found for each Power Mode. Next, the efficiency maps of the electric machines were studied in order to select a proper generator. Finally, several simulations were performed in order to find the gear ratios that correspond to the operation points with the highest efficiency of the generator.

Nevertheless, any operation point that exceeded the continuous power of the generator was neglected. Additionally, the operation points of the generator were analyzed only for speeds over 1000 rpm and varied in increments of 250 rpm.

Selecting the operation points of the prototype engine was easy since only data regarding one operating speed was available. On the other hand, the Ford Sigma engine needed a previous analysis of the electric motor power demand in order to properly define the engine's operation points.

This analysis was conducted for both vehicles, and for the five standard driving cycles. The analysis consisted on looking for the most frequent power demands of each cycle. The analysis process is presented in appendix C for the Ford Fiesta and in appendix D for the Volvo XC60. At the end of the analysis, eight different Power Modes of the Sigma engine were selected for each vehicle.

Section 3.5.1 describes the matching process between the Sigma engine and the generator EMRAX 208, for the Ford Fiesta case. Similarly, section 3.5.2 describes the matching process between the Sigma engine and the generator EMRAX 228, for the Volvo XC60 case. Finally, section 3.5.3 presents the matching process between the prototype engine and their generators, for both the Ford Fiesta and the Volvo XC60.

3.5.1 FORD SIGMA ENGINE AND FORD FIESTA VEHICLE

The analysis of the motor power demand for the Ford Fiesta vehicle resulted in the selection of the next eight Power Modes: 2 kW, 4 kW, 6 kW, 10 kW, 13 kW, 16 kW, 20 kW, and 23 kW. The complete analysis of the Ford Fiesta power demand can be consulted in appendix C.

In order to find the lowest fuel consumption of each Power Mode, it was utilized a linear interpolation of the engine's BSFC. Figure 77 shows the BSFC for the 2, 4, 6, and 10 kW Power Modes, while figure 76 shows the BSFC for the 13, 16, 20, and 23kW Power Modes.

FIGURE 77 – BSFC AT DIFFERENT ENGINE SPEEDS FOR THE 2, 4, 6, AND 10 KW OPERATION MODES OF THE FORD FIESTA

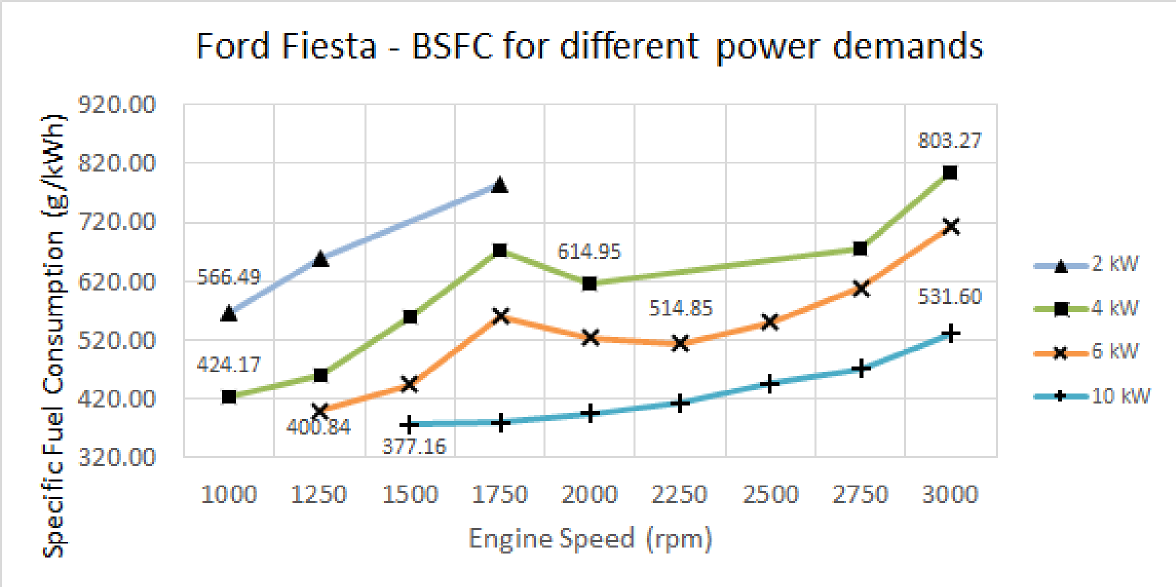

Source: adapted from data obtained from the CTM laboratory at the UFMG.

FIGURE 78 – BSFC AT DIFFERENT ENGINE SPEEDS FOR THE 13, 16, 20 AND 23 KW OPERATION MODES OF THE FORD FIESTA

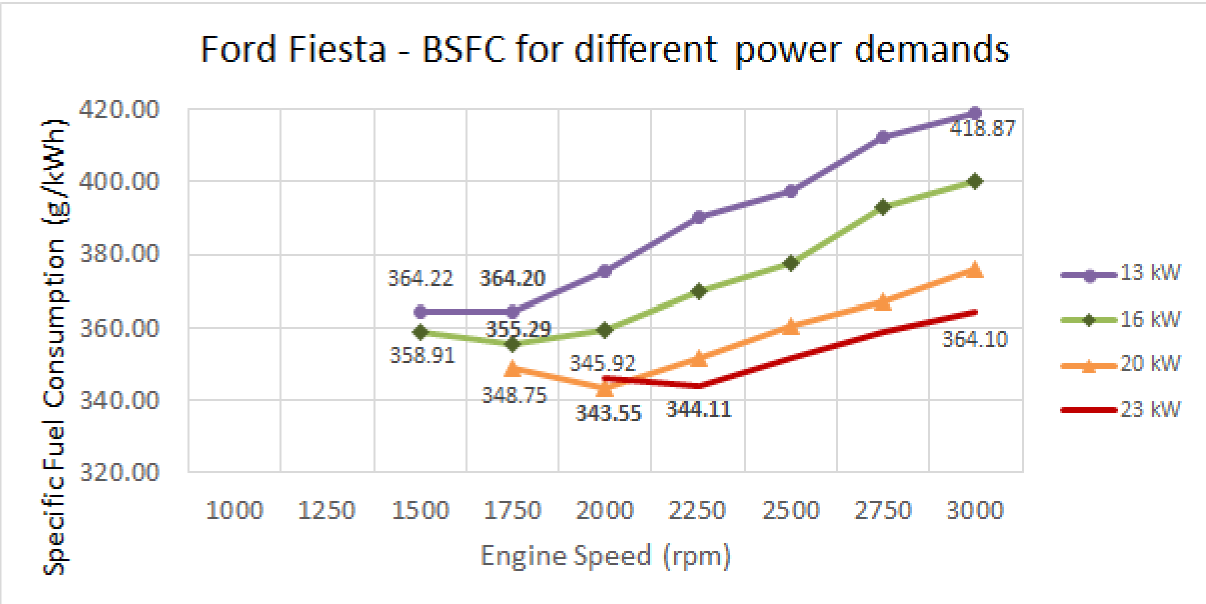

Source: adapted from data obtained from the CTM laboratory at the UFMG.

Once defined the operation points with the lowest BSFC of each Power Mode, the torque of each operation point was found with the same interpolation method. Even though the torque is not needed to simulate, it is needed to find the operation points of the generator. To find the generator operation points, first, the 'GearRatio2' was calculated by using equation 86. Where the ω_1 corresponded to the ICE operation speed and ω_2 corresponds to the generator operation speed analyzed. Then, the generator's torque was found with equation 88:

$$\tau_2 = GR_{Total} * \tau_1 \tag{88}$$

Where:

- τ_1 corresponds to the ICE operation torque;
- τ_2 corresponds to the generator operation torque, and;
- GR_{Total} corresponds to the 'GearRatio2', given by equation 86.

Among the seven electric machines found (see table 22), the EMRAX 208 showed to be the best match due to the power demands found. Figure 79 shows the EMRAX 208 efficiency map and each operating point covered by the gear ratio analysis. On the other hand, annex I presents the power, torque, and efficiency maps of the EMRAX 208.

FIGURE 79 – EFFICIENCY MAP OF EMRAX 208 AND EACH OPERATION POINT ANALYZED FOR THE FORD FIESTA POWER MODES

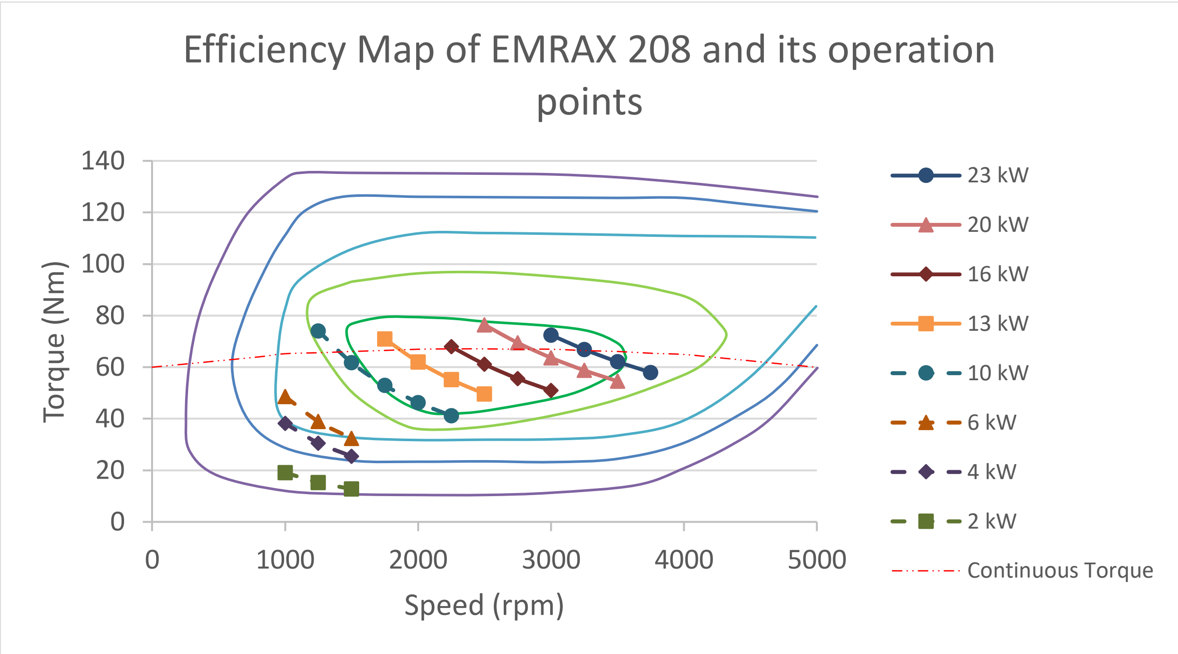

Source: adapted from EMRAX d.o.o. (2018).

In summary, the next eight Power Modes were defined for the Sigma engine when running in the Ford Fiesta: 2 kW, 4 kW, 6 kW, 10 kW, 13 kW, 16 kW, 20 kW, and 23 kW. In this case, the EMRAX 208 was chosen as the generator, for which 31 operation points were simulated. Table 23 shows a summary of all the operation points selected for each Power Mode of the Ford Fiesta, to see the complete results consult the appendix E.

TABLE 23 – SUMMARY OF THE POWER MODES SELECTED FOR THE SIGMA ENGINE AND THE FORD FIESTA

Power Mode	ICE Speed (rpm)	ICE Load (Nm)	ICE BSFC (g/kWh)	GR2 Value	GR2 Efficiency	Gen. Speed (rpm)	Gen. Torque (Nm)	Gen. Efficiency	Electric Machine
23 kW	2250	97.61	343.63	0.6923	97.00%	3250	65.55	93.52%	EMRAX 208
20 kW	2000	95.49	344.20	0.6154	97.00%	3250	59.99	93.53%	
16 kW	1750	87.30	353.75	0.7000	97.00%	2500	59.28	95.99%	
13 kW	1750	70.93	362.21	0.8750	97.00%	2000	60.20	91.13%	
10 kW	1500	63.66	370.80	0.8571	97.00%	1750	52.93	92.31%	
6 kW	1250	45.87	395.43	1.0000	100.00%	1250	45.83	89.64%	
4 kW	1000	38.19	433.27	0.8000	97.00%	1250	29.64	89.64%	
2 kW	1000	19.11	554.47	0.8000	97.00%	1250	14.82	89.64%	

Source: elaborated by the author.

3.5.2 FORD SIGMA ENGINE AND VOLVO XC60 VEHICLE

The analysis of the Volvo XC60 showed higher power demands than for the Ford Fiesta. This difference is attributed to the higher drag coefficient and higher weight of the Volvo XC60. The complete analysis of the Volvo XC60 power demands is presented in appendix D. The analysis showed 22 power demands that were considered relevant, which were classified into eight groups as shown in table 24.

TABLE 24 – MOST RELEVANT POWER DEMANDS FOR THE VOLVO XC60

Group 1	Group 2	Group 3	Group 4	Group 5	Group 6	Group 7	Group 8
3 kW	7 kW	12 kW	18 kW	23 kW	29 kW	37 kW	40 kW
	9 kW	14 kW	20 kW	24 kW	30 kW	38 kW	
5 kW	10 kW	15 kW	22 kW	26 kW	31 kW	39 kW	
	-	-	-	-	33 kW	-	

Source: elaborated by the author

Figure 80 to 83 show the BSFC for each of the 22 power demands at different speeds. For each group, only the operation point with the lowest BSFC of the engine was selected. Resulting in the next Power Modes chosen: 5 kW, 10 kW, 15 kW, 20 kW, 26 kW, 30 kW, 37 kW, and 40 kW.

As mention before, the Volvo XC60 requires higher power demands from the engine, thus the electric generator also needs to tolerate higher continuous power. Therefore, the EMRAX 228 was chosen because of its higher continuous power. Annex J presents the power, torque and efficiency maps of the EMRAX 228.

Next, it was proceeded to find the most efficient operation points of the generator for each of the eight Power Modes. Figure 84 overlaps the operation points simulated into the efficiency map of the EMRAX 228, from which the center loop represents the highest efficiency (96%). In total, 40 operation points were simulated, to see the complete results consult the appendix F.

FIGURE 80 – BSFC AT DIFFERENT ENGINE SPEEDS FOR GROUP 1 AND 2 OF THE VOLVO XC60

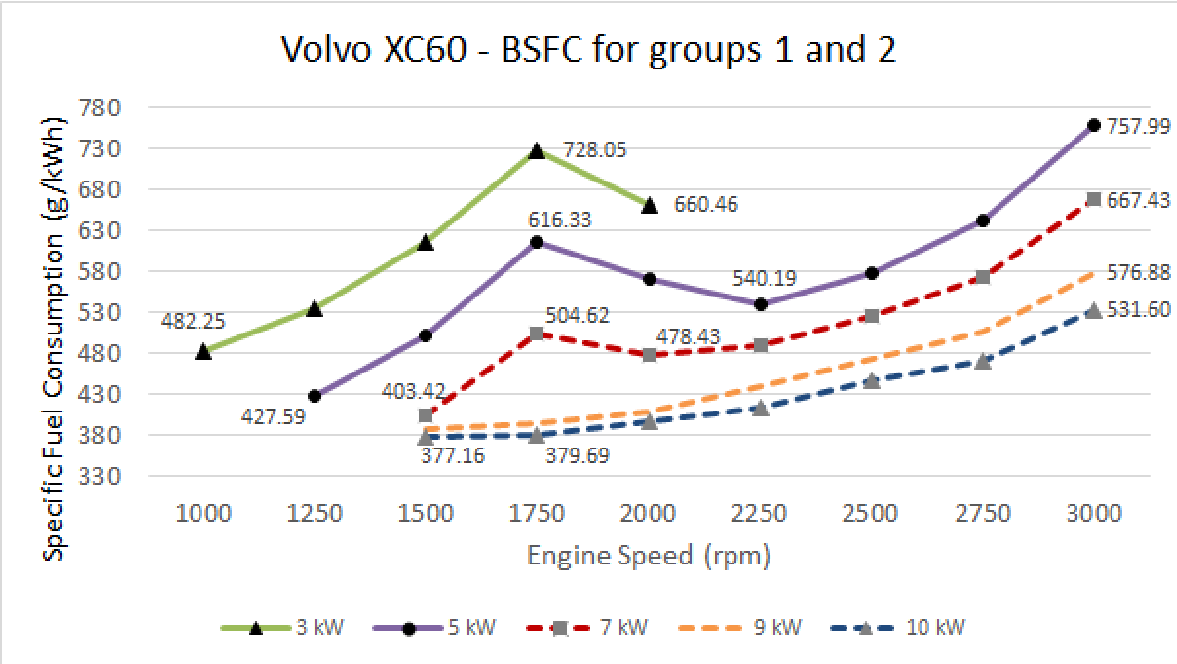

Source: elaborated by the author.

FIGURE 81 – BSFC AT DIFFERENT ENGINE SPEEDS FOR GROUP 3 AND 4 OF THE VOLVO XC60

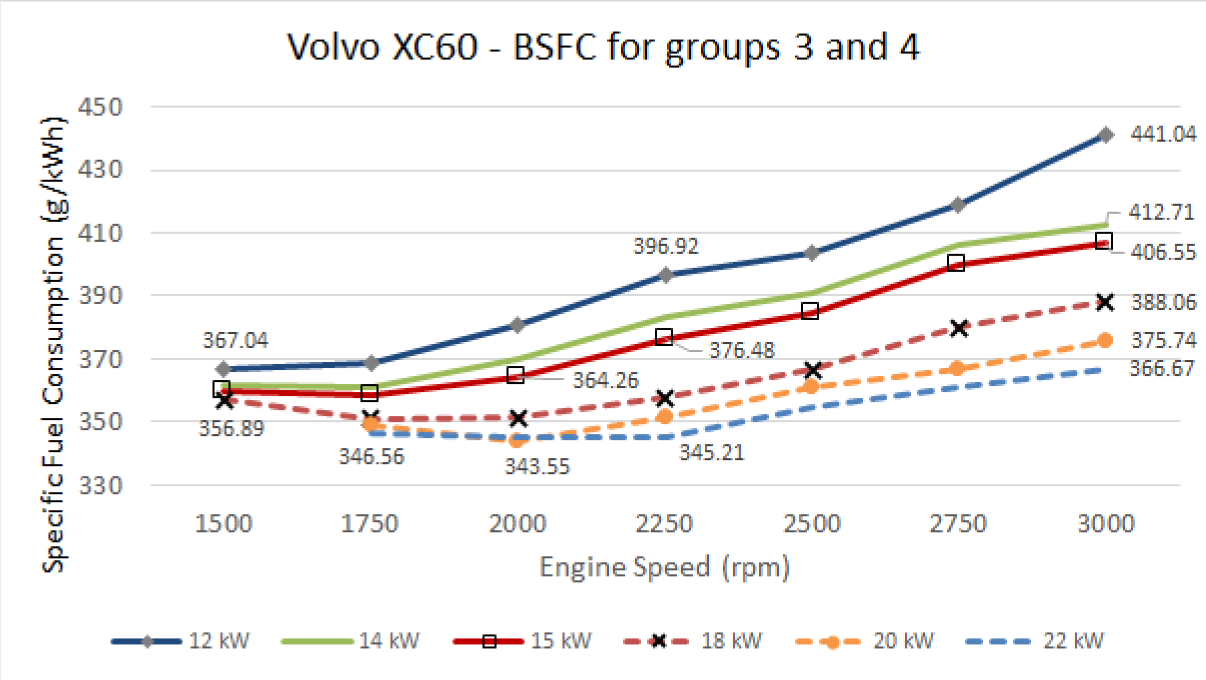

Source: elaborated by the author.

FIGURE 82 – BSFC AT DIFFERENT ENGINE SPEEDS FOR GROUP 5 OF THE VOLVO XC60

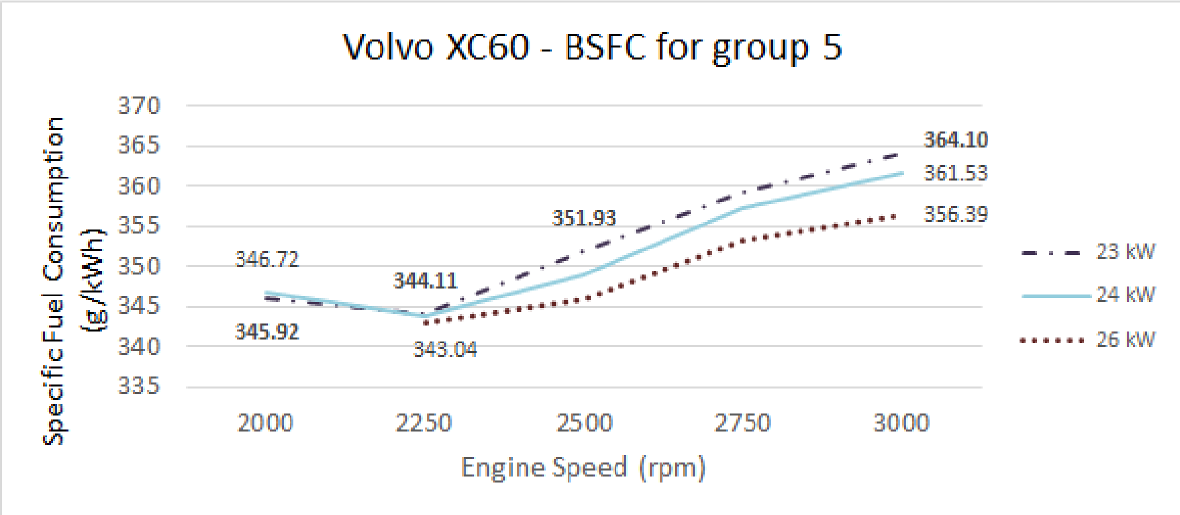

Source: elaborated by the author.

FIGURE 83 – BSFC AT DIFFERENT ENGINE SPEEDS FOR GROUP 8, 7, AND 6 OF THE VOLVO XC60

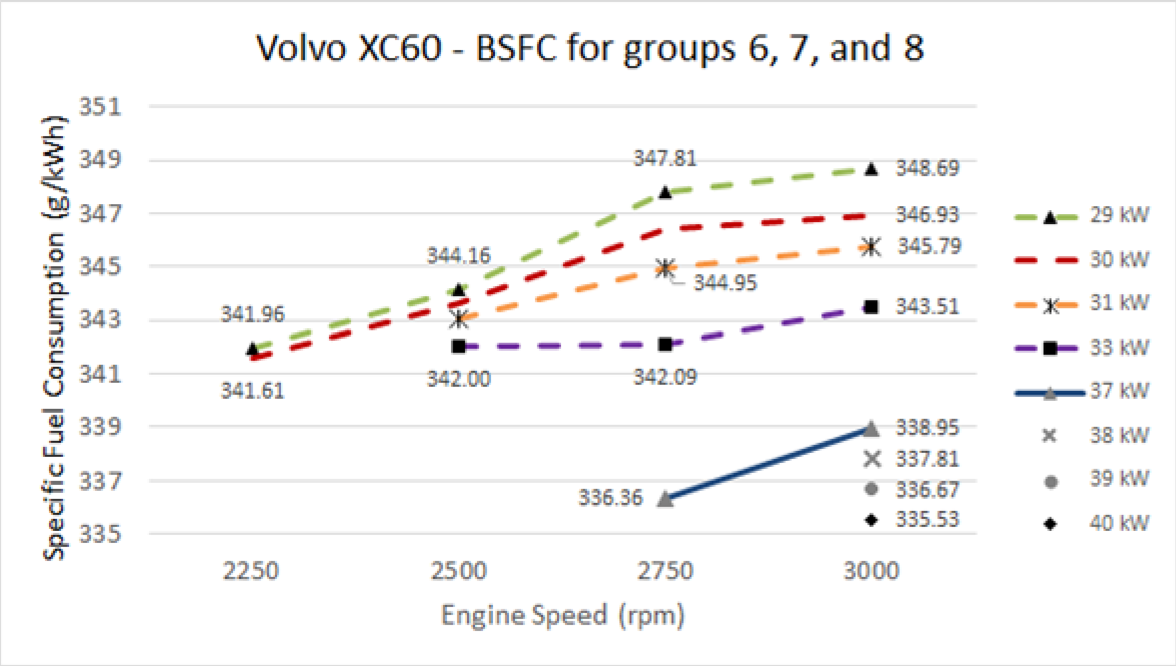

Source: elaborated by the author.

FIGURE 84 – EFFICIENCY MAP OF EMRAX 228 AND EACH OPERATION POINT ANALYZED FOR THE VOLVO XC60 POWER MODES

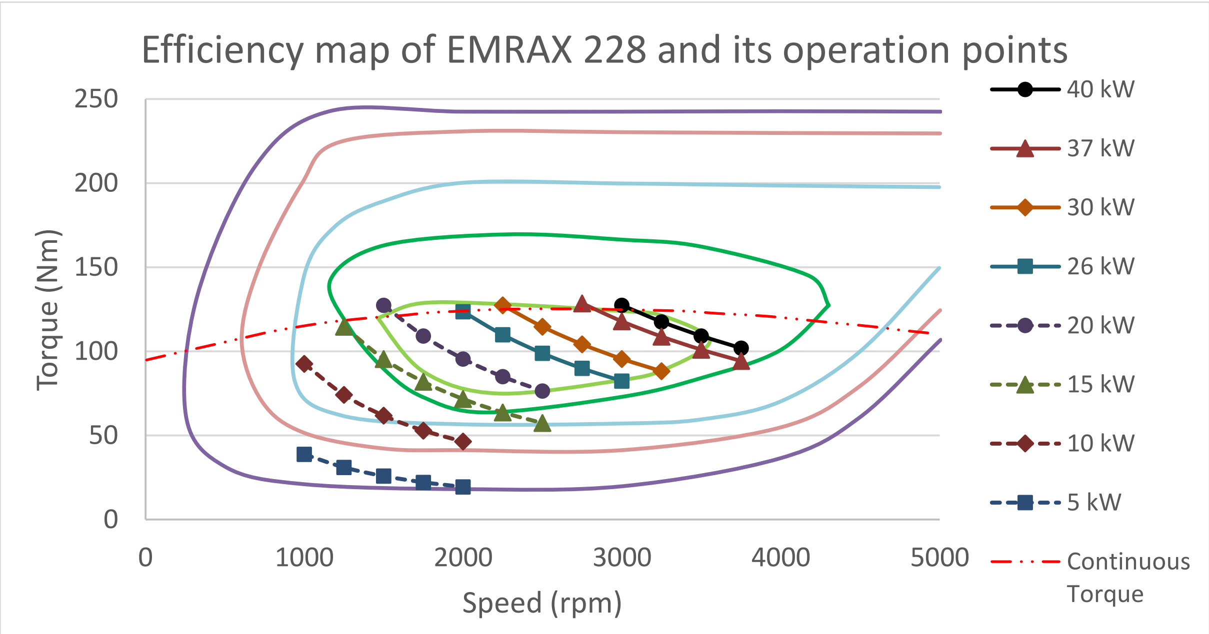

Source: adapted from EMRAX d.o.o. (2018).

In summary, the next eight Power Modes were defined for the Sigma engine when running in the Volvo XC60: 5 kW, 10 kW, 15 kW, 20 kW, 26 kW, 33 kW, 37 kW, and 40 kW. In this case, the EMRAX 228 was chosen as the generator, due to its higher continuous power. Finally, table 25 shows a summary of all the operation points selected for each Power Mode of the Volvo XC60.

TABLE 25 – SUMMARY OF THE POWER MODES SELECTED FOR THE SIGMA ENGINE AND THE VOLVO XC60

Power Mode	ICE Speed (rpm)	ICE Load (Nm)	ICE BSFC (g/kWh)	GR2 Value	GR2 Efficiency	Gen. Speed (rpm)	Gen. Torque (Nm)	Gen. Efficiency	Electric Machine
40 kW	3000	127.32	317.90	0.9231	97.00%	3250	114.86	95.84%	EMRAX 228
37 kW	3750	128.48	329.12	0.8462	97.00%	3250	106.26	95.83%	
30 kW	2250	127.32	340.63	0.9000	97.00%	2500	111.15	95.99%	
26 kW	2250	110.36	342.45	0.9000	97.00%	2500	96.92	95.99%	
20 kW	2000	95.60	344.22	0.8000	97.00%	2500	74.19	95.99%	
15 kW	1750	81.85	356.18	0.7000	97.00%	2500	55.88	95.99%	
10 kW	1500	63.66	370.86	0.8571	97.00%	1750	52.97	94.86%	
5 kW	1250	38.19	414.56	0.7143	97.00%	1750	26.47	94.86%	

Source: elaborated by the author.

3.5.3 For the prototype engine

As mention in section 3.3, the prototype engine operates just in two different Power Modes. These are the 66 kW mode for the E100 and WI injection fuel strategy and the 50 kW mode for only E100 injection fuel strategy. Both Power Modes were simulated for both the Ford Fiesta and the Volvo XC60 vehicles.

Due to the high power demands of the prototype engine, the Yasa P400 and Yasa 750R were studied as possible generator match. Figures 85 and 86 shows the efficiency maps for the Yasa P400 and Yasa 750R, from which the loops most to the right represents the area with the highest efficiency.

Figure 85, shows that the 66 kW Power Mode exceeds the continuous power of the Yasa P400; thus the Yasa 750R was chosen for this Power Mode. On the other hand, the 50 kW Power Mode was suitable to operate with both electric machines. Nonetheless, the Yasa P400 was chosen for showing the operation point with the highest efficiency, obtained at 6500 rpm. Moreover, the Yasa 750R machine seems to be oversized for the 50 kW Power Mode.

FIGURE 85 – OPERATION POINTS ANALYZED FOR THE YASA P400

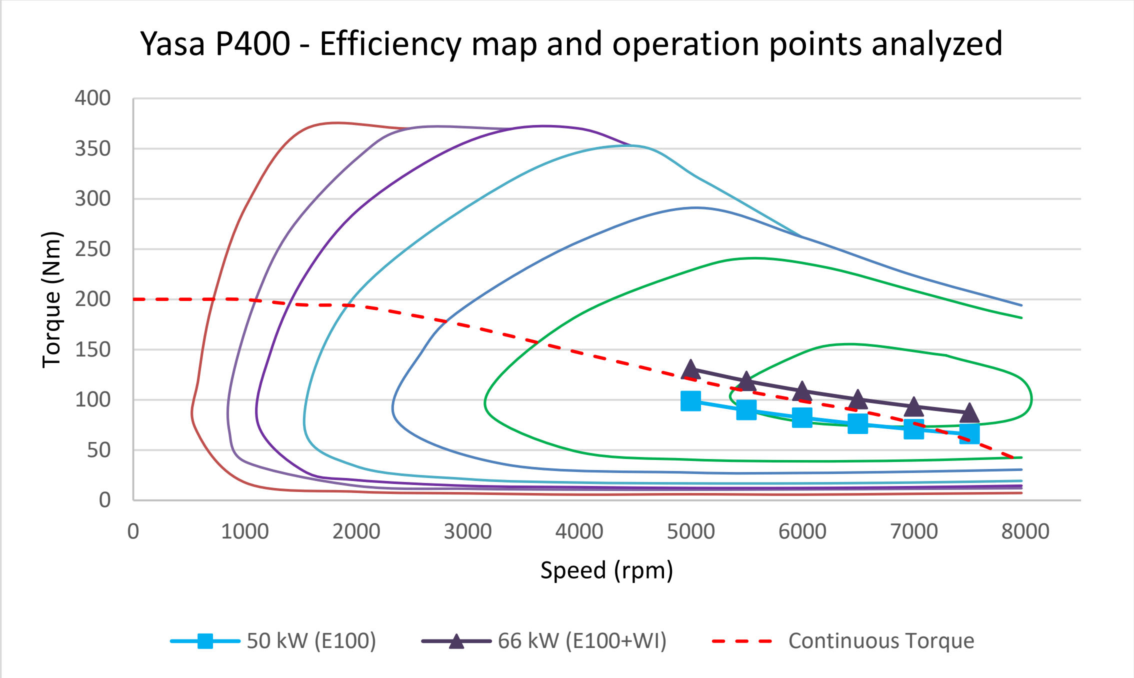

Source: adapted from YASA Limited (2018a).

FIGURE 86 – OPERATION POINTS ANALYZED FOR THE YASA 750R

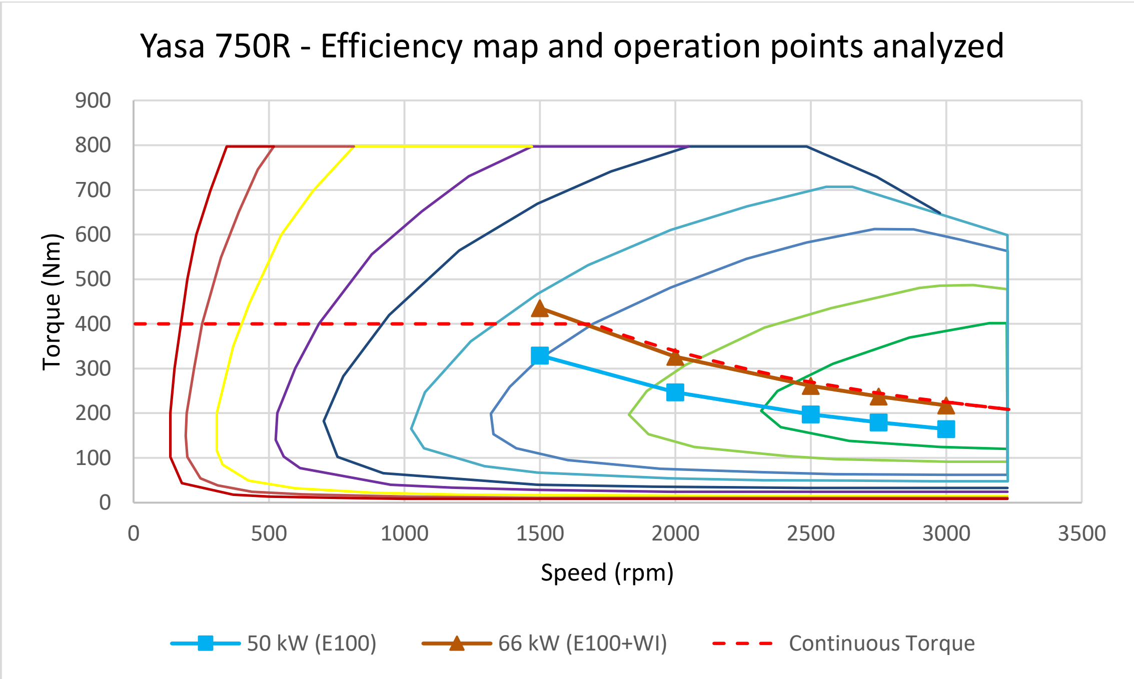

Source: adapted from YASA Limited (2018b).

In total, 16 operation points were simulated; appendix G shows the complete results of all operation points. While table 26 summarizes the two Power Modes selected for the prototype engine.

TABLE 26 – SUMMARY OF THE POWER MODES SELECTED FOR THE PROTOTYPE ENGINE USED IN BOTH VEHICLES

Power Mode	ICE Speed (rpm)	ICE Load (Nm)	ICE BSFC (g/kWh)	GR2 Value	GR2 Efficiency	Gen. Speed (rpm)	Gen. Torque (Nm)	Gen. Efficiency	Electric Machine
50 kW	2500	190.98	399.40	0.3846	97.00%	6500	75.90	93.56%	YASA P400
66 kW	2505	251.59	341.95	0.8350	97.00%	3000	217.71	93.00%	YASA 750R

Source: elaborated by the author.

3.6 SIMULATIONS MADE

This section focus on detailing the simulations that were done, and on giving more information about the two real-wolrd driving cycles. As mention before, the series HEV model was simulated with characteristics of a 2005 Ford Fiesta sedan and a 2018 Volvo XC60 (see table 15) Each vehicle was simulated for 10 Power Modes; eight Power Modes for the Sigma engine and two Power Modes for the prototype engine. appendix H lists the characteristics used for each simulation.

Additionally, each Power Mode was simulated in seven driving cycles, from which five were standard driving cycles and the other two were real-wolrd driving cycles. The five standard driving cycles simulated were the FTP-75, the HWFET, the US06, the NEDC, and the WLTC Class 3. On the other hand, the two real driving cycles represent the Brazilian driving style at low and intense traffic conditions.

3.6.1 REAL DRIVING CYCLES

The two real-world driving cycles were obtained from Roso (2016), from now on named as Low Traffic and Intense Traffic. Both real cycles corresponded to cumulative real driving measurements at three different days and followed the same path through Santa Maria city, in Rio Grande do Sul. Figure 87 shows the path followed in both cycles. Therefore, both cycles represent the same topography. Nevertheless, each cycle was measure at different times of the day.

One cycle began the trip at 12:00 PM, and represents road conditions with low traffic, while the other cycle began at 17:00 PM and represents road conditions with intense traffic. More detailed information about both real driving cycles can be found in Roso (2016).

FIGURE 87 – ELEVATION PROFILE AND PATH FOLLOWED BY BOTH REAL DRIVING CYCLES: LOW TRAFFIC AND INTENSE TRAFFIC

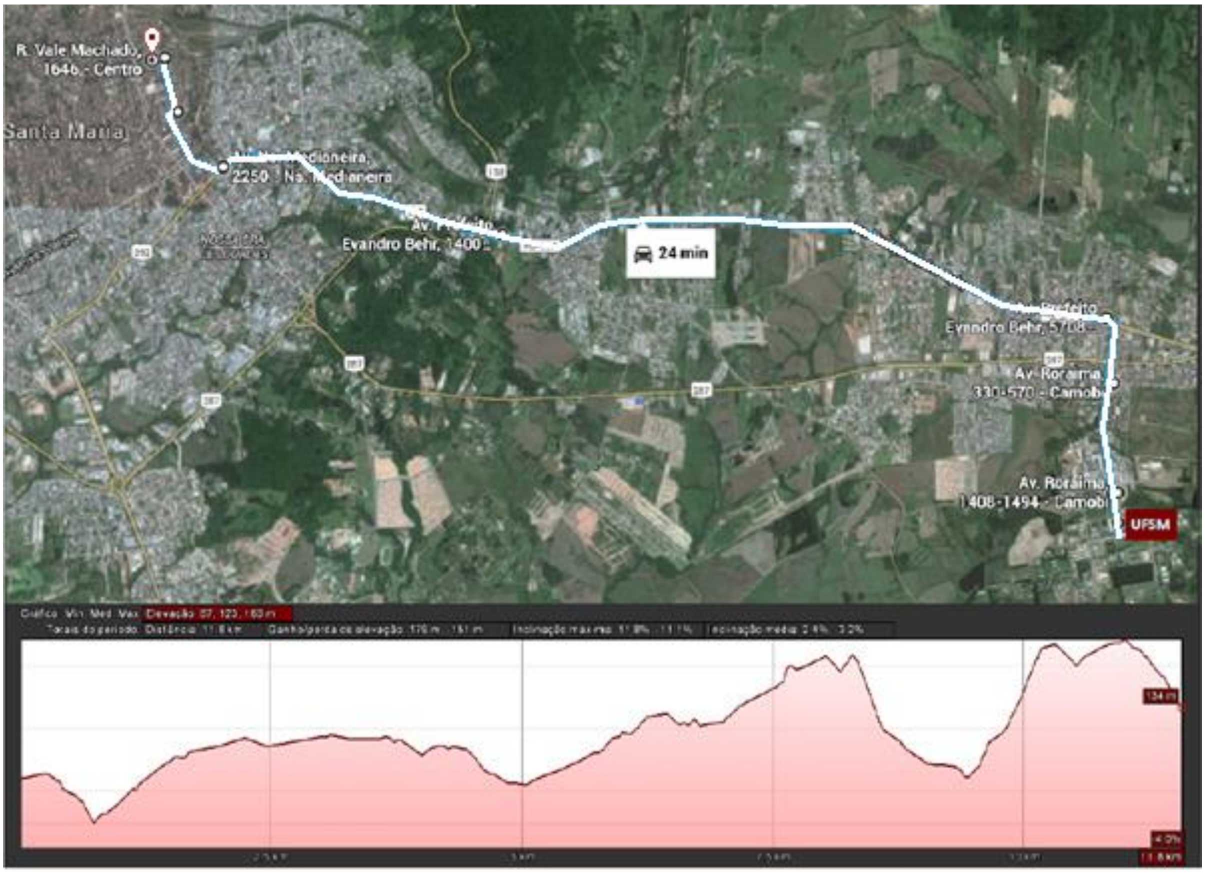

Source: Roso (2016).

3.6.2 CONVENTIONAL VEHICLE

Additionally, a conventional vehicle was simulated in order to compare the performance of the series HEV model. The model of the conventional vehicle was based on the GT-Suite “Vehicle Driveline and HEV” tutorial (GAMMA TECHNOLOGIES, 2016).

The simulations of the conventional vehicle used the Sigma engine, the characteristic of the Ford Fiesta, and the transmission gear ratios showed in table 27. These gear ratios represent the transmission used in a Ford Fiesta sedan 2011 (CORREIO BRAZILIENSE, [201-]). Furthermore, the shift strategy change to an upper gear when the engine reaches 2500 rpm, and change to a lower gear when the engine falls below 1500 rpm.

TABLE 27 – TRANSMISSION GEAR RATIOS OF FORD FIESTA WITH A SIGMA 1.6L ENGINE

Transmission Gear Ratios					
Gear #1	Gear #2	Gear #3	Gear #4	Gear #5	Reverse
3.55	2.05	1.28	0.95	0.76	3.62

Source: adapted from Correio Braziliense ([201-])

3.6.3 STATE OF THE ART COMPARISON

Finally, the series HEV model also was simulated with vehicle characteristics shown in papers of Al-Samari (2017), Asfoor, Sharaf, and Beyerlein (2014), Solouk et al. (2017), and Williamson, Lukic, and Emadi (2006). This was done to compare the results found for E100 fuel, with the results found for gasoline and diesel fuels of the four papers. Thus, the characteristics of the vehicle were changed according to those of the papers. In addition, both the Sigma engine and the prototype engine were simulated.

Since these papers only showed some variables of their simulations, each simulation was modified based on the characteristics of the Ford Fiesta or Volvo XC60 shown in table 15. Due to similar weights, the simulations corresponding to Asfoor, Sharaf, and Beyerlein (2014) were based on the Volvo XC60. While simulations corresponding to Al-Samari (2017), Solouk et al. (2017), and Williamson, Lukic, and Emadi (2006) were based on the Ford Fiesta. This is summarized in table A8 of appendix H, together with the driving cycles simulated in each case.

It is important to mention that only the vehicle and battery specifications that are shown in tables 28 to 31 were changed, all other variables were kept the same. In addition, neither the battery maps, nor the engine, motor, or generator maps were altered. Moreover, the characteristics of the ICE-Generator ensemble were maintained the same for their respective Power Modes (see tables 23, 25, and 26).

According to Asfoor, Sharaf, and Beyerlein (2014), they used GT-Suite to simulate a 2.0L gasoline engine in a conventional vehicle, in a series, a parallel, and a series-parallel HEVs. Additionally, their model used the specifications shown in table 28. Therefore, the initial SOC of our model was also changed to 0.5, so that the engine starts when the vehicle begins to move. This simulation was based on the Volvo XC60; thus, the Volvo XC60 Power Modes were used (see table 25 and 26).

TABLE 28 – VEHICLE SPECIFICATIONS USED IN ASFOOR, SHARAF, AND BEYERLEIN (2014)

Vehicle Specifications			
Weight	2000 kg	Frontal Area	2.5 m²
Drag coeff.	0.31	Wheelbase	2 m
Battery/Inverter Specifications			
Max. Charge current	50 A	Batt. Capacity	23 Ah
Max. Discharge current	100 A	SOC max. Limit	0.7
Max. Voltage	400 V	SOC min. limit	0.5
Min. Voltage	200 V		

Source: adapted from Asfoor, Sharaf, and Beyerlein (2014).

On the other hand, Solouk et al. (2017) researched the use of HCCI and RCCI engines for EREV. Table 29 shows the vehicle and electric specifications changed from the base model. Notice that the total weight introduced was 1316.5 kg, and the rotational inertia of the “Shaft1” and “Shaft2” parts also was changed to 0.067. Moreover, the battery capacity was divided by the nominal voltage; hence, the battery capacity introduced was of 13 Ah.

TABLE 29 – VEHICLE SPECIFICATIONS USED IN SOLOUK ET AL. (2017)

Vehicle Specifications			
Curb weight	1170 kg	Drag Coeff.	0.32
Frontal area	1.8 m²		
Electric Specifications			
Batt. Capacity	5 kWh	Batt. Mass	90 kg
Maximum Voltage	410 V	Inverter Mass	7.5 kg
Minimum Voltage	260 V	E-motor Mass	49 kg
Nominal Voltage	360 V	E-motor Rotational Intertia	0.067
SOC operating range	30% to 70%		

Source: adapted from Solouk et al. (2017).

In addition, Williamson, Lukic, and Emadi (2006) simulated an HEV with a 41 kW gasoline engine through the software ADVISOR. The vehicle specifications changed from the base model are shown in table 30. It is highlighted that the total weight of the vehicle introduced was 1625 kg. Additionally, the *Horizontal Dist. Between First and Last Rear Axle* parameter, from the "Car-1" part, was defined as 1.04 m in order to obtain a front wheel weight fraction of 0.6.

TABLE 30 – VEHICLE SPECIFICATIONS USED IN WILLIAMSON, LUKIC, AND EMADI (2006)

Vehicle Specifications			
Drag Coeff.	0.33	Glider Mass	1000 kg
Frontal Area	2.04 m²	ICE Mass	350 kg
Wheelbase	2.6 m	Battery Mass	275 kg
Front Wheel Weight Fraction	0.6	Battery Capacity	26 Ah

Source: adapted from Williamson, Lukic, and Emadi (2006).

Finally, Al-Samari (2017) simulated a parallel HEV in the Autonomie software. Table 31 presents the vehicle specifications that were changed from the base model.

TABLE 31 – VEHICLE SPECIFICATIONS USED IN AL-SAMARI (2017)

Vehicle Specifications			
Frontal Area	2.25 m²	Drag Coeff.	0.3
Total Vehicle Mass	1161 kg	Rolling Resist. Coeff.	0.008

Source: adapted from Al-Samari (2017).

4 RESULTS

This section presents the results of the simulations of the series HEV model developed through this work. The model simulated a Ford Fiesta sedan and a Volvo XC60 Hybrid. Additionally, the model simulated a Ford Sigma 1.6 L engine and a prototype 1.0 L engine, both running with Brazilian hydrated ethanol. The battery characteristics and maps were constant throughout all the simulations. The values of each object attribute of the model are detailed in appendix A.

In order to compare the results of the series HEV model, there were conducted simulations of a conventional vehicle as well as simulations based on Al-Samari (2017), Asfoor, Sharaf, and Beyerlein, (2014), Solouk et al. (2017), and Williamson, Lukic, and Emadi, (2006). The results obtained for the conventional vehicle simulations are included within the Ford Fiesta HEV results.

A summary of the average autonomy obtained for each Power Mode of the Ford Fiesta and Volvo XC60 are presented in table 32 and 33, respectively. Due to the different distances of each cycle, the resulting autonomies are shown in kilometers per liters.

TABLE 32 – AVERAGE AUTONOMY FOR EACH POWER MODE SIMULATED IN THE FORD FIESTA

Ford Fiesta - Average Fuel Consumption (km/l)								
Power Mode	**FTP-75**	**HWFET**	**US06**	**NEDC**	**WLTC**	**Intense Traffic**	**Low Traffic**	**Average**
02 kW	*25.1**	*56.4**	*57.6**	*24.7**	*34.1**	*24.7**	*15.3**	*34.00*
04 kW	*16.4**	*37.8**	*38.8**	*16.3**	*22.3**	15.8	*13.5**	*22.99*
06 kW	11.7	*26.5**	*26.7**	11.6	16.0	16.9	15.6	17.87
10 kW	16.7	*17.0**	*17.2**	15.3	16.3	19.1	15.6	16.73
13 kW	13.5	*13.4**	*13.5**	14.5	14.5	17.1	16.3	14.68
16 kW	12.5	11.2	*11.3**	13.8	12.9	15.0	16.4	13.29
20 kW	12.2	12.8	9.3	14.9	11.8	17.5	15.6	13.45
23 kW	11.9	12.4	8.7	14.5	14.2	18.6	15.0	13.61
50 kW (E100)	13.6	10.5	7.4	9.2	10.0	17.9	13.5	11.73
66 kW (E100+WI)	15.8	12.6	8.7	9.6	11.4	20.8	15.8	13.55
Conv. Veh.	13.6	19.1	12.9	14.0	14.0	13.8	10.6	14.01

*Power Mode unable to recharge the battery during the cycle

Source: elaborated by the author.

TABLE 33 – AVERAGE AUTONOMY OBTAINED FOR EACH SIMULATION OF THE VOLVO XC60

Volvo XC60 - Average Fuel Consumption (km/l)								
Power Mode	**FTP-75**	**HWFET**	**US06**	**NEDC**	**WLTC**	**Intense Traffic**	**Low Traffic**	**Average**
05 kW	*13.4**	*30.4**	*30.5**	*13.3**	*18.3**	*13.2**	*8.2**	*18.2*
10 kW	10.0	*17.0**	*17.2**	10.5	12.8	10.3	8.7	12.4
15 kW	8.5	*11.8**	*11.9**	11.5	11.0	10.0	8.7	10.5
20 kW	10.7	9.6	*9.2**	10.8	10.8	11.2	9.0	10.2
26 kW	9.1	10.2	*7.1**	9.3	10.3	10.7	9.2	9.4
30 kW	8.8	9.8	6.2	8.7	9.8	10.8	9.3	9.1
37 kW	9.3	10.6	7.1	7.9	9.5	11.7	10.0	9.4
40 kW	10.5	11.3	6.5	8.2	9.6	12.2	10.1	9.8
50 kW (E100)	8.8	9.4	5.6	7.0	7.1	9.7	7.4	7.9
66 kW (E100+WI)	10.0	11.6	6.5	9.1	8.2	11.4	8.7	9.3

*Power Mode unable to recharge the battery during the cycle

Source: elaborated by the author.

From table 32, observe that the conventional vehicle obtained the highest autonomy of the HWFET and US06 cycles. On the other hand, the conventional vehicle also presented the lowest autonomy of the Intense Traffic and Low Traffic cycles.

In addition, notice that the prototype engine presented higher autonomy with the water injection (E100+WI) fuel strategy than without the water injection (E100). Moreover, the E100+WI fuel strategy presented better autonomies than the conventional vehicle in urban cycles, like the FTP-75, Intense Traffic, and Low Traffic.

Table 32 also shows that the Ford Fiesta with the prototype engine had higher autonomies for the FTP-75 than for the HWFET cycle, however, in table 33 the Volvo XC60 showed lower autonomies for the FTP-75 than for the HWFET.

Next, table 34 and 35 shows the percentage of time that the engine was on during each driving cycle, for the Ford Fiesta and Volvo XC60 respectively. Notice that there are no values of 100% this is because the HEV model began with the engine off and it was turned on when the vehicle starts moving.

It was noticed that, in general, the higher the Power Mode the less the engine is on; however, lower times with the engine on was not necessarily traduced in lower fuel consumptions. Moreover, the Intense Traffic cycle showed similar autonomy in all

Power Modes, and no clear influence of the engine power nor the time with the engine on was noted.

TABLE 34 – PERCENTAGE OF TIME THE ENGINE WAS ON THROUGHOUT EACH SIMULATION OF THE FORD FIESTA

Ford Fiesta - Percentage ICE remains on							
Power Mode	FTP-75	HWFET	US06	NEDC	WLTC Class 3	Low Traffic	Intense Traffic
02 kW	98.82%	99.60%	97.74%	98.94%	99.34%	99.61%	99.87%
04 kW	98.82%	99.60%	99.07%	98.94%	99.34%	99.74%	69.78%
06 kW	98.82%	99.60%	99.07%	98.81%	99.34%	69.05%	48.02%
10 kW	44.08%	99.60%	99.07%	48.02%	63.24%	37.71%	28.30%
13 kW	44.47%	99.60%	99.07%	41.27%	56.39%	36.02%	21.64%
16 kW	40.26%	99.60%	99.07%	36.24%	52.70%	34.33%	17.93%
20 kW	34.21%	71.09%	99.07%	28.17%	46.38%	22.50%	19.46%
23 kW	29.34%	65.52%	92.02%	25.40%	35.18%	18.47%	14.21%
50 kW (E100)	10.79%	31.56%	44.81%	16.67%	20.03%	8.19%	6.53%
66 kW (E100+WI)	8.42%	23.87%	34.44%	13.76%	15.81%	6.24%	5.12%

Source: elaborated by the author.

TABLE 35 – PERCENTAGE OF TIME THE ENGINE WAS ON THROUGHOUT EACH SIMULATION OF THE VOLVO XC60

Volvo XC60 - Percentage ICE remains on							
Power Mode	FTP-75	HWFET	US06	NEDC	WLTC Class 3	Low Traffic	Intense Traffic
05 kW	98.81%	99.47%	99.07%	98.94%	99.34%	99.87%	99.87%
10 kW	74.57%	99.60%	98.80%	70.50%	79.84%	69.83%	54.74%
15 kW	61.40%	99.60%	99.07%	45.50%	65.09%	50.33%	35.90%
20 kW	39.00%	94.82%	99.07%	38.10%	52.31%	35.37%	26.92%
26 kW	35.57%	70.78%	99.07%	34.52%	42.82%	31.34%	20.64%
30 kW	31.23%	64.01%	99.07%	32.41%	39.92%	25.23%	17.95%
37 kW	25.16%	49.67%	73.44%	30.03%	34.91%	19.51%	14.10%
40 kW	21.61%	45.15%	77.56%	26.85%	33.20%	18.08%	17.44%
50 kW (E100)	16.86%	35.33%	57.77%	20.63%	28.06%	14.56%	11.92%
66 kW (E100+WI)	13.44%	25.90%	45.15%	14.42%	21.87%	11.57%	9.10%

Source: elaborated by the author.

This chapter is further devided in three sections. First, the results of the Ford Fiesta will be detailed in section 4.1. Then, the results of the Volvo XC60 will be presented in section 4.2. Lastly, section 4.3 will shows the comparisons with the state of the art papers. In addition, the analysis of the results omitted the Power Modes that were unable to recharge the battery, thus, appendixes I to N presents the charging capacity analysis of all simulations. Both the 50 and 66 kW Power Modes of the prototype engine were able to recharge the battery in all simulations; thus, they are not shown in the charging capacity analysis.

4.1 FORD FIESTA SEDAN

This section details the results of the Ford Fiesta simulations, covering the conventional vehicle simulations, the eight Power Modes of the Sigma engine (see table 23) and the two Power Modes of the prototype engine (see table 26).

Figure 88 to 92 compare the autonomies obtained for each of the five standard driving cycles. The horizontal lines represents the autonomies declared by the manufacturers for the Toyota Prius and for the conventional Ford Fiesta flex-fuel, running with both gasoline and ethanol fuels (CORREIO BRAZILIENSE, [s.d.]; UNITED STATES ENVIRONMENTAL PROTECTION AGENCY, 2018).

FIGURE 88 – AVERAGE AUTONOMY OF THE FORD FIESTA THROUGH THE FTP-75 STANDARD DRIVING CYCLE

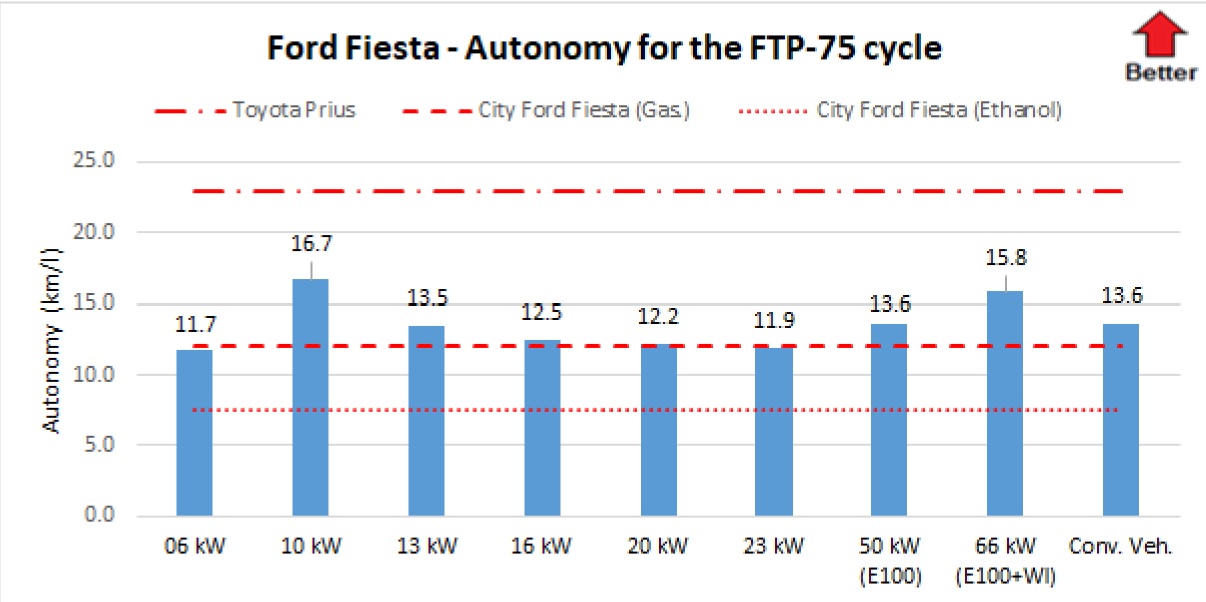

Source: elaborated by the author.

FIGURE 89 – AVERAGE AUTONOMY OF THE FORD FIESTA THROUGH THE HWFET STANDARD DRIVING CYCLE

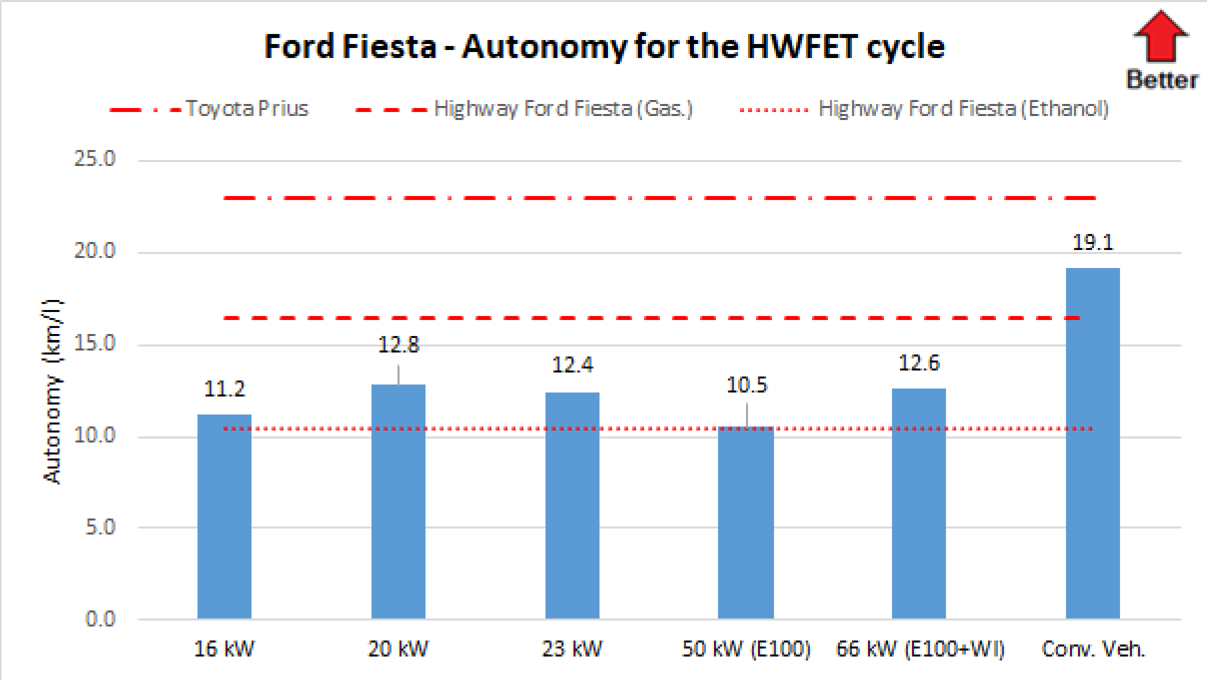

Source: elaborated by the author.

FIGURE 90 – AVERAGE AUTONOMY OF THE FORD FIESTA THROUGH THE US06 STANDARD DRIVING CYCLE

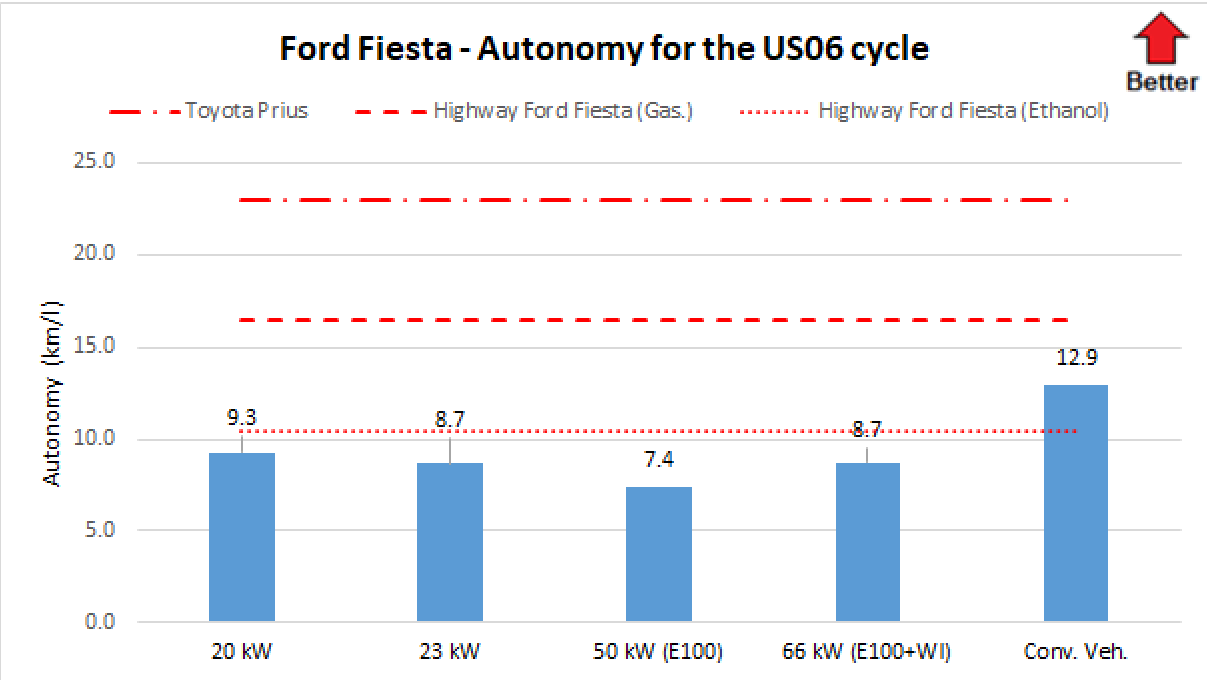

Source: elaborated by the author.

FIGURE 91 – AVERAGE AUTONOMY OF THE FORD FIESTA THROUGH THE NEDC STANDARD DRIVING CYCLE

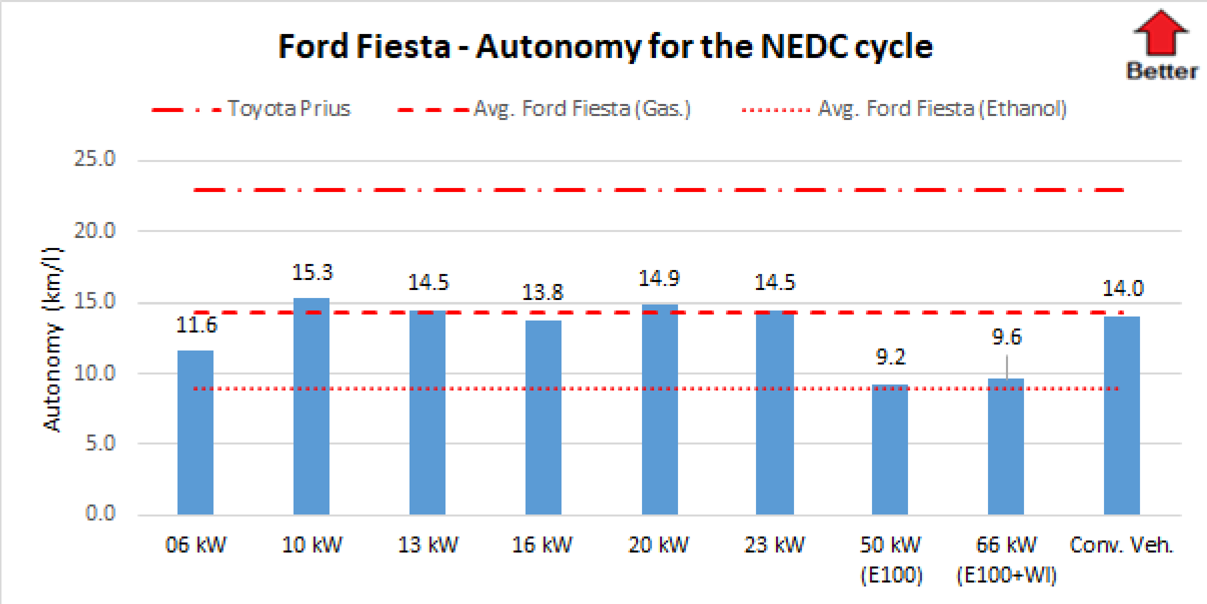

Source: elaborated by the author.

FIGURE 92 – AVERAGE AUTONOMY OF THE FORD FIESTA THROUGH THE WLTC CLASS 3 STANDARD DRIVING CYCLE

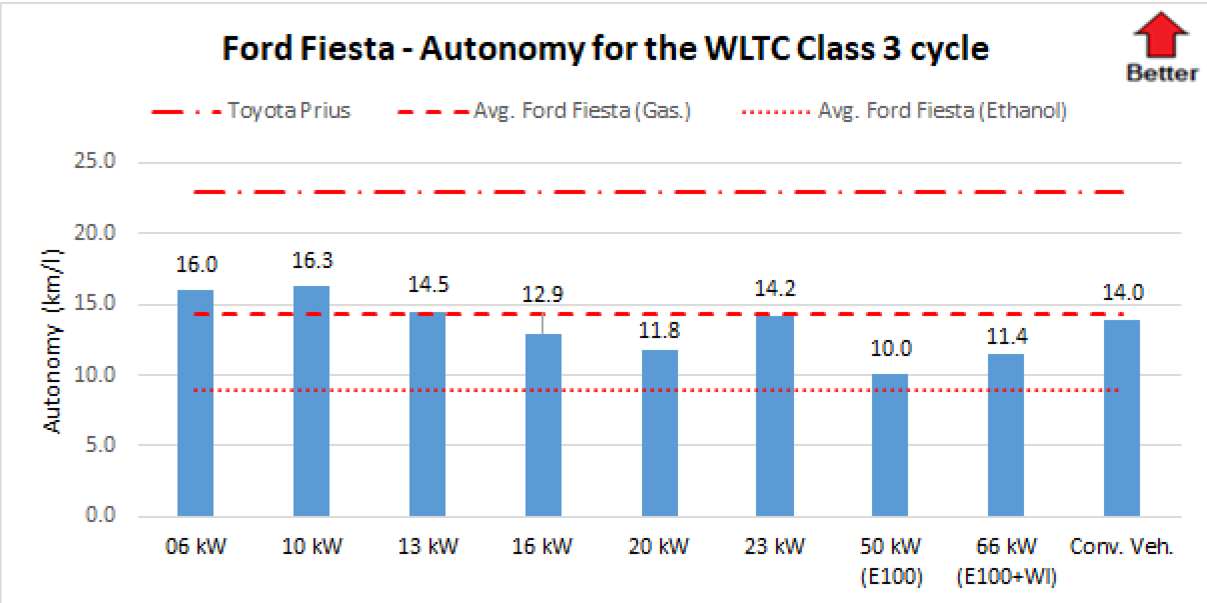

Source: elaborated by the author.

Notice that only in the US06 the Ford Fiesta HEV presented lower autonomies than the 10.4 km/l declared for the conventional Ford Fiesta flex-fuel running with ethanol in highway. For all 5 standard driving cycles, the Ford Fiesta HEV had an average autonomy of 12.5 km/l, which represents a 38.7% improvement over the average autonomy of 9 km/l declared by the manufacturer.

Moreover, during the FTP-75 cycle the Ford Fiesta HEV had an autonomy improvement of 11.5% when compared with the city autonomy of 12.1 km/l declared by the manufacturer for the conventional Ford Fiesta running with gasoline.

On the other hand, figure 93 compares both real driving cycles. Observe that the 16 kW mode was the only Power Mode that presented higher autonomy for the Low Traffic cycle than for the Intense Traffic cycle. Moreover, the WI strategy (66 kW mode) presented the lowest autonomy of the Low Traffic cycle. In addition, the conventional vehicle showed the lowest autonomy for both real driving cycles.

FIGURE 93 – COMPARISON OF AUTONOMIES OBTAINED FOR THE FORD FIESTA AT INTENSE AND LOW TRAFFIC DRIVING CYCLES

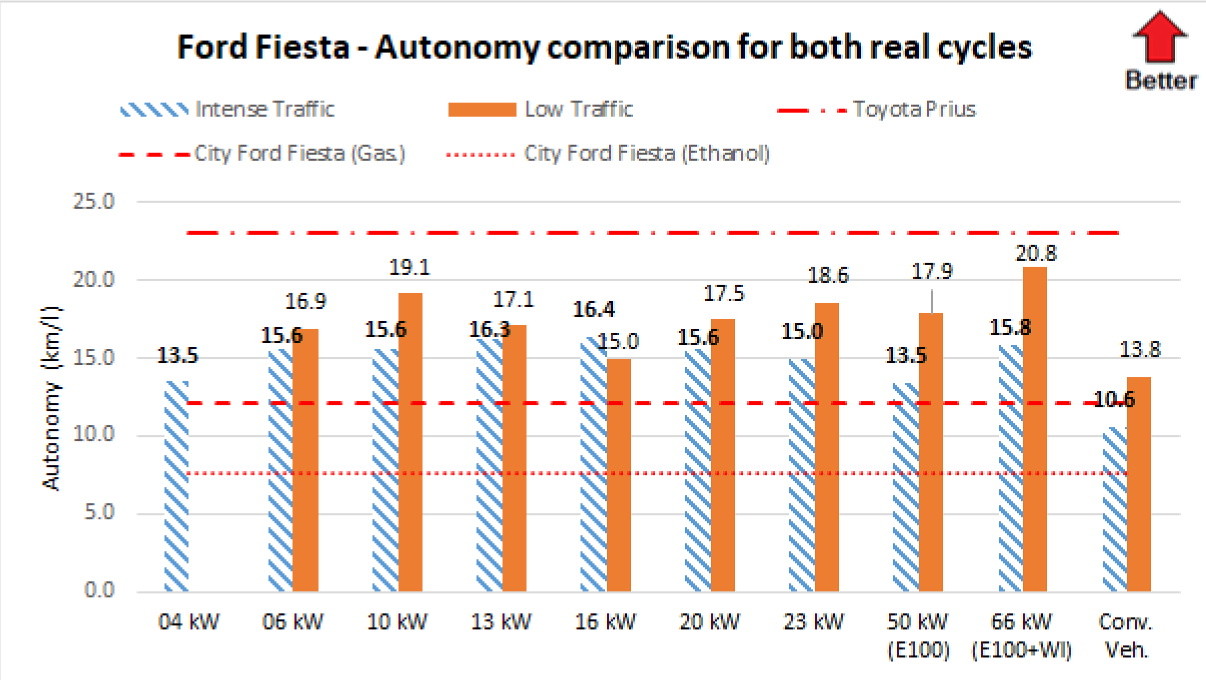

Source: elaborated by the author.

In the Intese Traffic cycle, the Ford Fiesta HEV obtained an average autonomy of 15.8 km/l. These means an improvement over the conventional vehicle simulation of 49.1%, and an improvement over the city autonomy declared by the manufacturer of 107.9% when running on ethanol, and of 30.6% when running on gasoline.

Moreover, for the Low Traffic cycle it was obtained an average autonomy of 20.8 km/l. These means an improvement over the conventional vehicle simulation of 50.7%, and an improvement over the city autonomy declared by the manufacturer of 173.7% when running on ethanol, and of 71.9% when running on gasoline.

Finally, figure 94 presents the average autonomy of each Power Mode, coonsidering all seven driving cycles. Observe that the 10 kW Power Mode obtained the best autonomy, with a 21.2% improvement over the conventional vehicle simulation. Nevertheless, this mode was unable to recharge the battery throughout the HWFET and US06 cycles. In addition, the WI strategy (66 kW) presented 15.4% higher autonomy than without the WI strategy (50 kW).

Figure 94 shows that

FIGURE 94 – AVERAGE AUTONOMY OF THE SEVEN DRIVING CYCLES FOR EACH POWER MODE OF THE FORD FIESTA

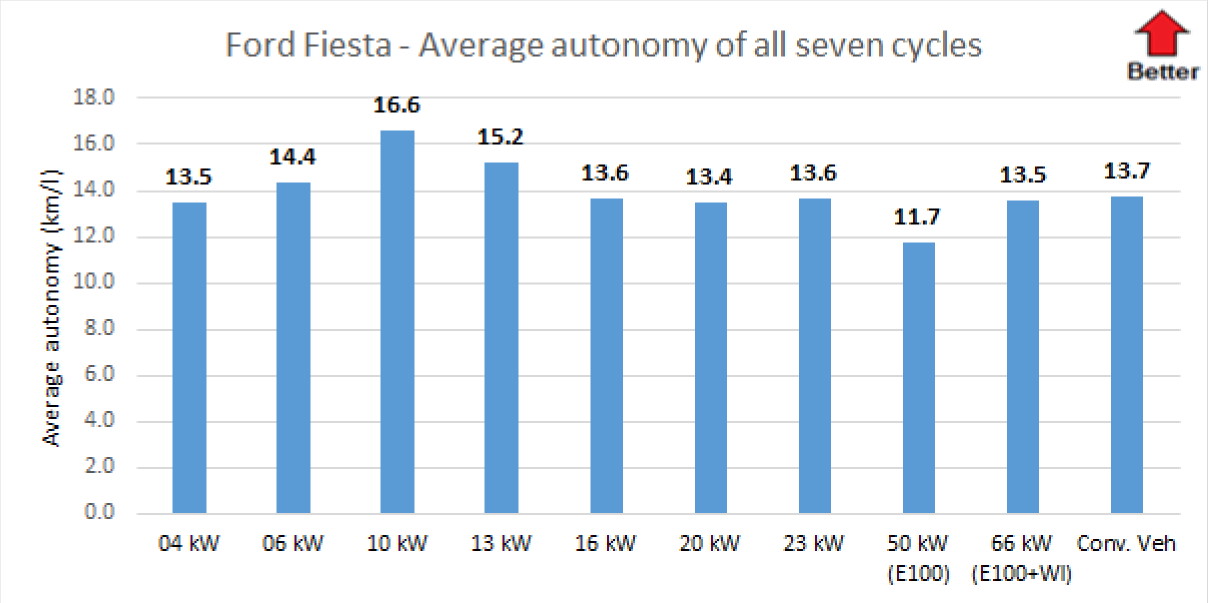

Source: elaborated by the author.

4.2 VOLVO XC60 HYBRID

This section details the results of the Volvo XC60 simulations, covering the eight Power Modes of the Sigma engine (see table 25) and the two Power Modes of the prototype engine (see table 26).

Figure 95 to 99 compare the average autonomies of each Power Mode for each of the five standard driving cycles, and figure 100 compares the autonomies of both real driving cycles. In these figures the horizontal lines represents the autonomies declared by the manufacturers of the Toyota Prius and of the Volvo XC60 (UNITED STATES ENVIRONMENTAL PROTECTION AGENCY, 2018; VOLVO GROUP, 2018a).

FIGURE 95 – AVERAGE AUTONOMY OF THE VOLVO XC60 THROUGH THE FTP-75 STANDARD DRIVING CYCLE

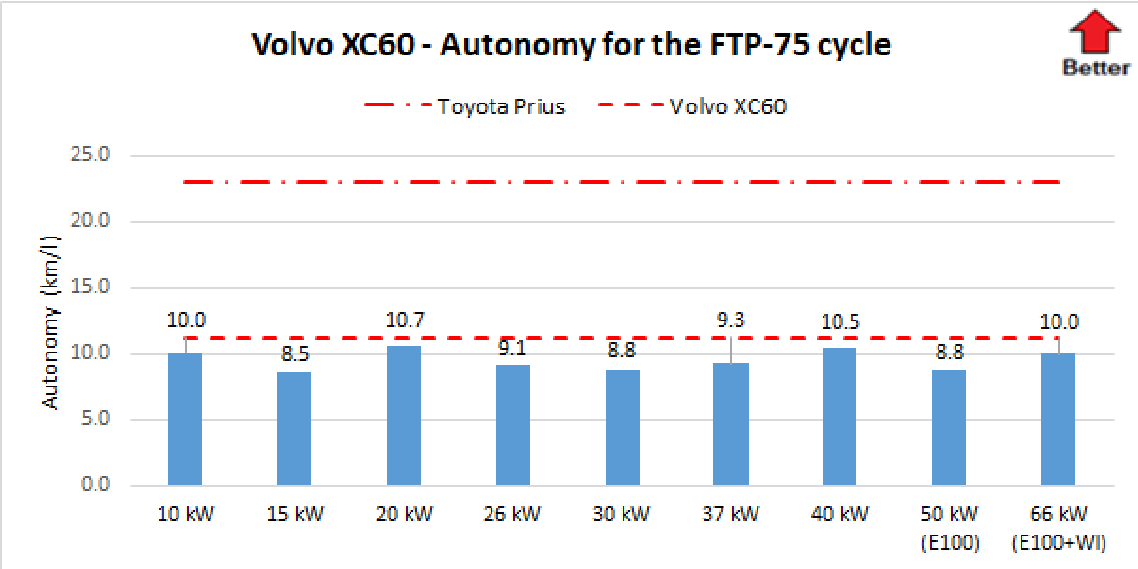

Source: elaborated by the author.

FIGURE 96 – AVERAGE AUTONOMY OF THE VOLVO XC60 THROUGH THE HWFET STANDARD DRIVING CYCLE

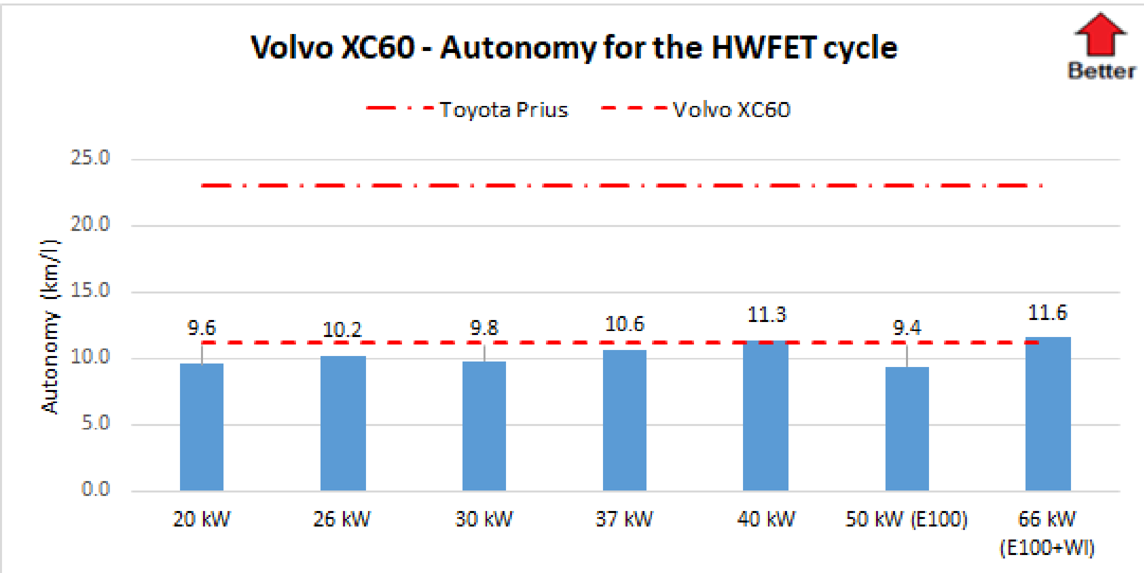

Source: elaborated by the author.

FIGURE 97 – AVERAGE AUTONOMY OF THE VOLVO XC60 THROUGH THE US06 STANDARD DRIVING CYCLE

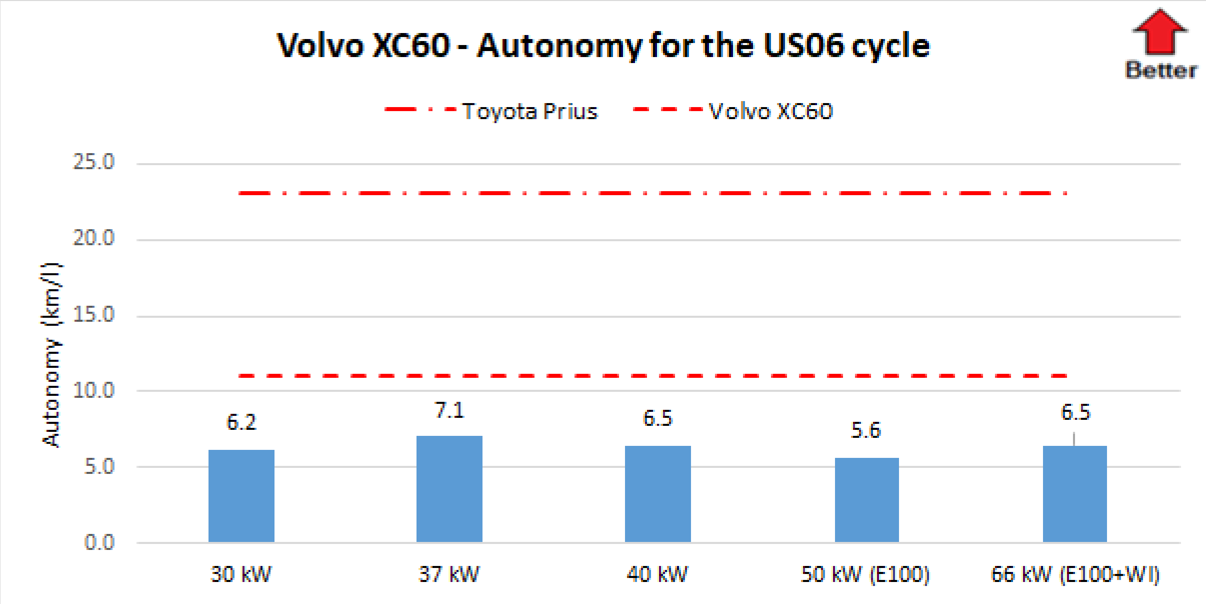

Source: elaborated by the author.

FIGURE 98 – AVERAGE AUTONOMY OF THE VOLVO XC60 THROUGH THE NEDC STANDARD DRIVING CYCLE

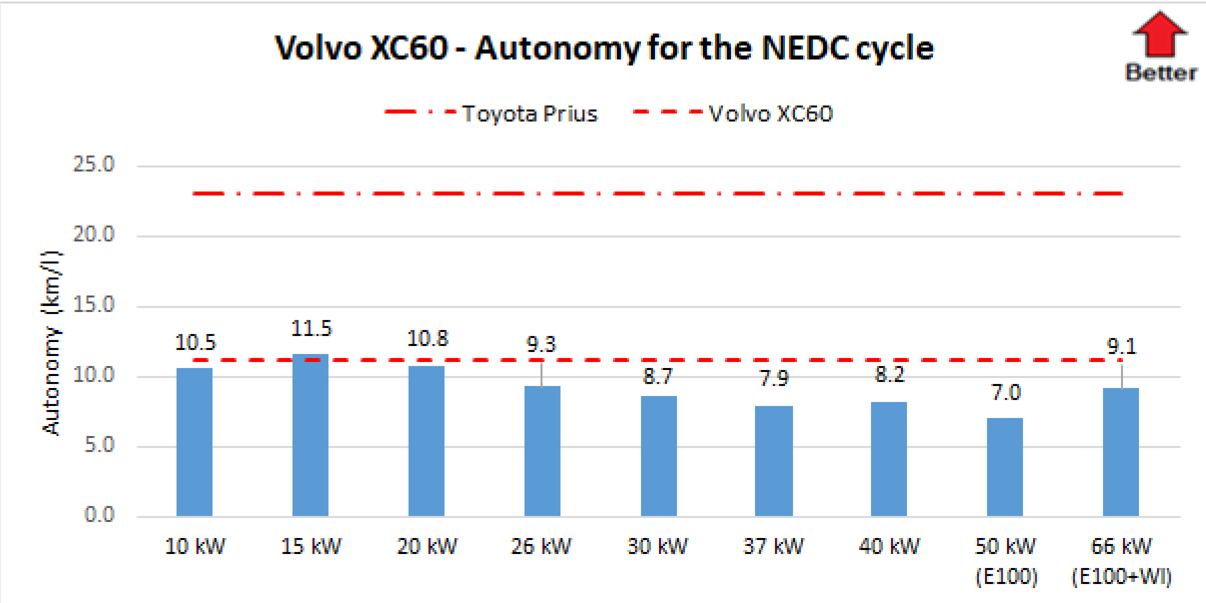

Source: elaborated by the author.

FIGURE 99 – AVERAGE AUTONOMY OF THE VOLVO XC60 THROUGH THE WLTC CLASS 3 STANDARD DRIVING CYCLE

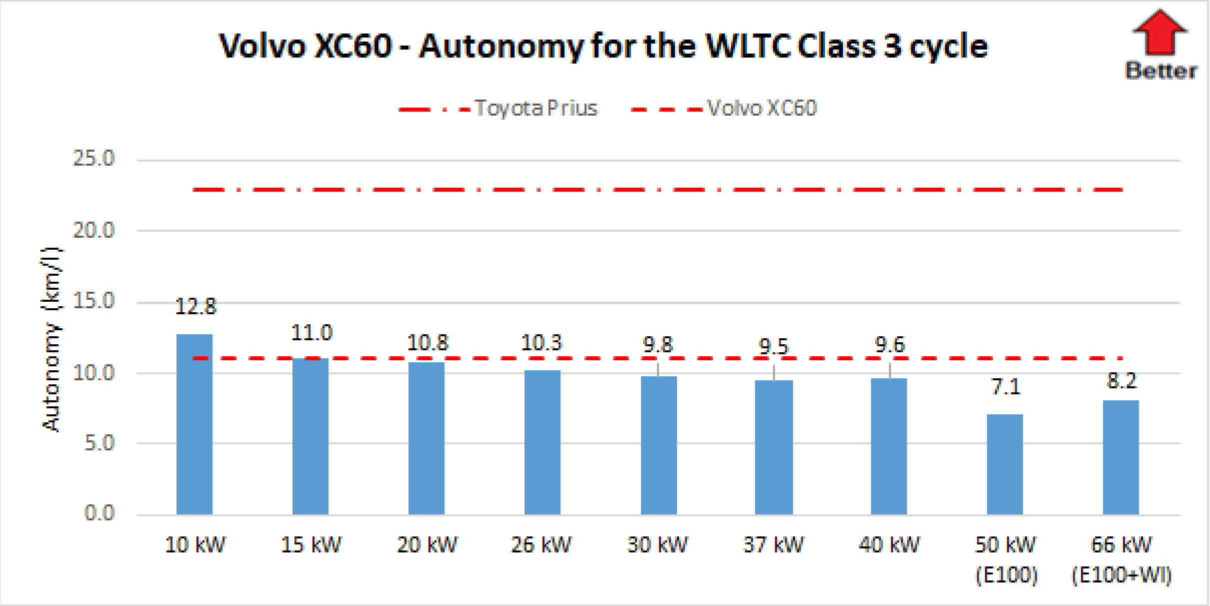

Source: elaborated by the author.

FIGURE 100 – COMPARISON OF AUTONOMIES OBTAINED FOR THE VOLVO XC60 AT INTENSE AND LOW TRAFFIC DRIVING CYCLES

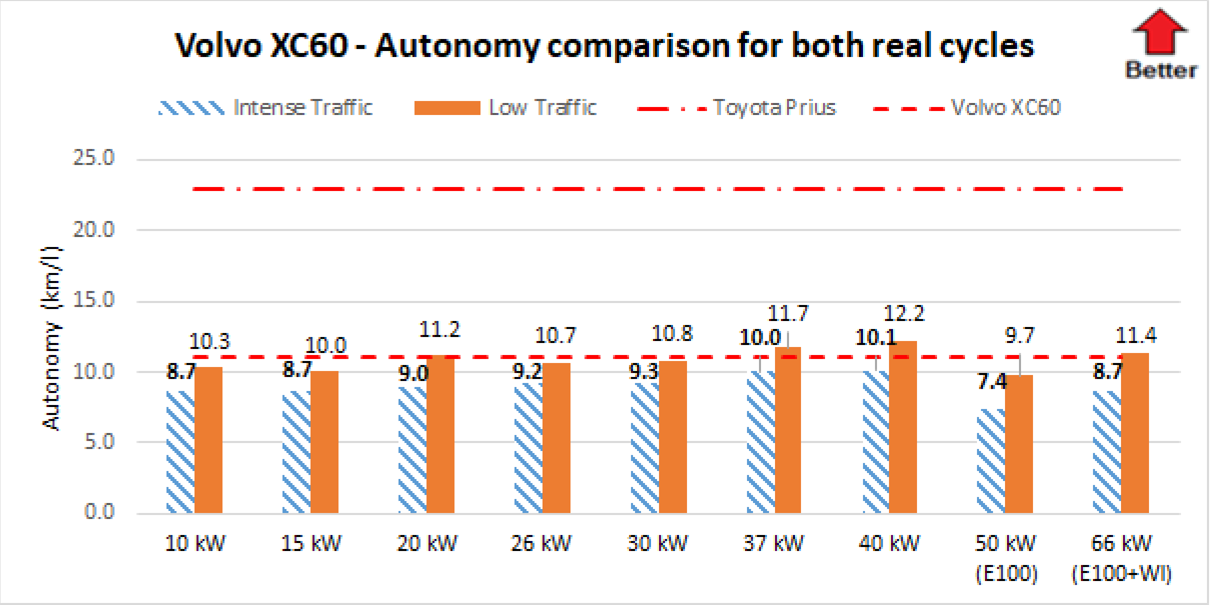

Source: elaborated by the author.

For the Volvo XC60 simulated, the Low Traffic cycle was the one with the highest average autonomy of 10.9 km/l, followed by the HWFET cycle with 10.36 km/l.

Nevertheless, these are still lower than the autonomy reported by the manufacturer, which was 11.1 km/l.

Figure 101 shows average autonomy obtained for all seven driving cycles, and for each Power Mode. Notice that the 10 kW Power Mode obtained the highest autonomy, although this mode was unable to recharge the battery during the NEDC and US06 cycles. Similar to the Ford Fiesta, the Volvo XC60 presented 19% higher autonomy for the WI strategy (66 kW), when compared to no WI strategy (55kW).

FIGURE 101 – AVERAGE AUTONOMY OF THE SEVEN DRIVING CYCLES FOR EACH POWER MODE OF THE VOLVO XC60

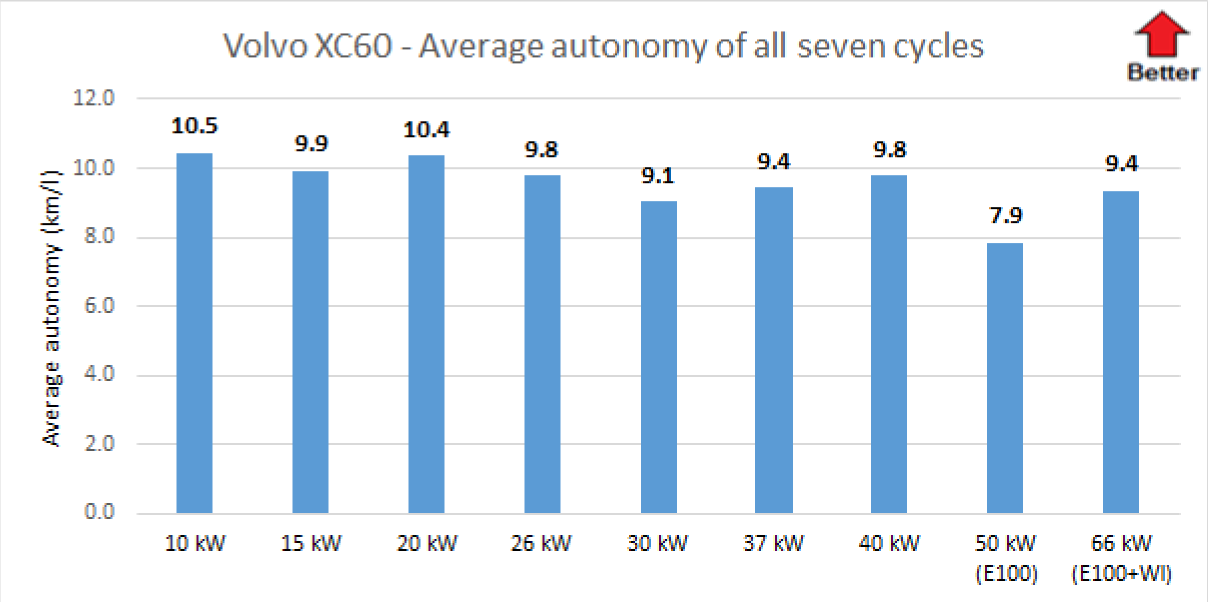

Source: elaborated by the author.

In addition, figure 102 to 105 compares the autonomy of both vehicles for the 10, 20, 50, and 66 kW Power Modes. Three cases presented the same autonomies for both vehicles, these cases are the 10 kW mode in the HWFET and the US06 cycles, and the 20 kW mode in the US06 cycle. This is attributed to both vehicles operate the engines at the same point and during the same time length. This also explains the lower autonomies of the Volvo XC60, when comparing the same cycle, since it operated the engine for longer time lengths.

FIGURE 102 – AUTONOMY COMPARISON OF THE 10 KW POWER MODE BETWEEN BOTH VEHICLES

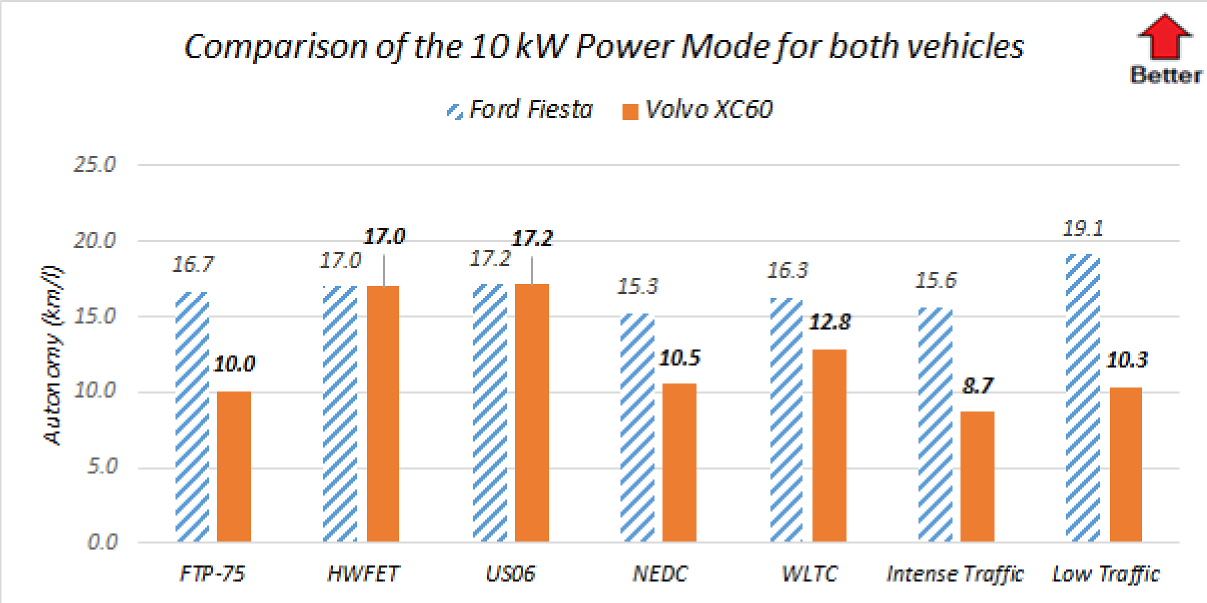

Source: elaborated by the author.

FIGURE 103 – AUTONOMY COMPARISON OF THE 20 KW POWER MODE BETWEEN BOTH VEHICLES

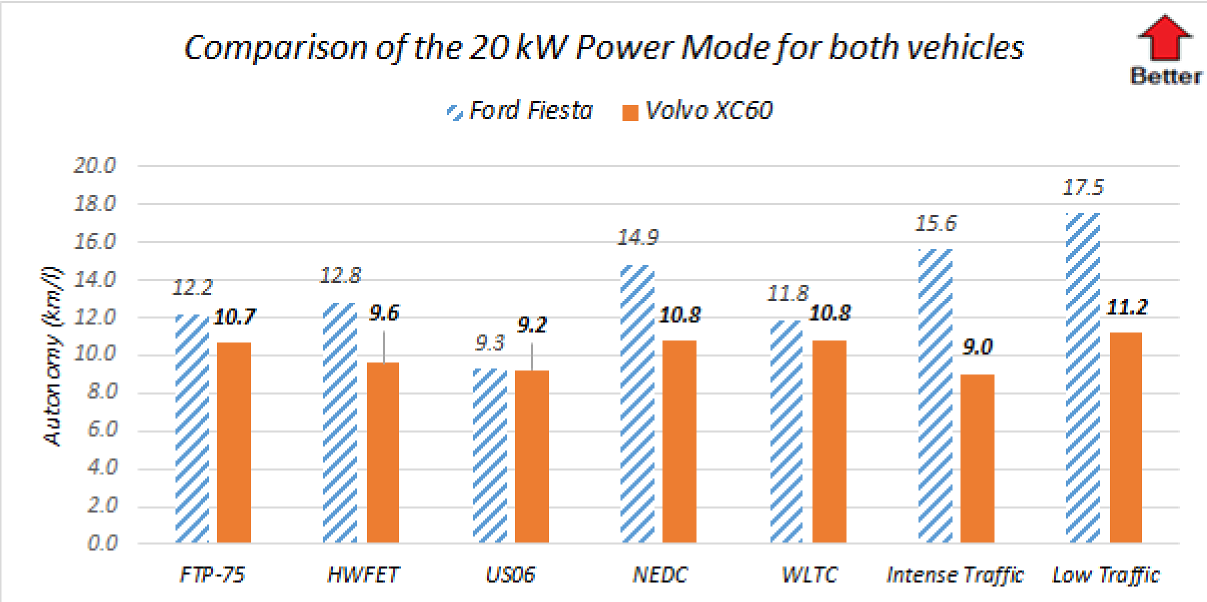

Source: elaborated by the author.

FIGURE 104 – AUTONOMY COMPARISON OF THE 50 KW POWER MODE BETWEEN BOTH VEHICLES

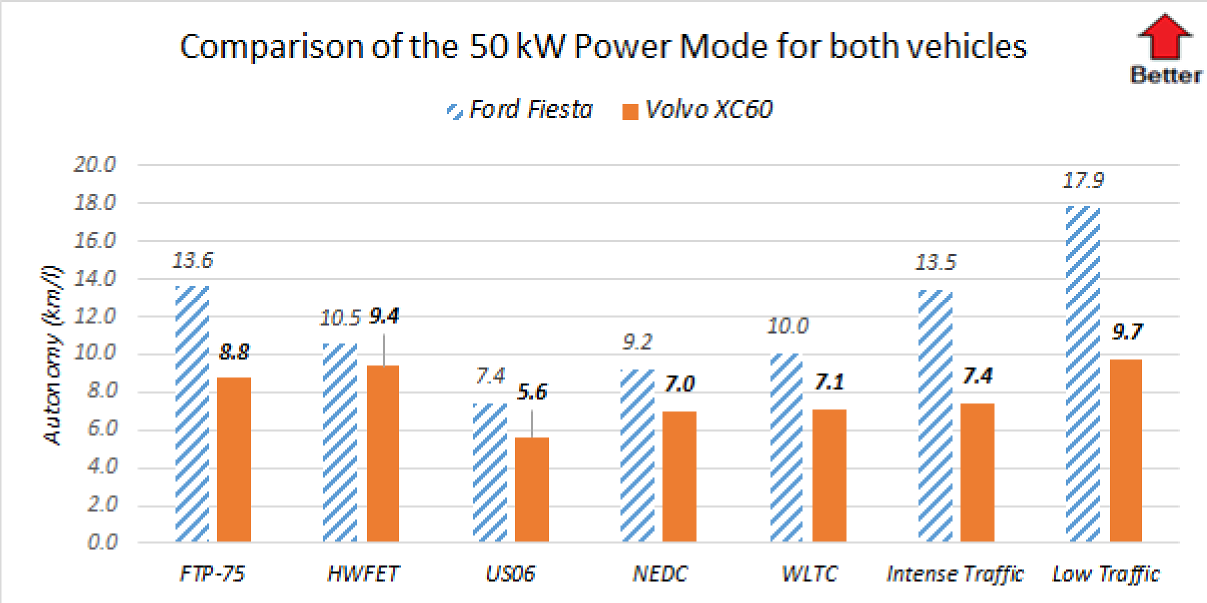

Source: elaborated by the author.

FIGURE 105 – AUTONOMY COMPARISON OF THE 66 KW POWER MODE (WI STRATEGY) BETWEEN BOTH VEHICLES

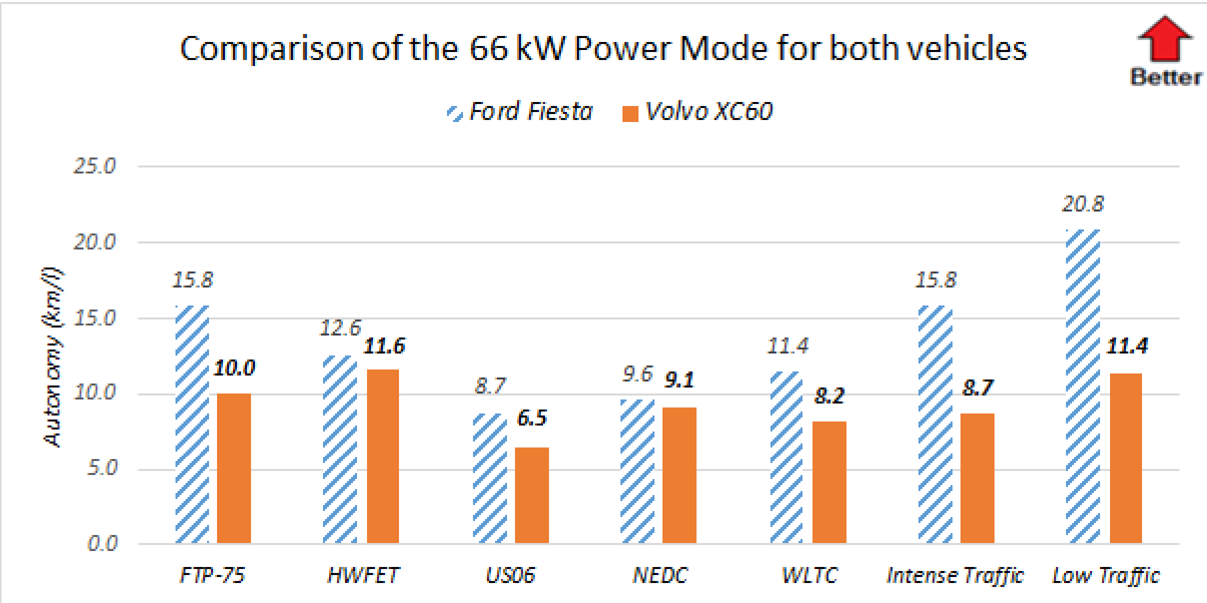

Source: elaborated by the author.

From figure 104 and 105, the Volvo XC60 shown higher autonomies for the HWFET than for the FTP-75, showing the opposite trend of the Ford Fiesta. This is attributed to the different motor gear ratio. As seen in figure 106, during the HWFET cycle the motor of the Volvo XC60 operated at higher efficiencies than the Ford Fiesta. This reduced the power demanded by the motor throughout the cycle, hence, reducing the discharge rate of the battery.

FIGURE 106 – COMPARISON OF MOTOR EFFICIENCY BETWEEN BOTH VEHICLES, AT 50 KW POWER MODE

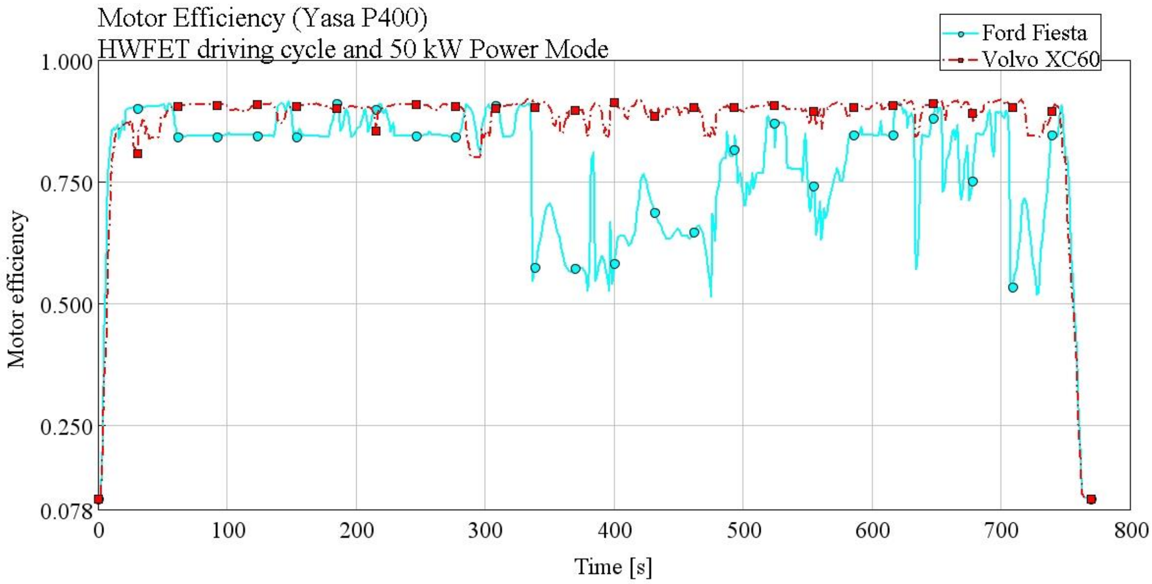

Source: elaborated by the author.

4.3 STATE OF THE ART COMPARISON

This section compares the series HEV model results with the ones found by Al-Samari (2017), Asfoor, Sharaf, and Beyerlein (2014), Solouk et al. (2017), and Williamson, Lukic, and Emadi (2006). Thus, the vehicle characteristics mentioned in each paper were used in the series HEV model. Section 3.6.3 details these vehicle characteristics, while table A8 in the appendix H details the vehicle in which is based on, the driving cycles and the Power Modes used for each simulation. In addition, a previous description of the four papers can be found in the state of the art (section 2.5).

In addition, the battery maps were kept the same, moreover, the engine and generator maps correspond to their respective Power Modes and vehicles as shown in tables 23, 25, and 26.

Figures 107 to 110 show the autonomies found for thesimulations based on Asfoor, Sharaf, and Beyerlein (2014).

FIGURE 107 – RESULTS OF SIMULATIONS BASED ON ASFOOR, SHARAF, AND BEYERLEIN (2014), FOR FTP-75 CYCLE

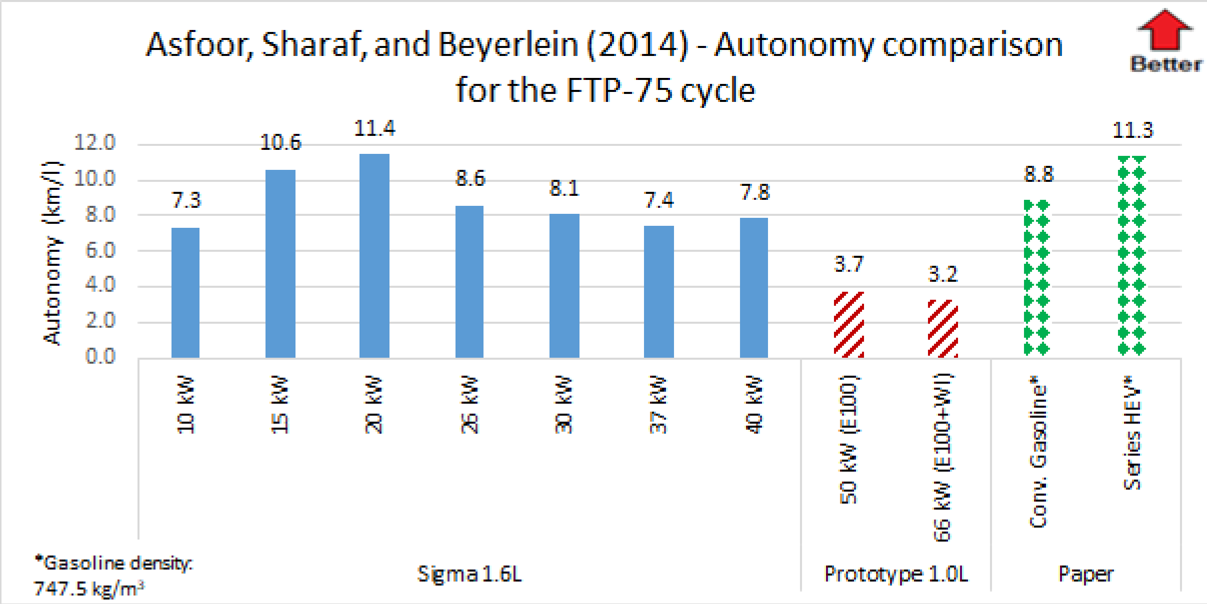

Source: elaborated by the author.

FIGURE 108 – FUEL CONSUMPTION RESULTS OF SIMULATIONS BASED ON ASFOOR, SHARAF, AND BEYERLEIN (2014), FOR HWFET CYCLE

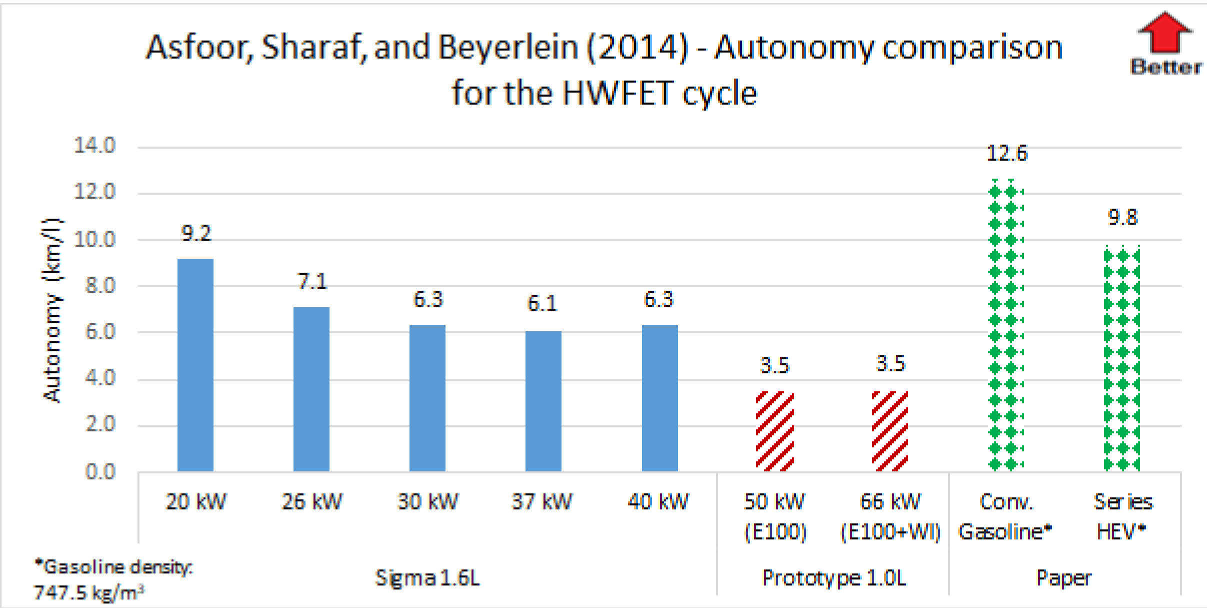

Source: elaborated by the author.

FIGURE 109 – FUEL CONSUMPTION RESULTS OF SIMULATIONS BASED ON ASFOOR, SHARAF, AND BEYERLEIN (2014), FOR US06 CYCLE

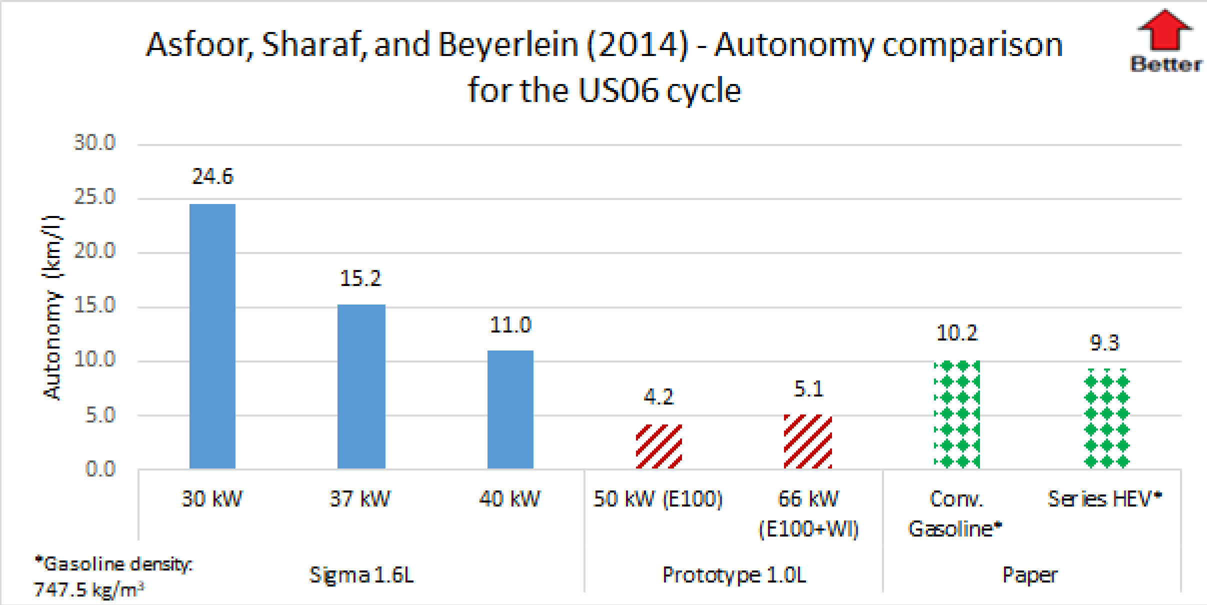

Source: elaborated by the author.

FIGURE 110 – FUEL CONSUMPTION RESULTS OF SIMULATIONS BASED ON ASFOOR, SHARAF, AND BEYERLEIN (2014), FOR NEDC

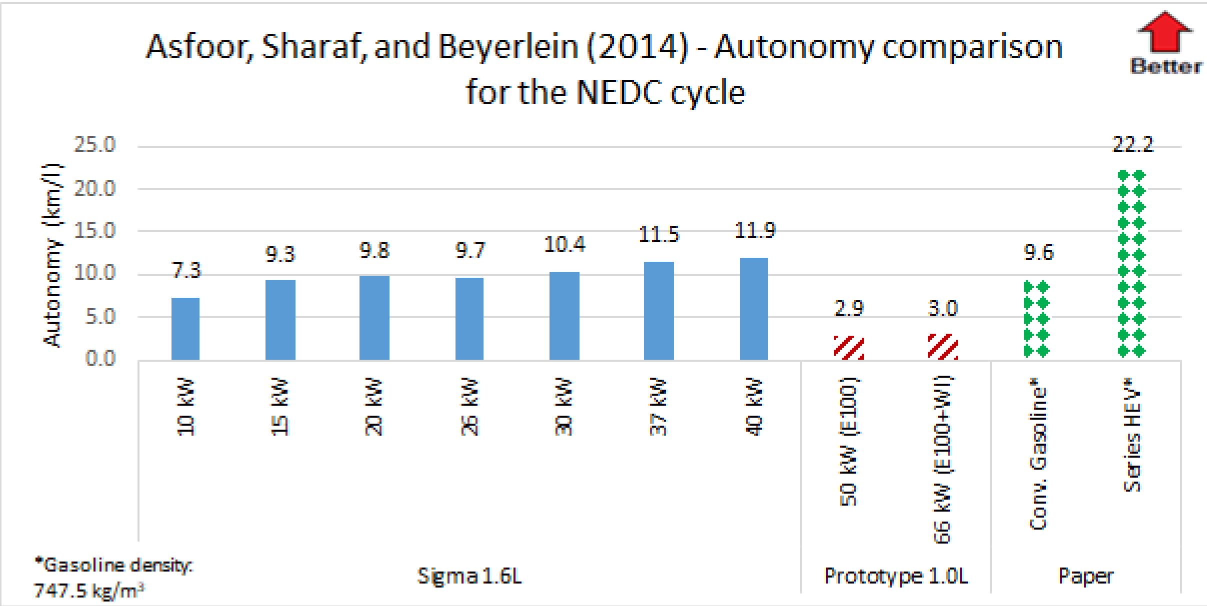

Source: elaborated by the author.

Notice that the FTP-75, US06 , and NEDC cycles presented higher autonomies than the conventional vehicle with gasoline engine simulated in the paper. Nonetheless, these simulations presented a poor vehicle performance and a high dependency on the power delivered by the engine. This can be seen in figure 111, which shows the battery SOC, the target speed and the actual speed of the vehicle.

FIGURE 111 – PERFORMANCE ANALYSIS FOR THE 50 KW POWER MODE FOR ASFOOR, SHARAF, AND BEYERLEIN (2014), FOR US06 CYCLE

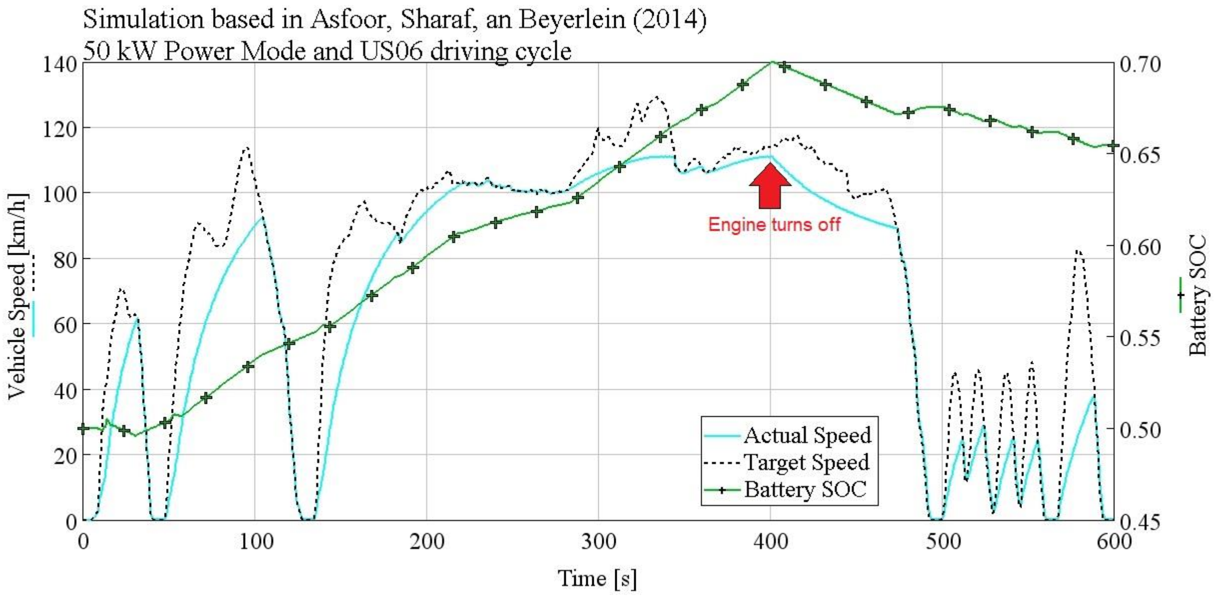

Source: elaborated by the author.

Observe that the actual speed falls at the moment the battery is fully charged and the engine is turned off. This engine dependency and bad performance could be due to the lower voltage and current limits of the battery used in Asfoor, Sharaf, and Beyerlein (2014). Since series HEV have the power of their motors limited by the ICE-Generator ensemble (JEAN-MARC ALLENBACH, 2005), then, vehicles without a battery or with low battery assistance had an increased dependency on the engine to supply the additional power needed. This could result in turning on the engine to maintain a good vehicle performance at high powers and, consequently, in the need of more complex engine controls.

Next, figures 112 to 114 compares the simulation results with the ones obtained by Solouk et al. (2017), which studied the use of HCCI and RCCI engines for EREV. In this case, the model developed only presented autonomy improvements for the UDDS cycle. In this cycle, the 66 kW Power Mode presented 24.8% higher autonomy than the EREV HCCI, while the 6 kW mode presented the second highest autonomy with 7.9% improvement over the EREV HCCI.

FIGURE 112 – FUEL CONSUMPTION RESULTS OF SIMULATIONS BASED ON SOLOUK ET AL. (2017), FOR HWFET CYCLE

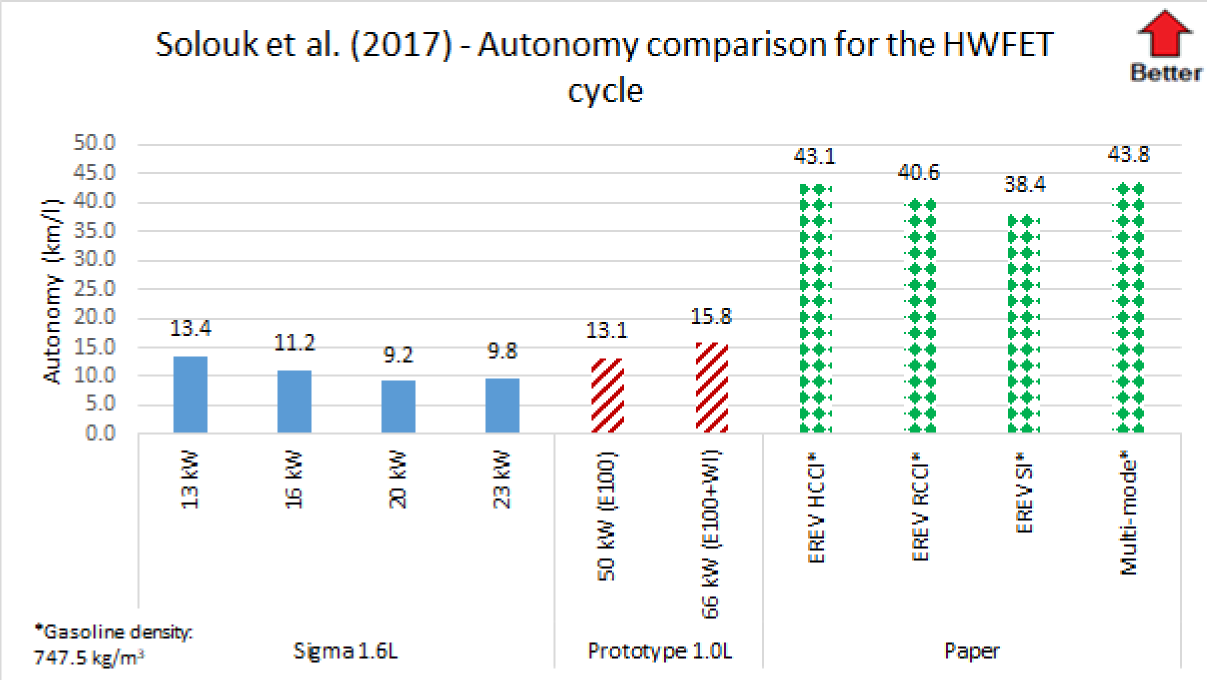

Source: elaborated by the author.

FIGURE 113 – FUEL CONSUMPTION RESULTS OF SIMULATIONS BASED ON SOLOUK ET AL. (2017), FOR US06 CYCLE

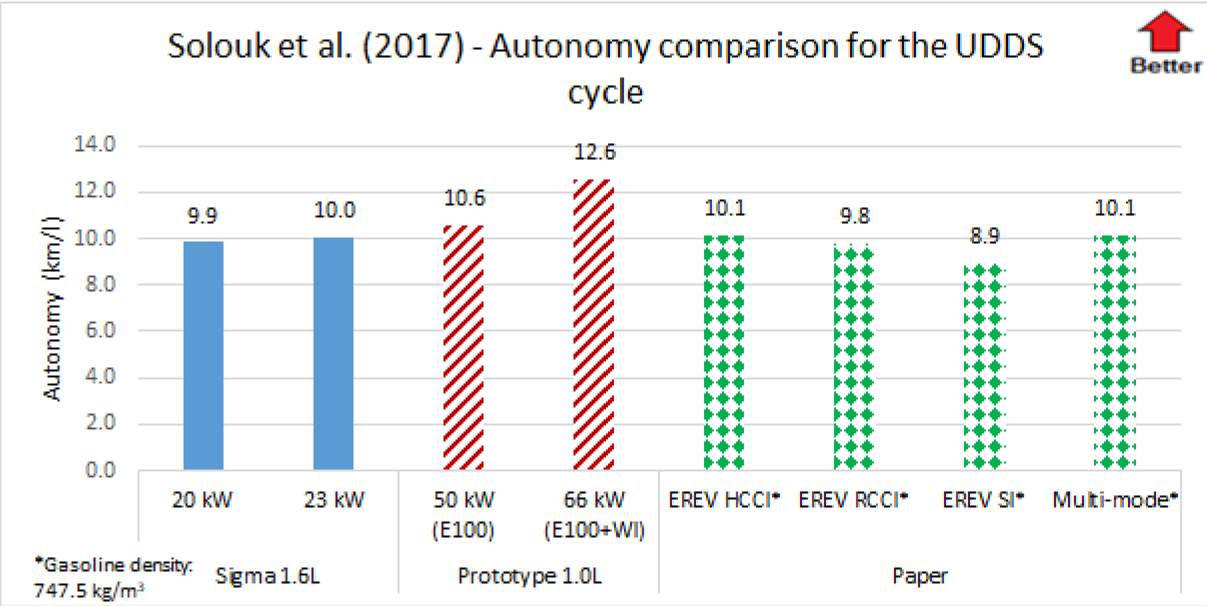

Source: elaborated by the author.

FIGURE 114 – FUEL CONSUMPTION RESULTS OF SIMULATIONS BASED ON SOLOUK ET AL. (2017), FOR UDDS CYCLE

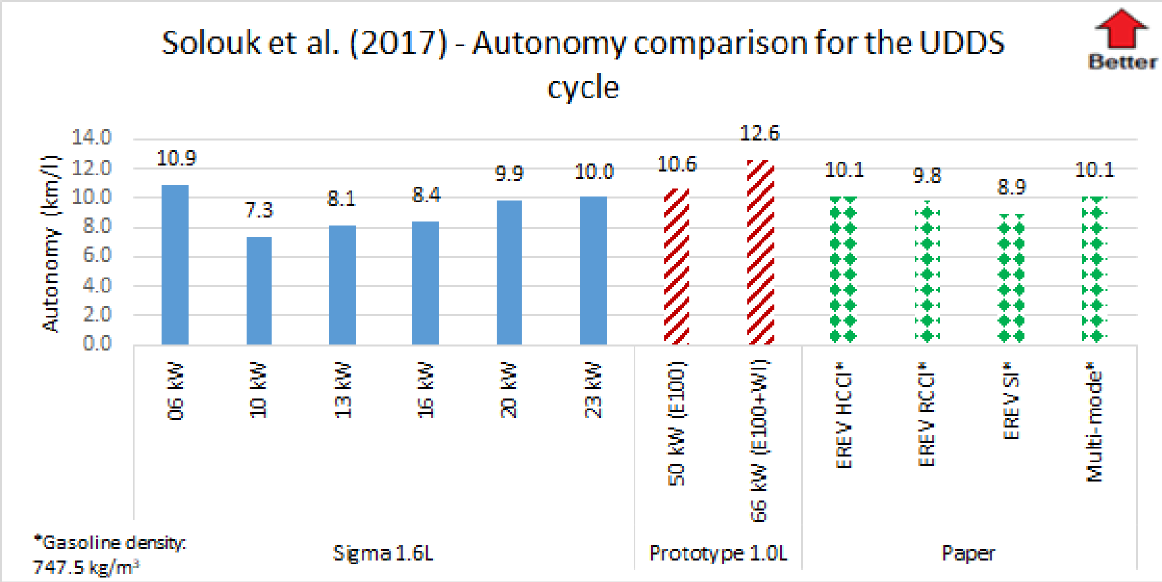

Source: elaborated by the author.

Next, figures 115 and 116 present the results of the simulations based on Williamson, Lukic, and Emadi (2006), which simulated two parallel HEVs: one with a gasoline engine and the other with a diesel engine.

FIGURE 115 – FUEL CONSUMPTION RESULTS OF SIMULATIONS BASED ON WILLIAMSON, LUKIC, AND EMADI (2006), FOR HWFET CYCLE

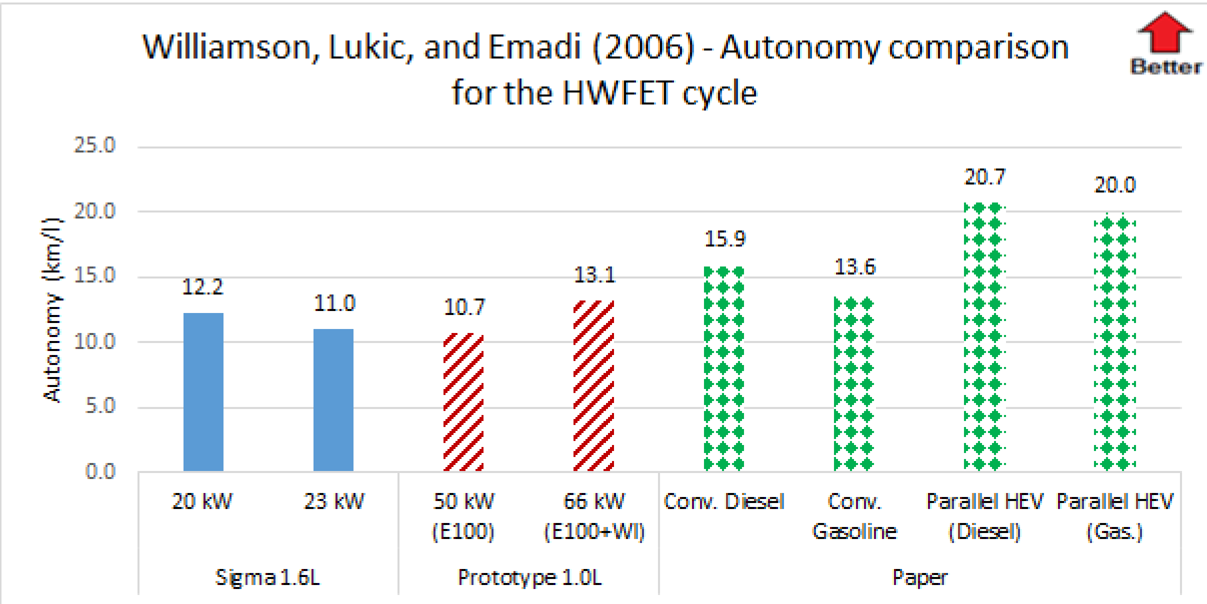

Source: elaborated by the author.

FIGURE 116 – FUEL CONSUMPTION RESULTS OF SIMULATIONS BASED ON WILLIAMSON, LUKIC, AND EMADI (2006), FOR UDDS CYCLE

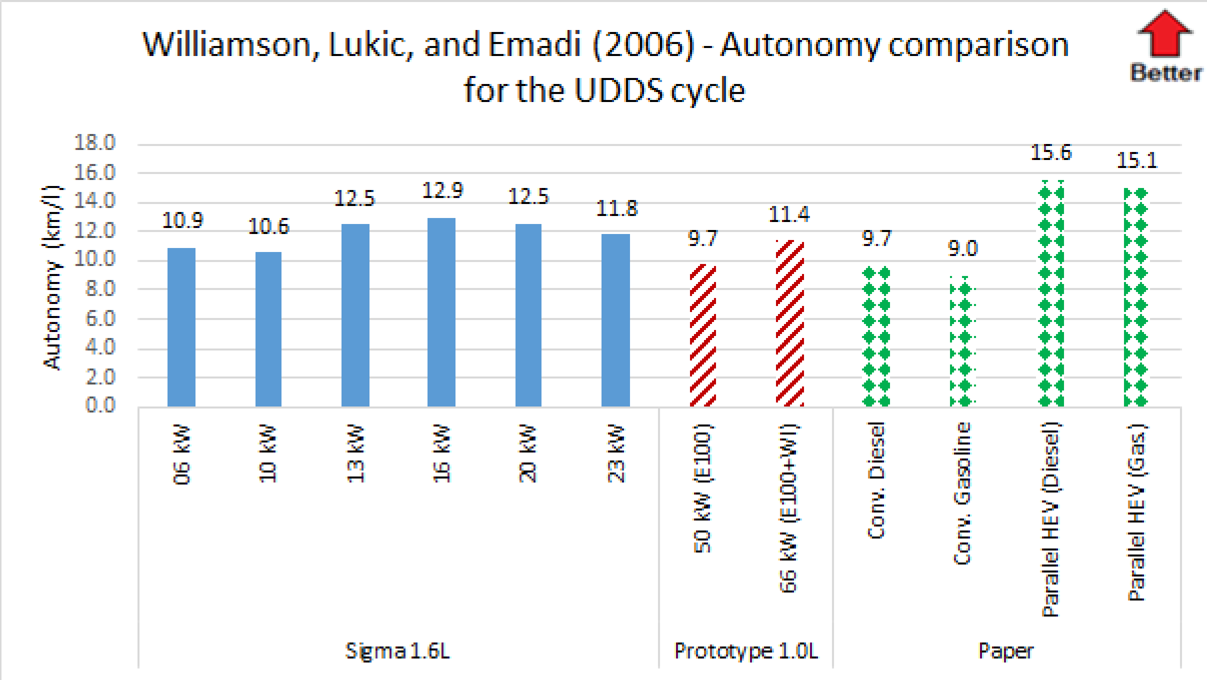

Source: elaborated by the author.

It can be seen that during highway operation both conventional vehicles presented better fuel economies than our series HEV modeled. On the other hand, during urban operation the series HEV presented up to 43.3% higher autonomy than the conventional gasoline and up to 33% higher than the conventional diesel. Although, the parallel HEVs simulated by Williamson, Lukic, and Emadi (2006) presented better autonomies than the series HEV simulations.

Finally, figure 116 shows the fuel consumption results of the simulations based on Al-Samari (2017), which simulated a parallel HEV in the Autonomie software. Observe that from all the Power Modes the 20 kW mode showed the best results, obtaining up to 32.8% higher autonomy than the conventional gasoline.

FIGURE 117 – AUTONOMY RESULTS OF SIMULATIONS BASED ON AL-SAMARI (2017), FOR UDDS CYCLE

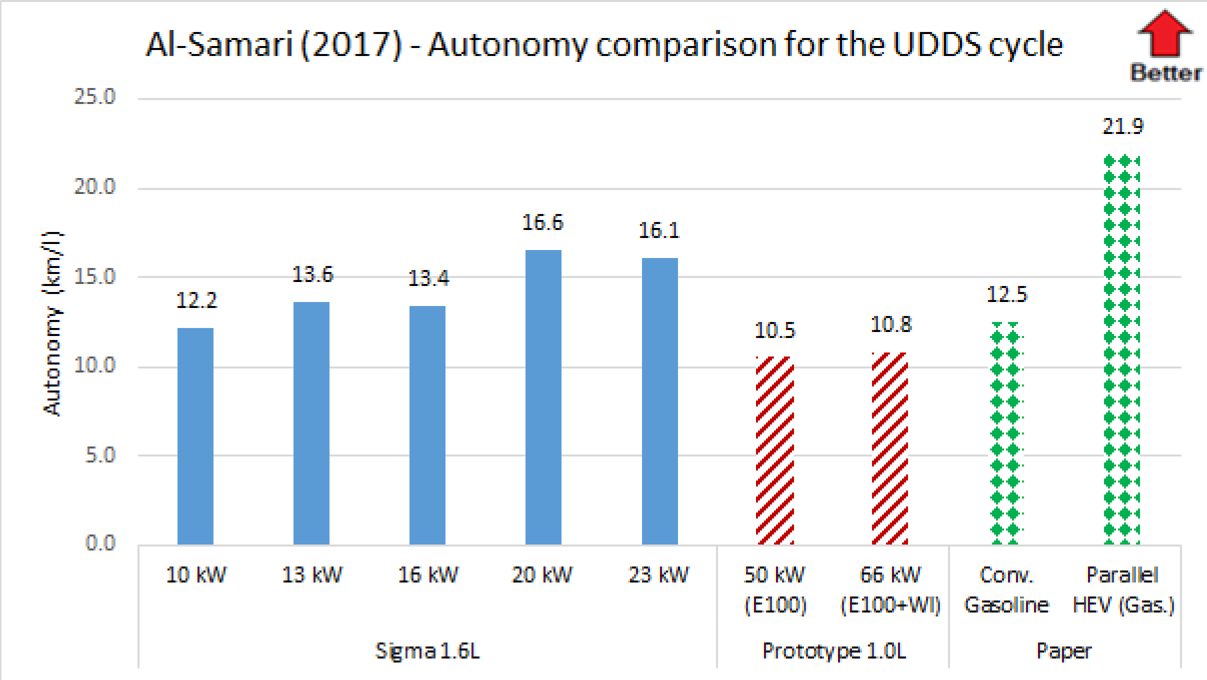

Source: elaborated by the author.

5 CONCLUSIONS

Essentially, the series HEV model showed better fuel economies in urban driving, like in the FTP-75, Intense Traffic, and Low Traffic cycles. Nevertheless, Volvo XC60 presented higher autonomies for the HWFET than for the FTP-75 cycle. This was attributed to the higher gear ratio of the Volvo XC60, whic allowed the motor to operate at higher efficiencies in highway speeds; therefore, reducing the power demand of the motor, which in consequence aids the recharge of the battery. This demonstrates the critical importance of utilize the transmission to operate the motor at the highest efficiencies, which could be addressed with the Hybrid Synergy Drive that operates as a continuous variable transmission.

Additionally, the state of the art comparison showed that, in general, the series HEV model could have lower fuel consumptions than conventional vehicles while in urban driving, like in FTP-75 and UDDS driving cycles. Contrarily, the conventional vehicles presented better fuel economies in highway driving (HWFET cycle).

This agrees with Asfoor, Sharaf, and Beyerlein (2014), which indicated that best fuel consumptions of series HEVs are in the FTP-75 cycle. While Al-Samari (2017) showed that HEVs have high fuel consumption improvements when in urban real-world driving cycles. On the other hand, Williamson, Lukic, and Emadi (2006) indicated that conventional vehicles have their best fuel consumption in the HWFET cycle. This was attributed to the ICE operating in regions of higher efficiency when at high speeds.

Moreover, the results of this work suggest that using E100 fuel in HEV's engines can present lower fuel consumptions than conventional vehicles, especially during urban driving conditions; thus, it is concluded that the fuel consumption of the HEV mainly depends on the engine's operation point and its control strategy.

In addition, the water injection fuel strategy of the prototype engine resulted in better fuel consumption than the EREV with the HCCI engine, for the UDDS cycle. This means that HEVs designed for urban driving conditions (for example: taxis, buses, delivery trucks, etc.) could be more benefited from using hydrated ethanol with water injection engines than from using HCCI engines. Remembering that HCCI technology is still in development, while the technology for water injection is already available.

Recommended future works could be to compare a flex-fuel engine and a pure ethanol engine. This was not possible due to the engines operating points being at different powers.

In addition, the propulsion motor control of the model could be improved. In our model, the maximum power of the motor is established as the peak power, instead of the continuous power. A better control design would limit the motor to continuous power, but allow it to deliver higher powers for short periods of time when needed.

It also could be done an study which compare the CO_2 emission benefits from utilizing pure ethanol engines in HEVs against other types of engines, like for example gasoline engines, diesel engines, HCCI engines, lean combustion engines, etc.

Finally, it could by studied the cold start operation since it is more critical than in conventional vehicles due to the intermittent operation of the engine in HEVs (ENOSHITA, 2018; RIBEIRO, 2018). Moreover, the ethanol presents starting problems in temepratures below 10°C due to its low volatility. Thus, heating devices and technologies should be needed for countries with colder climates than Brazil.

REFERENCES

AL-SAMARI, A. Study of emissions and fuel economy for parallel hybrid versus conventional vehicles on real world and standard driving cycles. **Alexandria Engineering Journal**, v. 56, n. 4, p. 721–726, 2017.

ANDWARI, A. M. et al. A review of Battery Electric Vehicle technology and readiness levels. **Renewable and sustainable energy review**, v. 78, p. 414–430, 2017.

ARATA, M. et al. EV and HEV motor development in TOSHIBA. **2014 International Power Electronics Conference, IPEC-Hiroshima - ECCE Asia 2014**, v. 4, n. 3, p. 1874–1879, 2014.

ASFOOR, M. S.; SHARAF, A. M.; BEYERLEIN, S. **USE OF GT-SUITE TO STUDY PERFORMANCE DIFFERENCES BETWEEN INTERNAL COMBUSTION ENGINE (ICE) AND HYBRID ELECTRIC VEHICLE (HEV) POWERTRAINS**. 16th International Conference on Aplplied Mechanics and Mechanical Engineering. **Anais**...Cairo, Egypt: 2014

ASSOCIAÇÃO NACIONAL DOS FABRICANTES DE VEÍCULOS AUTOMOTORES. **Carta da anfavea 2018**. [s.l: s.n.].

BAETA, J. G. C. et al. Full spark authority in a highly boosted ethanol DISI prototype engine. **Applied Thermal Engineering**, v. 139, n. April, p. 35–46, 2018.

BAYINDIR, K. Ç.; GÖZÜKÜÇÜK, M. A.; TEKE, A. A comprehensive overview of hybrid electric vehicle: Powertrain configurations, powertrain control techniques and electronic control units. **Energy Conversion and Management**, v. 52, n. 6, p. 1305–1313, 2010.

BORETTI, A. Towards 40% efficiency with BMEP exceeding 30 bar in directly injected, turbocharged, spark ignition ethanol engines. **Energy Conversion and Management**, v. 57, p. 154–166, 2012.

CHAN, C. C. The state of the art of electric, hybrid, and fuel cell vehicles. **Proceedings of the IEEE**, v. 95, n. 4, p. 704–718, 2007.

CHAPMAN, S. J. **Electric Machinery Fundamentals**. 2 ed. ed. Singapore:

Mc Graw Hill, 1991.

CHAU, K. T.; CHAN, C. C.; LIU, C. Overview of permanent-magnet brushless drives for electric and hybrid electric vehicles. **IEEE Transactions on Industrial Electronics**, v. 55, n. 6, p. 2246–2257, 2008.

CHAU, K. T.; WONG, Y. S. Overview of power management in hybrid electric vehicles. **Energy Conversion and Management**, v. 43, p. 1953–1968, 2002.

CORREIO BRAZILIENSE. **Ficha Técnica Fiesta Hatch 1.6L 8V Flex Manual 4P**. Disponível em: <https://correiobraziliense.vrum.com.br/fichatecnica/ford/fiesta/2011/003289-1>. Acesso em: 5 dec. 2018.

DUARTE, G. O. et al. Effect of battery state of charge on fuel use and pollutant emissions of a full hybrid electric light duty vehicle. **Journal of Power Sources**, v. 246, p. 377–386, 2014.

EHSANI, M.; GAO, Y.; EMADI, A. **Modern electric, hybrid electric and fuel cell vehicles: fundamental, theory and design**. Second Edi ed. [s.l.] Crc Press, 2013. v. 53

EMPRESA DE PESQUISA ENERGÉTICA. **Balanço Energético nacional 2017: Ano base 2016, Relatório SínteseEmpresa de Pesquisa Energética**. Rio de Janeiro: [s.n.]. Disponível em: <www.epe.gov.br>.

EMRAX D.O.O. **Technical Data and Manual for EMRAX Motors / Generators**. [s.l: s.n.]. Disponível em: <http://emrax.com/wp-content/uploads/2017/10/user_manual_for_emrax_motors.pdf>.

ENOSHITA, E. **Toyota apresenta o primeiro Prius flex do mundo**. Disponível em: <https://motorshow.com.br/toyota-apresenta-o-primeiro-prius-flex-do-mundo/>. Acesso em: 11 apr. 2018.

FOLHA DE LONDRINA. **Ficha Técnica Ford Fiesta Sedan SE 1.6 16V Flex 4p**. Disponível em: <https://folhadelondrina.vrum.com.br/fichatecnica/ford/fiesta/2005/003340-5>. Acesso em: 5 dec. 2018.

FOTOUHI, A. et al. A Review on Electric Vehicle Battery Modelling: from Lithium-ion toward Lithium-Sulfur. **Renewable & Sustainable Energy Reviews**, v. 56, p. 1008–1021, 2016.

GAMMA TECHNOLOGIES, L. **GT-Suite**. Disponível em: <https://www.gtisoft.com/gt-suite/gt-suite-overview/>. Acesso em: 13 oct. 2018.

GAMMA TECHNOLOGIES, L. **GT-Suite Vehicle Driveline and HEV Tutorials**. [s.l: s.n.].

GAO, W. Performance comparison of a fuel cell-battery hybrid powertrain and a fuel cell-ultracapacitor hybrid powertrain. **IEEE Transactions on Vehicular Technology**, v. 54, n. 3, p. 846–855, 2005.

GIACOSA, D. **Motores Endotérmicos**. Third Edit ed. [s.l.] Editorial Dossat S. A., 1979.

HANNAN, M. A.; AZIDIN, F. A.; MOHAMED, A. Hybrid electric vehicles and their challenges: A review. **Renewable and Sustainable Energy Reviews**, v. 29, p. 135–150, 2014.

HEYWOOD, J. B. **Internal Combustion Engine Fundementals**. [s.l.] McGraw-Hill, Inc., 1988. v. 21

HOPFERWIESER, S. E. **Electric motors and their applications: a guide to the planning of electric drives**. 1. ed. Switzerland: Brown Boveri & Company, 1956.

HOWEY, D. A. et al. Comparative measurements of the energy consumption of 51 electric, hybrid and internal combustion engine vehicles. **Transport Research Part D**, v. 16, p. 459–464, 2011.

HUTCHINSON, T.; BURGESS, S.; HERRMANN, G. Current hybrid-electric powertrain architectures: Applying empirical design data to life cycle assessment and whole-life cost analysis. **Applied Energy**, v. 119, p. 314–329, 2014.

IBGE. **Instituto Brasileiro de Geografia e Estatística (IBGE)**. Disponível em: <https://cidades.ibge.gov.br/brasil/panorama>. Acesso em: 8 may. 2018.

IDAHO NATIONAL LABORATORY. **Idaho National Laboratory - Advance Vehicle Testing**. Disponível em: <https://avt.inl.gov/>. Acesso em: 5 dec. 2018.

IDAHO NATIONAL LABORATORY. **Battery Pack Laboratory Testing Results - 2016 Chevrolet Volt VIN 4673Idaho National Laboratory**. [s.l: s.n.].

JACK, A. G.; MECROW, B. C.; WEINER, C. Switched reluctance and permanent magnet motors suitable for vehicle drives-a comparison. **IEEE International Electric Machines and Drives Conference, IEMDC 1999 - Proceedings**, p. 505–507, 1999.

JEAN-MARC ALLENBACH. **Railway Technology**. [s.l: s.n.].

KIM, N.; CHA, S.; PENG, H. Optimal Control of Hybrid Electric Vehicles Based on Pontryagin's Minimum Principle. **IEEE Transactions on Control Systems Technology**, v. 19, n. 5, p. 1279–1287, 2010.

KITAYAMA, S. et al. Torque control strategy and optimization for fuel consumption and emission reduction in parallel hybrid electric vehicles. **Structural and Multidisciplinary Optimization**, v. 52, p. 595–611, 2015.

LEDUC, P. et al. Downsizing of Gasoline Engine: an Efficient Way to Reduce CO2 Emissions. **Oil & Gas Science and Technology**, v. 58, n. 1, p. 115–127, 2003.

LG CHEM. **LG Chem Automotive Battery**. Disponível em: <http://www.lgchem.com/global/vehicle-battery/car-batteries-Different/product-detail-PDEB0002>. Acesso em: 23 oct. 2018.

MANZETTI, S.; MARIASIU, F. Electric vehicle battery technologies: From present state to future systems. **Renewable and Sustainable Energy Reviews**, v. 51, p. 1004–1012, 2015.

MILLER, T. J. E. **Switched Reluctance Motors and Their Control**. Oxford: Magna Physics Publishing and Clarendon Press, 1993.

MOREDA, G. P.; MUÑOZ-GARCÍA, M. A.; BARREIRO, P. High voltage electrification of tractor and agricultural machinery - A review. **Energy Conversion and Management**, v. 115, n. x, p. 117–131, 2016.

OGILVIE, A. R. **GT-SUITE SIMULATION OF A POWER SPLIT HYBRID ELECTRIC VEHICLE**. [s.l.] University of Alabama, 2011.

OLIVEIRA JR., F. DE. Etanol, a quarta propulsão. **Engenharia Automotiva e**

Aeroespacial, p. 22–25, 2017.

PELLEGRINO, G. et al. Comparison of Induction and PM Synchronous Motor Drives for EV Application Including Design Examples. **IEEE TRANSACTIONS ON INDUSTRY APPLICATIONS**, v. 48, n. 6, p. 2322–2332, 2012.

POULLIKKAS, A. Sustainable options for electric vehicle technologies. **Renewable and Sustainable Energy Reviews**, v. 41, p. 1277–1287, 2015.

QIN, K. et al. Development and experimental validation of a novel hybrid powertrain with dual planetary gear sets for transit bus applications. **Science China Technological Sciences**, v. 58, n. 12, p. 2085–2096, 2015.

RIBAU, J. et al. Analysis of four-stroke, Wankel, and microturbine based range extenders for electric vehicles. **Energy Conversion and Management**, v. 58, p. 120–133, 2012.

RIBEIRO, R. **Rodagem curta e frio são os maiores desafios do Prius Flex**. Disponível em: <https://quatrorodas.abril.com.br/noticias/rodagem-curta-e-frio-sao-os-maiores-desafios-do-prius-flex/>. Acesso em: 16 nov. 2018.

ROHATGI, A. **Web Plot Digitizer**, 2018. Disponível em: <https://automeris.io/WebPlotDigitizer/>

ROSO, V. R. **CICLOS REAIS DE CONDUÇÃO VEICULAR EM SANTA MARIA E SEUS IMPACTOS EM CONSUMO E EMISSÕES**. [s.l.] Universidade Federal de Santa Maria, 2016.

SANTUCCI, A.; SORNIOTTI, A.; LEKAKOU, C. Power split strategies for hybrid energy storage systems for vehicular applications. **Journal of Power Sources**, v. 258, p. 395–407, 2014.

SHEN, C.; SHAN, P.; GAO, T. A comprehensive overview of hybrid electric vehicles. **International Journal of Vehicular Technology**, v. 2011, p. 7, 2011.

SHEN, D.; BENSCH, V.; MÜLLER, S. Model predictive energy management for a range extender hybrid vehicle using map information. **IFAC-PapersOnLine**, v. 28, n. 15, p. 263–270, 2015.

SHUKLA, A. **Modeling and Simulation of Hybrid Electric Vehicles**. [s.l.]

Imperial College London, 2005.

SOARES, L. H. DE B. et al. Mitigação das emissões de gases efeito estufa pelo uso de etanol da cana-de-açúcar produzido no Brasil. **Circular Técnica**, v. 27, p. 14, 2009.

SOLOUK, A. et al. Fuel consumption assessment of a multi-mode low temperature combustion engine as range extender for an electric vehicle. **Energy Conversion and Management**, v. 148, p. 1478–1496, 2017.

STONE, R. **Introduction to Internal Combustion Engines**. 2. ed. Uxbridge, Middlesex: THE MACMILLAN PRESS LTD, 1992.

SUAREZ-BERTOA, R.; ASTORGA, C. Unregulated emissions from light-duty hybrid electric vehicles. **Atmospheric Environment**, v. 136, p. 134–143, 2016.

TATE, E. D.; HARPSTER, M. O.; SAVAGIAN, P. J. The Electrification of the Automobile: From Conventional Hybrid, to Plug-in Hybrids, to Extended-Range Electric Vehicles. **SAE International Journal of Passenger Cars - Electronic and Electrical Systems**, v. 1, n. 1, p. 2008- 01–0458, 2008.

TESLA MOTORS INC. **FORM 10-K (Annual Report)Harvard Business Review**. Palo Alto, CA: [s.n.]. Disponível em: <http://www.annualreports.com/HostedData/AnnualReportArchive/t/NASDAQ_TSLA_2010.pdf>.

UNITED STATES ENVIRONMENTAL PROTECTION AGENCY. **www.fueleconomy.gov**. Disponível em: <https://www.fueleconomy.gov/feg/PowerSearch.do?action=noform&path=1&year1=2018&year2=2018&make=Toyota&baseModel=Prius&srchtyp=ymm>. Acesso em: 29 apr. 2018.

VOLVO GROUP. **Volvo XC60 Specs**. Disponível em: <https://www.volvocars.com/us/cars/new-models/xc60/specs#/specscompare>. Acesso em: 5 dec. 2018a.

VOLVO GROUP. **Car Compare**. Disponível em: <https://www.media.volvocars.com/global/en-gb/models/new-

xc60/2018/specifications>. Acesso em: 13 jul. 2019b.

WANG, C. et al. Ethanol blends in spark ignition engines: RON, octane-added value, cooling effect, compression ratio, and potential engine efficiency gain. **Applied Energy**, v. 191, p. 603–619, 2017.

WANG, E.; GUO, D.; YANG, F. System design and energetic characterization of a four-wheel-driven series-parallel hybrid electric powertrain for heavy-duty applications. **Energy Conversion and Management**, v. 106, p. 1264–1275, 2015.

WILLIAMSON, S. S.; LUKIC, S. M.; EMADI, A. Comprehensive drive train efficiency analysis of hybrid electric and fuel cell vehicles based on motor-controller efficiency modeling. **IEEE Transactions on Power Electronics**, v. 21, n. 3, p. 730–740, 2006.

WORLD HEALTH ORGANIZATION. **9 out of 10 people worldwide breathe polluted air, but more countries are taking action**. Disponível em: <http://www.who.int/news-room/detail/02-05-2018-9-out-of-10-people-worldwide-breathe-polluted-air-but-more-countries-are-taking-action>. Acesso em: 10 may. 2018.

XUE, X. D.; CHENG, K. W. E.; CHEUNG, N. C. Selection of electric motor drives for electric vehicles. **Power Engineering Conference, 2008. AUPEC ’08. Australasian Universities**, p. 1–6, 2008.

YAN, F.; WANG, J.; HUANG, K. Hybrid electric vehicle model predictive control torque-split strategy incorporating engine transient characteristics. **IEEE Transactions on Vehicular Technology**, v. 61, n. 6, p. 2458–2467, 2012.

YANG, Z. et al. Comparative study of interior permanent magnet, induction, and switched reluctance motor drives for EV and HEV applications. **IEEE Transactions on Transportation Electrification**, v. 1, n. 3, p. 245–254, 2015.

YASA LIMITED. **P400 R Series E-Motor Datasheet**. [s.l: s.n.]. Disponível em: <https://www.yasa.com/yasa-p400/>.

YASA LIMITED. **750R Series E-Motor Datasheet**. [s.l: s.n.].

YOUNG, K. et al. Electric Vehicle Battery Technologies. In: GARCIA-VALLE, R.; LOPES, J. A. P. (Eds.). . **Electric Vehicle Integration into Modern Power Networks**. 1. ed. New Dheli, India: Springer-Verlag New York, 2013. p. 15–56.

YU, H. et al. Real time energy management strategy for a fast charging electric urban bus powered by hybrid energy storage system. **Energy**, v. 112, p. 322–331, 2016.

APPENDIX A – LIST OF MODEL VARIABLES

Table A1 and A2 show the values adopted for each attribute of the model objects of the “Main” assembly and of all subassemblies, respectively. Any value not included in the list was assumed as “0”, “def”, or “ign”. Figures A1 to A7 details each ‘IfThenElse’ and ‘EventManager’ objects, as well as the “BrakeMap” used

TABLE A1 – VALUES /OF THE MODEL ATTRIBUTES OF THE “MAIN” ASSEMBLY

Assembly	Template Object	Object Name	Attribute	Unit	Value
Main	EngineState	Engine-1	Engine Type	-	4-stroke
Main	EngineState	Engine-1	Engine Displacement	cm3	Table 20
Main	EngineState	Engine-1	Minimum Operation Speed	RPM	def
Main	EngineState	Engine-1	Engine Inertia	kg*m2	0.25
Main	EngineState	Engine-1	Fuel Density	kg/m3	808.7
Main	EngineState	Engine-1	Fuel Heating Value	MJ/kg	24.76
Main	EngineState	Engine-1	Initial Speed	rpm	0
Main	EngineState	Engine-1	Initial Angula Position	deg	0
Main	EngineState	Engine-1	Accelerator Postion	%	100
Main	EngineState	Engine-1	Mechanical Output Map	MEP (bar)	Annex F
Main	EngineState	Engine-1	Engine Friction Map	MEP (bar)	Annex F
Main	EngineState	Engine-1	Fuel Consumption Map	MEP (bar)	Annex F
Main	Battery	Battery-1	Power Request	W	0
Main	Battery	Battery-1	Initial State of Charge	-	0.7
Main	Battery	Battery-1	SOC Model	-	Conventional
Main	Battery	Battery-1	Battery Capacity	-	28.8
Main	Battery	Battery-1	Open Circuit Voltage Map, Discharge	V	Figure 74
Main	Battery	Battery-1	Open Circuit Voltage Map, Charge	V	Figure 74
Main	Battery	Battery-1	Internal Resistance Map, Discharge	Ohm	Figure 76
Main	Battery	Battery-1	Internal Resistance Map, Charge	Ohm	Figure 75
Main	Battery	Battery-1	Battery Temperature	K	300
Main	BatteryPowerLim	BatteryPowerLim1	Maximum Battery Power Fraction	-	0.6
Main	BatteryPowerLim	BatteryPowerLim1	Maximum Discharge Current Limit	A	1050
Main	BatteryPowerLim	BatteryPowerLim1	Maximum Charge Current Limit	A	-1060
Main	BatteryPowerLim	BatteryPowerLim1	Maximum Charge Voltage Limit	V	360
Main	BatteryPowerLim	BatteryPowerLim1	Minimum Discharge Voltage Limit	V	0
Main	MotorGeneratorMap	Generator-1	Electromechanical Conversion Eff.	-	Annex G, H, I, or J
Main	MotorGeneratorMap	Generator-1	Load Control Option	-	Power-Brake
Main	MotorGeneratorMap	Generator-1	Maximum Brake Torque	Nm	Annex G, H, I, or J
Main	MotorGeneratorMap	Generator-1	Minimum Brake Torque	Nm	Annex G, H, I, or J
Main	MotorGeneratorMap	Motor-1	Electromechanical Conversion Eff.	-	Annex G
Main	MotorGeneratorMap	Motor-1	Load Control Option	-	Power-Brake
Main	MotorGeneratorMap	Motor-1	Maximum Brake Torque	Nm	Annex G
Main	MotorGeneratorMap	Motor-1	Minimum Brake Torque	Nm	Annex G
Main	Shaft	Shaft1	Shaft Moment of Inertia	kg*mm2	0.1
Main	Shaft	Shaft2	Shaft Moment of Inertia	kg*mm2	0.1
Main	GearConn	GearRatio1	Gear Ratio		1.57 (Ford) or 1.59 (Volvo)
Main	GearConn	GearRatio1	Mechanical Efficiency		0.97
Main	GearConn	GearRatio2	Gear Ratio		Table 23, 25, or 26
Main	GearConn	GearRatio2	Mechanical Efficiency		Table 23, 25, or 26

Source: elaborated by the author.

TABLE A2 – VALUES OF THE MODEL ATTRIBUTES OF THE 5 SUBASSEMBLIES

Assembly	Template Object	Object Name	Attribute	Unit	Value
Vehicle	VehicleBody	Car-1	Vehicle Mass	kg	Table 15
Vehicle	VehicleBody	Car-1	Vehicle Initial Speed	km/h	0
Vehicle	VehicleBody	Car-1	Vehicle Drag Coefficient	-	Table 15
Vehicle	VehicleBody	Car-1	Vehicle Frontal Area	m^2	Table 15
Vehicle	VehicleBody	Car-1	Vehicle Lift Coefficient	-	0
Vehicle	VehicleBody	Car-1	Vehicle Wheelbase	mm	Table 15
Vehicle	VehicleBody	Car-1	Horizontal Distance From Last...	m	1
Vehicle	TireConnRigid	Tire-1, 2, 3, and 4	Explicit Tire Rolling Radius		Table 15
Vehicle	TireConnRigid	Tire-1, 2, 3, and 4	Tire Rolling Resistance Factor	-	0.01
Vehicle	TireConnRigid	Tire-1, 2, 3, and 4	Number of Tires on Axle	-	1
Vehicle	Axle	Axle-FL, FR, RL, and RR	Axle Moment of Inertia	kg*m2	1.25
Vehicle	Brake	Brake-1, 2, 3, and 4	Interpretation of Actuator...	-	Brake-actuator
Vehicle	Brake	Brake-1, 2, 3, and 4	Braking Torque Model	-	Map
Vehicle	Brake	Brake-1, 2, 3, and 4	Brake Map Object	-	Figure A7
Vehicle	Shaft	Driveshaft	Shaft Moment of Inertia	kg*m2	0.01
Vehicle	Differential	Differential-1	Input Inertia	kg*m2	0.01
Vehicle	Differential	Differential-1	Output Inertia	kg*m2	0.01
Vehicle	Differential	Differential-1	Final Drive Ratio	-	3.2
Vehicle	Differential	Differential-1	Efficiency	fraction	1
Vehicle	VehicleAmbient	Environment-1	Altitude-Corrected for SATP Air	-	-
Vehicle	Road	Road	All		def
ECU	ICEController	ICEController-1	Engine Starter Shutoff Speed	RPM	1000
ECU	ICEController	ICEController-1	Resume Speed	RPM	1500
ECU	ICEController	ICEController-1	Time Delay (for fuel cut)	s	0.5
ECU	ICEController	ICEController-1	Maximum Engine Fueling Speed	RPM	2700
ECU	ICEController	ICEController-1	Engine Idle Speed	RPM	950
ECU	ICEController	ICEController-1	PID Controller Proportional Gain	-	1
ECU	ICEController	ICEController-1	PID Controller Integral Gain	-	0.05
ECU	ICEController	ICEController-1	PID Controller Derivative Gain	-	ign
ECU	IfThenElse	SOC_Control1	All	-	Figure A1
ECU	IfThenElse	ICE_State1	All	-	Figure A2
ECU	TimeDelay	TimeDelay1	Delay Type	-	SingleTimeStep
ECU	TimeDelay	TimeDelay1	Initial Output	-	0
ECU	TimeDelay	TimeDelay1	Delay Method	-	interpolate-linear
ECU	TimeDelay	TimeDelay1	Interpretation of "SingleTimeStep"	-	MasterFlow
ECU	PIDController	ICE_Accel1	Proportional Gain	-	1
ECU	PIDController	ICE_Accel1	Integral Gain	-	0.5
ECU	PIDController	ICE_Accel1	Derivative Gain	-	ign
Generator_Control	IfThenElse	GenPowerManagement	All	-	Figure A5
Generator_Control	EventManager	Ignition1	All	-	Figure A6
Generator_Control	Lookup1D	Lookup1D1	Table or Function Object Name	-	Annex G, H, I, or J
Motor_Control	ControllerHEVehicle	ControllerHEVehicle1	Controller Mode	-	Speed_Targeting
Motor_Control	ControllerHEVehicle	ControllerHEVehicle1	Vehicle Mass	kg	Table 15
Motor_Control	ControllerHEVehicle	ControllerHEVehicle1	Vehicle Frontal Area	m^2	Table 15
Motor_Control	ControllerHEVehicle	ControllerHEVehicle1	Vehicle Drag Coefficient	-	Table 15
Motor_Control	ControllerHEVehicle	ControllerHEVehicle1	Tire Rolling Radius	mm	Table 15
Motor_Control	ControllerHEVehicle	ControllerHEVehicle1	Tire Rolling Resistance Factor	-	Table 15
Brake_Control	BrakeController	BrakeController1	Maximum Braking Torque	Nm	750
Brake_Control	BrakeController	BrakeController1	Number of Braking Axles	-	2
Brake_Control	Lookup1D	Torque_Limit_Motor1	Table or Function Object Name	-	Annex G, H, I, or J
Brake_Control	IfThenElse	Regen_Mode1	All	-	Figure A3
Brake_Control	IfThenElse	BrakePowerManagement	All	-	Figure A4

Source: elaborated by the author.

FIGURE A1 – CONFIGURATION OF “SOC_CONTROL1” PART

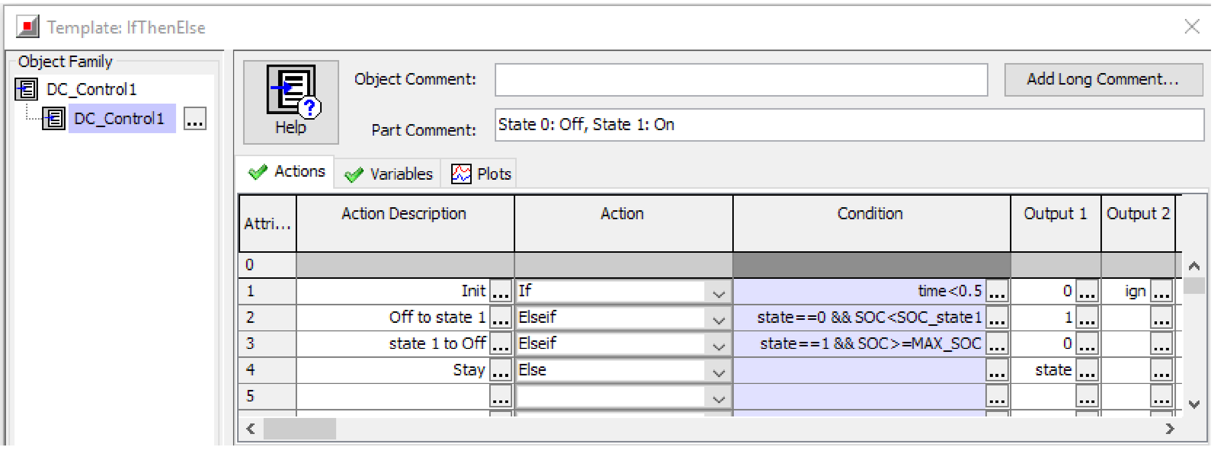

Source: elaborated by the author.

FIGURE A2 – CONFIGURATION OF “ICE_STATE1” PART

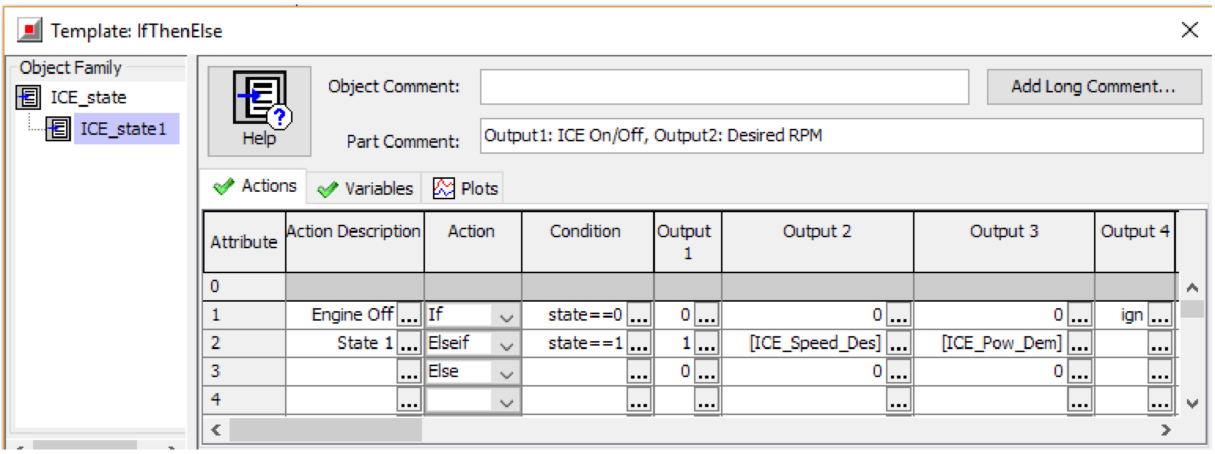

Source: elaborated by the author.

FIGURE A3 – CONFIGURATION OF “REGEN_MODE1” PART

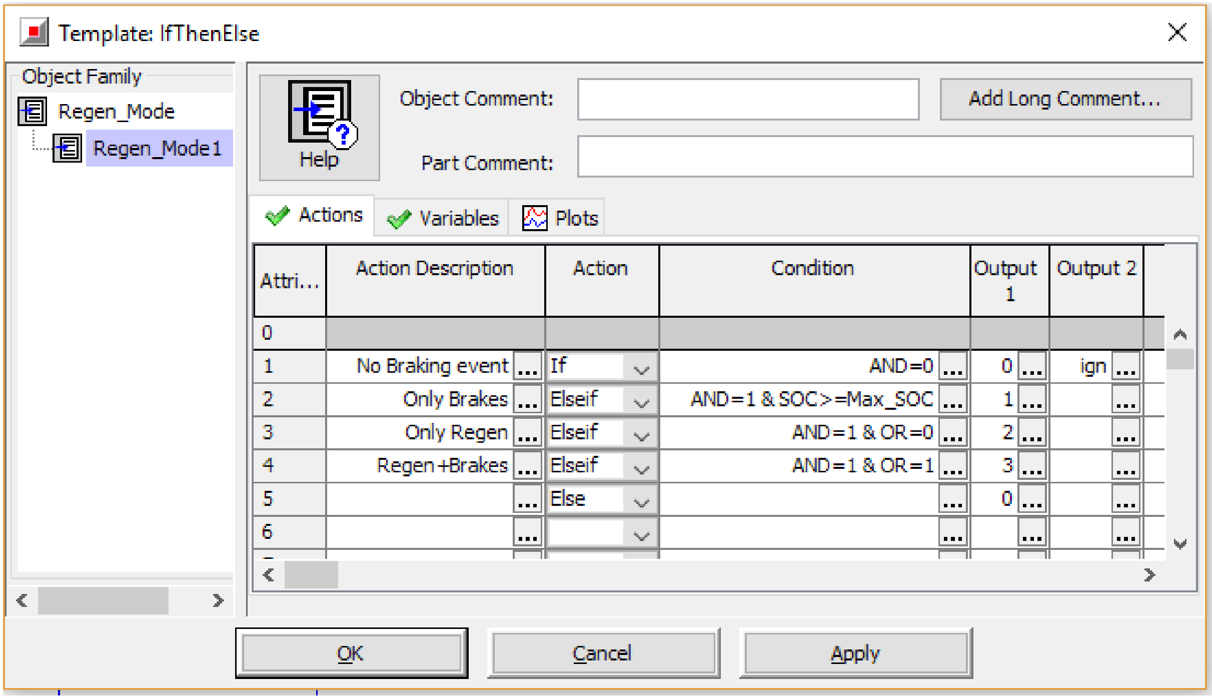

Source: elaborated by the author.

FIGURE A4 – CONFIGURATION OF “BRAKEPOWERMANAGEMENT” PART

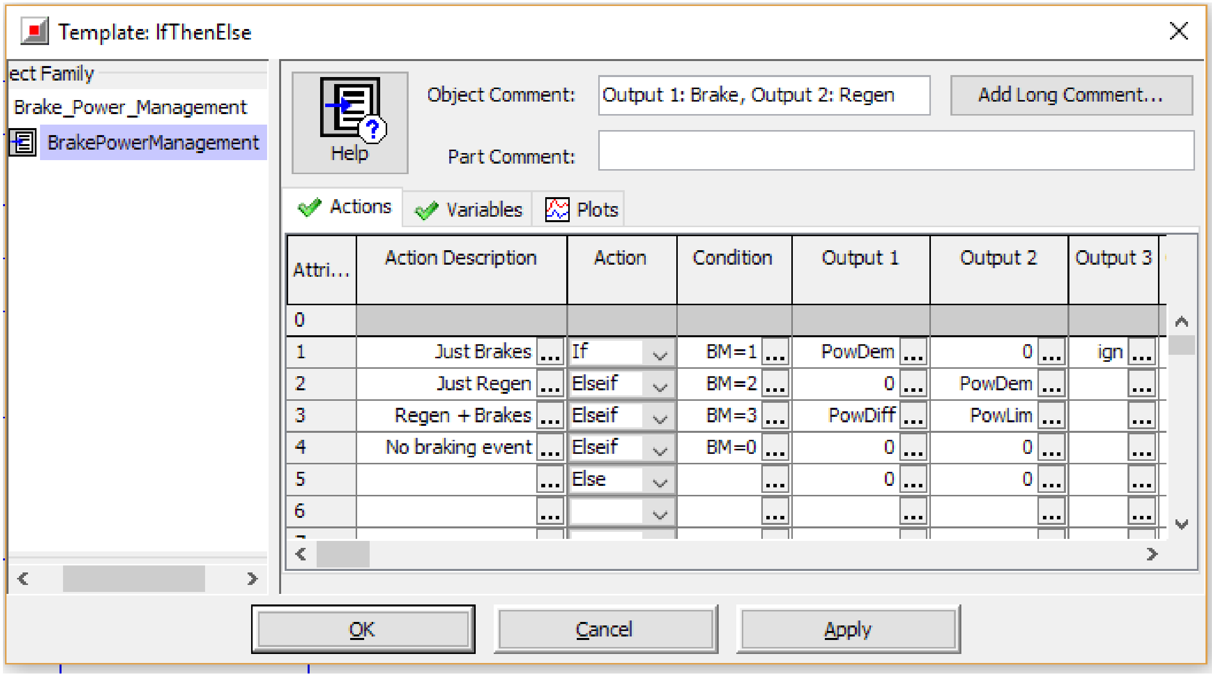

Source: elaborated by the author.

FIGURE A5 – CONFIGURATION OF "GENPOWERMANAGEMENT" PART

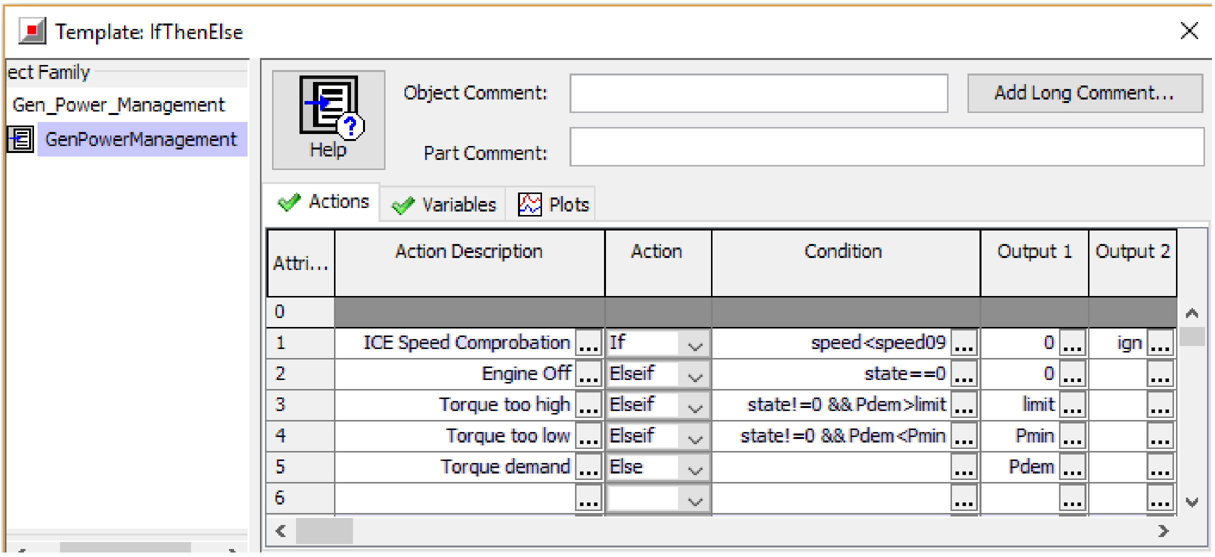

Source: elaborated by the author.

FIGURE A6 – CONFIGURATION OF "IGNITION1" PART

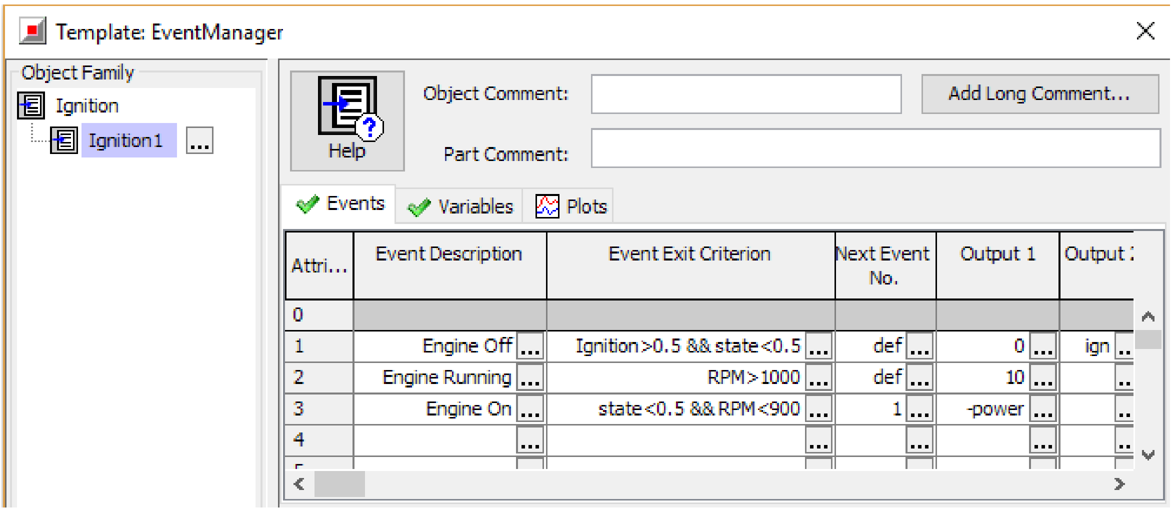

Source: elaborated by the author.

FIGURE A7 – VALUES OF THE "BRAKEMAP"

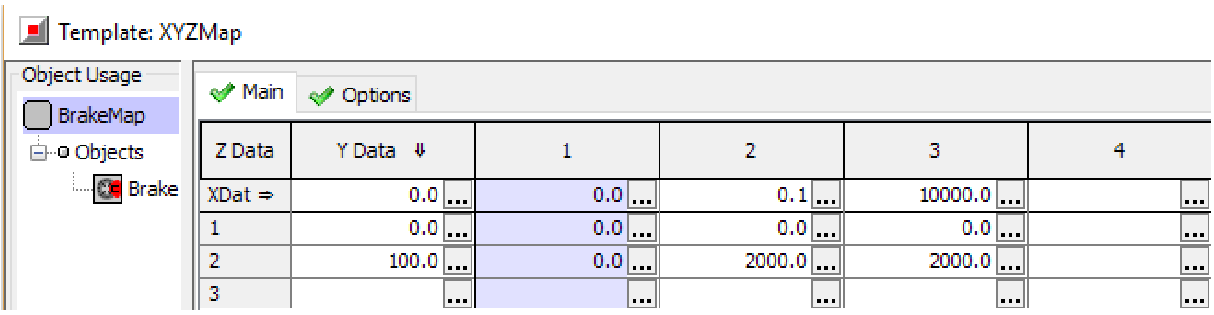

Source: elaborated by the author.

APPENDIX B – MOTOR SELECTION ANALYSIS

This analysis was done in order to select the electric motor used in the model. The motor power demand was analyzed for the Volvo XC60 vehicle. The analysis was done for all five standard driving cycles (FTP-75, HWFET, UD06, NEDC, and WLTC Class 3). However, this annex only shows the most relevant results.

The motor map used through the analysis is from the GT-Suite libraries and corresponds to the same one used in the “Tutorial 5: Dynamic Hybrid Electric Vehicle” (GAMMA TECHNOLOGIES, 2016). It had a starting peak torque of 238 Nm that was constant until a base speed of 1000 rpm, after which the torque fell exponentially until the maximum speed of 6000 rpm. Additionally, the “GearRatio1” was kept as 1:1, with an efficiency of 100%. Figures A8 to A10 shows the power demand through the FTP-75, US06, and NEDC, respectively.

As expected, the motor was not able to completely follow the driving cycles. The simulation showed that the vehicle had a top speed of 107 km/h, as it can be seen in figure A9. Probably, this was due to the lack of a gear ratio, which resulted in a vehicle with low torque at high speed. Moreover, it was observed that the power demand increased dramatically when the vehicle was unable to follow the target speed. This is easily observed at the end of the NEDC cycle, as shown in figure A10.

FIGURE A8 – POWER DEMAND OF FTP-75 FOR THE MOTOR ANALYSIS

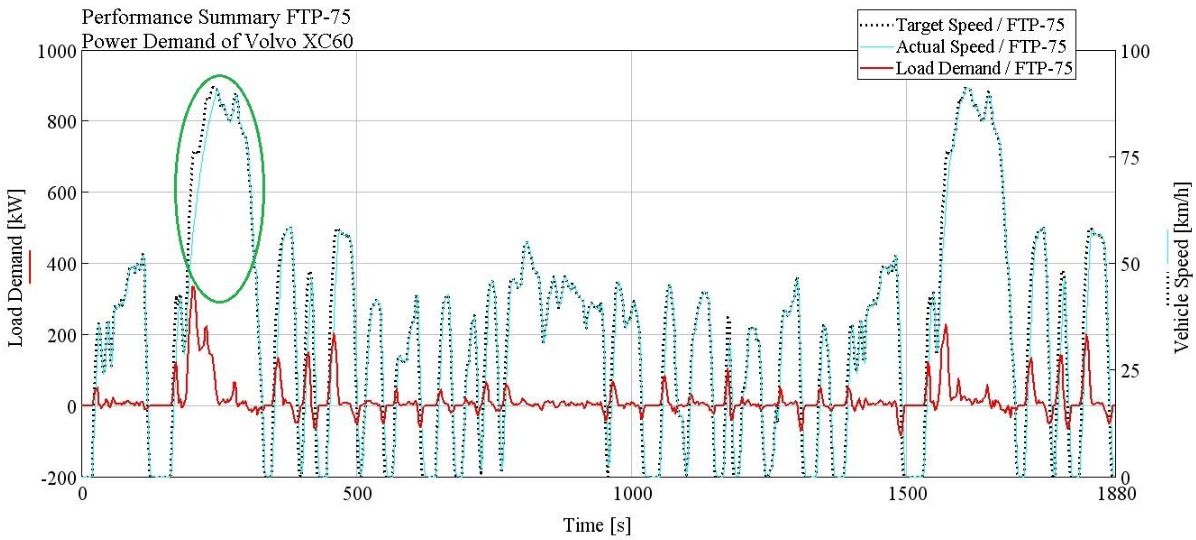

Source: elaborated by the author.

FIGURE A9 – POWER DEMAND OF US06 FOR THE MOTOR ANALYSIS

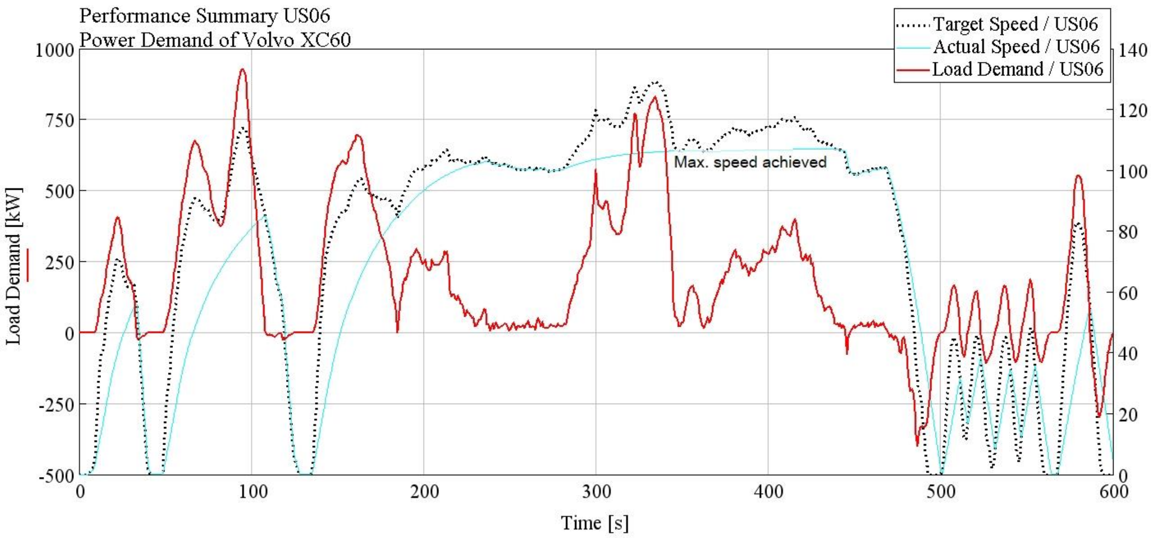

Source: elaborated by the author.

FIGURE A10 – POWER DEMAND OF NEDC FOR THE MOTOR ANALYSIS

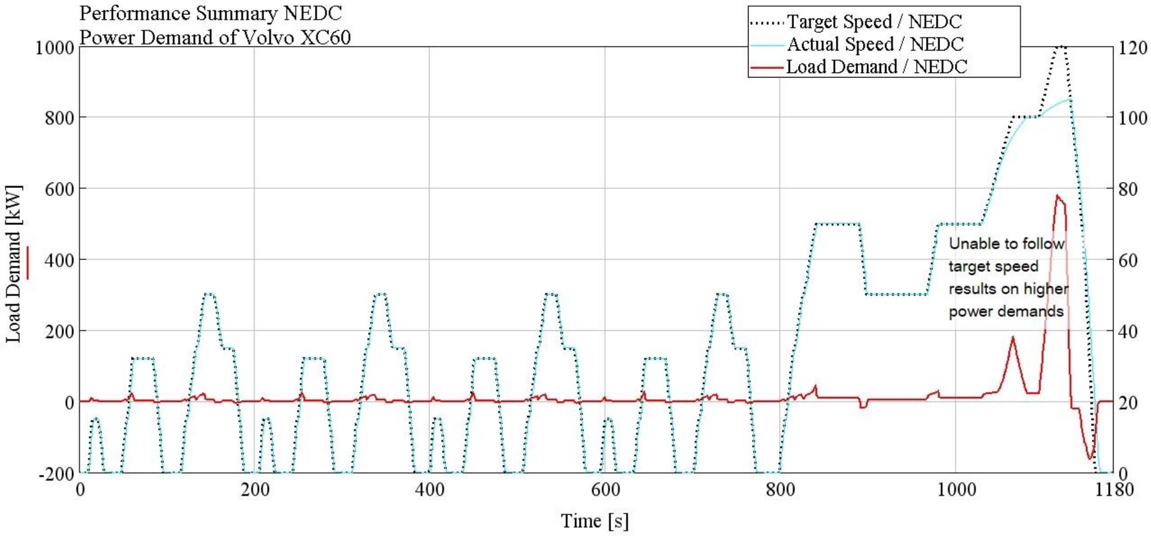

Source: elaborated by the author.

Finally, it is concluded that a motor with a peak power higher than 100 kW is needed in order to ensure good performance for the Volvo XC60.

APPENDIX C – ANALYSIS OF THE ELECTRICAL POWER DEMAND FOR THE CHARACTERISTICS OF THE FORD FIESTA SEDAN

First, the Volvo XC60 was simulated for five standard driving cycles (HWFET, FTP-75, US06, NEDC, and WLTC Class 3). This simulation utilizes the motor Yasa P400 and a 'GearRatio1' of 1.57, as defined in section 3.4. Then, the most frequents power demands of the motor were analyzed. Figure A11 to A15 presents the histogram frequency of the power demand for each driving cycle. While figure A16 compares the five histograms.

Notice that the FTP-75, WLTC Class 3, and NEDC cycles have high frequencies at idling (0 kW power demand), this is typical of urban driving cycles, where frequent stops are common. Additionally, negative power demands represent opportunities for regenerative braking.

From figure A11, it is observed that the FTP-75 cycle have most of its power demand near to idling. In fact, 44.21% of the cycle time happened between 1 to 8 kW, with 4 kW being its most frequent power demand.

FIGURE A11 – FREQUENCY HISTOGRAM OF POWER DEMAND FOR THE FORD FIESTA AT THE FTP-75 DRIVING CYCLE

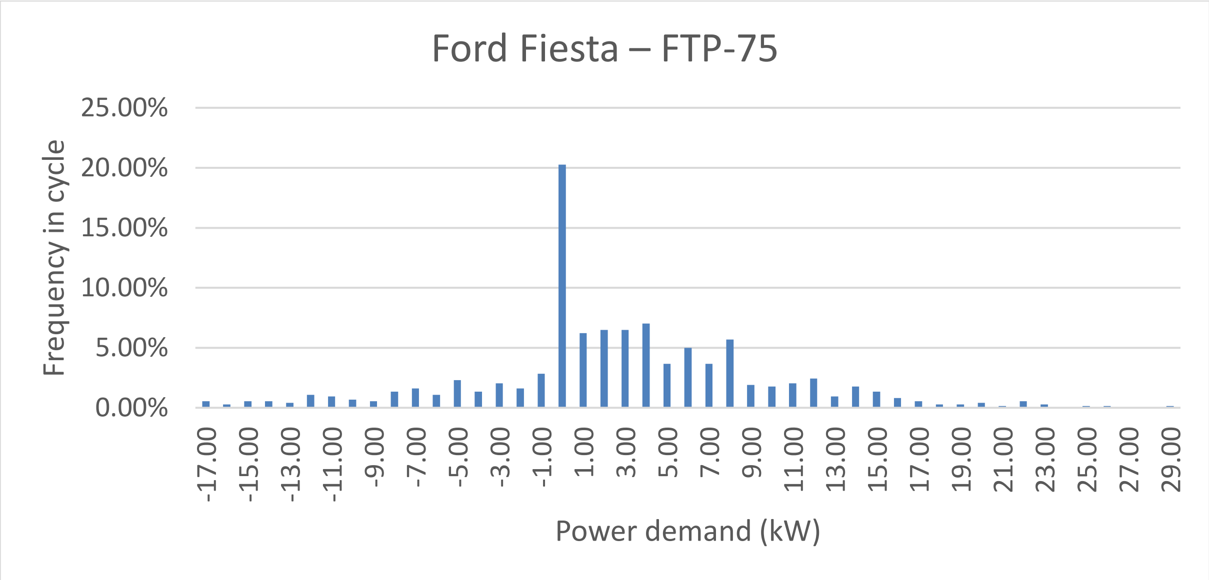

Source: elaborated by the author.

On the other hand, figure A12 shows that the HWFET cycle is highly concentrated between 7 to 13 kW, representing 52.72% of the demanded power through the cycle. This is because this cycle represents highway driving conditions and, hence, it operates at higher speeds and higher power demands.

FIGURE A12 – FREQUENCY HISTOGRAM OF POWER DEMAND FOR THE FORD FIESTA AT THE HWFET DRIVING CYCLE

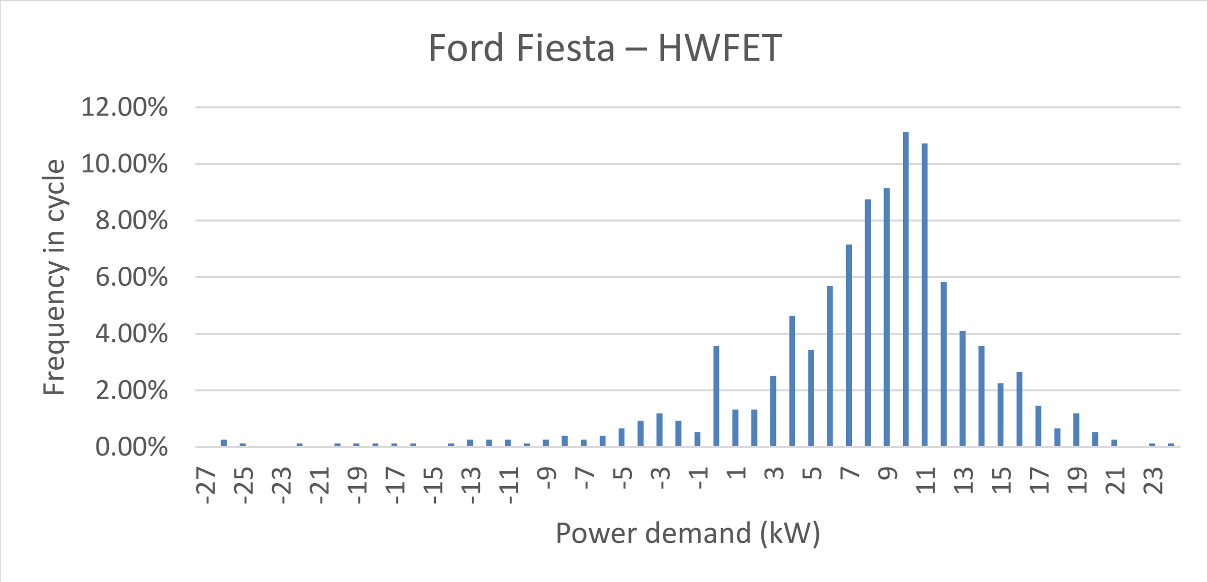

Source: elaborated by the author.

Figure A13 shows that the US06 cycle had a similar trend to the HWFET, however, the US06 cycle had even higher power demands. With a 4.07% of the cycle time, 16 kW it's the most frequent power demand, while 42.47% of the driving cycle is found through 9 to 23 kW. This is because the US06 cycle is designed for high speed and quick accelerations.

In the case of the NEDC cycle, figure A14 shows that 35.15% of the power demand is concentrated in three points: 2 kW, 3 kW, and 6 kW, corresponding to 13.54%, 11.9% and 9.71% of the cycle time, respectively.

Finally, figure A15 shows that the WLTC Class 3 cycle had a more disperse power demand, with a tendency to concentrate near idling. For this cycle, 46.44% of the power demand is concentrated between 1 to 13 kW, from which 13.31% of the cycle time corresponds to 1 kW, 9.98% to 3 kW, 9.08% to 6 kW, and 7.87% to 9 kW.

FIGURE A13 – FREQUENCY HISTOGRAM OF POWER DEMAND FOR THE FORD FIESTA AT THE US06 DRIVING CYCLE

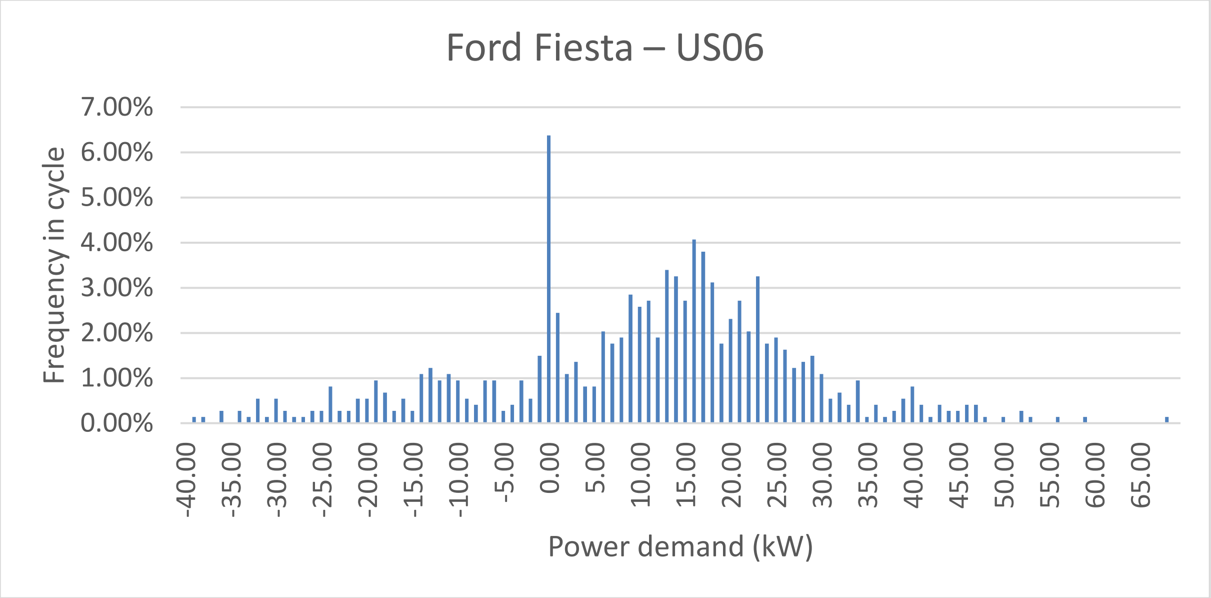

Source: elaborated by the author.

FIGURE A14 – FREQUENCY HISTOGRAM OF POWER DEMAND FOR THE FORD FIESTA AT THE NEDC DRIVING CYCLE

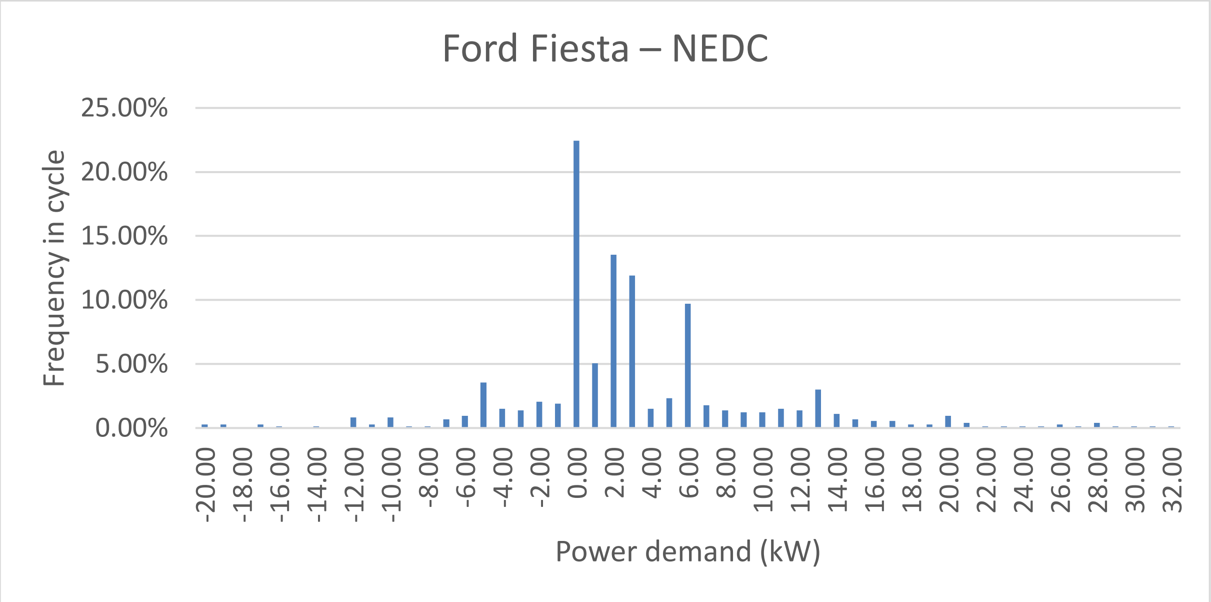

Source: elaborated by the author.

FIGURE A15 – FREQUENCY HISTOGRAM OF POWER DEMAND FOR THE FORD FIESTA AT THE WLTC CLASS 3 DRIVING CYCLE

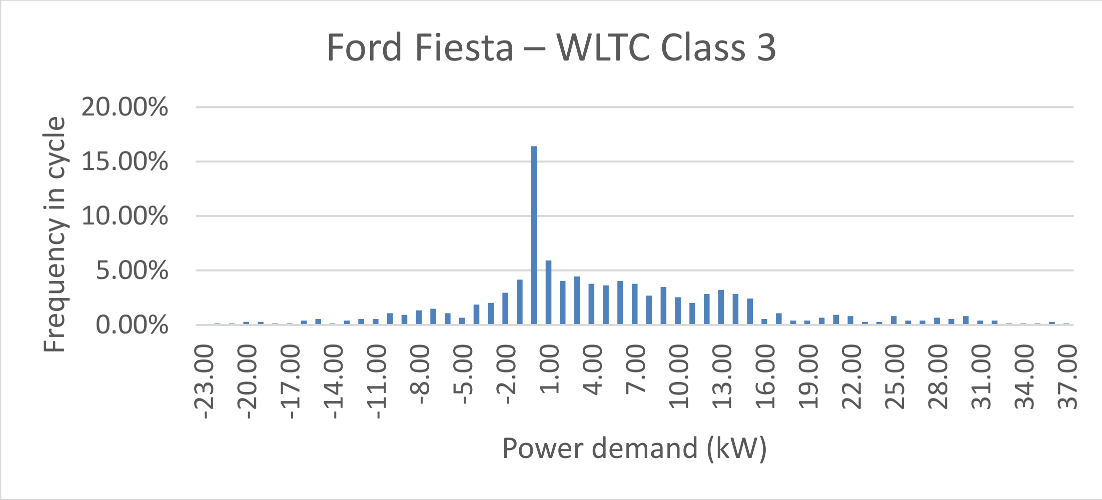

Source: elaborated by the author.

FIGURE A16 – COMPARISON BETWEEN THE HISTOGRAMS OF THE FIVE DRIVING CYCLES, FOR THE FORD FIESTA

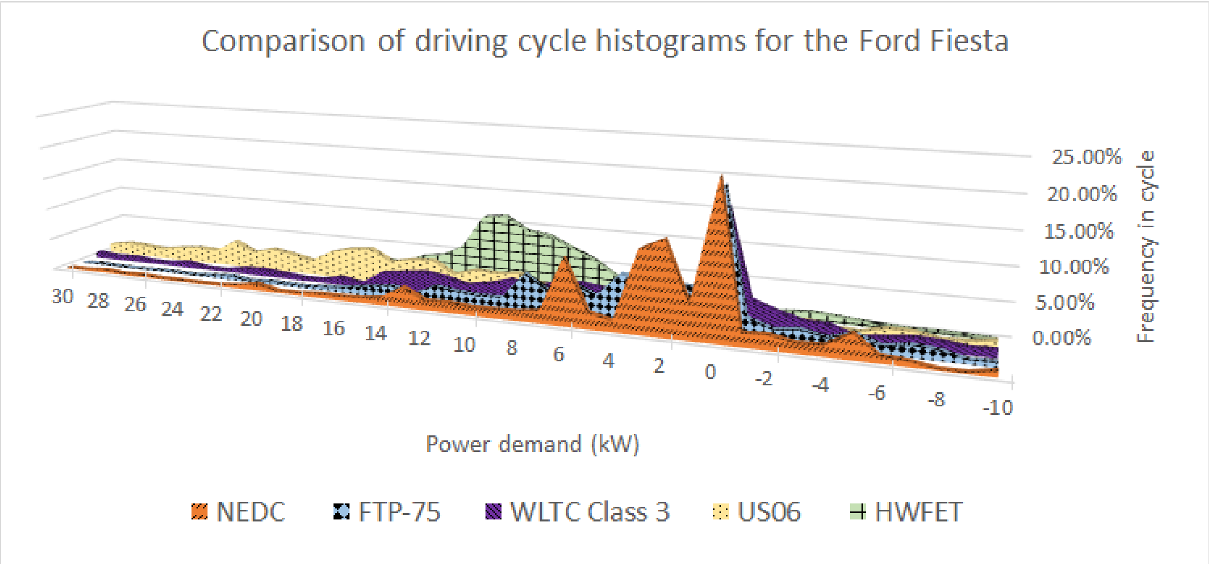

Source: elaborated by the author.

From the previous analysis, four of the power modes selected corresponded to the highest frequency points of the FTP-75 (4 kW), HWFET (10 kW), US06 (16 kW), and NEDC (2 kW). Additionally, the power modes of 6 kW, 13 kW, 20 kW, and 23 kW were selected to cover other frequency peaks presented in the cycles, as well as some intermediate distributions.

APPENDIX D – ANALYSIS OF THE ELECTRICAL POWER DEMAND FOR THE CHARACTERISTICS OF THE VOLVO XC60 HYBRID

First, the Volvo XC60 was simulated for five standard driving cycles (HWFET, FTP-75, US06, NEDC, and WLTC Class 3). This simulation utilize the motor Yasa P400 and a 'GearRatio1' of 1.59, as defined in section 3.4. Then, the most frequents power demands of the motor were analyzed. Figure A17 to A21 presents the histogram frequency of the power demand for each driving cycle. While figure A22 compares the five histograms.

Figures A17 to A21 showed that the five driving cycles have similar frequency distributions that in the Ford Fiesta analysis, although, the power demands tend to be higher. Thus, the most frequent power demands of each cycle is compared between both vehicles.

Without counting idle (0 kW), figure A17 shows that the 3 kW mode was the most frequent power demand for the FTP-75 cycle, with 5.04% of the cycle time, while for the Ford Fiesta it was 4 kW. In addition, the Volvo XC60 spend 45.47% of the cycle time between 1 to 13 kW, instead of 1 to 8 kW for the Ford Fiesta.

FIGURE A17 – FREQUENCY HISTOGRAM OF POWER DEMAND FOR THE VOLVO XC60 AT THE FTP-75 DRIVING CYCLE

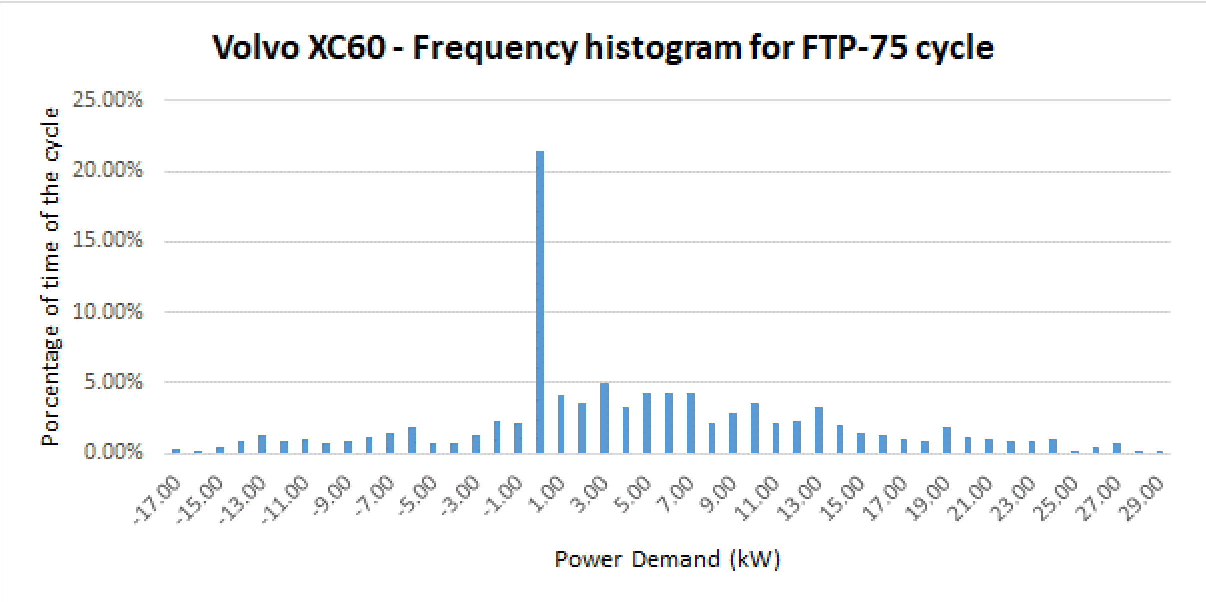

Source: elaborated by the author.

Figure A18 shows the results for the HWFET cycle, which most frequent power demand was at 14 kW, while 51.68% of the cycle time happened between 11 to 20 kW. In comparison, the highest power demand for the Ford Fiesta was at 10 kW, while half of the cycle time was between 7 to 13 kW.

FIGURE A18 – FREQUENCY HISTOGRAM OF POWER DEMAND FOR THE VOLVO XC60 AT THE HWFET DRIVING CYCLE

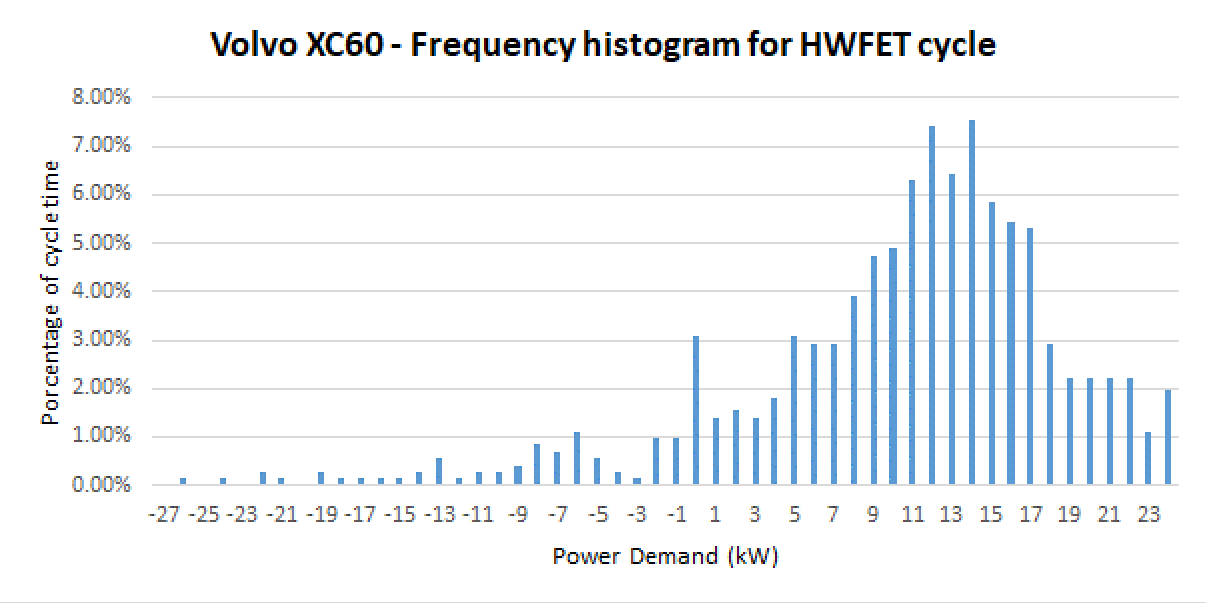

Source: elaborated by the author.

Figure A19 shows only the power demands between -40 to 70 kW, of the cycle US06. Nevertheless, the highest power demand was up to 228 kW. This could be due to the motor inability to completely follow the driving cycle. On the other hand, its most frequent power demand was at 24 kW, while in the Ford Fiesta it was at 16 kW. In comparison, the Volvo XC60 spent 27.67% of the cycle between powers of 9 to 23 kW, while the Ford Fiesta spend 42.47% of the cycle in the same power demands.

As seen in figure A20, the NEDC cycle shows three power demand peaks, which were located at power demands of 3 kW, 5 kW, and 8 kW, corresponding to 12.98%, 11.70% and 9.84% of the cycle time. In comparison, the Ford Fiesta showed these three points at 2 kW, 3 kW, and 6 kW.

Finally, figure A21 presents that the most frequent power demands for the WLTC Class 3 cycle, wich was at 1 kW with a 4.15% of the cycle time. This contrast with the Ford Fiesta, which spends 13.31% cycle time in the same power demand.

Additionally, 48.42% of the cycle time was between 1 to 19 kW, while the Ford Fiesta spends a similar cycle time between 1 to 13 kW.

FIGURE A19 – FREQUENCY HISTOGRAM OF POWER DEMAND FOR THE VOLVO XC60 AT THE US06 DRIVING CYCLE

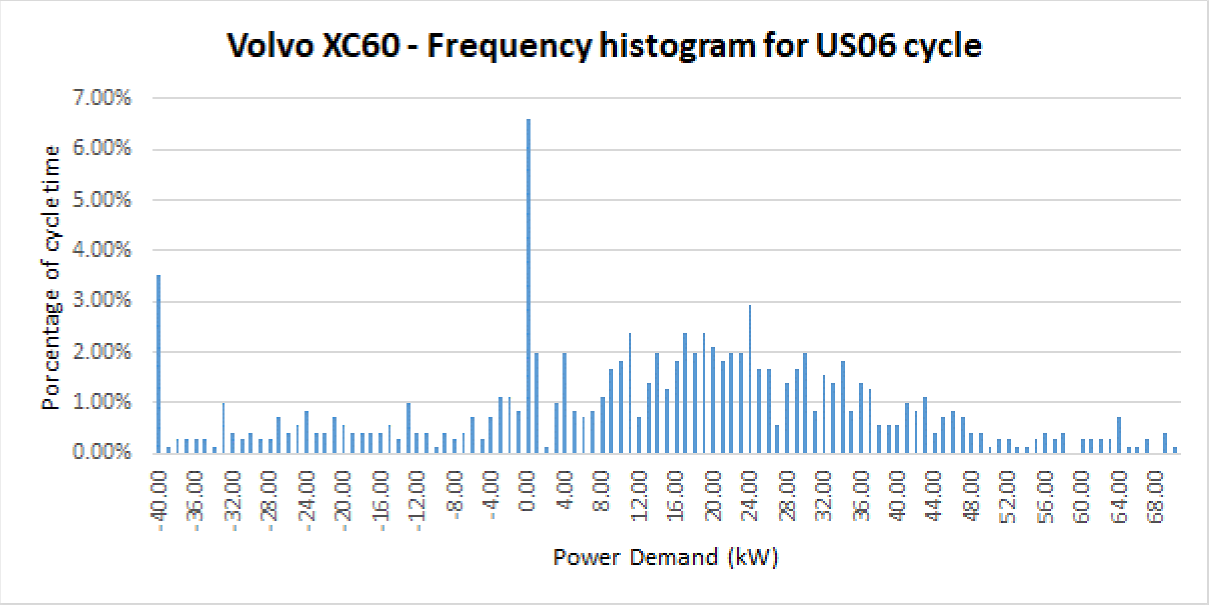

Source: elaborated by the author.

FIGURE A20 – FREQUENCY HISTOGRAM OF POWER DEMAND FOR THE VOLVO XC60 AT THE NEDC DRIVING CYCLE

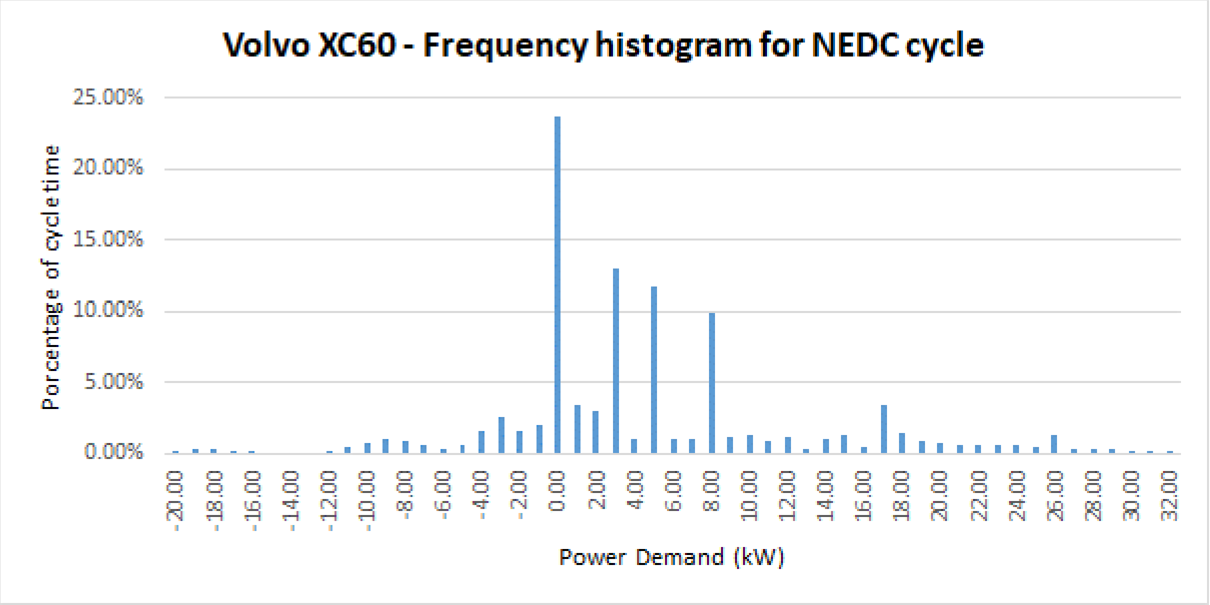

Source: elaborated by the author.

FIGURE A21 – FREQUENCY HISTOGRAM OF POWER DEMAND FOR THE VOLVO XC60 AT THE WLTC CLASS 3 DRIVING CYCLE

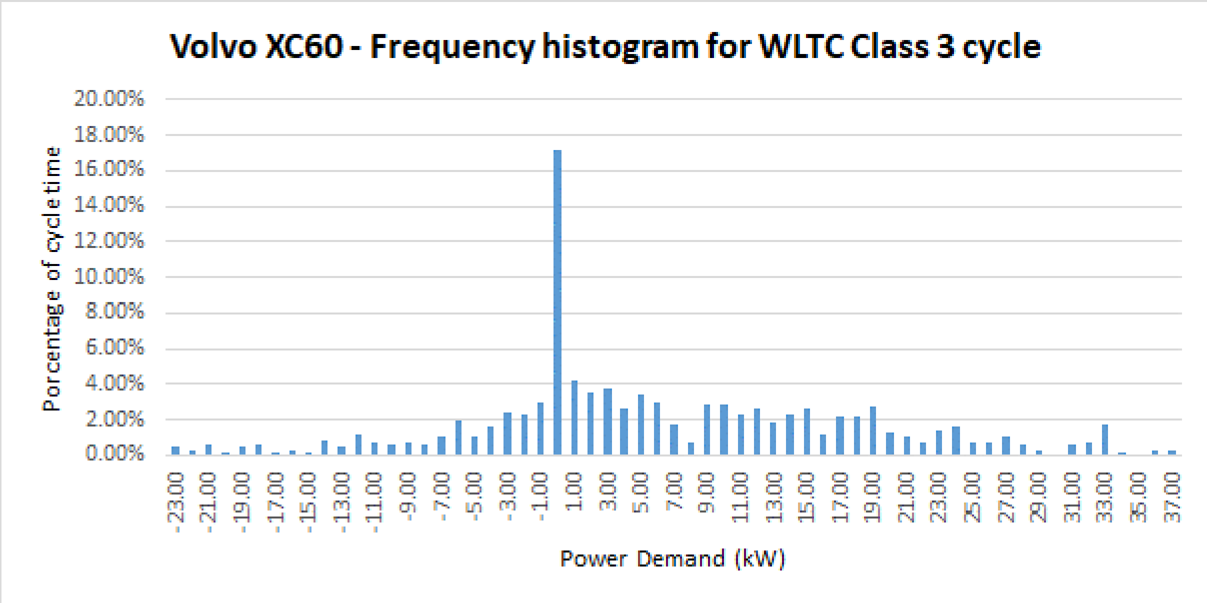

Source: elaborated by the author.

FIGURE A22 – COMPARISON BETWEEN THE HISTOGRAMS OF THE FIVE DRIVING CYCLES, FOR THE VOLVO XC60

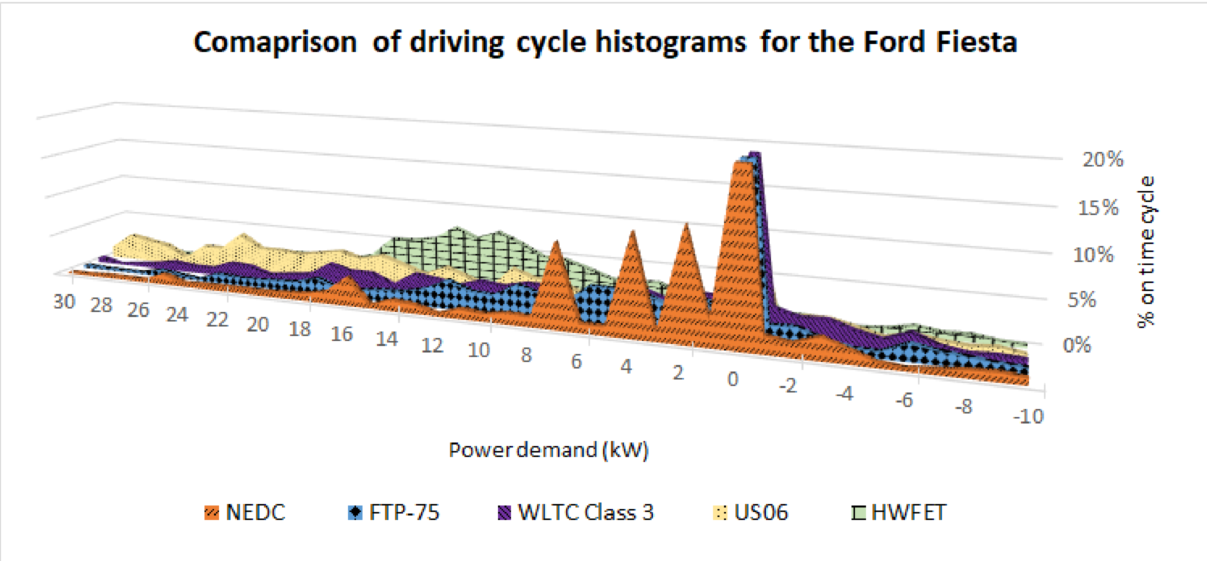

Source: elaborated by the author.

This analysis divided the most relevant power demands into eight groups, which are shown in table 24 in section 3.5.2. For each group, only the power demand with the lowest fuel consumption was selected.

APPENDIX E – RESULTS OF EACH GENERATOR OPERATION POINT SIMULATED FOR THE SIGMA ENGINE AND THE FORD FIESTA

Table A3 shows the analyzed operation points of the ICE-Generator for the Volvo XC60. Highlighted rows correspond to the selected Power Mode, while the strike rows correspond to operation points above the continuous power limit. Gear ratios equal to 1 have a 'GearRatio2' efficiency of 100%, to simulate a shaft without gears.

TABLE A3 – RESULTS OF EACH GENERATOR OPERATION POINT ANALYZED FOR THE SIGMA ENGINE AND EMRAX 208 MATCH

Power Mode	ICE Speed (rpm)	ICE load (Nm)	ICE BSFC (g/kWh)	GR2 Value	GR2 Efficiency	Gen. Speed (rpm)	Gen. Torque (Nm)	Gen. Efficiency
23 kW	2250.00	~~96.13~~	~~343.88~~	~~0.7500~~	~~97.00%~~	~~3000.00~~	~~69.93~~	~~88.22%~~
		97.61	343.63	**0.6923**	**97.00%**	**3250.00**	**65.55**	**93.52%**
				0.6429	97.00%	3500.00	60.86	89.97%
				0.6000	97.00%	3750.00	56.81	86.60%
20 kW	2000.00	~~90.00~~	~~346.47~~	~~0.8000~~	~~97.00%~~	~~2500.00~~	~~69.84~~	~~86.74%~~
		95.49	344.20	0.7273	97.00%	2750.00	67.36	86.00%
				0.6667	97.00%	3000.00	61.74	88.22%
				0.6154	**97.00%**	**3250.00**	**59.99**	**93.53%**
				0.5714	97.00%	3500.00	52.92	89.97%
16 kW	1750.00	87.30	353.75	0.7778	97.00%	2250.00	65.86	95.85%
				0.7000	**97.00%**	**2500.00**	**59.28**	**95.99%**
				0.6364	97.00%	2750.00	53.88	94.34%
				0.5833	97.00%	3000.00	49.39	86.37%
13 kW	1750.00	~~68.91~~	~~363.72~~	~~1.0000~~	~~100.00%~~	~~1750.00~~	~~68.91~~	~~92.30%~~
		70.93	362.21	**0.8750**	**97.00%**	**2000.00**	**60.20**	**91.13%**
				0.7778	97.00%	2250.00	53.51	89.92%
				0.7000	97.00%	2500.00	48.16	86.73%
10 kW	1500.00	~~57.28~~	~~377.49~~	~~1.2000~~	~~97.00%~~	~~1250.00~~	~~66.68~~	~~89.64%~~
		63.66	370.80	1.0000	100.00%	1500.00	63.66	89.55%
				0.8571	**97.00%**	**1750.00**	**52.93**	**92.31%**
				0.7500	97.00%	2000.00	46.31	91.12%
				0.6667	97.00%	2250.00	41.14	89.92%
6 kW	1250.00	45.87	395.43	1.2500	97.00%	1000.00	55.57	87.25%
				1.0000	**100.00%**	**1250.00**	**45.83**	**89.64%**
				0.8333	97.00%	1500.00	37.05	89.55%
4 kW	1000.00	38.19	433.27	1.0000	100.00%	1000.00	38.19	87.25%
				0.8000	**97.00%**	**1250.00**	**29.64**	**89.64%**
				0.6667	97.00%	1500.00	24.70	89.55%
2 kW	1000.00	19.11	554.47	1.0000	100.00%	1000.00	19.09	87.25%
				0.8000	**97.00%**	**1250.00**	**14.82**	**89.64%**
				0.6667	97.00%	1500.00	12.35	89.55%

Source: elaborated by the author.

APPENDIX F – RESULTS OF EACH GENERATOR OPERATION POINT SIMULATED FOR THE SIGMA ENGINE AND THE VOLVO XC60

Table A4 shows the analyzed operation points of the ICE-Generator for theFord Fiesta. Highlighted rows correspond to the selected Power Mode, while the strike rows correspond to operation points above continuous power limit. Gear ratios equal to 1 have a 'GearRatio2' efficiency of 100%, to simulate a shaft without gears.

TABLE A4 – RESULTS OF EACH GENERATOR OPERATION POINT ANALYZED FOR THE SIGMA ENGINE AND EMRAX 228 MATCH

Power Mode	ICE speed (rpm)	ICE load (Nm)	ICE BSFC (g/kWh)	GR2 Value	GR2 Efficiency	Gen. Speed (rpm)	Gen. Torque (Nm)	Gen. Efficiency
40 kW	3000	~~124.34~~	~~326~~	~~1.0000~~	~~100.00%~~	~~3000~~	~~124.41~~	~~86.38%~~
		127.32	317.9	**0.9231**	**97.00%**	**3250**	**114.86**	**95.84%**
				0.8571	97.00%	3500	106.66	94.18%
				0.8000	97.00%	3750	99.55	94.37%
37 kW	2750	~~124.96~~	~~333.69~~	~~1.0000~~	~~100.00%~~	~~2750~~	~~124.92~~	~~95.18%~~
		128.48	329.12	0.9167	97.00%	3000	115.11	86.38%
				0.8462	**97.00%**	**3250**	**106.26**	**95.83%**
				0.7857	97.00%	3500	98.65	94.18%
				0.7333	97.00%	3750	92.09	94.37%
30 kW	2250	~~124.53~~	~~341.47~~	~~1.0000~~	~~100.00%~~	~~2250~~	~~127.32~~	~~95.45%~~
		127.32	340.63	**0.9000**	**97.00%**	**2500**	**111.15**	**95.99%**
				0.8182	97.00%	2750	101.039	95.18%
				0.7500	97.00%	3000	92.62	86.38%
				0.6923	97.00%	3250	85.5	95.84%
26 kW	2250	110.36	342.45	1.1250	97.00%	2000	121.14	86.28%
				1.0000	100.00%	2250	110.99	95.37%
				0.9000	**97.00%**	**2500**	**96.92**	**95.99%**
				0.8182	97.00%	2750	88.17	95.18%
				0.7500	97.00%	3000	80.83	86.50%
20 kW	2000	~~95.39~~	~~344.32~~	~~1.3333~~	~~97.00%~~	~~1500~~	~~123.65~~	~~90.06%~~
		95.6	344.22	1.1429	97.00%	1750	105.98	94.86%
				1.0000	100.00%	2000	95.61	86.22%
				0.8889	97.00%	2250	82.44	95.35%
				0.8000	**97.00%**	**2500**	**74.19**	**95.99%**
15 kW	1750	81.85	356.18	1.4000	97.00%	1250	111.71	93.75%
				1.1667	97.00%	1500	93.07	90.06%
				1.0000	100.00%	1750	82.52	94.86%
				0.8750	97.00%	2000	69.82	86.22%
				0.7778	97.00%	2250	62.09	95.44%
				0.7000	**97.00%**	**2500**	**55.88**	**95.99%**
10 kW	1500	63.66	370.86	1.5000	97.00%	1000	92.69	86.04%
				1.2000	97.00%	1250	74.16	93.76%
				1.0000	100.00%	1500	63.71	90.06%
				0.8571	**97.00%**	**1750**	**52.97**	**94.86%**
				0.7500	97.00%	2000	46.35	86.21%
5 kW	1250	38.19	414.56	1.2500	97.00%	1000	46.32	86.04%
				1.0000	100.00%	1250	38.2	93.76%
				0.8333	97.00%	1500	30.88	90.06%
				0.7143	**97.00%**	**1750**	**26.47**	**94.86%**
				0.6250	97.00%	2000	23.16	86.21%

Source: elaborated by the author.

APPENDIX G – RESULTS OF EACH GENERATOR OPERATION POINT SIMULATED FOR THE PROTOTYPE ENGINE

Table A5 shows the operation points analyzed for the prototype engine when cupled to the Yasa P400 generator, while table A6 shows the operation points analyzed when coupled to the Yasa 750R generator. Highlighted rows correspond to the selected Power Mode, while the strike rows correspond to operation points above the continuous power limit. Gear ratios equal to 1 have a 'GearRatio2' efficiency of 100%, in order to simulate a shaft without gears.

TABLE A5 – RESULTS OF EACH GENERATOR OPERATION POINT ANALYZED FOR THE PROTOTYPE ENGINE AND THE YASA P400 MATCH

Power Mode	ICE speed (rpm)	ICE load (Nm)	ICE BSFC (g/kWh)	GR2 Value	GR2 Efficiency	Gen. Speed (rpm)	Gen. Torque (Nm)	Gen. Efficiency
50 kW (E100)	2500	190.98	399.4	0.5000	97.00%	5000	92.62	93.01%
				0.4545	97.00%	5500	84.19	93.15%
				0.4167	97.00%	6000	77.17	75.23%
				0.3846	**97.00%**	**6500**	**71.24**	**93.56%**
				0.3571	97.00%	7000	66.15	93.11%
			~~399.92~~	~~0.3333~~	~~97.00%~~	~~7500~~	~~59.33~~	~~92.25%~~

Source: elaborated by the author.

TABLE A6 – RESULTS OF EACH GENERATOR OPERATION POINT ANALYZED FOR THE PROTOTYPE ENGINE AND THE YASA 750R MATCH

Power Mode	ICE speed (rpm)	ICE load (Nm)	ICE BSFC (g/kWh)	GR2 Value	GR2 Efficiency	Gen. Speed (rpm)	Gen. Torque (Nm)	Gen. Efficiency
50 kW (E100)	2500	190.98	399.4	1.6667	97.00%	1500	308.7	82.00%
				1.2500	97.00%	2000	231.58	74.00%
				1.0000	100.00%	2500	191	64.00%
				0.9091	97.00%	2750	173.6	91.88%
				0.8333	**97.00%**	**3000**	**154.4**	**93.00%**
60 kW (E100+WI)	2505	251.59	341.95	1.6700	97.00%	1500	407.62	82.83%
				1.2525	97.00%	2000	305.7	74.67%
				1.0020	97.00%	2500	244.56	64.13%
				0.9109	97.00%	2750	222.3	91.86%
				0.8350	**97.00%**	**3000**	**203.78**	**93.00%**

Source: elaborated by the author.

APPENDIX H – LIST OF SIMULATIONS DONE IN THIS WORK

Table A7 details the Power Modes used in every simulation, from which each “X” was simulated for all seven driving cycles. On the other hand, table A8 details the characteristics of the simulations based on the four papers.

TABLE A7 – DETAILS OF FORD FIESTA AND VOLVO XC60 SIMULATIONS

	Vehicle	Ford Fiesta			Volvo XC60		
	Engine	**Sigma 1.6L**	**Prototype 1.0L**		**Sigma 1.6L**	**Prototype 1.0L**	
	Fuel injection strategy	**E100**	**E100**	**E100+WI**	**E100**	**E100**	**E100+WI**
	Generator	**EMRAX 208**	**Yasa P400**	**Yasa 750R**	**EMRAX 228**	**Yasa P400**	**Yasa 750R**
Power Mode	66 kW			X			X
	50 kW		X			X	
	40 kW				X		
	37 kW				X		
	30 kW				X		
	26 kW				X		
	23 kW	X					
	20 kW	X			X		
	16 kW	X					
	15 kW				X		
	13 kW	X					
	10 kW	X			X		
	6 kW	X					
	5 kW				X		
	4 kW	X					
	2 kW	X					

Source: elaborated by the author.

TABLE A8 – DETAILS OF SIMULATIONS BASED ON STATE OF THE ART PAPERS

Paper	Engine	Power Modes	Vehicle based on	Driving cycle FTP-75	HWFET	NEDC	US06	UDDS
Asfoor, Sharaf, and Beyerlein (2014)	Sigma 1.6L	40, 37, 30, 26, 20, 15, 10, and 5 kW	Volvo XC60	X	X	X	X	
Al-Samari (2017)		23, 20, 16, 13, 10, 6, 4, and 2 kW	Ford Fiesta					X
Solouk et al. (2017)					X		X	X
Williamson, Lukic, and Emadi (2006)					X			X
Asfoor, Sharaf, and Beyerlein (2014)	Prototype 1.0L	50 kW (E100) and 66 kW (E100+WI)	Volvo XC60	X	X	X	X	
Al-Samari (2017)			Ford Fiesta					X
Solouk et al. (2017)					X		X	X
Williamson, Lukic, and Emadi (2006)					X			X

Source: elaborated by the author.

APPENDIX I – CHARGING CAPACITY ANALYSIS FOR THE FORD FIESTA SIMULATIONS

Figure A23 to A29 show the variance in battery SOC of the Ford Fiesta through each driving cycle, however, some figures do not show all the Power Modes in order to facilitate their understanding. If the SOC stayed under 0.7 when the engine is on, then the power supplied by the engine was not enough to recharge the battery. Additionally, neither the 50 kW nor 66 kW Power Modes are shown, since both were able to recharge the battery in every driving cycle.

This analysis showed that the 2 kW was unable to recharge the battery in any of the seven driving cycles. Similarly, the 4 kW Power Mode only was able to recharge the battery for the Intense Traffic cycle. In addition, Power Modes lower than 16 kW were unable to recharge the battery during the HWFET cycle, while Power Modes lower than 20 kW were unable to recharge the battery during the US06 cycle.

FIGURE A23 – VARIATION IN THE BATTERY STATE OF CHARGE DURING THE FTP-75 DRIVING CYCLE, FOR THE FORD FIESTA

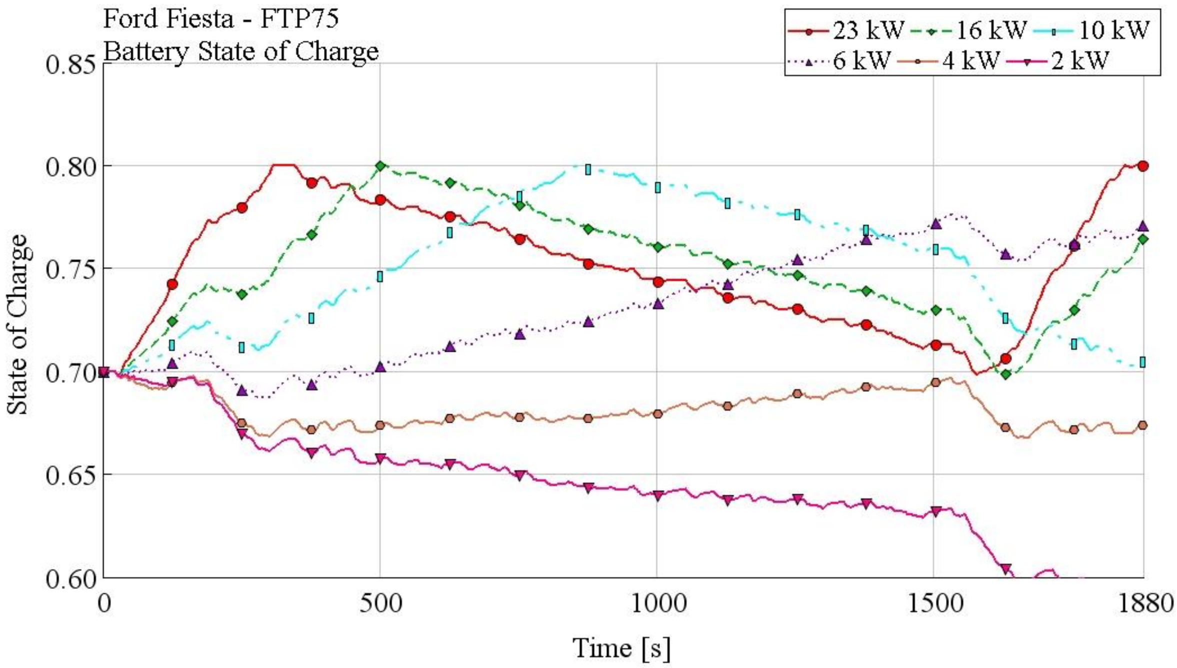

Source: elaborated by the author.

FIGURE A24 – VARIATION IN THE BATTERY STATE OF CHARGE DURING THE HWFET DRIVING CYCLE, FOR THE FORD FIESTA

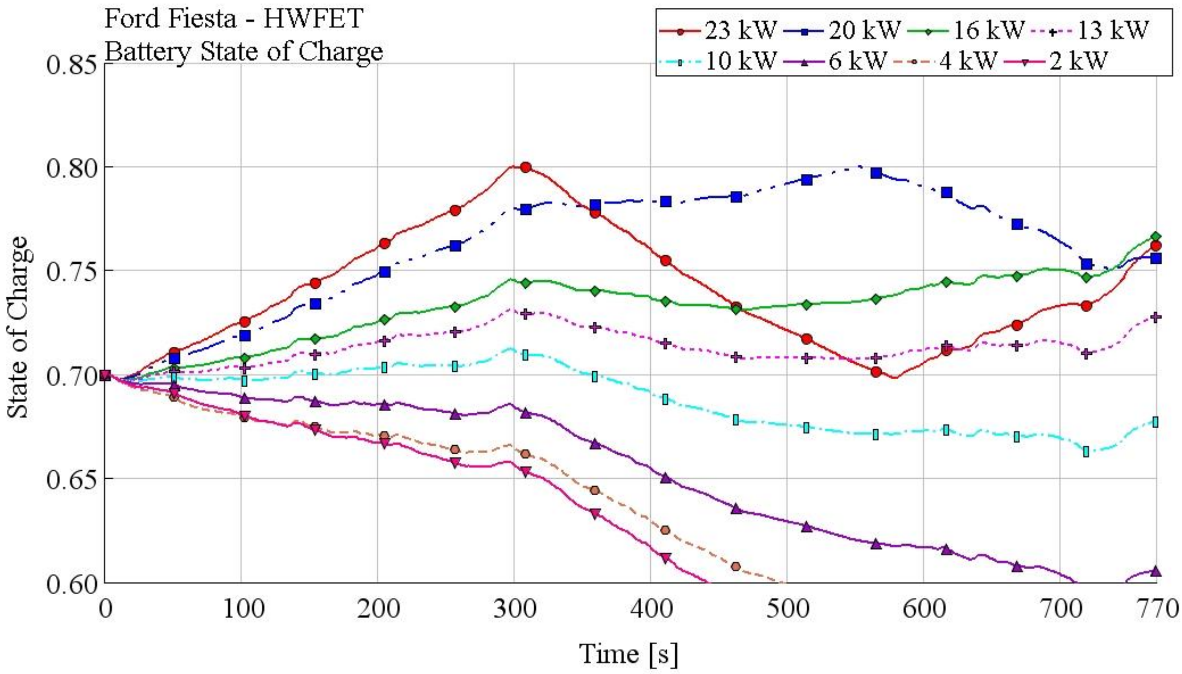

Source: elaborated by the author.

FIGURE A25 – VARIATION IN THE BATTERY STATE OF CHARGE DURING THE US06 DRIVING CYCLE, FOR THE FORD FIESTA

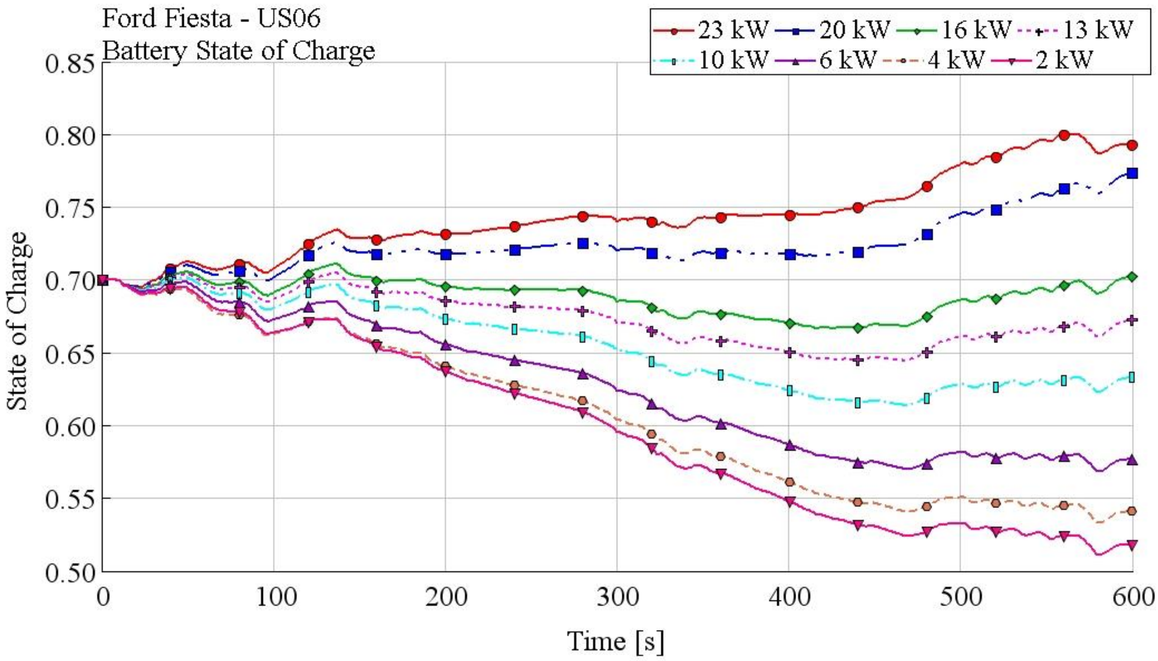

Source: elaborated by the author.

FIGURE A26 – VARIATION IN THE BATTERY STATE OF CHARGE DURING THE WLTC CLASS 3 DRIVING CYCLE, FOR THE FORD FIESTA

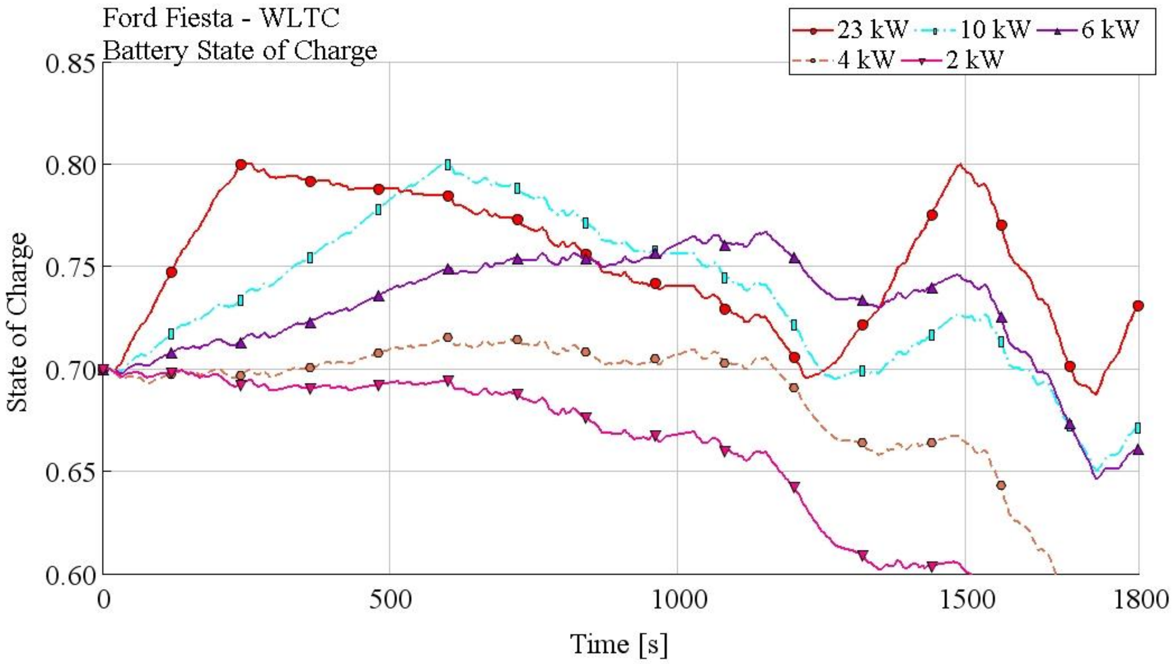

Source: elaborated by the author.

FIGURE A27 – VARIATION IN THE BATTERY STATE OF CHARGE DURING THE NEDC DRIVING CYCLE, FOR THE FORD FIESTA

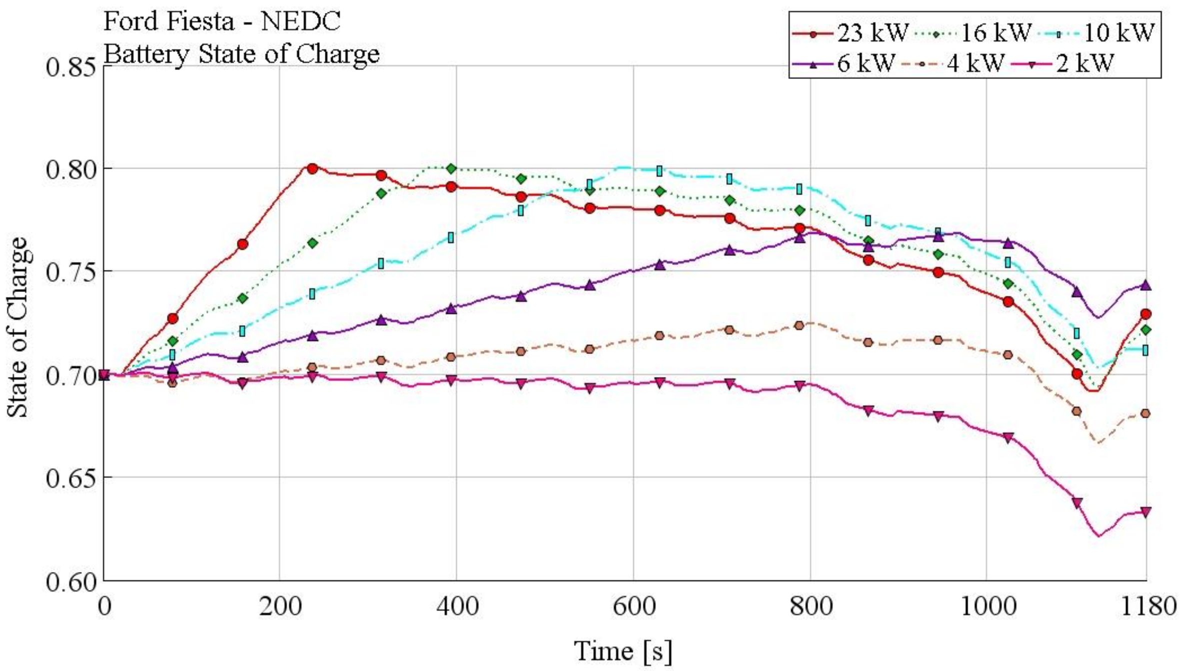

Source: elaborated by the author.

FIGURE A28 – VARIATION IN THE BATTERY STATE OF CHARGE DURING THE INTENSE TRAFFIC REAL DRIVING CYCLE, FOR THE FORD FIESTA

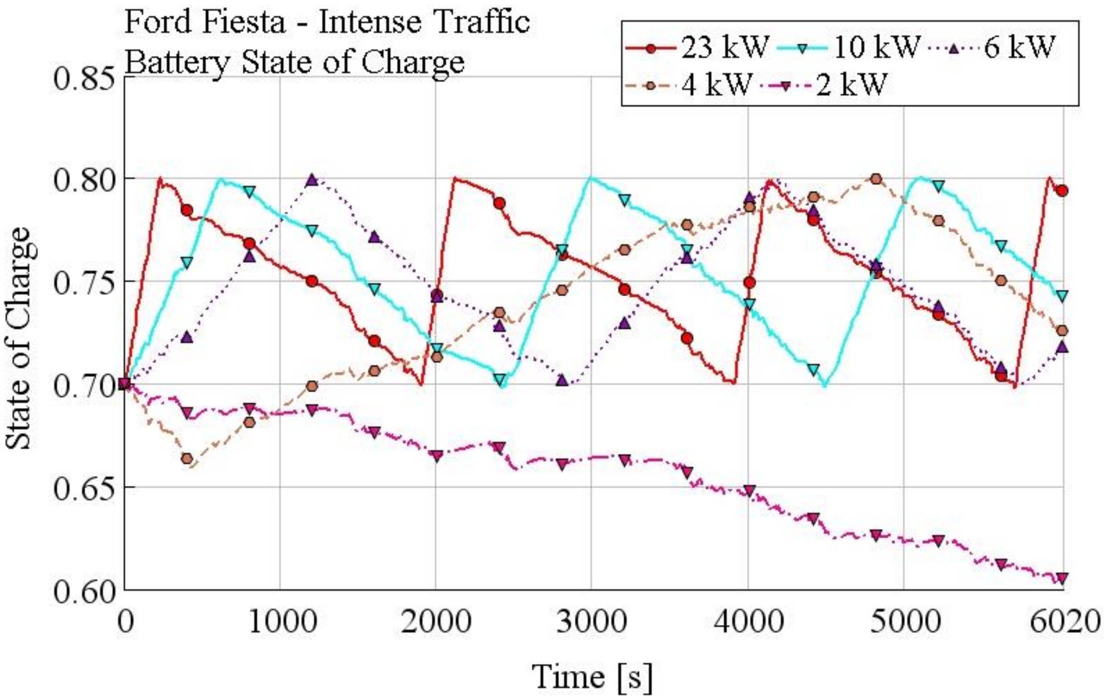

Source: elaborated by the author.

FIGURE A29 – VARIATION IN THE BATTERY STATE OF CHARGE DURING THE LOW TRAFFIC REAL DRIVING CYCLE, FOR THE FORD FIESTA

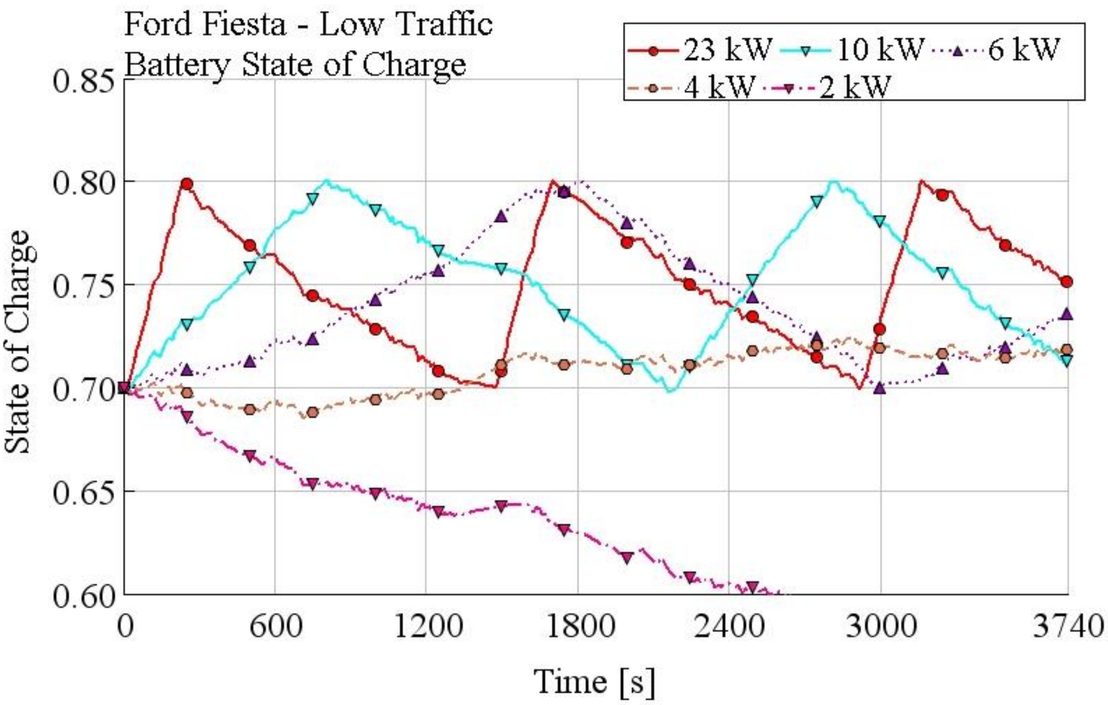

Source: elaborated by the author.

APPENDIX J – CHARGING CAPACITY ANALYSIS FOR THE VOLVO XC60 SIMULATIONS

Figure A30 to A36 show the variance in battery SOC of the Volvo XC60 through each driving cycle, however, some figures do not show all the Power Modes in order to facilitate their understanding. If the SOC stayed under 0.7 when the engine is on, then the power supplied by the engine was not enough to recharge the battery. Additionally, neither the 50 kW nor 66 kW Power Modes are shown, since both were able to recharge the battery in every driving cycle.

This analysis shows that the 5 kW Power Mode was unable to recharge the battery in any of the seven driving cycles. In addition, Power Modes lower than 20 kW were unable to charge the battery during the HWFET cycle, while Power Modes lower than 30 kW were unable to recharge the battery during the US06 cycle.

FIGURE A30 – VARIATION IN THE BATTERY STATE OF CHARGE DURING THE FTP-75 DRIVING CYCLE, FOR THE VOLVO XC60

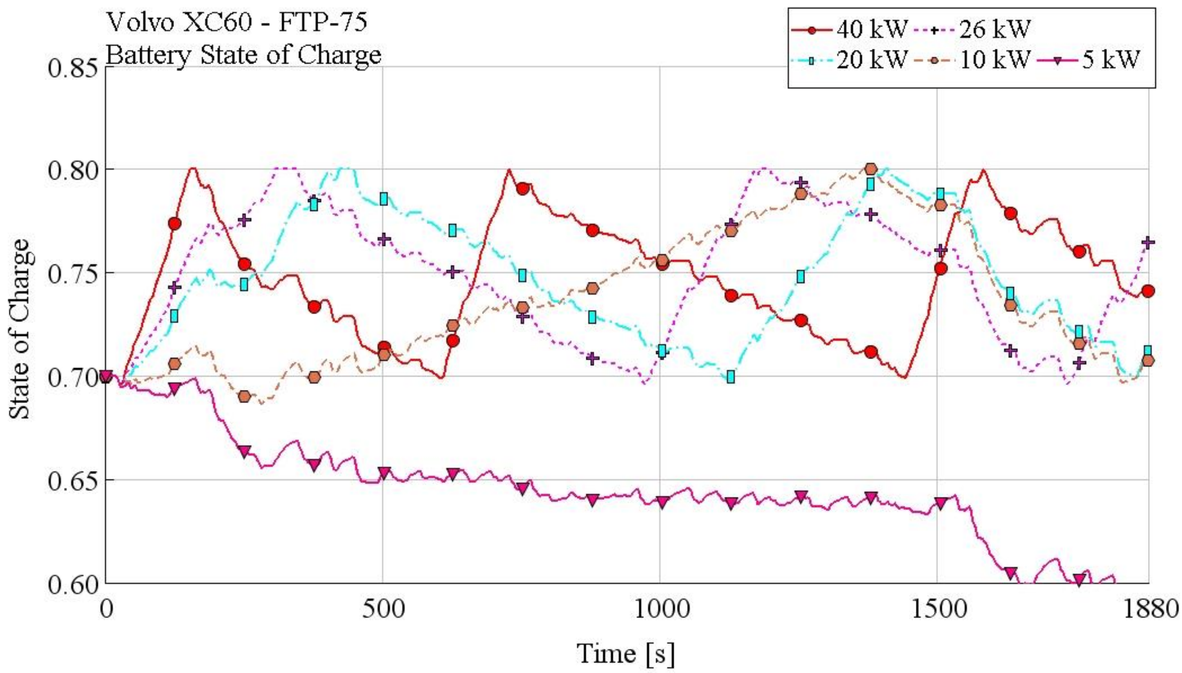

Source: elaborated by the author.

FIGURE A31 – VARIATION IN THE BATTERY STATE OF CHARGE DURING THE HWFET DRIVING CYCLE, FOR THE VOLVO XC60

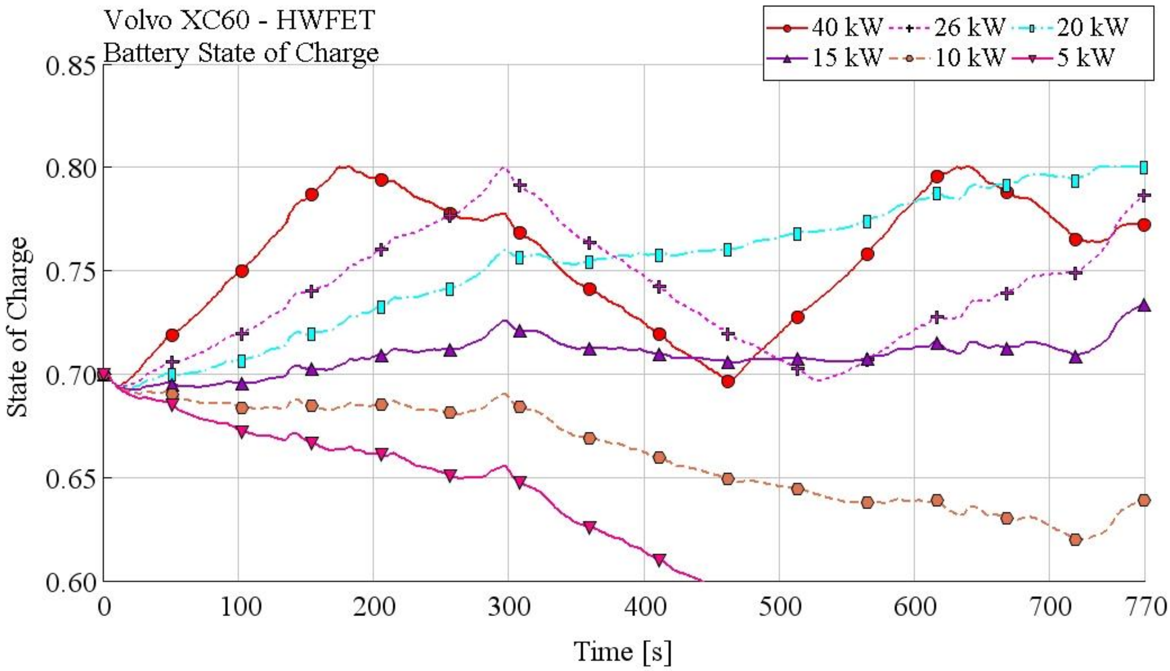

Source: elaborated by the author.

FIGURE A32 – VARIATION IN THE BATTERY STATE OF CHARGE DURING THE US06 DRIVING CYCLE, FOR THE VOLVO XC60

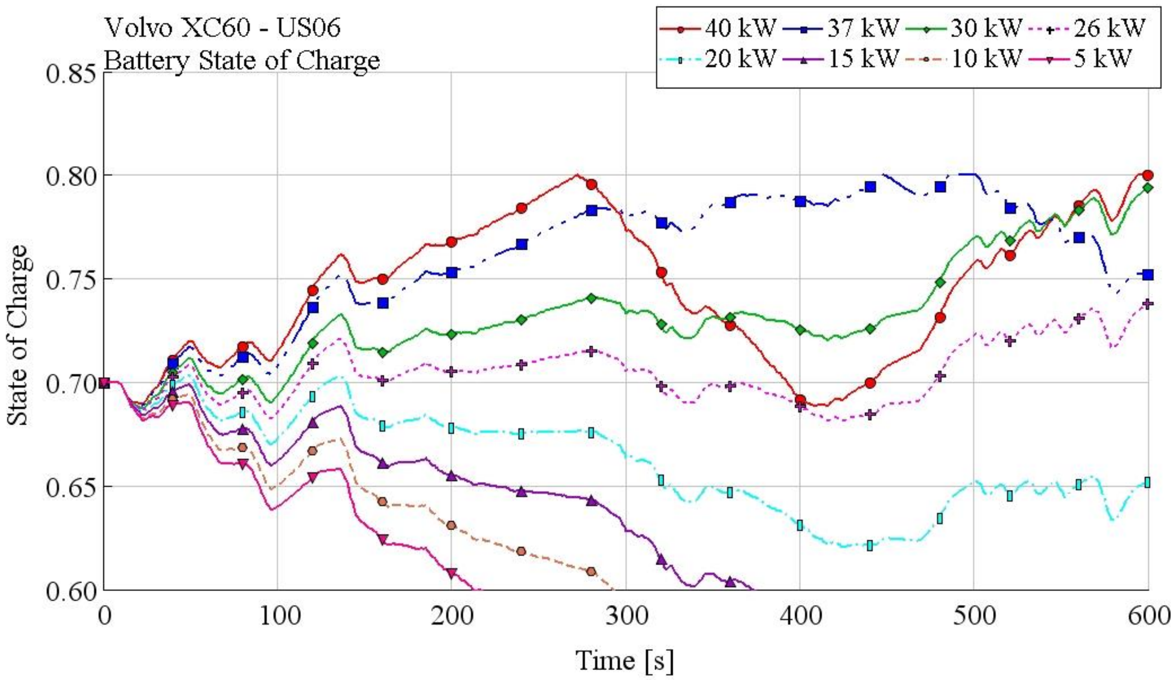

Source: elaborated by the author.

FIGURE A33 – VARIATION IN THE BATTERY STATE OF CHARGE DURING THE NDEC DRIVING CYCLE, FOR THE VOLVO XC60

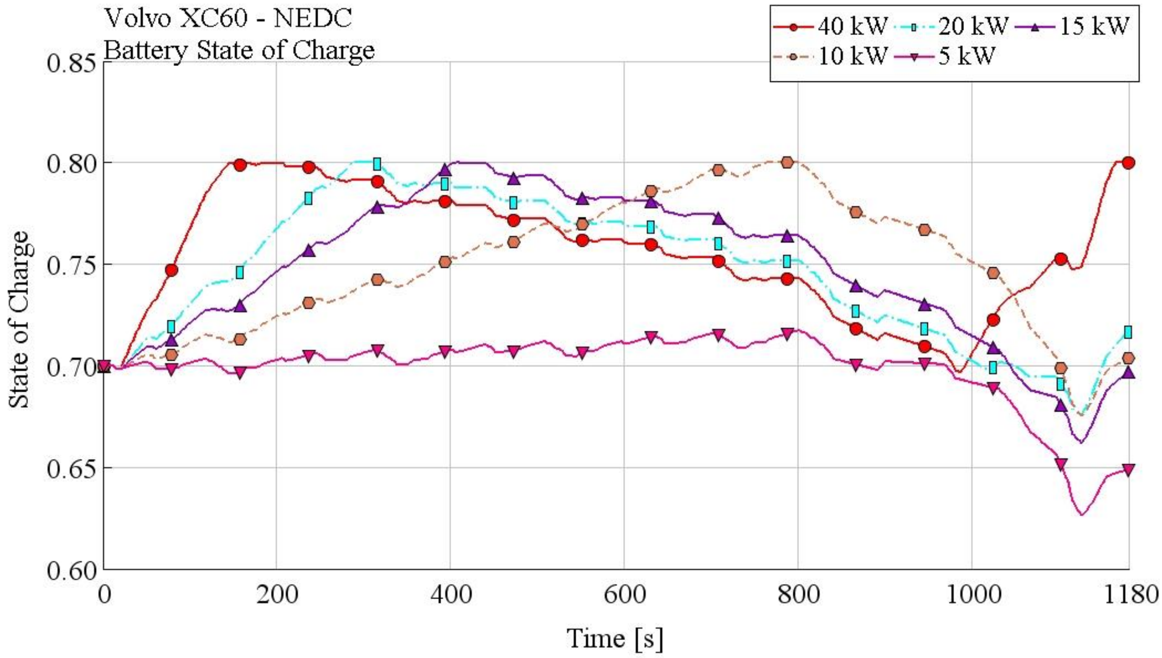

Source: elaborated by the author.

FIGURE A34 – VARIATION IN THE BATTERY STATE OF CHARGE DURING THE WLTC CLASS 3 DRIVING CYCLE, FOR THE VOLVO XC60

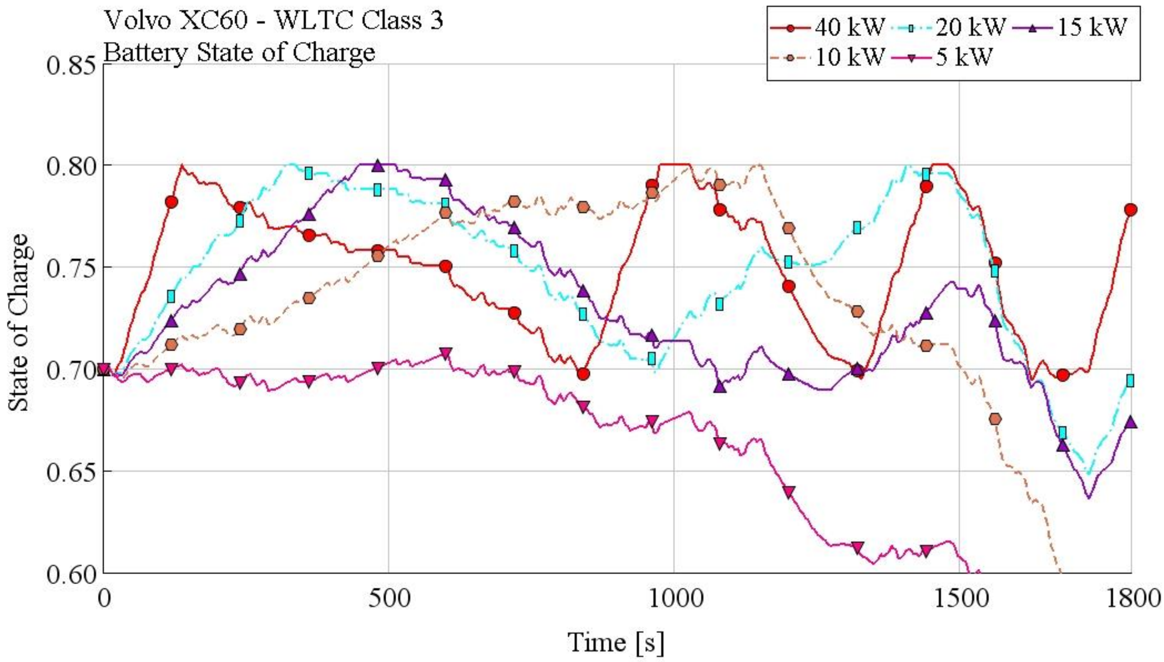

Source: elaborated by the author.

FIGURE A35 – VARIATION IN THE BATTERY STATE OF CHARGE DURING THE LOW TRAFFIC REAL DRIVING CYCLE, FOR THE VOLVO XC60

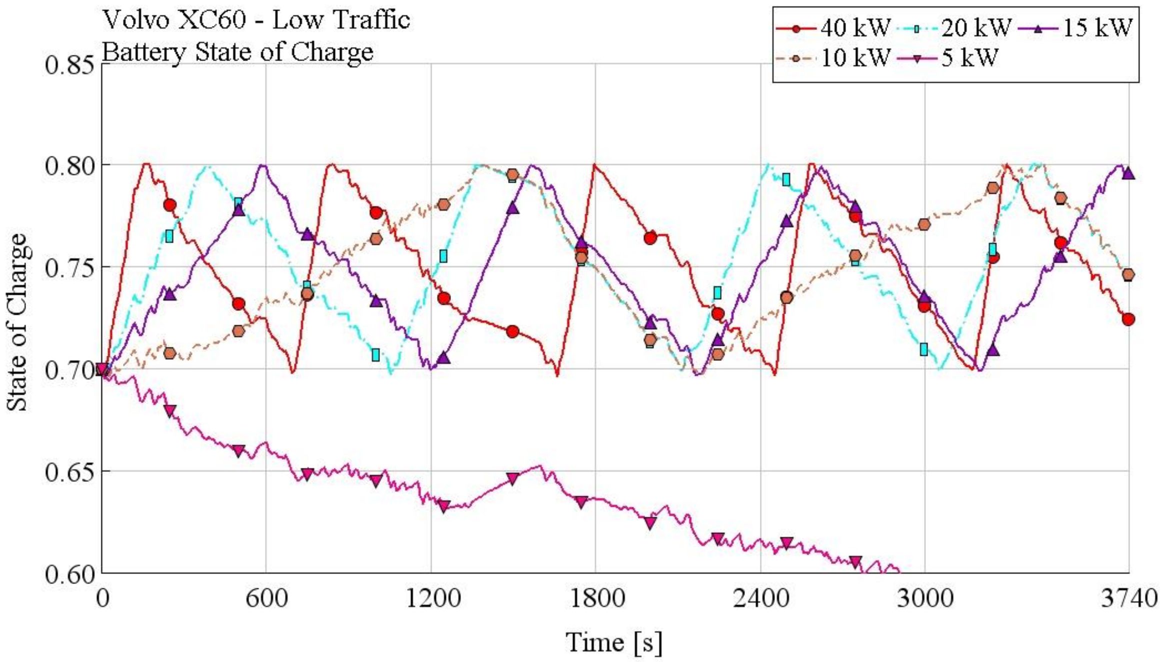

Source: elaborated by the author.

FIGURE A36 – VARIATION IN THE BATTERY STATE OF CHARGE DURING THE INTENSE TRAFFIC REAL DRIVING CYCLE, FOR THE VOLVO XC60

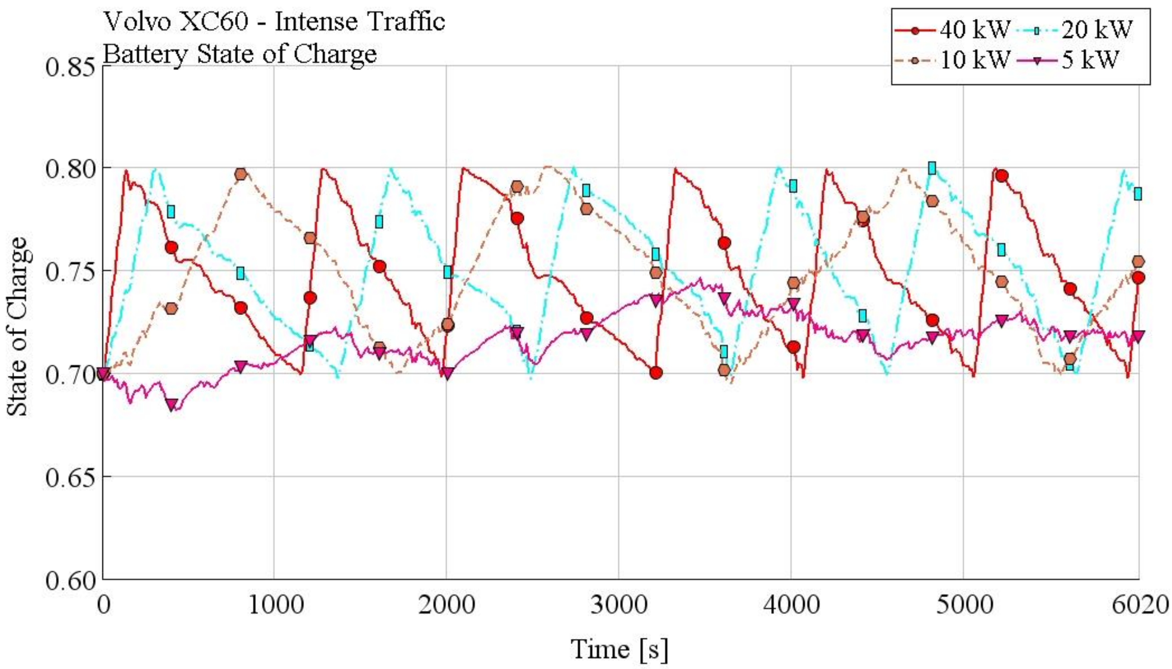

Source: elaborated by the author.

APPENDIX K – CHARGING CAPACITY ANALYSIS FOR SIMULATIONS BASED ON ASFOOR, SHARAF, AND BEYERLEIN (2014)

Figure A37 to A40 show the variance in battery SOC through each driving cycle for the simulations based on Asfoor, Sharaf, and Beyerlein (2014). If the SOC stayed under 0.5 when the engine is on, then the power supplied by the engine was not enough to recharge the battery. Additionally, neither the 50 kW nor 66 kW Power Modes are shown, since both were able to recharge the battery in every driving cycle.

FIGURE A37 – VARIATION IN THE BATTERY SOC DURING THE FTP75 CYCLE, SIMULATION BASED ON ASFOOR, SHARAF, AND BEYERLEIN (2014)

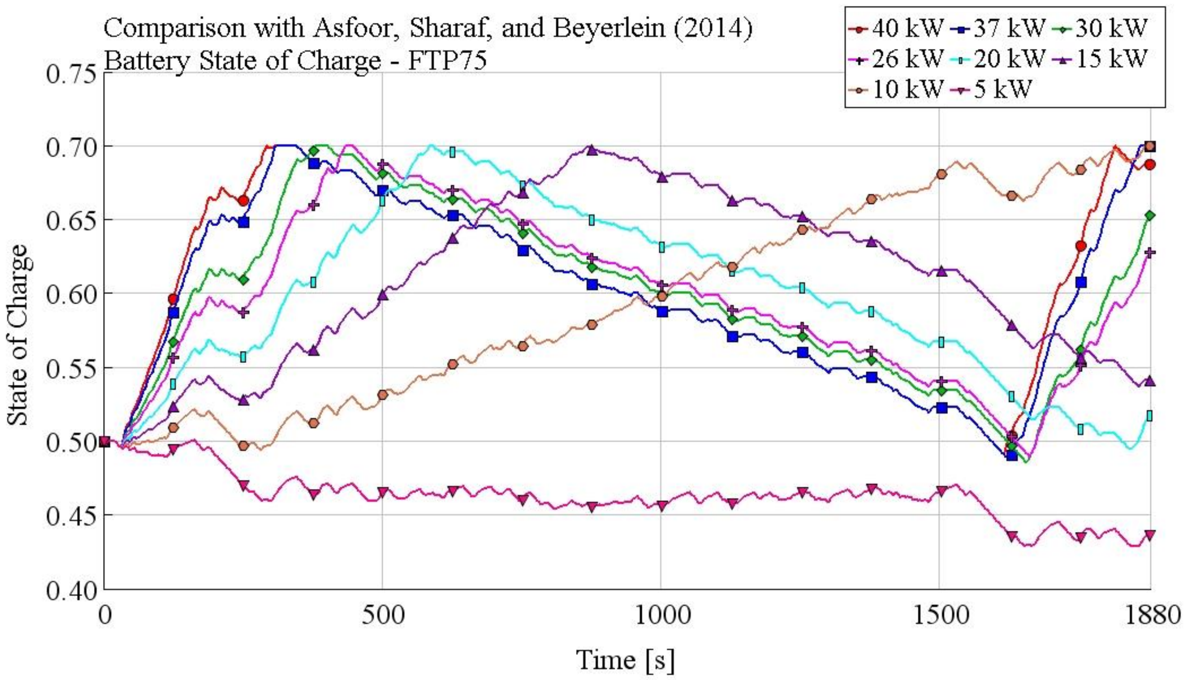

Source: elaborated by the author.

FIGURE A38 – VARIATION IN THE BATTERY SOC DURING THE HWFET CYCLE, SIMULATION BASED ON ASFOOR, SHARAF, AND BEYERLEIN (2014)

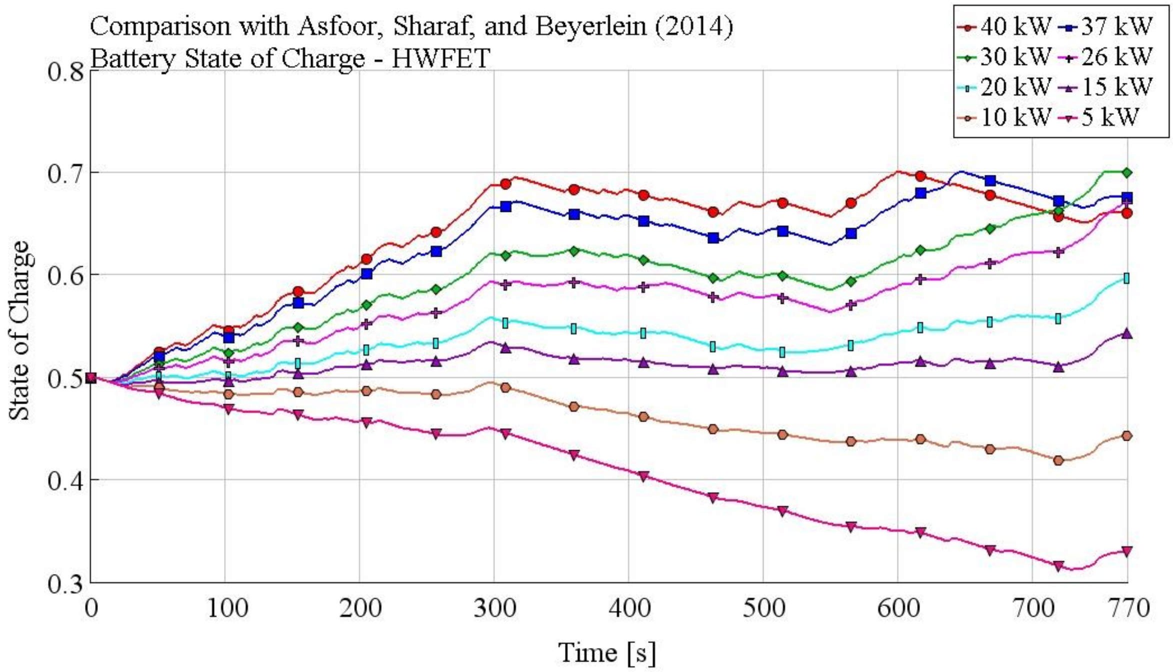

Source: elaborated by the author.

FIGURE A39 – VARIATION IN THE BATTERY SOC DURING THE US06 CYCLE, SIMULATION BASED ON ASFOOR, SHARAF, AND BEYERLEIN (2014)

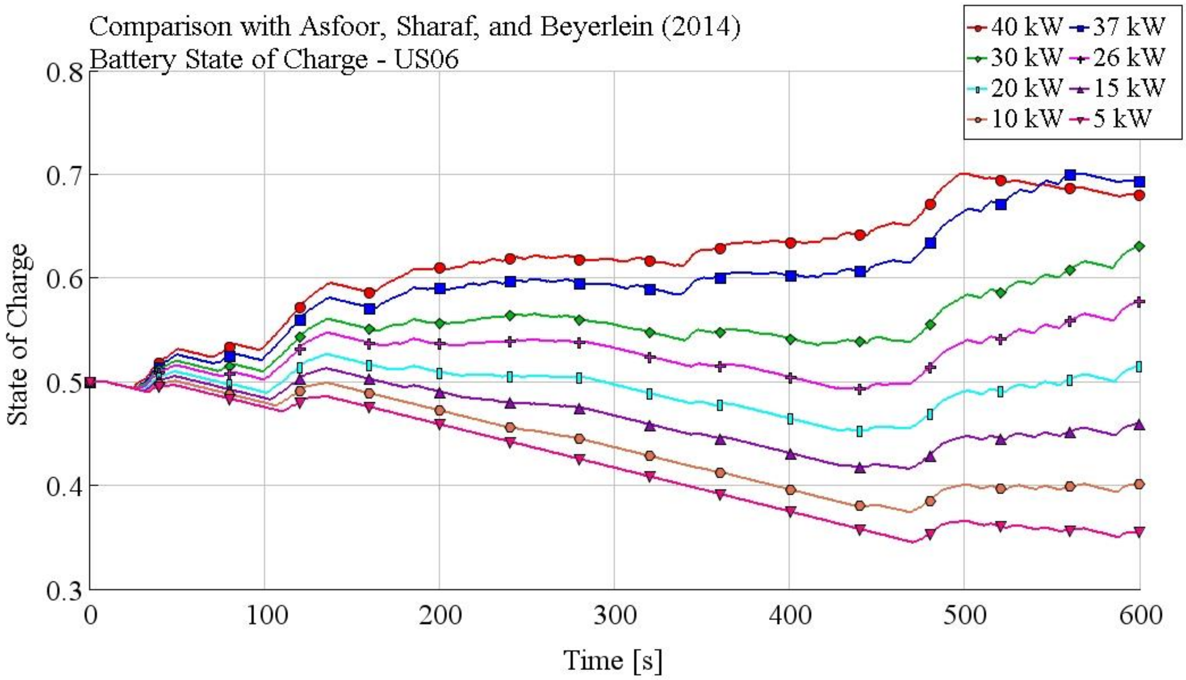

Source: elaborated by the author.

FIGURE A40 – VARIATION IN THE BATTERY SOC DURING THE NEDC CYCLE, SIMULATION BASED ON ASFOOR, SHARAF, AND BEYERLEIN (2014)

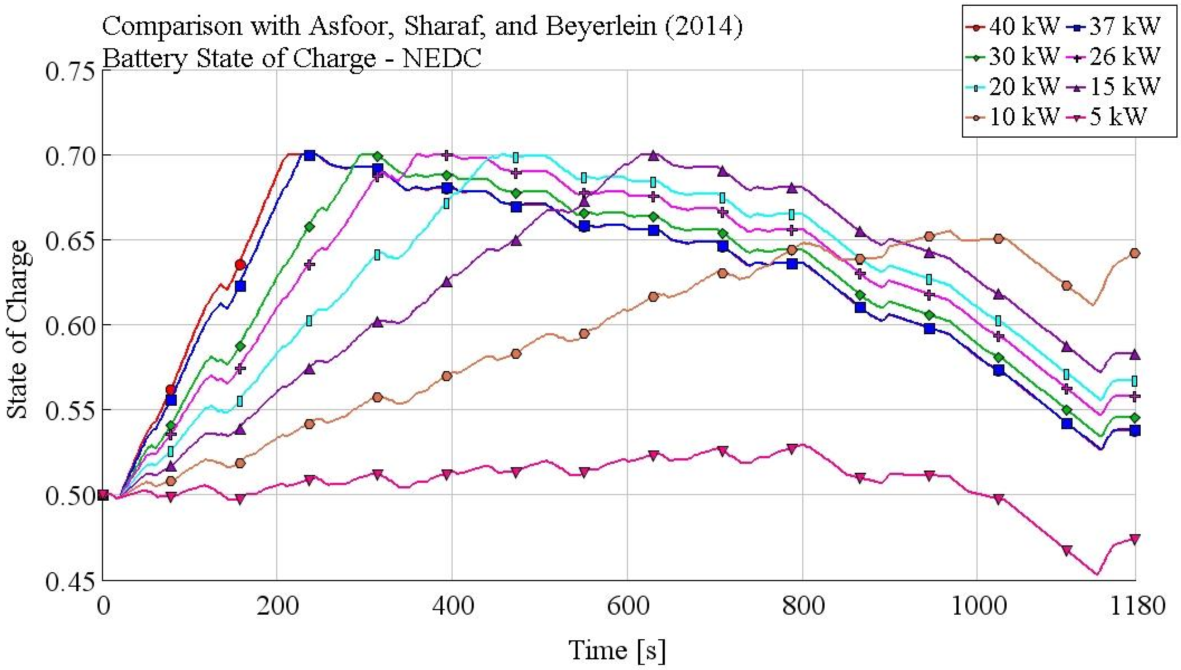

Source: elaborated by the author.

APPENDIX L – CHARGING CAPACITY ANALYSIS FOR SIMULATIONS BASED ON SOLOUK ET AL. (2017)

Figure A41 to A43 show the variance in battery SOC through each driving cycle for the simulations based on Solouk et al. (2017). If the SOC stayed under 0.3 when the engine is on, then the power supplied by the engine was not enough to recharge the battery. Additionally, neither the 50 kW nor 66 kW Power Modes are shown, since both were able to recharge the battery in every driving cycle.

FIGURE A41 – VARIATION IN THE BATTERY SOC DURING THE HWFET CYCLE, SIMULATION BASED ON SOLOUK ET AL. (2017)

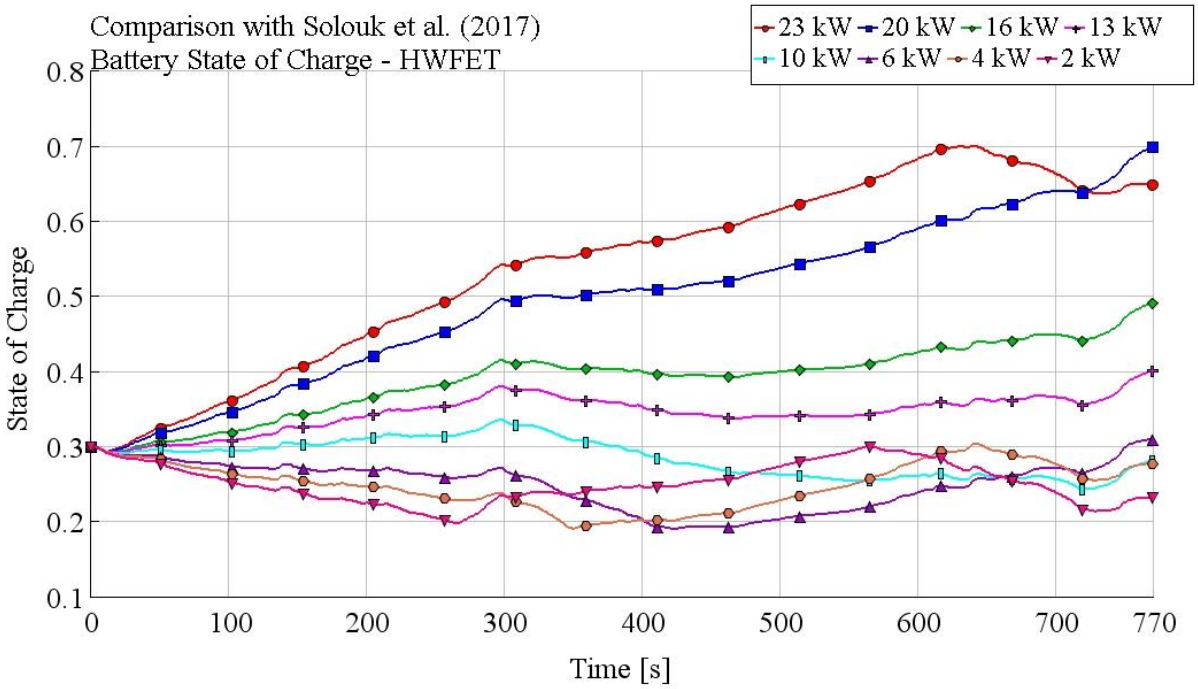

Source: elaborated by the author.

FIGURE A42 – VARIATION IN THE BATTERY SOC DURING THE US06 CYCLE, SIMULATION BASED ON SOLOUK ET AL. (2017)

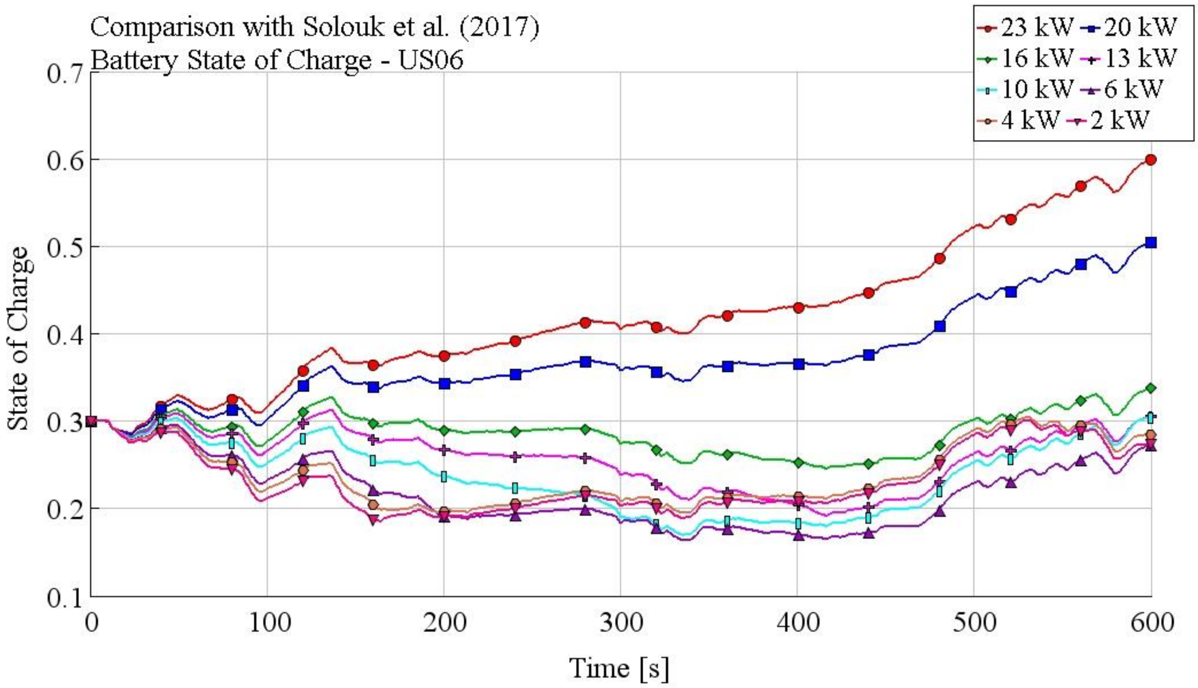

Source: elaborated by the author.

FIGURE A43 – VARIATION IN THE BATTERY SOC DURING THE UDDS CYCLE, SIMULATION BASED ON SOLOUK ET AL. (2017)

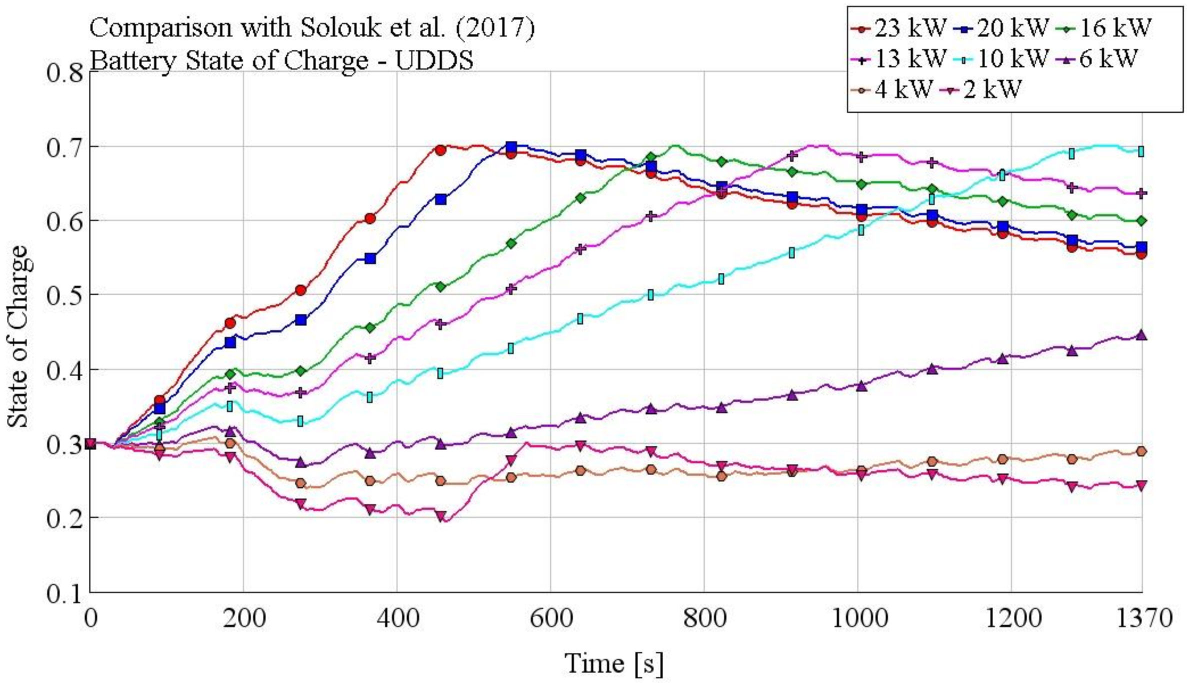

Source: elaborated by the author.

APPENDIX M – CHARGING CAPACITY ANALYSIS FOR SIMULATIONS BASED ON WILLIAMSON, LUKIC, AND EMADI (2006)

Figure A44 and A45 show the variance in battery SOC through each driving cycle for the simulations based on Williamson, Lukic, and Emadi (2006). If the SOC stayed under 0.7 when the engine is on, then the power supplied by the engine was not enough to recharge the battery. Additionally, neither the 50 kW nor 66 kW Power Modes are shown, since both were able to recharge the battery in every driving cycle.

FIGURE A44 – VARIATION IN THE BATTERY SOC DURING THE HWFET CYCLE, SIMULATION BASED ON WILLIAMSON, LUKIC, AND EMADI (2006)

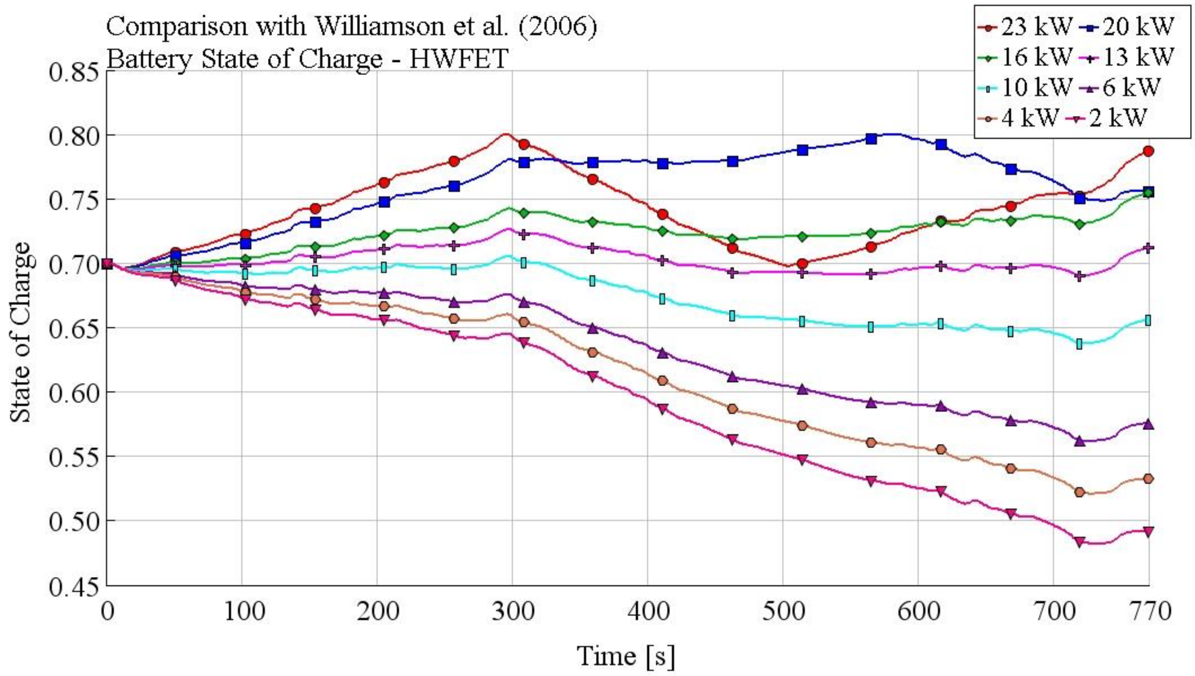

Source: elaborated by the author.

FIGURE A45 – VARIATION IN THE BATTERY SOC DURING THE UDDS CYCLE, SIMULATION BASED ON WILLIAMSON, LUKIC, AND EMADI (2006)

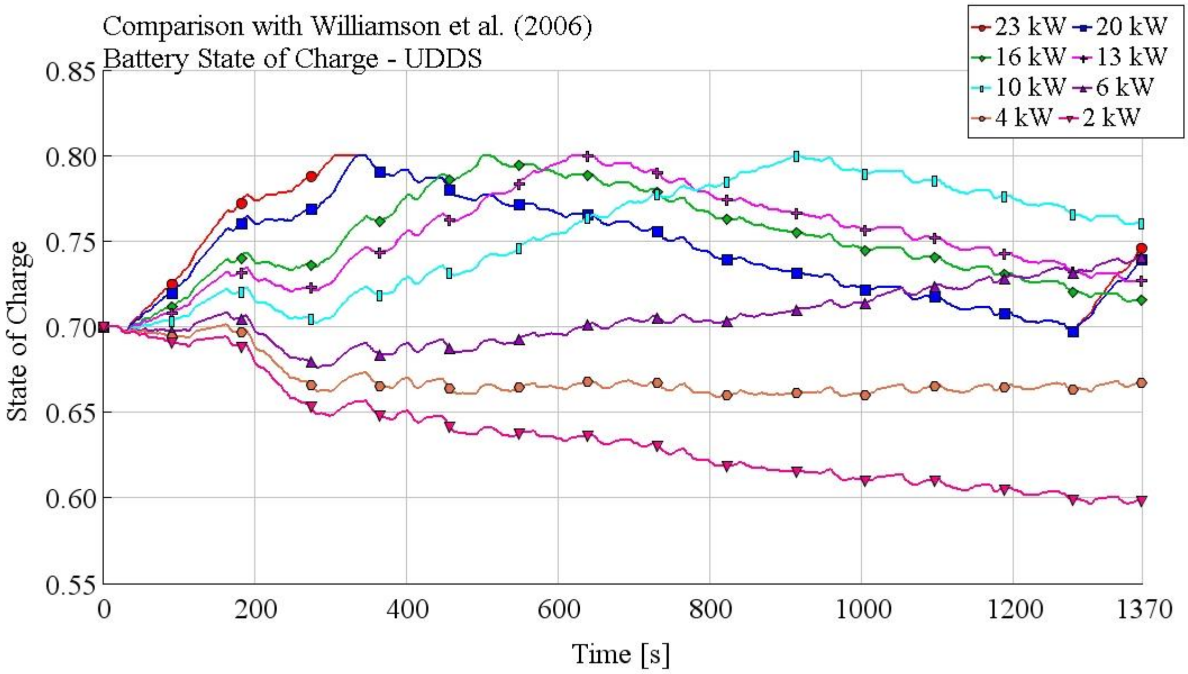

Source: elaborated by the author.

APPENDIX N – CHARGING CAPACITY ANALYSIS FOR SIMULATIONS BASED ON AL-SAMARI (2017)

Figure A46 shows the variance in battery SOC through the UDDS cycle for the simulations based on Al-Samari (2017). If the SOC stayed under 0.7 when the engine is on, then the power supplied by the engine was not enough to recharge the battery. Additionally, neither the 50 kW nor 66 kW Power Modes are shown, since both were able to recharge the battery through the UDDS cycle.

FIGURE A46 – VARIATION IN THE BATTERY SOC DURING THE UDDS CYCLE, SIMULATION BASED ON AL-SAMARI (2017)

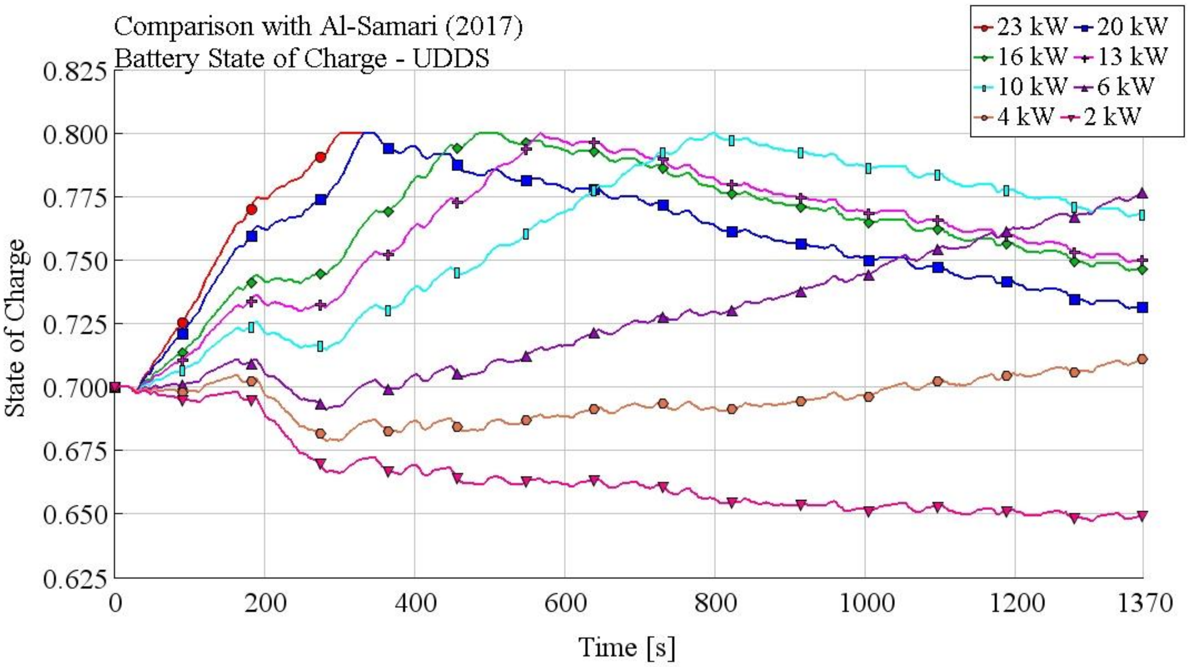

Source: elaborated by the author.

ANNEX A – GT-SUITE MODEL FOR THE BATTERY OBJECT

Conventional SOC Model: The energy that flows in and out of the battery is calculated from a First Principle analysis of the battery/motor circuit:

$$IV_{OC} - I^2 R_{int} - C * P_{REQUEST} = 0$$

For each time step, the above quadratic equation is solved for instantaneous current:

$$I = \frac{-V_{OC} \pm \sqrt{{V_{OC}}^2 - 4(-R_{int})(-P_{request} * C)}}{2(-R_{int})}$$

If the equation above returns real roots, then it means that the battery can supply the power requested ($P_{supplied}$=$P_{requested}$), thus:

$$I = \frac{V_{OC} - \sqrt{{V_{OC}}^2 - 4\mathrm{C} * R_{int} * P_{request}}}{2 * R_{int}}$$

$$V = V_{OC} - IR_{int}$$

Also, it is possible to obtain imaginary roots during battery discharge, when $P_{REQUEST}$ is negative, then the following equations are used:

$$I = I_{max} = \frac{V_{OC}}{2R_{int}}$$

$$V = V_{OC} - I_{max} R_{int}$$

$$P_{supplied} = I_{max} * V$$

Therefore, the maximum power that the battery can supply is given by:

$$P_{max} = \frac{{V_{OC}}^2}{4R_{int}}$$

In both cases, with real and imaginary roots, the instantaneous current is integrated over time to obtain the used capacity in Ah. Therefore, the state of charge of the battery is given by the next equation:

$$SOC = \frac{Instantaneous\ Capacity}{Maximum\ Capacity}$$

Where:

$$Instantaneous\ Capacity = Q - \int_t I\ dt$$

$$Q_0 = SOC_0 * Maximum\ Capacity$$

(GAMMA TECHNOLOGIES, [s.d.])

ANNEX B – GT-SUITE MODEL OF THE MOTORGENERATORMAP OBJECT

Power-Brake Load: The next equations are used when the “Power-Brake” is selected as the “Load Control Option” of a ‘MotorGeneratorMap’ object.

The electric power request is calculated by:

$$P_E = P_I / E(\omega, T_B) \qquad when\ P_I > 0$$

$$P_E = P_I * E(\omega, T_B) \qquad when\ P_I < 0$$

The user must define a Static Torque Limit (T_S) when P_I<0.

The indicated power, indicated torque and brake torque are calculated by:

$$P_I = T_I * \omega$$

$$T_I = T_B + T_F$$

$$T_B = \frac{P_B}{\omega} = \frac{P_B}{\pi * rpm/30}$$

Where:

- P_E is the electrical power request (from map);
- P_I is the indicated power;
- $E(\omega,T_B)$ is the electrical-mechanical conversion efficiency (function of speed and brake torque);
- T_I is the indicated torque;
- ω is the machine speed, in rad/s;
- T_B is the brake torque;
- T_F is the friction torque (function of speed), and;
- P_B is the mechanical brake power (from map).

(GAMMA TECHNOLOGIES, [s.d.])

ANNEX C – GT-SUITE MODEL OF THE ENGINESTATE OBJECT

The relationship between BMEP and Torque used by the 'EngineState' object is given by:

$$BMEP = \frac{2 * \pi * T_{ENG} * n}{V}$$

Where:

- T_{ENG} is the torque before any accessory loads are connected;
- V is the engine displacement, and;
- n is the number of crank revolutions per power stroke (2 for 4-strokes and 1 for 2-strokes engines).

Additionally, there is a difference between the engine torque taken from the Mechanical Output Map and the load torque seen at the engine flywheel. This relationship is calculated using the following equation:

$$T_{ENG} = T_{LOAD} - T_{ACC} + I * \alpha$$

Where:

- T_{ENG} is the torque from the mechanical output map;
- T_{LOAD} is the torque that is output at the flywheel;
- T_{ACC} are the accessory loads imposed in the engine;
- I is the engine inertia, and;
- α is the engine angular acceleration.

However, if the engine speed is keeped constant and no accessory load is imposed on the engine, then T_{ENG}=T_{LOAD} (GAMMA TECHNOLOGIES, [s.d.]).

ANNEX D – GT-SUITE MODEL OF THE CONTROLLERHEVEHICLE OBJECT

Calculation of Power Demand: The power demand calculated by the 'ControllerHEVehicle' includes the tire rolling resistance, aerodynamic drag, the road grade, and road curvature. The torque request also includes the torque necessary to accelerate the vehicle and cargo mass as well as major vehicle system inertias and the overall driveline efficiency. The torque request is calculated based on the acceleration request, according to the next equation:

$$Acc\ Demand = \frac{Vehicle\ Speed_{target} - Vehicle\ Speed_{actual}}{1s} * Precontrol\ Agressivness$$

If the 'Trailer' template is used, the effect of its additional mass is not taken into account unless its mass is added to the Trailer, Passenger and Cargo Mass attribute. Additionally, the transmission input and output inertias are assumed as a fraction of the engine inertia (GAMMA TECHNOLOGIES, [s.d.]).

ANNEX E – GT-SUITE MODEL OF THE BRAKECONTROLLER OBJECT

According to Gamma Technologies ([s.d.]), the ‘BrakeController’ object calculates the *Brake Pedal Position* signal using the next equation:

$$Brake\ Pedal = -\left(\frac{30000 * Brake\ Demand}{2 * \pi * Axle\ Speed * Brake\ Torque_{max} * Number_{Axles}}\right) * 100\%$$

In addition, the brake map used was presented in figure A7 of appendix A.

ANNEX F – DATA MAPS USED FOR THE SIGMA 1.6L ENGINE

Table A9 shows the emission and consumption maps of the Sigma engine.

TABLE A9 – CHARACTERISTICS OF THE SIGMA ENGINE

Power	Torque	Speed	Throttle Position	IMEP	BSFC	Emissions				
						CO	CO_2	H_2O	HC	NO
kW	Nm	RPM	%	Bar	g/kWh	g/kWh	g/kWh	g/kWh	g/kWh	g/kWh
0.22	2.84	743.48	5.30	0.5300	1898.26	110.41	3317.43	1981.82	54.84	0.55
1.37	13.08	999.72	6.70	1.3151	650.96	81.53	1098.03	732.74	8.25	1.66
2.34	22.39	998.79	7.50	2.0052	520.35	20.52	953.40	631.56	4.59	4.62
4.11	39.27	999.88	8.69	3.2408	417.60	17.63	763.12	510.69	3.75	5.85
1.44	11.04	1249.01	7.00	1.1347	726.23	40.23	1303.07	788.41	9.80	2.05
3.43	26.23	1249.51	8.50	2.2460	480.43	20.67	878.13	572.49	4.03	4.79
5.60	42.81	1249.47	9.97	3.5227	407.20	18.30	743.52	491.95	3.24	5.97
6.89	52.67	1249.88	10.63	4.2982	386.47	19.44	702.61	471.79	3.01	6.58
2.08	13.21	1503.40	7.80	1.2953	668.05	32.65	1215.73	836.06	5.31	2.08
6.69	42.59	1480.50	10.70	3.5144	406.14	16.91	745.49	513.44	2.58	6.12
10.75	68.48	1466.09	13.10	5.5752	370.55	24.68	660.59	457.86	4.19	7.11
14.26	90.77	1520.42	16.48	7.3302	360.67	20.37	638.39	440.00	7.83	8.88
18.81	119.73	1471.40	93.70	9.6689	356.07	16.44	632.36	429.01	9.06	10.52
1.78	9.71	1749.27	7.90	1.0329	796.21	33.05	1453.22	1017.65	8.13	1.73
9.15	49.94	1749.19	12.18	4.1462	384.39	15.51	707.17	489.96	2.14	6.17
12.55	68.51	1749.70	14.20	5.6101	365.52	21.28	657.44	462.83	3.77	6.93
17.15	93.61	1749.97	18.50	7.6052	351.86	18.12	629.43	443.82	6.23	8.59
22.27	121.52	1750.54	93.70	9.7808	346.26	12.41	629.58	443.96	5.53	10.19
2.79	13.30	1999.40	8.90	1.3401	670.21	39.03	1211.96	863.68	4.54	2.51
8.34	39.81	1999.46	12.00	3.3744	417.53	21.61	760.76	541.14	2.30	5.58
10.51	50.17	1999.94	13.00	4.2000	388.87	17.32	712.74	506.32	2.21	6.38
15.55	74.25	2000.04	15.90	6.1135	361.25	20.22	653.36	467.91	2.88	7.41
19.95	95.24	1998.96	19.58	7.7937	343.50	15.07	627.06	445.03	3.00	9.07
25.78	123.08	1998.26	93.69	9.9569	348.12	11.97	627.15	448.88	7.97	10.41
4.82	20.47	2250.77	10.50	1.9346	544.68	19.39	1007.98	712.77	2.36	4.29
10.16	43.12	2248.12	13.10	3.6879	409.47	13.91	757.73	533.66	2.17	6.98
17.54	74.46	2248.76	16.78	6.1232	359.15	13.17	661.82	465.95	2.37	8.87
22.27	94.50	2249.66	20.08	7.6888	344.37	12.29	633.71	444.16	2.78	9.39
30.22	128.24	2242.21	93.70	10.3930	341.53	9.46	623.92	436.94	5.97	10.76
4.46	17.03	2499.86	10.59	1.6735	591.74	19.27	1097.98	765.69	2.53	4.24
11.46	43.78	2499.43	13.93	3.7305	407.27	12.27	756.58	525.37	1.99	7.17
17.50	66.86	2498.98	16.80	5.5356	368.08	11.95	681.48	472.81	2.14	8.70
24.89	95.09	2498.91	21.28	7.7637	346.37	11.70	639.48	441.48	2.41	8.95
33.84	129.28	2499.45	93.70	10.5422	341.55	9.29	623.16	433.41	6.36	11.13
3.95	13.72	2749.55	10.60	1.4614	678.67	22.98	1256.46	873.42	3.43	5.02
11.38	39.53	2749.45	14.20	3.4498	423.08	13.28	785.66	544.63	1.87	6.94
20.40	70.82	2749.60	18.10	5.8460	364.36	13.97	672.28	466.21	1.74	7.80
27.74	96.32	2748.53	22.90	7.8251	349.61	18.30	635.94	444.13	2.19	8.28
37.69	130.86	2749.06	93.69	10.5755	335.38	9.77	618.32	456.59	3.55	10.49
3.18	10.11	3002.44	10.60	1.2506	840.55	33.95	1546.70	1149.25	4.55	3.55
12.41	39.50	2998.57	14.80	3.4642	422.51	14.32	782.86	576.57	1.90	7.36
21.10	67.15	2997.64	18.50	5.5792	368.99	12.59	683.71	500.79	1.60	7.56
29.43	93.69	2991.94	23.13	7.6099	347.57	10.10	646.89	466.89	1.47	8.63
40.82	129.95	2996.10	93.68	10.4673	334.59	8.79	620.15	437.64	2.88	10.46

Source: all data was obtained experimentally by the CTM laboratory at UFMG

ANNEX G – TORQUE AND EFFICIENCY CURVES FOR THE YASA P400 ELECTRIC MACHINE

FIGURE A47 – EFFICIENCY CURVE OF THE YASA P400 ELECTRIC MACHINE

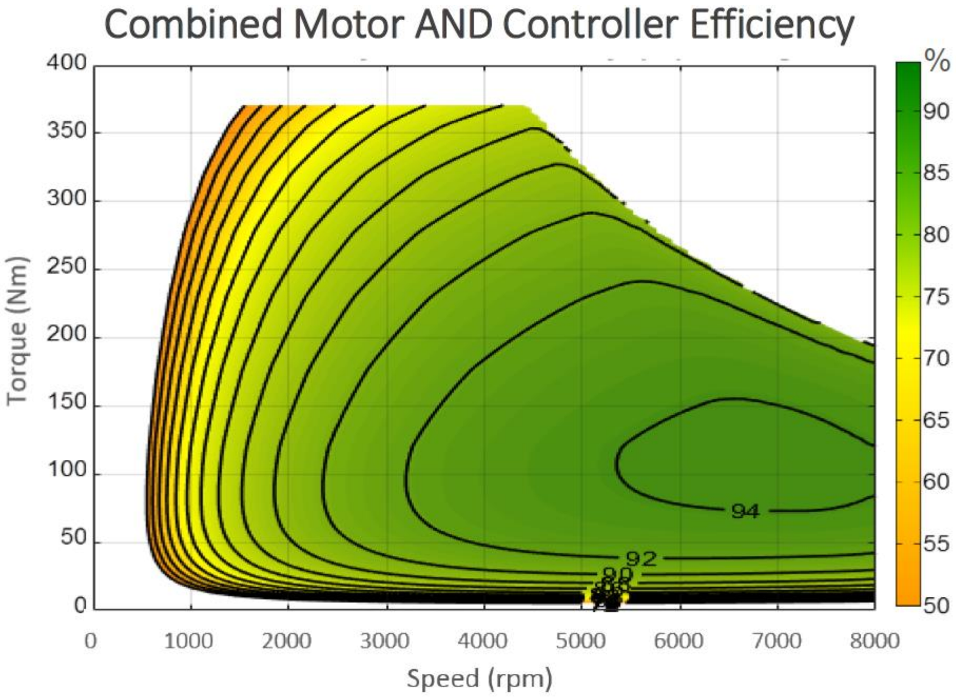

Source: YASA Limited (2018a).

FIGURE A48– CONTINUOUS POWER, PEAK TORQUE AND PEAK POWER OF THE YASA P400 ELECTRIC MACHINE

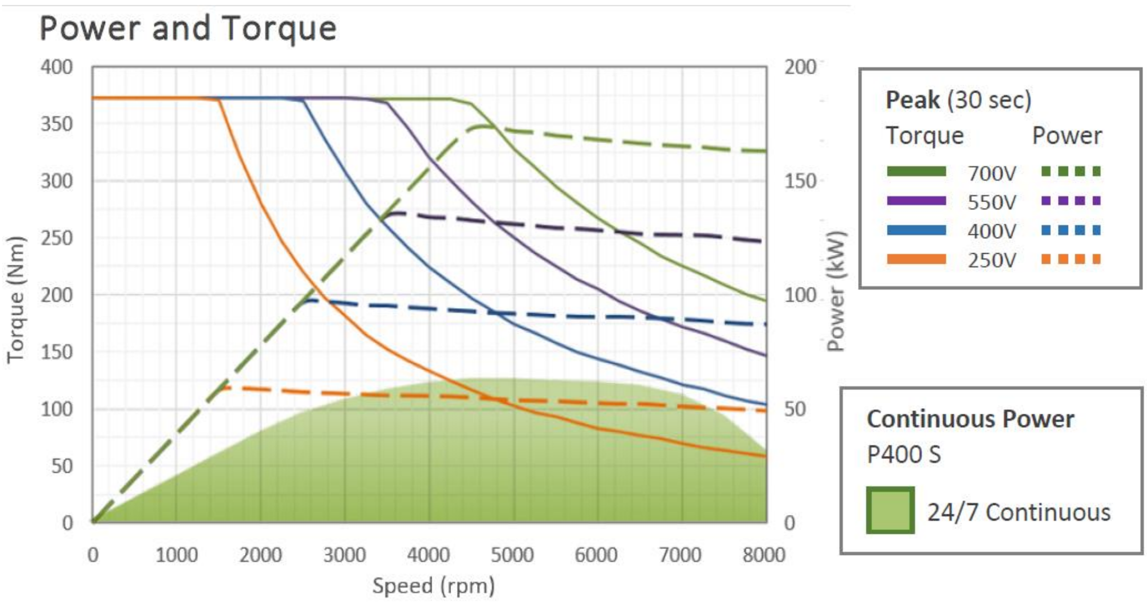

Source: YASA Limited (2018a).

ANNEX H – TORQUE AND EFFICIENCY CURVES FOR THE YASA 750R ELECTRIC MACHINE

FIGURE A49 – EFFICIENCY CURVE OF THE YASA 750R ELECTRIC MACHINE

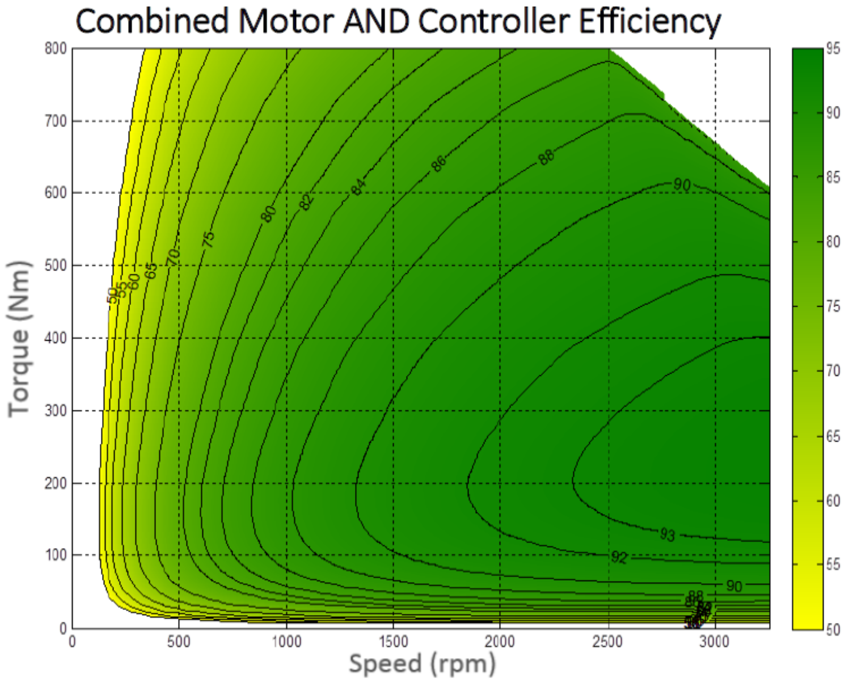

Source: YASA Limited (2018b).

FIGURE A50 – PEAK TORQUE AND POWER OF THE YASA 750R

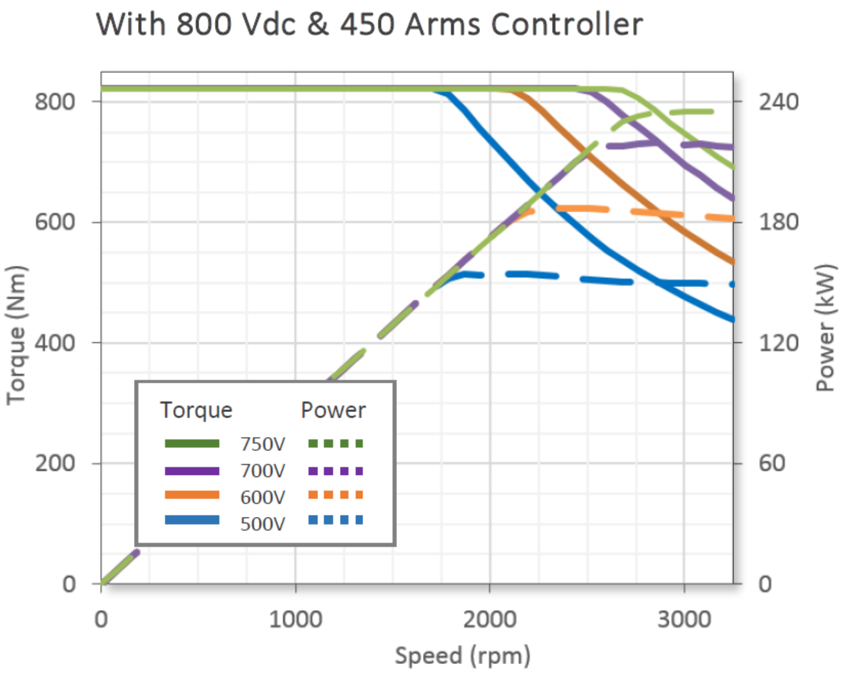

Source: YASA Limited (2018b).

FIGURE A51 – CONTINUOUS POWER (250 V), PEAK TORQUE AND PEAK POWER OF THE YASA 750R

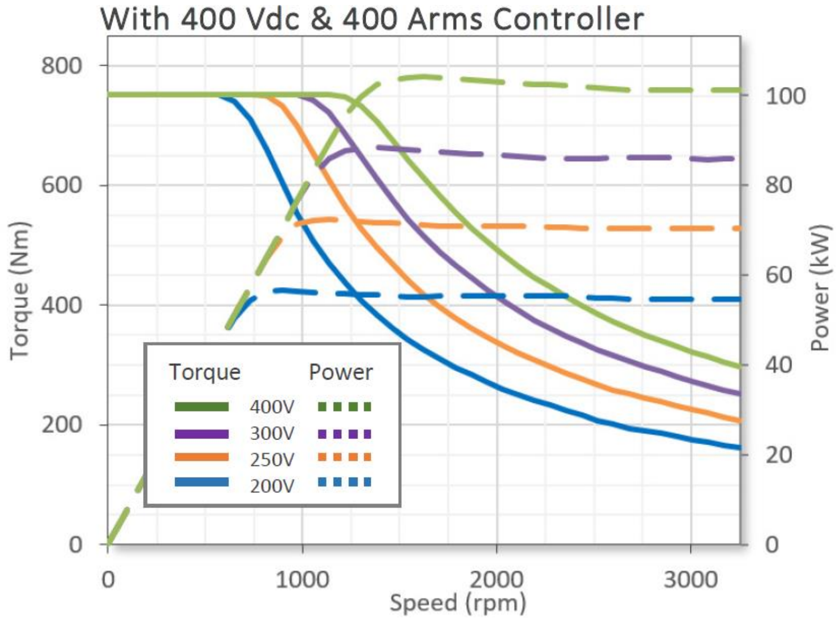

Source: YASA Limited (2018b).

The data sheet specified a continuous power up to 70 kW at 3000 rpm, when using a 40ºC coolant. Thus, the power curve of 250 V was assumed to be the continuous power.

ANNEX I – TORQUE AND EFFICIENCY CURVES FOR THE EMRAX 208 ELECTRIC MACHINE

FIGURE A52 – EFFICIENCY CURVE OF THE EMRAX 208 ELECTRIC MACHINE

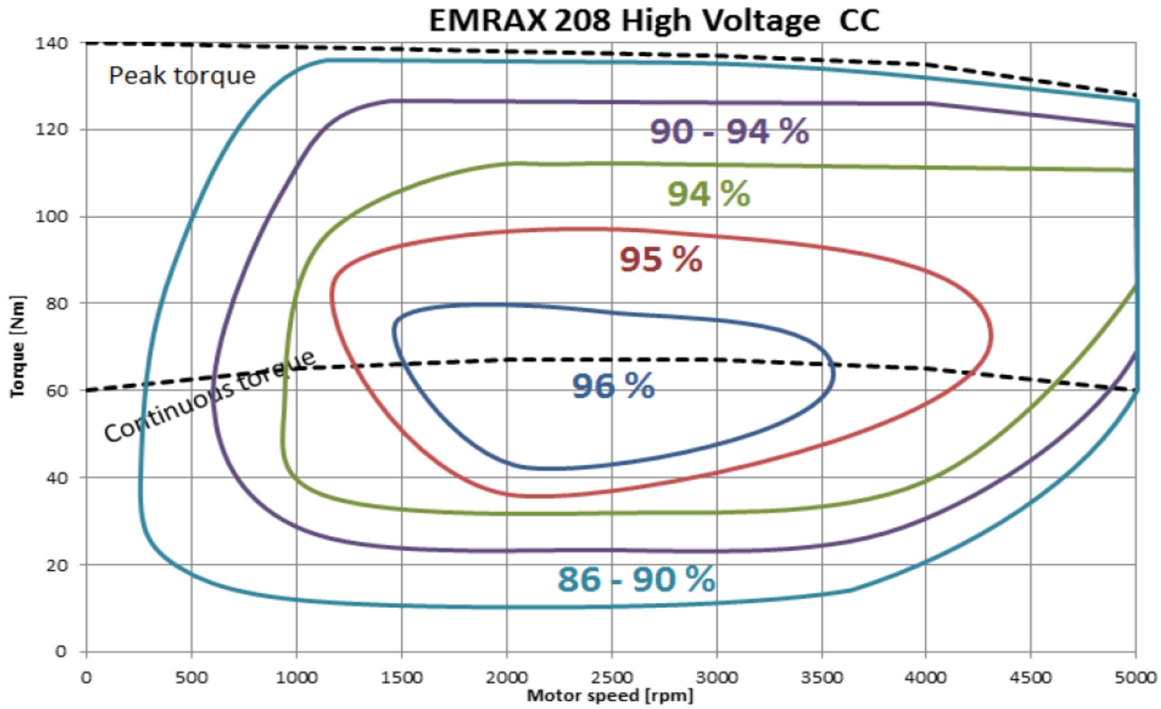

Source: EMRAX d.o.o. (2018).

FIGURE A53 – CONTINUOUS POWER AND TORQUE, AND PEAK TORQUE AND POWER OF THE EMRAX 208 ELECTRIC MACHINE

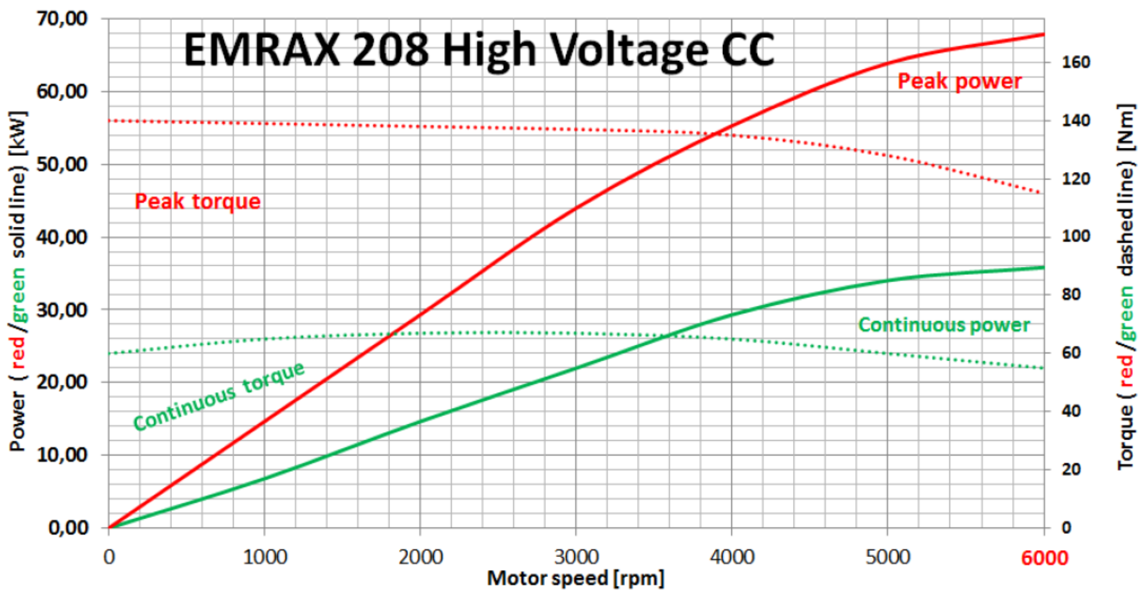

Source: EMRAX d.o.o. (2018).

ANNEX J – TORQUE AND EFFICIENCY CURVES FOR THE EMRAX 228 ELECTRIC MACHINE

FIGURE A54 – EFFICIENCY CURVE OF THE EMRAX 228 ELECTRIC MACHINE

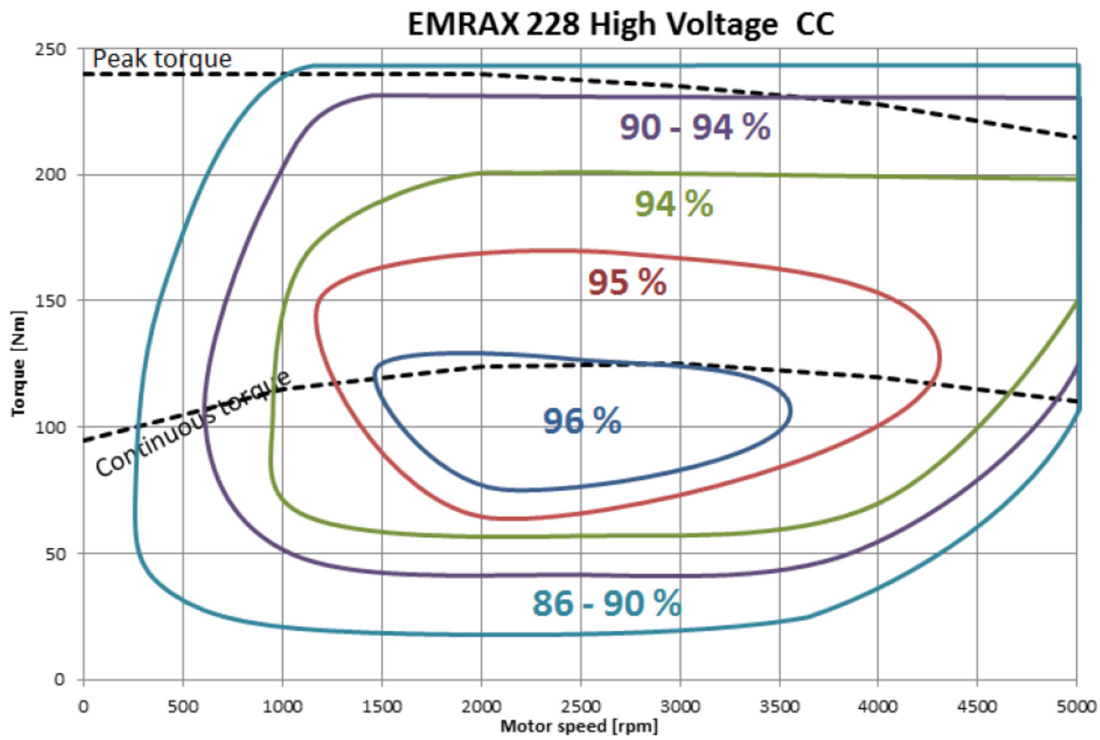

Source: EMRAX d.o.o. (2018).

FIGURE A55 – CONTINUOUS POWER, PEAK TORQUE AND PEAK POWER OF THE EMRAX 228 ELECTRIC MACHINE

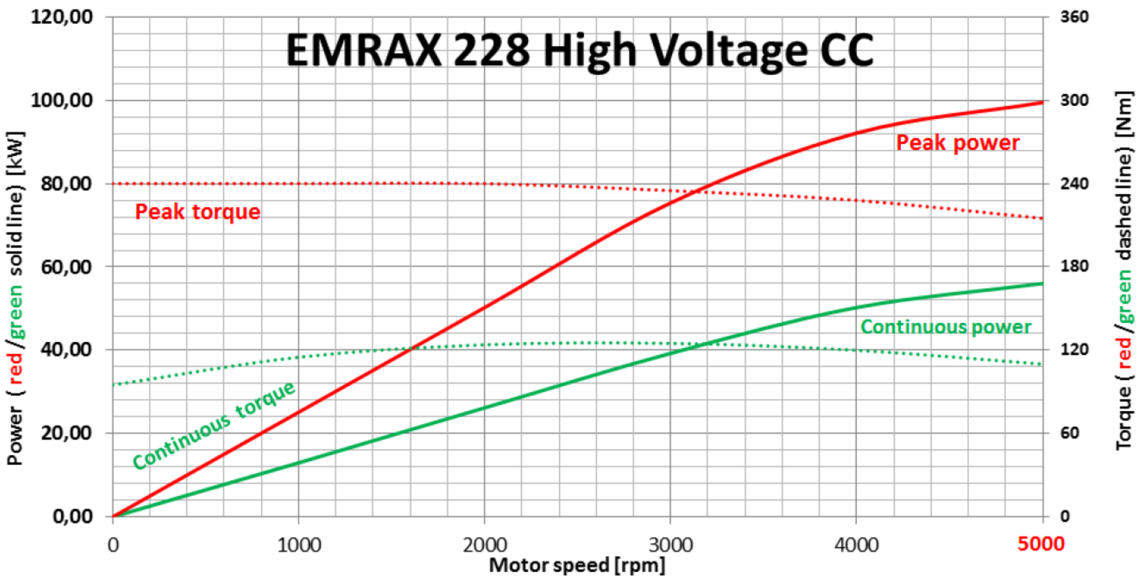

Source: EMRAX d.o.o. (2018).

ANNEX K – BATTERY REPORT SUMMARY OF THE VIN 4673

FIGURE A56 – OPEN CIRCUIT VOLTAGE (OCV) MAP OF VIN 4673

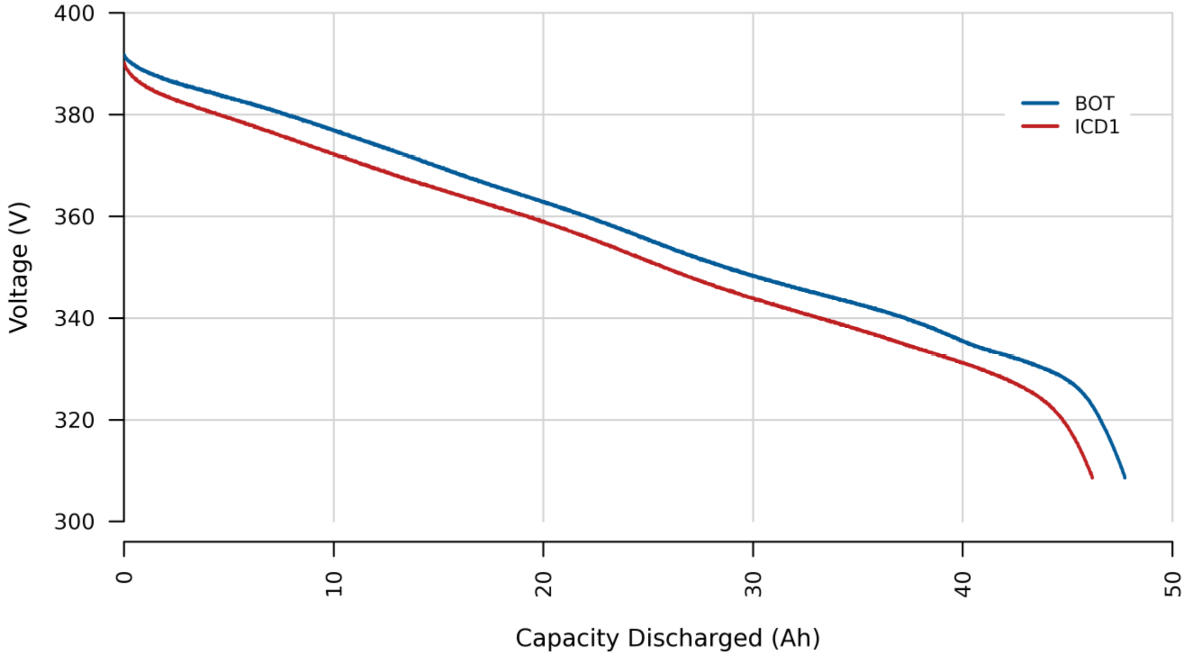

Source: Battery Pack Laboratory Testing Results - 2016 Chevrolet Volt VIN 4673 (IDAHO NATIONAL LABORATORY, [s.d.]).

FIGURE A57 – INTERNAL RESISTANCE MAP OF VIN 4673, WHILE CHARGING

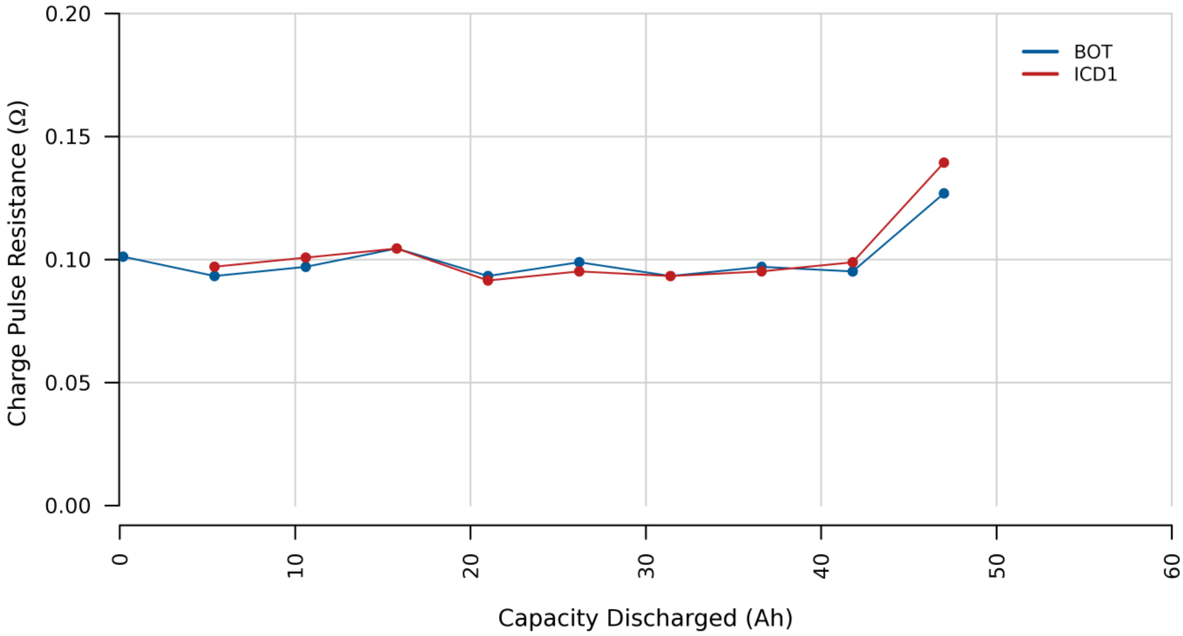

Source: Battery Pack Laboratory Testing Results - 2016 Chevrolet Volt VIN 4673 (IDAHO NATIONAL LABORATORY, [s.d.]).

FIGURE A58 – INTERNAL RESITANCE MAP OF VIN 4673, WHILE DISCHARGING

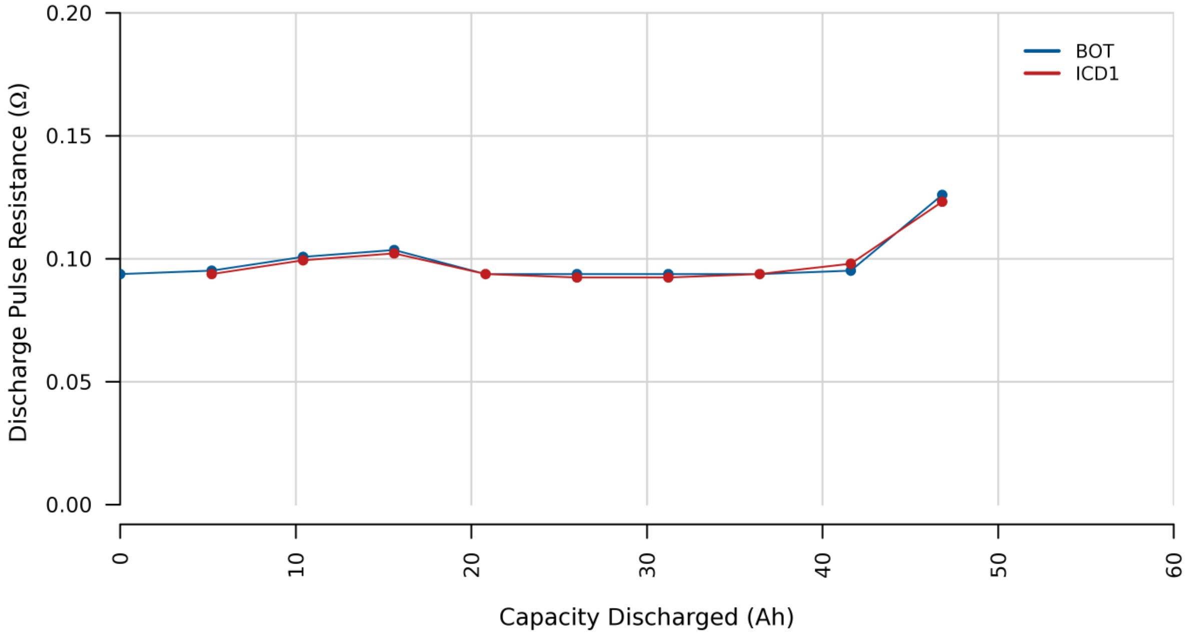

Source: Battery Pack Laboratory Testing Results - 2016 Chevrolet Volt VIN 4673 (IDAHO NATIONAL LABORATORY, [s.d.]).

FIGURE A59 – BATTERY CHARGE AND DISCHARGE POWER CAPABILITIES IN FUNCTION OF THE ENERGY DISCHARGED OF VIN 4673

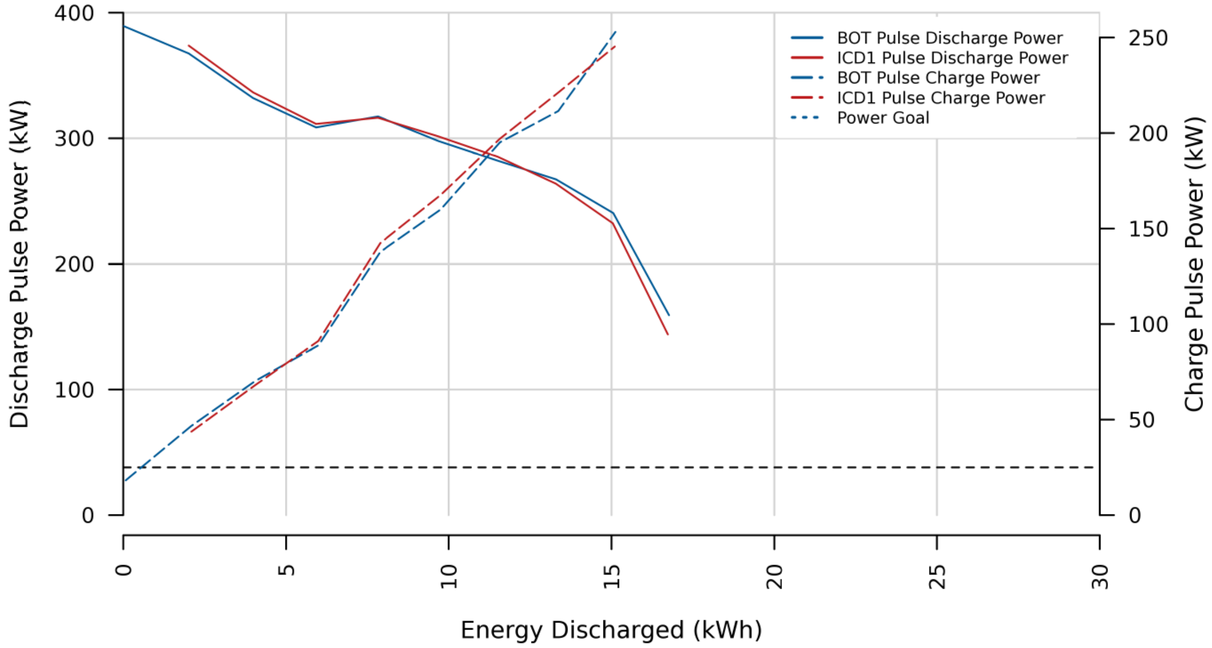

Source: Battery Pack Laboratory Testing Results - 2016 Chevrolet Volt VIN 4673 (IDAHO NATIONAL LABORATORY, [s.d.]).

ANNEX L – DATA MAPS USED FOR THE PROTOTYPE 1.0L ENGINE

Table A10 shows the mechanical output and fuel consumption maps used in the prototype engine, for both fuel strategies, while table A11 shows its engine friction map.

TABLE A10 – CHARACTERISTICS OF THE SIGMA ENGINE

Mechanical Output Map						Fuel Consumption Map					
E100 Fuel Strategy			E100+WI Fuel Strategy			E100 Fuel Strategy			E100+WI Fuel Strategy		
Engine Speed (rpm)	Accel. Position (%)	IMEP (bar)	Engine Speed (rpm)	Accel. Position (%)	IMEP (bar)	Engine Speed (rpm)	BMEP (bar)	ISFC (g/kWh)	Engine Speed (rpm)	BMEP (bar)	ISFC (g/kWh)
0	0	0	0	0	0	0	0	0	0	0	0
0.1	0	0	0.1	0	0	0.1	0	0	0.1	0	0
2750	0	0	2750	0	0	2750	0	0	2750	0	0
0	100	0	0	100	0	0	25	0	0	33.03	0
0.1	100	25	0.1	100	33.03	0.1	25	399.3	0.1	33.03	341.8
2750	100	25	2750	100	33.03	2750	25	399.3	2750	33.03	341.8

Source: all data was obtained experimentally by the CTM laboratory at UFMG.

TABLE A11 – CHARACTERISTICS OF THE SIGMA ENGINE

Engine Friction Map					
E100 Fuel Strategy			E100+WI Fuel Strategy		
Engine Speed (rpm)	BMEP (bar)	FMEP (bar)	Engine Speed (rpm)	BMEP (bar)	FMEP (bar)
0	0	0	0	0	0
0.1	0	0.01	0.1	0	0.01
800	0	0.2	800	0	0.2
1000	0	0.3	1000	0	0.3
2000	0	0.5	2000	0	0.5
2500	0	0.8	2500	0	0.8
2750	0	1	2750	0	1
0	0	0	0	0	0
0.1	25	2.33	0.1	33.03	2.47
800	25	2.33	800	33.03	2.47
1000	25	2.33	1000	33.03	2.47
2000	25	2.33	2000	33.03	2.47
2500	25	2.33	2500	33.03	2.47
2750	25	2.33	2750	33.03	2.47

Source: all data was obtained experimentally by the CTM laboratory at UFMG.